**FACULTY
OF MATHEMATICS
AND PHYSICS**
Charles University

DOCTORAL THESIS

Jiří Doležal

Spectroscopy of single molecules in STM nanocavity

Department of surfaces and molecular structures, Institute of Physics of the
Czech Academy of Sciences

Supervisor of the doctoral thesis: Mgr. Martin Švec, PhD

Study programme: Physics of Surfaces and Interfaces

Prague 2023

Title: Spectroscopy of single molecules in STM nanocavity

Author: Jiří Doležal

Institute: Department of surfaces and molecular structures, Institute of Physics of the Czech Academy of Sciences

Supervisor: Mgr. Martin Švec, PhD, Department of surfaces and molecular structures, Institute of Physics of the Czech Academy of Sciences

Abstract:

Scanning tunneling microscopy-induced luminescence (STML) combined with high-resolution atomic force microscopy (AFM) is a powerful tool for studying the photophysics of individual molecular emitters on surfaces. However, the mechanism of energy conversion between tunneling electrons and photons in decoupled systems placed in a nanocavity of STM is not fully understood as it depends on many variables.

This thesis presents a range of proof-of-concept experimental approaches. The viability of CO-terminated tips for STML is demonstrated by performing subnanometer-resolved spectroscopy and mapping of photon intensity acquired over zinc phthalocyanine on NaCl/metal substrate. For the same molecule, time-resolved phase fluorometry is devised and is used to reveal the exciton and charge dynamics as a function of the applied bias voltage. Of more fundamental character, the role of the chromophore environment on its exciton emission and binding energy is studied. For the first time, we observed and explained the presence of molecular librations in molecules on the surface from a comb-like emission line resulting from the exciton-libron coupling and the chiral adsorption geometry. Finally, exciton delocalization in molecular aggregates is mapped using the tip nanocavity capable of detecting the dark states, inaccessible in far-field spectroscopies. The experimental results are compared to theoretical simulations and discussed extensively.

Keywords: STM, AFM, STML, luminescence, molecules, libration, chromophore

Contents

Introduction

The miniaturization of electric circuits in information technology during the past 70 years revolutionized almost every aspect of life in societies worldwide. Currently, electronic devices are dominantly based on silicon technology utilizing only a few elements from the periodic table for building the units in a top-down approach. However, as the size of the transistors approaches the single-atom dimensions, where the quantum effects will hamper their reliable operation, research of more efficient and elegant principles is of great importance for our sustainable future. The concept of quantum computing using qubits instead of classical bits is attaining a lot of attention but its wide application in practice needs to overcome many fundamental challenges such as finding a suitable physical system for creating qubits performing quantum operations free of spurious decoherence effects. Another strategy is to mimic processes in nature. Software/hardware neural networks inspired by biological systems are now the main problem-solving methods in artificial intelligence. The utilization of molecules, which are the basic building blocks in nature, offers a very rich building kit with a choice of millions of well-defined objects with distinct properties. This approach has been put to work in organic light-emitting diodes (OLEDs), sensors and organic solar cells and it was also proposed for molecular-scale electronics [1]. For a correct understanding of the phenomena on the atomic level, an adequate theoretical description is necessary, based on precise and thorough experimental data.
But how to address objects as small as individual atoms and molecules?

Industrial progress had to be always preceded by characterization and visualization tools. One of the most influential instruments invented in human history was the optical microscope. Its resolution is inherently limited by the wave nature of photons which are diffracted on the observed objects. The nearest distance between two objects that can be resolved using visible light is around 250 nm, far more than the scale of atoms and molecules. The diffraction of X-rays or particles like electrons of much shorter wavelengths can be harnessed to obtain information about atomic positions in a crystal lattice. However, focusing and the observation of individual atoms remained elusive until the scanning version of the transmission electron microscope was improved in the 1970s [2]. The scanning tunneling microscope (STM) invented one decade later [3] enabled not only nondestructive imaging of electronic landscapes of surfaces with atomic precision but also opened the way to direct atomic manipulation [4] with use of the sharp scanning probe. After almost half a century since its invention, this methodology is, quite surprisingly, still developing and has evolved into a precise method capable of atomic and molecular spin sensing, ultimate-resolution atomic force microscopy (AFM) [5] or time- and energy-resolved spectroscopies [6, 7]. In particular, the combination of ultra-high vacuum cryogenic STM and AFM is a great tool for studying the electronic properties of molecules and their atomic structure.

With the capabilities of such a powerful technique as the combined STM/AFM methodology certainly offers, it would be of utmost importance and impact to enhance it by adding sensitivity to optical properties of the nanoscopic objects. The main questions are how to achieve such a challenging task, seemingly defy-

ing limitations imposed by physics known for centuries. The STM tip provides a sub-nm localized channel of tunneling electrons, which can create excitations. Moreover, localized plasmonic modes emerge when a cavity is formed between the metallic tip and the sample. The plasmonic modes mediate the radiative decay of excitations out to the far field. The concept of electric field enhancement on plasmonic nanostructures has been known from the surface- and tip-enhanced Raman scattering techniques capable of detecting signals from single molecules, but they had never achieved the spatial resolution of STM until 2013 [8]. First, the STM-induced light emission showed sub-nm variation when scanning over metallic samples [9] and in 2003, Qui et al. [10] demonstrated intrinsic emission of a single electronically decoupled molecule using STM-induced luminescence (STML). The enhancement of the radiative decay rate of molecules in the optical cavity enabled them to obtain sufficiently intense signals from single chromophores. It took 13 years from the publication of this exceptional work until another substantial improvement, using NaCl trilayer on noble metals as a decoupling platform for molecules, was realized. Tip manipulation of the adsorbed molecules on NaCl permitted the study of fundamental processes of energy transfer [11] and superradiance [12] at the atomic scale.

I started my PhD two years after these observations were reported. At that time, there was only about a dozen publications using STML as a tool to address the single-molecule luminescence on NaCl. Many fundamental questions about the principles and applicability of STML were open, these among others: What can we learn from the spatial dependence of the luminescence signal (photon maps)? What is the origin of the lineshapes observed in STML? How does the NaCl layer influence the molecular emission? Is Kasha's rule valid in STML? Can we observe both fluorescence and phosphorescence? How long do the excited states live? How localized is the electromagnetic field in the tip-sample cavity? Does photoluminescence in the nanocavity work in analogy to electroluminescence? And can we reach a strong-coupling regime?

I can say now that since that, the general understanding of the result observed in STML has advanced significantly. However, the progress was far from straightforward. Many top published results and especially their interpretations including ours have been overcome and corrected. In my thesis, I take the great opportunity to provide up-to-date explanations regarding these works, based on the current understanding of the problems, without lessening their importance to the development of the field.

The thesis is divided into 8 chapters. Chapter 1 summarizes the history and the theoretical concepts of the used methods and the key results in the STML field. Chapter 2 describes the experimental setup which has been gradually improved to the current state during my PhD studies. One section is devoted to the fabrication of tips suitable for photoexcitation for the implementation of STM-photoluminescence and tip-enhanced Raman scattering. Chapters 3–8 are based on the 6 published works. The performance of CO-tips in STML is studied in chapter 3 and the possibility of the combination of STM, AFM and STML is demonstrated. The role of the environment on the electrical and optical properties of molecules is studied in chapter 4. Time-resolved methods for measuring the time constants in STM electroluminescence process are presented in chapter 5. A methodology for calibration of the frequency-dependent transfer function of

the high-frequency bias wiring, based on the broadening of the plasmon cutoff in the electroluminescence spectrum, is presented in chapter 6. Visualization of the exciton delocalization in molecular aggregates involving the possibility of the dark state detection with the nanocavity is shown in chapter 7. Observation of the exciton coupling to molecular librations on chirally adsorbed chromophores in luminescence spectra is reported in chapter 8.

1. Theoretical background

In the scope of this thesis, two well-established surface science techniques were used, the Scanning tunneling microscopy (STM) and the non-contact Atomic force microscopy (nc-AFM). This chapter starts with a brief historical outline of Scanning probe microscopy followed by a basic theoretical description of its operation and its utilization in the study of single molecules on thin insulating surfaces. In the second part of the chapter, we describe the optical properties of molecules and reveal how the light emitted by a single molecule can be detected in the near-field of the scanning probe.

1.1 History of scanning probe microscopy

The history of scanning probe microscopy dates back to the early 1970s when Russel D. Young presented the Topografiner [13], a predecessor of today's STM. The instrument consisted of a metallic tip and a conductive sample and was operated in a field emission regime, where the tip-sample separation was around 100 nm. Feedback control as well as the rough vacuum was already present. Young was aware that for the lateral resolution better than 20 nm, which was the estimated theoretical limit, operation in a tunneling regime would be necessary. However, he never succeeded in the realization of tunneling current feedback mostly due to the instability in the tip-sample distance caused by vibrations. One decade later in 1981, IBM researchers G. Binnig and H. Rohrer constructed the first STM [3]. It was the first instrument capable of imaging the probed conductive sample with atomic precision [14]. Soon after the STM invention, they turned their attention to the Si(111)-(7 × 7) surface reconstruction. They were able to resolve individual Si adatoms in the reconstruction in real space [15] and solved one of the most intriguing problems in surface science at that time. This was a breakthrough in the popularity of the STM, which led to the award of the Nobel Prize in Physics in 1986 to G. Binnig and H. Rohrer.

G. Binnig continued in his pursuit to foster the scanning probe methodology and together with C. Quate and C. Gerber invented the atomic force microscope [16]. The unique idea in the concept of measuring atomic force acting between the tip and the sample lies in its applicability in all kinds of surfaces as no conductivity and tunneling current is necessary. When the original rather complicated detection scheme using a scanning probe at the end of a flexible cantilever and STM as a deflection measure was replaced by the laser-based optical lever scheme AFM quickly found its way to the research and also industry. Nowadays, many instruments working at ambient or liquid conditions and operated at contact mode with force feedback are commercially available. AFM as a surface science tool capable of atomic resolution was not so widespread in the 80s and 90s. The biggest problem of the contact AFM is the large contact area that hinders obtaining atomic resolution. It cannot be easily used in ultra-high vacuum (UHV) as the clean surfaces tend to stick together. Therefore, the dynamic AFM using an oscillating probe with high amplitudes was used to prevent the jump-to-contact problem. The short time spent in the reach of short-range forces responsible for atomic corrugation was the limiting factor of soft cantilevers used at that time.

It took several years till the first scientist Franz Giessibl obtained atomic resolution on highly reactive and therefore challenging Si(111) -7 × 7 surface in 1994 [17]. Later in the 2000s, stiffer cantilevers such as qPlus tuning fork or length extension resonator [18] sensors in combination with improved feedback electronics enabled them to obtain atomic resolution [19, 18] routinely. The biggest leap forward, however, was the functionalization of the metal tip by a small moiety — CO molecule — that was first described in 2009 by Leo Gross [5]. It enabled even submolecular resolution due to the Pauli repulsion and flexibility of the CO-molecule on the tip apex [20, 21].

1.2 Scanning tunneling microscopy

The following section is modified from the author's Master thesis [22].

1.2.1 Tunneling effect

STM operation is based on the quantum tunneling effect. The wavelike nature of matter gives a certain probability to particles to overcome (tunnel through) potential barriers insurmountable in the picture of classical mechanics. The probability of tunneling decreases exponentially with the barrier height, width and particle mass thus limiting this process to the atomic scale. Tunneling is essential in many phenomena in nature such as nuclear fusion [23] and fission [24], chemical reactions [25] or DNA mutation [26, 27]. Let us consider a simplistic case, 1D rectangular barrier sketched in Fig. 1.1 of height W and width d and a particle of energy E and mass m. The probability P for the particle to traverse the barrier is given by the solution of stationary Schrödinger equation and reads

$$P \propto e^{-2kd}, \tag{1.1}$$

where

$$k = \sqrt{\frac{8\pi^2 m(W - E)}{h^2}} \tag{1.2}$$

and h is the Planck constant [28].

1.2.2 Principle of STM

The STM microscope comprises a sharp metallic tip and a conductive sample separated by several Å such that their orbitals overlap. The three-dimensional barrier is realized by the vacuum region in between the electrodes and its height is determined from the work functions of the electrodes. The probability of electron tunneling from one electrode to another and vice versa is similar and will result in zero net tunneling current unless a bias voltage is applied. Biasing one electrode offsets energy levels of the tip and sample and as a result, electrons will tunnel from the unoccupied electronic states of the negatively biased electrode to the occupied states of the positively biased electrode.

The tip or sample is attached to a piezoelectric scanner allowing positioning in x, y and z directions with picometer precision. The rigid mechanical loop and system on two external mechanical dampings protect the STM junction against
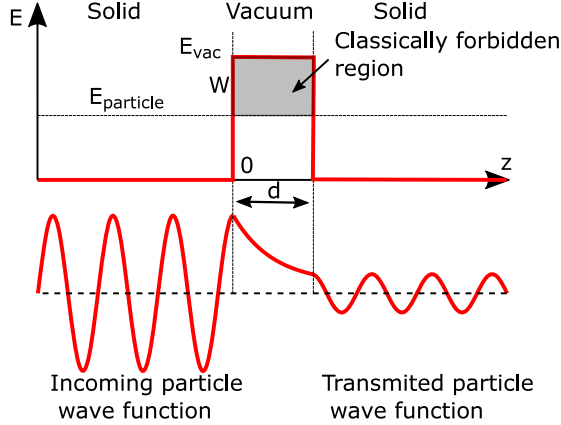
Figure 1.1: Illustration of electron tunneling through a 1D barrier of height W and width d. The upper graph shows the potential for a solid-vacuum-solid configuration, where vacuum is the barrier. The lower graph shows the real part of the electron wave function oscillating in front of the barrier, exponentially decaying inside the barrier and again oscillating past the barrier.

vibrations thus avoiding tip crashing and limiting noise propagated into tunneling current. The STM images of tunneling current, tip height or other parameters are recorded during scanning the tip along the surface. For voltages V_T below the barrier height and low temperatures the tunneling current can be expressed as [28]

$$I \approx 18 \frac{V_T k}{10^4 \Omega d} A_{\text{eff}} e^{-2kd}, \tag{1.3}$$

where $2k\,(\text{Å}^{-1}) = 1.025\sqrt{W}\,(\text{eV})$, W is the average work function of the electrodes representing the barrier height. The typical effective area involved in tunneling is expressed by A_{eff} and determines the lateral resolution, d is the tip-sample separation and Ω is the Ohm unit. Plugging typical $W = 5$ eV for metals in equation 1.3 we evaluate the change of the tunneling current I by one order of magnitude for the 1 Å change in the distance. This clarifies why even a macroscopically blunt tip can provide atomically resolved images. It is sufficient for scanning on flat crystalline samples if the tip apex is formed by a cluster of atoms where the majority of tunneling current flows through. On the other hand, due to the exponential current dependence, a successful operation of STM requires damping of the vibration amplitude in z on the order of a few pm.

There are two standard modes of operation of the STM – constant current mode and constant height mode. The **Constant current mode** is the most frequently used one. The tunneling current is held constant by a feedback loop. For an electronically homogeneous surface, constant current means constant separation d and the tip movement in the cartesian coordinate system aligned with the sample corresponds to the topography. Different measured physical quantities can be used as input for the feedback loop in various scanning probe microscopy (SPM) methods, e.g. frequency shift in nc-AFM. The major advantages of this mode are that it can be used for large scanning areas of various roughness without the risk of destroying the tip. Moreover, the thermal drift in the image can be post-processed e.g. by plane correction. In the **constant height mode** the tip is scanning on the predefined xy plane keeping the z constant. Several conditions have to be fulfilled for its utilization. Since the tip-sample distance providing a

useful signal is less than 1 nm, the surface roughness of the scanned area must be within that range. The thermal drift and creep have to be stabilized and compensated. Despite the limitations, the mode has been frequently used in this thesis. Its main advantage lies in the fast operation necessary for a frequency-modulated nc-AFM technique which encompasses additional feedback loops. The constant z eliminates the influence of tunneling current on other detected quantities such as dI/dV, frequency shift, photon signal in "photon maps" etc. It is therefore predominantly used for multichannel SPM as it can be easily compared to theoretical images generated on the same xy plane [21].
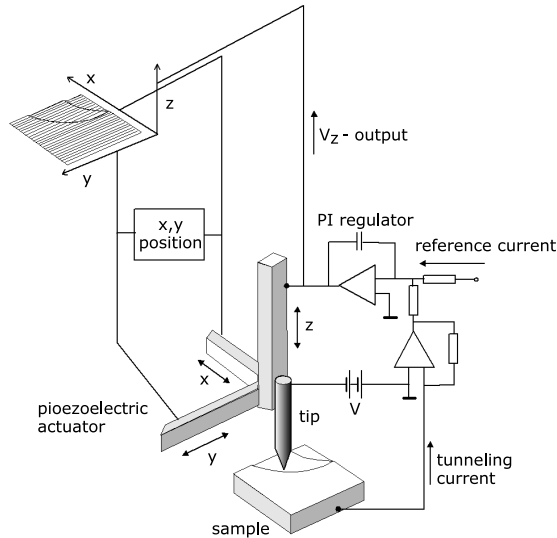
Figure 1.2: Schematic view of the STM. Tunneling current flows in a feedback loop which adjusts the z position of the tip. z as a function of x and y is plotted. Adapted from a Thin Films group archive.

1.2.3 Theory of tunneling

The first analytical approach to tunneling is the Bardeen model which was introduced before inventing the STM in 1961 for metal-insulator-metal heterostructures [29]. This model considers a tip plus barrier and a sample plus barrier as two separate systems. Specific theoretical approaches differ from each other in the wave functions of each electrode used. The wave functions of these two systems can be approximated as in the case of the 1D barrier depicted in Fig. 1.1, or in the 3D model, but they are more complicated taking the geometry of spherical symmetric tip and flat sample into account. The transition rate from one electrode to another is calculated using time-dependent perturbation theory and the tunneling current is proportional to the rate.

The general equation for the tunneling current in the low-temperature limit can be written as

$$I = \frac{8\pi^2 e}{h} \sum_{i,f} |M_{fi}|^2 \delta(E_f - E_i), \tag{1.4}$$

where we sum over all combinations of initial states and final states of electrons both for the tip and the sample in the applied bias window. $\delta(E_f - E_i)$ denotes

that the tunneling can occur only on the same energy levels. $|M_{fi}|$ is a matrix element that denotes the probability of an electron passing the barrier and depends on ψ_i and ψ_f as well as on the shape of the barrier [30].

Two kinds of approximation of Bardeen's equation (1.4) are the most widespread. In the **Tersoff-Hamann** approximation the applied voltage bias between the tip and the sample is considered to be small compared to the barrier height. Energy dependence of the matrix element and energy dependence of the densities of states is neglected. The tip wave function is approximated by a spherical s-wave. This approximation is often used for the simulation of STM images.

Energy-dependent approximation deals with a 1D barrier approximation of a rectangular shape but takes into account energy dependence of densities of states of the tip and the sample. With this approximation, we are able to derive important equations used in scanning tunneling spectroscopy (STS). Again, in the low-temperature limit, tunneling current can be approximated as

$$I(V, d) = \frac{8\pi^2 e}{h} \int_0^{eV} \rho_{\text{tip}}(\varepsilon - eV)\rho_{\text{sample}}(\varepsilon)T(\varepsilon, V, d)d\varepsilon, \qquad (1.5)$$

where ε is an energy relative to the Fermi energy of the sample depicted in Fig. 1.3, V the applied bias voltage to the sample, ρ_{tip} and ρ_{sample} are densities of states of the tip and the sample respectively and $T(\varepsilon, V, d)$ is the transmission factor given by

$$T(\varepsilon, V, d) \propto \exp\left[-2d\sqrt{\frac{8\pi^2 m}{h^2}\left(\frac{\Phi_{\text{tip}} + \Phi_{\text{sample}}}{2} + \frac{eV}{2} - \varepsilon\right)}\right] \qquad (1.6)$$

where m is the mass of the electron, Φ_{tip} and Φ_{sample} work functions of the tip and the sample respectively. For low bias voltages, the equation 1.5 can be further simplified if we neglect the energy and voltage dependence of T and remove it from the integral.
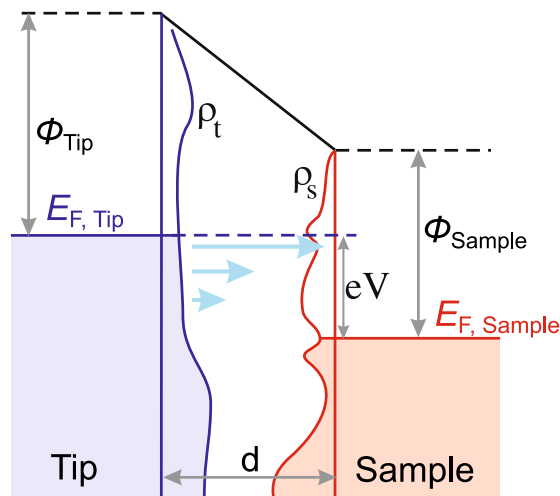
Figure 1.3: Energy level diagram of the tunneling junction. The applied bias shifts the Fermi level by eV. Density of states are represented by ρ_{tip} and ρ_{sample} (the filled states are coloured). Adapted from [30].

1.2.4 Scanning tunneling spectroscopy

As can be inferred from Eq. (1.5), the tunneling current is distance dependent and proportional to the density of states of the tip and the sample. If we consider constant density of states (often assumed for a clean metallic tip) the first derivative of the tunneling current with respect to the bias voltage is proportional to

$$\frac{\mathrm{d}I}{\mathrm{d}V} \propto \rho_{\mathrm{sample}}(d, \varepsilon) T(\varepsilon, V, d). \tag{1.7}$$

For a qualitative evaluation of the density of states (e.g. mapping the orbitals of molecules on thin insulating layers), that transmission factor bias dependence can be neglected and the differential conductance is directly interpreted as a local density of states (LDOS). STS measurements — obtaining the $\mathrm{d}I/\mathrm{d}V$ — can be done in two ways. A simple approach is to numerically differentiate the measured $I - V$ characteristics. Unfortunately, numerical differentiation amplifies the noise in the signal. Therefore, synchronous lock-in detection is often used for $\mathrm{d}I/\mathrm{d}V$ spectroscopy and enables also $\mathrm{d}I/\mathrm{d}V$ spatial mapping.

Lock-in detection

Lock-in amplifier adds a small modulation voltage $V_M \cos \omega t$ to a bias voltage and this modulation appears in the measured current: $I(t) = f(V + V_M \cos \omega t)$. The modulation frequency f should be higher than the cutoff frequency of the feedback loop and should be located in a low-noise region in the noise power density spectra (around 900 Hz). The modulation voltage has to be as small as possible providing a sufficient signal (1-20 mV yielding lockin current on the order of picoamperes in our case). The phase shift between the reference modulation signal and the measured signal which emerges due to the parasitic capacitance of the wires (consider a parallel RC circuit) in the STM must be eliminated. In practice, before each STS measurement, the tip is slightly retracted out of the contact and only the AC component of the measured current flows through the tunneling junction (the phase shift of the measured current is 90°) and the capacitance can be measured and the phase-shift eliminated with the lock-in amplifier. If we slowly change the voltage during an $I(V)$ measurement, the measured tunneling current can be estimated using Taylor expansion as:

$$I(V + V_M \cos \omega t) \propto I(V) + \frac{\mathrm{d}I(V)}{\mathrm{d}V} V_M \cos \omega t + \frac{\mathrm{d}^2 I(V)}{\mathrm{d}V^2} \frac{V_M{}^2}{2} \cos^2 \omega t + ... \tag{1.8}$$

and a trigonometric identity gives us

$$\cos^2 \omega t = \frac{1}{2} + \frac{1}{2} \cos 2\omega t. \tag{1.9}$$

We can see that the harmonic term with ωt has an amplitude proportional to the first derivative of the tunneling current with respect to the voltage and the term with $2\omega t$ – second harmonic is proportional to $\dfrac{\mathrm{d}^2 I(V)}{\mathrm{d}V^2}$. With the help of filters that are implemented in the lock-in amplifier, amplitudes of desired n-th harmonic frequencies are obtained. While in STS we use the first harmonic and the first derivative, the second derivative is used in inelastic tunneling spectroscopy. For

getting a high-quality spectrum, each voltage step should last at least 10 periods of modulation.

The energy resolution of the STS spectrum is limited by the thermal broadening of the Fermi level by 3.2 kT, by the instrumental broadening by the modulation voltage and by the inherent electrical noise in the bias voltage. The total error can be calculated as [30]:

$$\Delta E = \sqrt{(2eV_{\text{mod,RMS}})^2 + (0.28 \text{ meV/K} \cdot T)^2}.$$

(1.10)

At 5 K, the ultimate energy resolution is 1.4 meV.

1.2.5 Double-barrier tunneling junction

Study of energies of molecular orbitals close to their *in vacuo* state in scanning tunneling spectroscopy requires their sufficient decoupling from the conductive sample. When adsorbed on bare metal, molecular orbitals are hybridized with the substrate which leads to their broadening and HOMO-LUMO gap narrowing ([31]). To circumvent this, molecules can be either separated from the conduc-
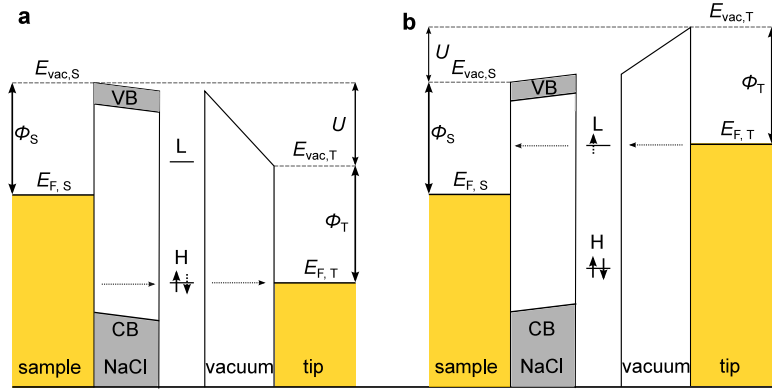
Figure 1.4: Energy scheme of the double-barrier tunneling junction consisting of a molecule adsorbed on NaCl/metal. The resonant tunneling takes place when the bias voltage U is applied such that molecular orbitals are aligned with one of the Fermi levels. a) Electron tunneling through HOMO and sample Fermi level $E_{\text{F,S}}$. b) Electron tunneling through LUMO and tip Fermi level $E_{\text{F,T}}$.

tive metallic sample by a few atomic layers of insulator [10, 31] or stacked in multilayers. For both cases, tunneling through a double-barrier (see Fig. 1.4) junction needs to be considered. The important aspect for interpreting the STS results is the voltage profile along the junction and especially the voltage drop on the dielectric spacer between the conductive sample and the molecule. In a simple approximation, the double-barrier tunneling junction can be treated as two capacitors C_{spacer} in series and the voltage drop on the spacer

$$U_{\text{spacer}} = \frac{U}{1 + \frac{\varepsilon_{\text{spacer}} d_{\text{vac}}}{\varepsilon_{\text{vac}} d_{\text{spacer}}}},$$

(1.11)

where the spacer and vacuum capacity are $C_{\text{spacer}} \propto \frac{\varepsilon_{\text{spacer}}}{d_{\text{spacer}}}$ and $C_{\text{vac}} \propto \frac{\varepsilon_{\text{vac}}}{d_{\text{vac}}}$ respectively. Plugging in the typical values for a molecule on 3 ML of NaCl and tip tunneling to/from frontier orbitals (10Å spacer thickness consisting of 7.8Å NaCl

+ 2.5 Å molecule and $d_{\text{vac}} = 5 - 9$ Å) one obtains a relative voltage drop of 16-25 %. This is a remarkably high value not consistent with the experiments on ZnPc/3 ML NaCl [32, 33] or pentacene on 2 ML NaCl [31], where the position of positive/negative ionic resonances in STS does not change with the tip-molecule separation significantly. We think that the negligible voltage drop on the thin NaCl layer can be attributed to these effects: 1) non-realistic 1D capacitor model overestimates the voltage drop on NaCl in contrast to the 3D model, where the voltage drop reduces almost by a factor of 2 for a sharp tip [34]; 2) 2–4 NaCl layers still enable propagation of the substrate surface state [35] and cannot be treated as a bulk insulator in contrast to thick (< 10 ML) NaCl layers. The detailed understanding of the voltage drop across NaCl certainly deserves further studies.

Another feature observed in STS, the broad PIR and NIR peaks on NaCl stems from a strong electron coupling to the phonons of ionic substrate [31]. The single-electron picture shown in Fig. 1.4 is indeed a simplification that attributes the contrast of observed positive ion resonance in dI/dV maps to the highest occupied molecular orbital (HOMO) and negative ion resonance to the lowest unoccupied molecular orbital (LUMO) for a closed-shell molecule. However, other peaks in STS can occur [36] which needs a complete many-body scheme for their explanation. The many-body scheme captures all kinds of processes such as orbital renormalization upon their depletion or occupation with electrons [37] and different tunneling channels depending on the valence and conduction bands of NaCl, metal surface states and many-body molecular states. Also, inelastic processes such as exciton formation followed by rapid decay and tunneling through other molecular orbitals [38] might play a role. It was also suggested that the in-gap image of the molecule out of the resonance condition is determined by its electronic structure [39] (sum of orbitals even far from the Fermi level with different weights) and not by its backbone geometry.

1.3   Atomic force microscopy

In AFM, the force between the tip and the sample is measured. Using a very sharp tip for its detection, the force can be mapped in real space with atomic resolution. Tip functionalization with a well-defined small flexible moiety — most commonly a CO molecule — can provide the desired sharp contrast of intramolecular bonds. Force spectroscopy can gain valuable insight into the system as the total force consists of many individual contributions - attractive van der Waals forces, electrostatic force and Pauli repulsion. Therefore, by varying the tip-sample distance, electric field and other parameters, individual force components can be in principle extracted.

1.3.1   Static AFM

The ideal force sensor is a spring, usually in the form of a cantilever on which the tip is mounted. Hooke's law directly expresses the force F as $F = -kz$ where k is the stiffness of the cantilever and z is the distance the cantilever is bent relative to its equilibrium position without the sample presence (deflection)[30]. The deflection is usually measured with a laser beam and its reflection from the

mirror mounted on the back of the cantilever on a photodiode. This scheme is called static AFM or contact AFM as the probe is in contact with the sample and there is no oscillation of the cantilever. There is a major drawback of the static AFM - instability of the junction preventing to obtain atomic resolution. The soft cantilevers providing on one hand low signal-to-noise ratio suffer from jump-to-contact problem [40]. If the force gradient exceeds the cantilever stiffness $\frac{\partial F}{\partial z} > k$ the jump-in-contact (or snap-in) will appear and the monoatomic sharp tip is destroyed. For realistic tips with a larger number of atoms (in the pyramid shape) and a large attractive van der Waals background a jump-to contact will always appear. Therefore a dynamic (or noncontact) mode is used.

1.3.2   Dynamic AFM

In the dynamic mode, the cantilever is excited to vibrate by an external stimulus close to its resonant frequency. It can be viewed as a driven damped harmonic oscillator. After several assumptions: 1) Friction is proportional to the speed of the moving mass $F_{\text{frict}} = -m\gamma\dot{z}$, 2) external driving amplitude is harmonic $z_{\text{drive}}(t) = A_{\text{drive}}\cos(\omega t)$, 3) the spring force is $F = -k(z - z_{\text{drive}})$ the equation of motion reads

$$m\ddot{z} = -m\gamma\dot{z} - k(z - z_{\text{drive}}). \tag{1.12}$$

After introducing new terms resonance frequency $w_0^2 = k/m$ and quality factor $Q = \frac{w_0}{\gamma}$ (characteristic for a given harmonic oscillator without external driving) the solution is again harmonic motion

$$z = A\cos(\omega t + \phi), \tag{1.13}$$

where the amplitude as a function of driving frequency ω is

$$A = \frac{A_{\text{drive}}}{\sqrt{\left(1 - \frac{\omega^2}{\omega_0^2}\right) + \frac{1}{Q^2}\frac{\omega^2}{\omega_0^2}}} \tag{1.14}$$

and the phase reads

$$\tan\phi = \frac{-\frac{\omega}{\omega_0}}{Q\left(1 - \frac{\omega^2}{\omega_0^2}\right)}. \tag{1.15}$$

The step-by-step derivation of the solution can be found in [30]. The dynamic mode has its major advantage in increased stability of the junction. The jump-to-contact can be avoided if the maximum attractive force at the bottom turnaround of the cantilever is smaller than the spring force of the cantilever given by the product of its amplitude A and stiffness k

$$kA > \max(-F). \tag{1.16}$$

Therefore, even very soft cantilevers can be operated in a dynamic regime. An additional problem can arise in the dissipation of energy during the oscillation cycle, but in vacuum, where no thin water layer is present, this is not a major problem.

Two modes of the dynamic operation of AFM exist: Frequency modulation (FM) and Amplitude modulation (AM).

AM-AFM

In the AM-AFM, the cantilever is driven by a fixed driving amplitude and driving frequency which is ideally identical to the w_0. When the tip on the cantilever is brought into contact with the sample, the resonance frequency will slightly change upon the influence of an external force. As a result the amplitude also changes according to Eq. (1.14) and ΔA is used as an imaging or feedback signal. The AM-AFM can be used at ambient conditions and room temperature where the Q-factors of cantilevers are rather low (100-500) and the time response of the system

$$\tau = \frac{2Q}{\omega_0} \tag{1.17}$$

is fast enough. Due to the very slow response, AM-AFM is not suitable in UHV and at low temperatures ($Q > 10000$) and FM-AFM, first demonstrated by Albrecht et al. [41], is nowadays the only method used.

FM-AFM

In this mode, the cantilever is driven always on resonance by a feedback loop (phase-locked loop). Another feedback loop is keeping a constant oscillating amplitude by adjustment of the drive amplitude. Even though the above-mentioned two feedback loops are necessary, a fast operation can be in principle obtained in UHV with cantilevers with high Q-factors such as quartz tuning forks or quartz length extension resonators.

The detailed scheme and the principle of the force measurement are sketched in Fig. 1.5. In our Createc microscope (described in chapter 2) qPlus third-generation tuning forks are used as cantilevers. The cantilever is mechanically actuated and its deflection is measured utilizing a piezoelectric effect in the quartz resonator [42] which generates a charge on the electrodes. The mechanical actuation is realised by coupling an AC voltage to the DC voltage applied on the z piezo scanner. The signal is filtered with an adjustable band-pass filter centered around the resonance frequency and routed to amplitude control and Phase-locked loop (PLL). The PLL maintains a constant $\phi = \pi/2$ between the drive signal and the deflection signal which fulfills the resonance condition as can be inferred from Fig. 1.5a. The frequency shift Δf can be determined from the difference between the actual and the center frequency. With the amplitude feedback loop, the amplitude and dissipation are measured and the amplitude of the drive signal is adjusted to keep it at a constant setpoint. The Δf can be used also for the z feedback. In practice, due to the problems with a non-monotonic $\Delta f(z)$ dependence and generally noisy Δf with slow response, this is used only on insulating samples where no tunneling current can be detected.

Four channels —Δf, ϕ, dissipation and amplitude — are output from AFM operation in addition to z and I_t from STM operation. While all of them can be useful, the frequency shift is the quantity related to the force. Let us now reveal what is the physical meaning of the Δf. The frequency shift can be expressed as

$$\Delta f = f - f_0 = -\frac{f_0}{k_0 A^2}\langle F_{ts}(t)A\cos(2\pi f_0 t)\rangle, \tag{1.18}$$

where f_0 is the intrinsic resonance frequency, k_0 is the cantilever stiffness, A oscillation amplitude and F_{ts} is the tip-sample force which is averaged over the

full oscillation period. This formula can be simplified if one considers small oscillation amplitudes where the added spring constant corresponding to the tip-sample interaction $k_{ts} = \partial F_{ts}/\partial z$ is much smaller than the cantilever stiffness k_0:

$$\Delta f \approx -\frac{f_0}{2k_0}\frac{\partial F_{ts}}{\partial z}. \qquad (1.19)$$

The equation 1.19 can be easily reverted and the force can be calculated as an integral. For larger amplitudes, k_{ts} is not constant over the cycle and the frequency shift for arbitrary amplitude can be calculated based on the Hamilton-Jacobi formalism [43]

$$\Delta f(z_{ltp}) = \frac{f_0}{2k_0}\frac{2}{\pi A^2}\int_{-A}^{A} k_{ts}(z_{ltp} + A - q')\sqrt{A^2 - q'^2}\,\mathrm{d}q', \qquad (1.20)$$

where z_{ltp} is the lower turnaround point of the cantilever. For the conversion of the frequency shift to the force Sader-Jarvis or Giessibl matrix deconvolution methods are used [44]. In practice, the conversion is done only for the $\Delta f(z)$ spectroscopy and the reverse approach of simulating the high-resolution experimental AFM images with a probe particle model [21] using equation 1.20 is adopted.
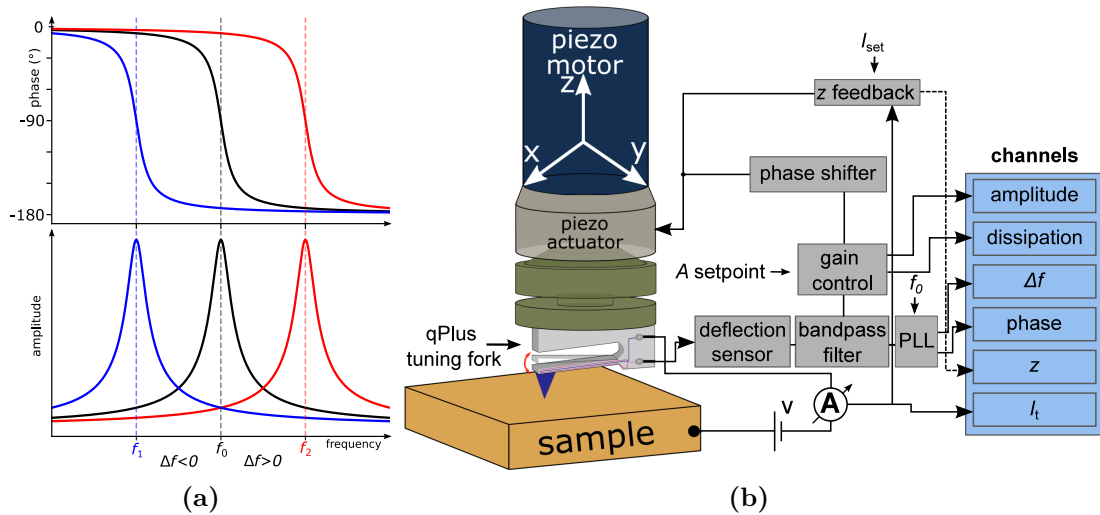
Figure 1.5: Working principle of FM-AFM. a) Amplitude and phase as of a driven damped harmonic oscillator (see eqs. (1.14) and (1.15)). Resonance frequency f_0 and Q-factor is intrinsic for each oscillator upon no tip-sample force. The phase of the oscillation is shifted by 90° in resonance. Attractive forces decrease the resonance frequency ($\Delta f < 0$ for f_1) and repulsive forces increase the resonance frequency ($\Delta f > 0$ for f_2) b) Scheme of the FM-AFM qPlus based setup. 6 channels are recorded and the current, amplitude and center frequency are the required user input quantities for feedback loops. Adapted from ref. [45].

1.3.3 Forces in AFM

There are different force components of the complex 3D force field which are summed in the total force interaction between the tip and the sample. Long-range van der Waals forces, electrostatic force and short-range Pauli repulsion

are the dominant ones in UHV nc-AFM (hereafter AFM will refer to the noncontact/dynamic AFM). Attractive short-range chemical force can be also present for reactive tips/samples.

Van der Waals forces are forces resulting from the dipolar interactions. They have three components: London dispersion force between instantaneous dipoles, Debye force between permanent and induced dipoles and Keesom force between permanent dipoles. The dominant is the dispersion force which is always attractive. The force is long-range on the order of nanometers and therefore does not provide atomic resolution [20] but it can be used as a measure of the sharpness of the tip.

Electrostatic force stems from the image charges of the tip created on the conductive sample and is always attractive. It is given as the force of a distance-dependent capacitor

$$F_{\mathrm{el}} = \frac{1}{2}\frac{\partial C}{\partial z}(V - V_0)^2 \tag{1.21}$$

where V_0 is the local contact potential difference (LCPD) between the electrodes. The distance behaviour of this force in AFM is both short- and long-range. Minimizing the electrostatic force is utilized in Kelvin Probe Force Spectroscopy. The LCPD contains information about the electric field distribution on the sample thus resolving different charge states of the atoms [46] and molecules [47] underneath the tip or observe an anisotropic charge redistribution on a halogen atom called σ-hole [48].

Pauli repulsion takes place when the tip and sample are brought so close that the distances between the foremost atom on the tip and the atoms on the sample are closer than in the chemical bond. According to the Pauli exclusion principle, no two electrons can occupy the same state which results in a repulsive force [30]. Due to it short-range character, this force is responsible for submolecular resolution.

The short-range interaction can be calculated quantum-mechanically, but the exact solution exists only for simple cases. Therefore, the tip-sample interaction is often modelled with a Lennard-Jones potential:

$$U_{\mathrm{LJ}}(r) = U_0 \left[\left(\frac{r_0}{r} \right)^{12} - 2 \left(\frac{r_0}{r} \right)^6 \right] \tag{1.22}$$

where U_0 is the depth of the potential well and r_0 is the equilibrium distance at which the U_{LJ} is minimal.

The Lennard-Jones potential, force and the corresponding frequency shift in the low amplitude limit are plotted in Fig. 1.6
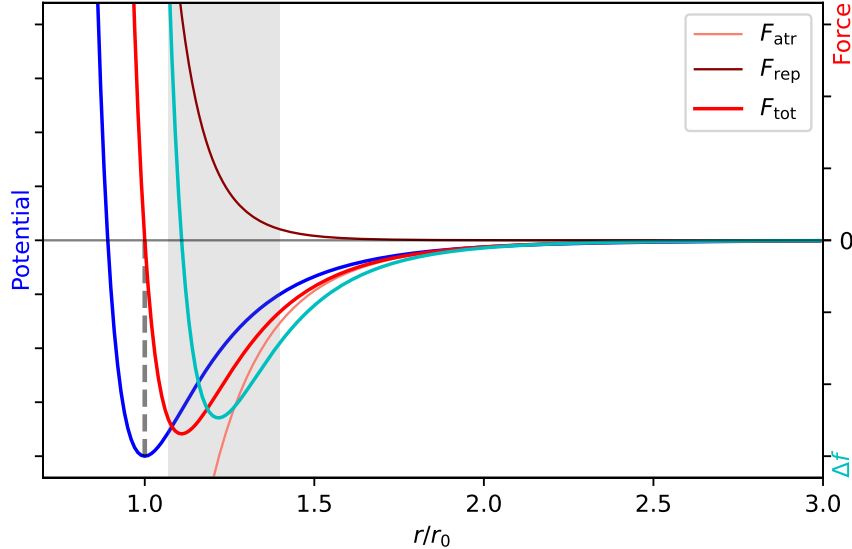
Figure 1.6: Potential, force and frequency shift in arbitrary units as a function of the normalized distance r/r_0. Potential (blue solid curve) is calculated from Eq. (1.22), force (red solid curve) is calculated as $F = -\frac{\partial U}{\partial r}$ and the frequency shift (cyan solid curve) as $\Delta f = -\text{const} \cdot \frac{\partial F}{\partial r}$ which holds for the low-amplitude limit (see Eq. (1.19)). The repulsive and attractive force components are plotted with thin lines. The gray-filled area denotes the working range of nc-AFM. The depth of the potential U_0 at the equilibrium position r_0 is illustrated with a dashed vertical line.

1.3.4 High resolution in AFM

The implementation of stiff sensors operating with sub-nm oscillation amplitudes in UHV scanning probe microscopy enabled simultaneous STM and AFM detection and has contributed to the development of a novel field of molecular identification. While the STM is a very valuable surface science tool for probing the electronic structure of samples it cannot provide atomic contrast within the molecules due to the delocalized nature of their orbitals. Conversely, AFM brings insight into the chemical structure of the probed samples. Due to the Pauli repulsion, which is very sensitive to high electron density above atoms and bonds, atomic and submolecular resolution of planar structures can be achieved in AFM. However, the metallic tip used for STM cannot operate at close enough distances since it is reactive and can interact with the molecule. The generally unknown apex shape makes the interpretation of its AFM contrast difficult. It was demonstrated by Gross et al. [5] in 2009 that the tip apex functionalization with a small passivating moiety can increase the AFM (and also STM) contrast. In this regard, the carbon monoxide (CO) molecule provides the best spatial resolution and is most commonly used, but other atoms and molecules such as Cl, Br and Xe or molecules N_2O, CuO have been tested since then.
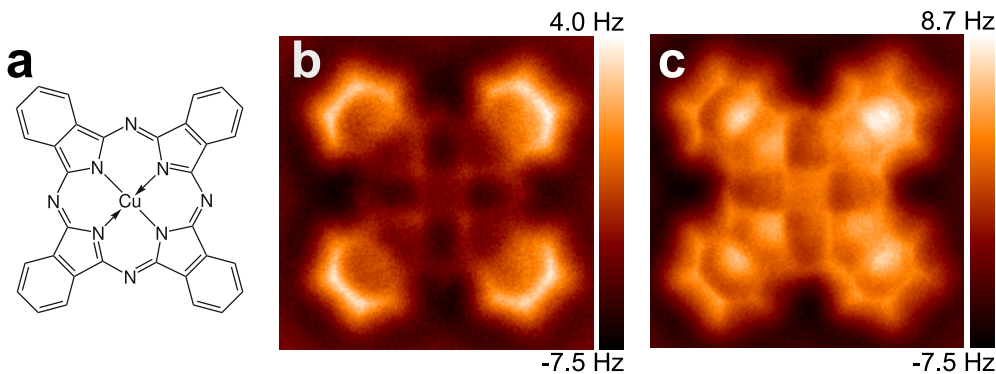
Figure 1.7: a) Structural model of copper phthalocyanine (CuPc), b) constant height frequency shift image of CuPc on Cu(100) at an intermediate distance and c) at a close distance (-20 pm from c) taken with a CO-terminated tip.

The current interpretation of the AFM and STM images taken with the functionalized tip is based on the Probe Particle model, introduced by Hapala et al. in 2014 [21, 49] and constantly developed until now [50]. It considers an atom or a molecule flexibly attached to the rigid metallic apex. The probe particle can be characterized by a potential, an effective charge Q (or its spatial distribution) and a spring constant k. These parameters define with sufficient precision how the probe particle reacts to the sum of the external force fields and how the characteristic submolecular contrast of the high-resolution AFM emerges. The example of the frequency shift image of a flat organic molecule at a close distance is shown in Fig. 1.7. At an intermediate distance, the image resolves the molecular backbone. At a closer distance, the contrast is inverted and the maximum exerted force is in the middle of the benzene rings. It is important to note that the sharp edges observed between neighbouring atoms do not necessarily mark a bond. They represent ridges in the potential energy landscape probed with the particle [21, 51] which can in some cases overlap with the real hydrogen bonds.

While for the majority of hydrocarbon molecules resolved with a CO-tip in a close distance, the force field can be simulated with pairwise Lennard-Jones potential, for polar molecules the electrostatics needs to be involved. The electrostatic forces and the van der Waals forces significantly contribute to the observed distortion in AFM images [49]. The CO molecule has a nearly zero total charge, but a deeper look reveals a quadrupole electric field distribution slightly negative towards the oxygen termination pointing to the sample. It can therefore probe electrostatic interaction, albeit only to a limited extent. The Xenon terminated tip with a positive total charge can sense the charge redistribution in the sample which results in the shrinking of the areas with a negative charge and expanding the areas with a positive charge.

1.4   Light emission in STM

Resolution in optical microscopy is limited by the well-known Abbe's diffraction limit which says that the minimum resolvable distance in the optical microscope is proportional to the wavelength of the light and inversely proportional to the

numerical aperture of the microscope

$$d = \frac{\lambda}{2\text{NA}} \tag{1.23}$$

[52]. For a better resolution, electron [53] or X-ray [54] microscopy exploiting much shorter wavelength can be used and resolve structures of nanometer size. However, a different approach than far-field spectromicroscopy is needed to obtain spatial resolution of visible light emitted or adsorbed by single molecules, quantum dots, or plasmonic nanostructures. Scanning near-field optical microscope [55, 56] working on the principle of detecting evanescent field decaying exponentially with the distance from the object is now commonly used to obtain sub-wavelength resolution. Another way how to optically access objects below the diffraction limit is to probe them in the presence of plasmonic structures. Fluorescence and Raman signals from molecules located near a plasmonic structure can be enhanced by a factor of $10^3 - 10^5$. This enables the detection of the optical signal even from a single molecule if the molecule is localized in the tip-sample junction with extreme field enhancement. While optical excitation is dominantly used in the aforementioned spectromicroscopies, electrical excitation, despite its obvious limitations can provide an extremely localized excitation pathway when employed in STM.

It was already Russel D. Young, the constructor of the Topographiner, who came with the idea of secondary photon collection from the specimen generated in the field emission regime of the scanning probe. The first light emission from the tunneling junction was reported in 1976 by Lambe and McCarthy [57]. They observed uniformly distributed light emission from a planar metal-insulator-metal tunneling junction upon applying a bias voltage. High-frequency cutoff of the photons corresponding to the applied bias leads them to the conclusion that inelastic tunneling electrons excite surface plasmon modes that decay radiatively. Later on in 1988, 7 years after the invention of the STM, Gimizewski et al. [58] showed the first light emission spectra from polycrystalline tantalum and Si(111)-(7×7). In the 90s, Richard Berndt was the pioneer in STM-induced luminescence (STML). He and his coworkers investigated the role of the material of the tip and sample on the luminescence spectra [9].

For a deeper understanding of the light emission in STM, introducing the concepts of plasmonics is necessary. In this section, we will describe the tunneling junction using classical electromagnetism and molecular excitation with a quantum-mechanical approach.

1.4.1 Plasmonics

When a metal is placed in an electromagnetic (EM) field, its conduction electrons will start to oscillate. The collective quantized oscillation of electron gas is called a plasmon. Its frequency satisfies Maxwell's equations and for a free electron gas model can be estimated as [59]:

$$\omega_p = \sqrt{\frac{ne^2}{\varepsilon_0 m}} \tag{1.24}$$

where n is the density of free electrons in metal, e elementary charge, ε_0 permitivity of vacuum and m mass of electron. For most of the metals, plasmon frequency

is between 5-15 eV. Below the plasma frequency, free electrons are able to follow and screen the EM radiation and the metal is therefore reflective. EM radiation of frequencies above the ω_p is no longer screened and the metals are transparent in the spectral region. This is not completely valid for noble metals, where interband transitions are responsible for absorption in the high energy visible spectral range [60]. Beer's law of adsorption says that the electromagnetic field intensity decreases exponentially with its penetration distance z in the metal $e^{-z/d}$ (skin effect). Since the skin depth d for metals in the visible spectral range is around 100 nm, the electron gas oscillation upon interaction with EM field can be only induced at the interface with dielectric (vacuum). Electromagnetic excitations propagating at the interface between a dielectric characterized by its permittivity ε_d and a conductor satisfying Maxwell's equations are called surface plasmon polaritons (SPP) and are sketched in Fig. 1.8a. Their characteristic frequency is given by the relation:

$$\omega_{SPP} = \frac{\omega_p}{\sqrt{1 + \varepsilon_d}}, \tag{1.25}$$

their dispersion relation between the wavevector k_x along the interface and frequency w is

$$k_x = \frac{\omega}{c}\sqrt{\frac{\varepsilon_d \varepsilon_m(\omega)}{\varepsilon_d + \varepsilon_m(\omega)}}, \tag{1.26}$$

where dielectric function of metal ε_m is a complex function. Considering zero damping γ in complex dielectric function of metal $\varepsilon_m = 1 - \frac{\omega_p^2}{\omega^2 + i\gamma\omega}$ one obtains a dispersion relation shown in Figure 1.8. Due to the momentum and energy conservation, the SPP has the intersection with free-space photons only at zero and therefore cannot be excited by photons. This can be overcome by several coupling methods [61] such as using a prism, grating, laser or near-field source for the photons or by using tunneling electrons as excitation source [57].
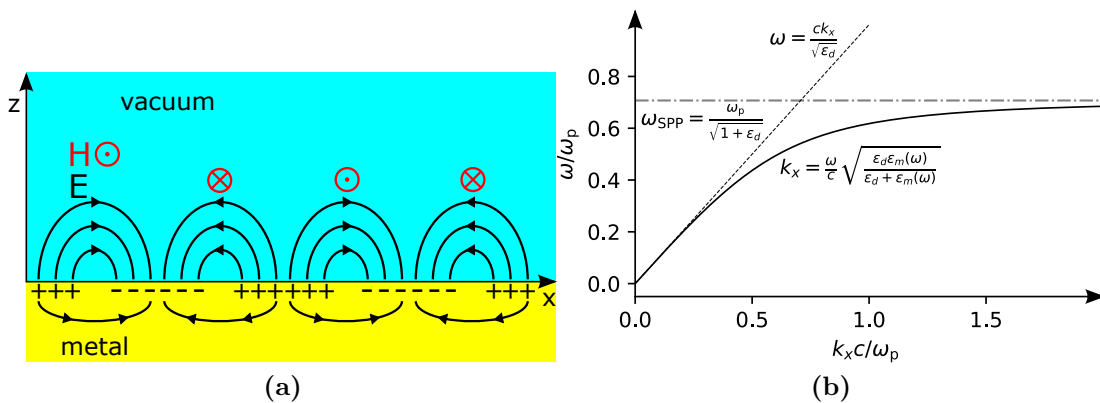
Figure 1.8: a) Schematic of the SPP propagation along k_x direction b) Dispersion relation of the SPP.

.

To address the light emission process from STM junction the concept of localized surface plasmons is needed. When a metal nanoparticle (e.g. sphere) is introduced in EM field of wavelength much larger than the size of the particle the difference between surface and bulk plasmon vanishes. Electric field penetrates

into the metal and offsets the electron density in the nanoparticle with respect to the ions. The intensity of the electric field around the nanoparticle can be 3 orders of magnitude larger than the intensity of the driving field in resonance conditions. The resonance plasmon frequency for a conductive sphere with zero damping and a radius much smaller than the wavelength of EM radiation is according to the Mie theory

$$\omega_{\text{Sph}} = \frac{\omega_p}{\sqrt{1 + 2\varepsilon_d}}. \tag{1.27}$$

This corresponds to the first mode - oscillating dipole [62]. When the damping in metal is considered, the resonant frequency depends also on the dimensions of the nanoparticle. ω_{res} increases with decreasing the size of the nanoparticle [63]. In contrast to SPPs, localized surface plasmons are non-propagating and radiative in nature and they can directly emit into the far field.

Tip-sample junction

The tunneling junction can be viewed as an optical cavity between a flat sample and a small nanoparticle (tip). Such a geometry is often called nanoparticle-on-mirror (NPoM) cavity [64] and was theoretically described both in a classical and quantum way [65]. The localized plasmon mode(s) hybridize with the SPPs of the sample and create new nanocavity plasmon (NCP) modes [66] in analogy with the formation of a chemical bond. The first theoretical treatment of the localized modes in tunnel junctions considering a sphere of radius a in the distance d from a metal surface revealed that the discrete nanocavity modes are confined to the region of order $L \approx 2ad$ and have frequencies ω_n depending on the plasma frequency of metal, dielectric constant of the gap and dimensions a and d. For a realistic shape of the STM tip, many modes from the atomistic protrusions on the tip hybridize and create a complex multi-frequency plasmon resonance. Also, the field enhancement is determined from the imaginary part of the dielectric function $\varepsilon_2(\omega)$ of the tip and the sample (see Fig. 1.9). Low ε_2 plotted in Fig. 1.9 means low ohmic losses and a high probability of exciting the nanocavity plasmon modes either with EM field or with tunneling electrons. The predicted probability of generating a photon with an inelastic electron for an Ag-Ag junction is 24% [67] while it is only 0.4% for the W-Ag junction, in fair agreement with experimental observations, when the different ratio of elastic and inelastic electrons in the tunneling process is considered. So far, the most commonly used materials for tip fabrication are Ag covering the whole visible-near infrared range, Au more suitable for the NIR range limited by the interband transitions above 2 eV or a standard W or Pt/Ir STM tip coated with the aforementioned materials. An Al tip was used to tune the plasmon resonance in the UV range [68].

One may ask what is the best achievable spatial resolution in tip-enhanced spectromicroscopies. Tip-enhanced Raman spectroscopy (TERS) can commonly provide a resolution better than 10 nm, but still far from the atomic scale resolving capabilities of STM. The tip radius of curvature is believed to be the limiting factor for spatial resolution in agreement with the theoretical prediction linking it to the nanocavity volume. It was a big surprise for the community when a submolecular resolved STML spectra from porphyrin molecule [10] and TERS from a similar molecule [8] were published. To reproduce the "photon maps" from STML by theoretical simulations, unrealistically small tip radii needed to
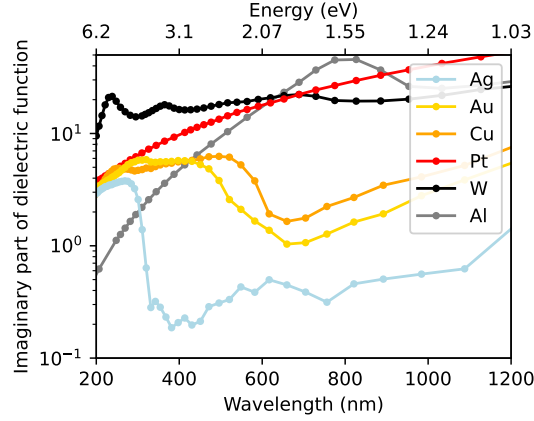
Figure 1.9: Imaginary part of the dielectric function for various metals used for STM tip fabrication. Ag, Au and Cu calculated from [69], Al, Pt and W from [70].

be considered to have a nanocavity field in sub-nm volume [71]. Recently, the discrepancy has been resolved with a classical model considering a sub-nm atomistic protrusion on the tip with moderate tip radius [72] (see Fig. 1.10) This "picocavity on nanocavity" provides the required field enhancement and localization and the protrusion is omnipresent for atomically sharp tips used in UHV STM and AFM.
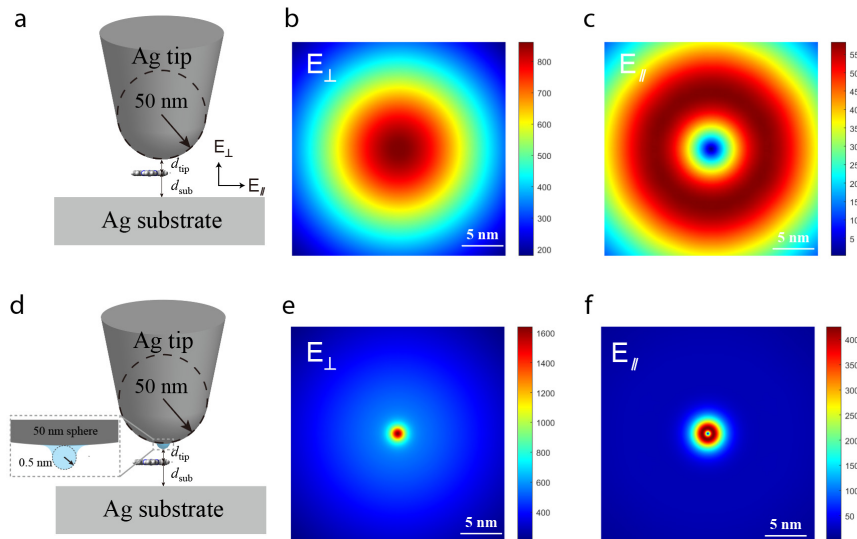
Figure 1.10: Simulations for the electric fields under plane wave excitation and molecular emission properties for different tip structures. a) Schematic for the configuration of the STM junction, where an Ag tip is placed above the lobe of ZnPc molecule. b) and c) Horizontal ($E_\parallel$) and vertical ($E_\perp$) components of the local electric fields simulated for the junction in a. d, Schematic for the configuration of the STM junction, where an Ag tip with an atomistic protrusion at the apex is placed above the lobe of ZnPc molecule. e) and f), Horizontal ($E_\parallel$) and vertical ($E_\perp$) components of the local electric field simulated for the junction in d. Reprinted with permission from ref. [72]. Copyright 2020 Nature Publishing Group.

1.4.2 Molecular excitation

To observe the excitonic emission from a molecule in STML, the molecule has to be sufficiently decoupled from the metallic substrate to avoid quenching. The first successful decoupling and observation of excitonic emission with submolecular resolution were performed in 2003 by Qui et al. [10]. The porphyrin molecule[10] was decoupled from a NiAl(100) substrate by a thin Al_22O_3 oxide layer. It took another 13 years to find a more suitable decoupling system – NaCl trilayer. The demonstration of dipolar coupling and superluminescence phenomena from artificial zinc phthalocyanine (ZnPc) aggregates [12] and energy transfer between two chromophores (H_2Pc and MgPc) with different emission energies [11] restarted the field of STML. The well-known decoupling NaCl layer adsorbed on metal surfaces allows electron tunneling at measurable rates for several layers and provides a perfect model system for the molecules [73]. Theoretical approach [74] revealed that the quenching is a result of an energy-conserving resonant electron transfer (RET) between the molecular orbitals and metal continuum states. The RET rate decreases exponentially with the NaCl thickness. For a molecule adsorbed directly on metal, the lifetime of the localized molecular state is in the femtosecond range while 2 and more layers of NaCl provide an already sufficient decrease of the RET rate necessary for radiative deexcitation.

Let us now describe the processes that take place in far-field spectroscopies. They are illustrated in a Jablonski diagram in Fig. 1.11. It gives an overview of the possible transitions usually considered during photoexcitation (absorption) but is valid also for electroexcitation. The molecule can be excited from its ground state to the excited state or to a particular vibronic state of the excited state. The transitions (both absorption and emission) are represented with a transition matrix or in a dipole approximation with a transition dipole moment $\boldsymbol{\mu} = \langle g|\hat{\mu}|e\rangle$, where $\hat{\mu}$ is the dipole operator and $\langle g|$ is the wave function corresponding to the ground state and $|e\rangle$ is the wave function corresponding to the excited state, both comprising electronic, vibrational and spin parts. For a closed-shell molecule, the transition $S_1 \rightarrow S_0$ can be in a simplified picture viewed as a transition between LUMO and HOMO. The intensities of observed vibrational manifolds in emission are given by the overlap integrals of the LUMO vibrational state wave function and the HOMO vibrational state wave functions - i.e. the Franck-Condon factors. This Franck-Condon principle is based on the Born–Oppenheimer approximation where a separation of vibrational and electronic parts of the wave function is possible. To describe transition not allowed by the Frack-Condon principle, the Herzberg-Teller approximation taking into account the change of the electronic wave functions upon vibrations is used.

When a molecule is placed in the nanocavity, the situation changes drastically. The molecular excitons couple with the nanocavity plasmons. As a consequence of the Purcell effect [75], the decay rate of the molecule is increased. The spontaneous decay rate γ of a two-level system with the ground and excited states in an arbitrary reference system characterized by the local density of photonic states ρ_μ can be expressed as

$$\gamma = \frac{4\omega}{3h\pi\varepsilon_0}|\boldsymbol{\mu}|^2\rho_\mu(\mathbf{r},\omega), \qquad (1.28)$$

where $\boldsymbol{\mu}$ is the transition dipole moment and $\mathbf{r}$ the position where the photon with frequency ω is emitted [59]. The excited state population decays exponentially in
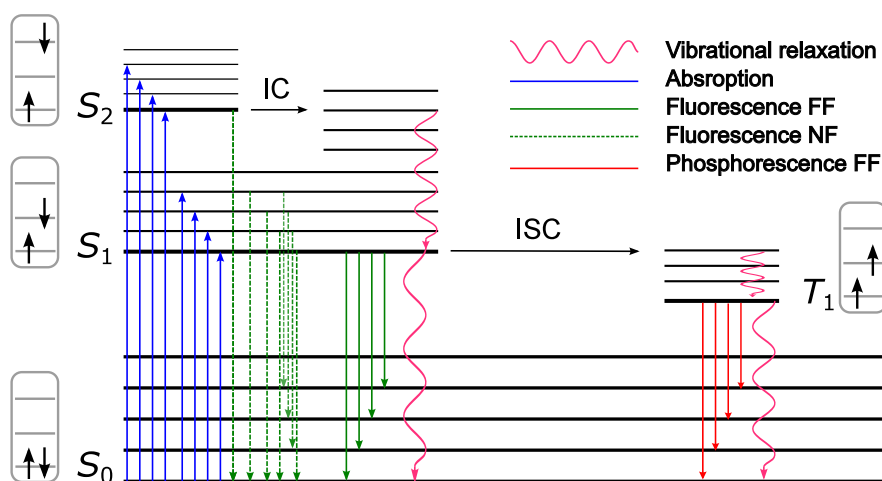
Figure 1.11: Jablonski diagram of energy levels of a closed-shell organic molecule. The molecule can be optically excited from its ground singlet state (S_0) to excited electronic states (S_1, S_2, etc.) sketched with thick solid black lines with corresponding vibronic states (thin lines). In the far field (FF), the excitation by absorption of the molecule (fs timescale) is followed by fast internal conversion (IC) to the vibronic ground state of the first excited state (Kasha's rule). The decay can be radiative (ps-ns fast fluorescence or μs-minute slow phosphorescence) or nonradiative via heat dissipation (wavy lines). For molecules with heavy elements, the spin–orbit coupling permits intersystem crossing (ISC) into a long-lived triplet state which relaxes through phosphorescence or non-radiatively. In the near-field (NF) spectroscopies, the nanocavity-induced Purcell effect increases decay rates and allows observation of hot luminescence (dashed green lines) from higher-lying vibronic states. Note that the scheme is also valid for the electroluminescence with the exception that the triplets can be directly excited with the tunneling electrons.

time $N = N_0 e^{-\gamma t}$. The Purcell effect is accompanied by the exciton line broadening due to the time-energy uncertainty and decreasing of the energy of exciton emission – Lamb shift [76]. The strength of the coupling between the exciton and plasmon has been theoretically estimated to be about 25 meV [77]. It is believed to be at the boundary between the weak coupling and the strong coupling limit. The strong coupling regime, which represents the ultimate light-matter interaction where the energy between the plasmon and exciton is coherently exchanged, was recently detected in the NPoM geometry via characteristic Rabi splitting [78] of the exciton line and Rabi oscillations in the electric field domain [79] but not in STML, as yet.

Excitation mechanism

There has been a vivid debate about the excitation mechanism since the first observation of excitonic emission in STML [10]. For a molecule adsorbed on a thin insulating layer, i.e. the double-barrier junction discussed in subsection 1.2.5, two mechanisms were originally suggested: 1) Diode-like mechanism requiring a substantial voltage drop across the decoupling layer to align the HOMO and LUMO of the molecule in between the Fermi level of the tip and the sample [12, 80] and 2) Plasmon induced generation of excitons utilizing the excitation of NCP modes by inelastic electron tunneling into metal [80, 81]. The former mechanism was originally suggested for the excitonic emission observed from molecular multilayers [82]. However, it was later shown that it does not play a role in molecules adsorbed on NaCl, where the voltage drop is small. The latter proposed mechanism has the advantage that it does not rely on a voltage drop across NaCl. It was supported by the observation of Fano resonances a few nanometers away from the molecule confirming the exciton-plasmon coupling [83, 84, 85, 86, 81, 87, 88]. However, the efficiency of this mechanism in electroluminescence is expected to be much lower than the direct charge carrier injection.

In 2019, Miwa et al. [37] came up with a many-body scheme that explains neutral ZnPc exciton formation as sequential electron tunneling to and out of molecular orbitals. This scheme does not require any voltage drop on the decoupling layer as the energy levels of the molecules renormalize upon charging and discharging. The large binding energy of a highly localized (Frenkel) exciton stemming from the Coulomb interaction explains the difference between the electronic gap measured in STS and the observed optical gap. This model was further generalized for charge excitons [36] considering also long-lived triplet states in molecules without heavy elements in the transitions. The basic condition necessary for electroluminescence of neutral exciton is to have the absolute value of the energy of negative or positive ion resonance (NIR, PIR) in dI/dV spectrum above the energy of the exciton [89]. On the other hand, plasmon-mediated exciton formation is believed to be the dominant process in STM photoluminescence (STM-PL). This was demonstrated by measuring the photoluminescence signal out of the tunneling contact [72] and with a resonant excitation utilizing a tunable laser [90].

1.5 Time-resolved measurement of luminescence

There are several ways how to measure the excited state lifetime of molecules. In the following chapter, I will briefly introduce them and give examples of their utilization in STML.
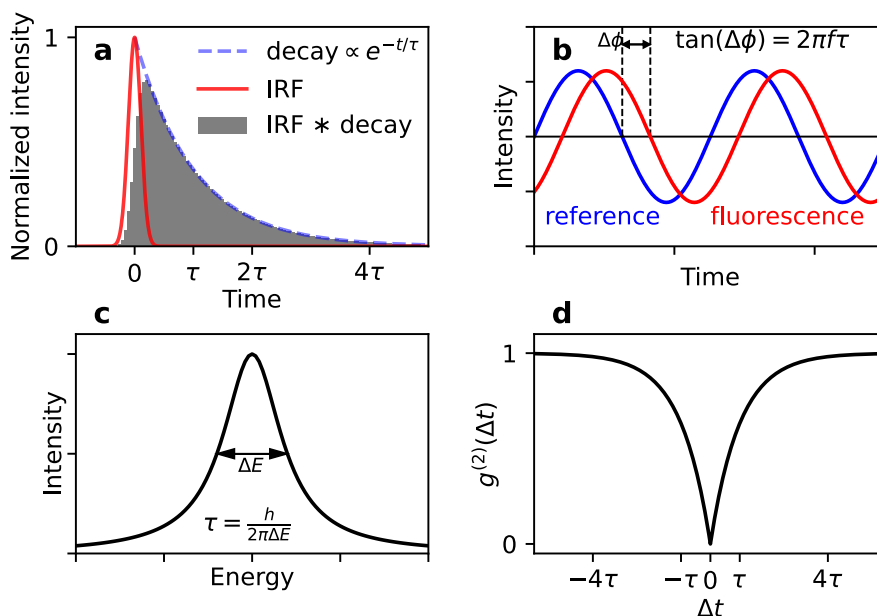
Figure 1.12: Illustration of the working principle of the time-resolved methods in luminescence for intrinsic lifetimes τ measurement. a) TCSPC-based lifetime measurement with a pulsed light source. The histogram of measured photon counts in time corresponds to the convolution of IRF (centered at $t = 0$) with monoexponential decay for a two-level system. b) Phase fluorometry scheme. c) Lifetime estimation from a homogeneous broadening of the Lorentzian exciton line. d) Fluorescence autocorrelation function for a single-photon emitter with a lifetime τ.

Fluorescence lifetime based on time-correlated single photon counting

Most commonly, fluorescence lifetime is measured in the time domain from the exponential fluorescence decay curve. Measuring exciton decay with Time-correlated single photon counting (TCSPC) requires a pulsed source of light, a photodetector with high temporal resolution and electronics for synchronizing the pulse event with the photon arrivals on the detector. The histogram of photon distribution in a selected time interval synchronized with light pulses is acquired during the accumulation (see Fig. 1.12a). The lifetime is obtained from fitting the histogram with an exponential function convolved with the instrumental response function (IRF) influenced by the pulse shape, jitter time of the detector and electronics. Since the lifetime of molecules in solution or matrices is usually on the order of nanoseconds and the pulse width of modern laser sources is much shorter, IRF is often neglected. Nowadays available MHz repetition rates permit very fast operation suitable for fluorescence imaging. TCSPC-based fluorescence

lifetime imaging microscopy is now a widespread operation technique in confocal microscopes. However, there are no STML works published up-to-date utilizing this technique yet. Our results are presented in Fig. 5.5.

Phase fluorometry

An alternative method operating in the frequency domain is phase fluorometry. It measures the phase difference between the driving signal and the modulated fluorescence signal as shown in Fig. 1.12b. This has the advantage that it can be used both for electroluminescence by modulating the bias voltage and for photoluminescence utilizing the electro-optic modulators. This method is used and explained in detail in chapter 5 and its Supplementary Information in Appendix C.

Exciton line broadening

If a single molecule is measured using the far-field single-molecule spectroscopy [91] with a resonant excitation the lifetime can be estimated by another means. For a two-level quantum system in a weak coupling limit the peak shape corresponding to the optical transition between the two states is Lorentzian and its homogeneously broadened optical frequency (FWHM) can be expressed as:

$$\Delta \nu = \frac{1}{2\pi T_1} + \frac{1}{2\pi T_2}, \tag{1.29}$$

where T_1 is the molecule lifetime and T_2 is the temperature-dependent dephasing lifetime $T_2 = A\exp(-\Delta E/kT)$. It has been shown that for very low temperatures (2K for a terrylene molecule in a p-terphenyl crystal [92]) the dephasing lifetime is approaching infinity and the line broadening can be directly converted into exciton lifetime (see Fig. 1.12c). This method has been applied in STML for qualitative and quantitative lifetime estimation [93, 11, 86, 94, 77, 95]. Unfortunately, the exact linewidth-to-lifetime calculated values (neglecting other effects such as dephasing) have been sometimes unconditionally trusted and led the authors to controversial claims. For instance, the sub-meV linewidth of the observed transition at 1.33 eV contrasting the broader singlet PTCDA transition at 2.45 eV was attributed to phosphorescence or a condition for the occurrence of quantum-coherent electron energy transfer in a phthalocyanine heterodimer [95] based on the lifetime estimated linewidth. The former interpretation is corrected in chapter 7. The origin of the linewidth of the neutral exciton (Q) observed in STML on phthalocyanine was studied by Imada et al. [90]. The authors attribute the 4.4 meV linewidth to the composite of higher-order vibronic transitions with the same vibrational quantum number, but with a slightly different energy, allowed in near-field luminescence where the tunneling electrons have enough excess energy provided by the bias voltage. They performed the resonance photoluminescence excitation and demonstrated the linewidth of 0.5 meV (corresponding to 1.3 ps lifetime) and further supported their interpretation by off-resonance photoexcitation [96], where the exciton line is broadened. A specific type of soft vibration, a libration of a molecule in its potential well, and its role in the linewidth and lineshape observed in STML is studied in chapter 8.

Analysis of fluorescence intensity autocorrelation function

The photons emitted by a single molecular emitter in a two-level approximation are antibunched, i.e. they are more equally spaced in time than photons from a random source. The photon statistics is described by a normalized fluorescence intensity second-order correlation (also called autocorrelation) function:

$$g^{(2)}(\Delta t) = \frac{\langle I(t)I(t + \Delta t)\rangle}{\langle I(t)\rangle^2}, \qquad (1.30)$$

where I is the normalized intensity over time t and Δt the time delay between two consecutive photons. For antibunched photons following the sub-Poissonian statistic the $g^{(2)}(0) = 0$. The exact $g^{(2)}(\Delta t)$ solution for a two-level system approximation can be found in refs. [97, 92]. When neglecting the dephasing (i.e. $T_2 \to \infty$) in Eq. (1.29) it follows the relation:

$$g^{(2)}(\Delta t) = 1 - B \exp(-\Delta t/T_1) \times C(\Omega, T_1), \qquad (1.31)$$

where B accounts for a background signal and detector jitter and C is an oscillatory function corresponding to the on-resonance Rabi frequency Ω. The lifetime T_1 of the excited state can be therefore obtained from the Eq. (1.31) describing the antibunching dip. In practice, due to the dead time of avalanche photodetectors, the autocorrelation of emitted photons is measured in a two-detector scheme in a Hanbury Brown-Twiss interferometer. It was shown, that in a low-temperature limit, this method yields precisely the lifetime value obtained from the Lorentzian width [92]. This method was used in STML in refs. [98, 99] (with the correction to the 3-state electroluminescence process) obtaining characteristic exciton time constants of 0.7 ns for C60 defects [98] and 0.5–2 ns on ZnPc/NaCl/Ag(111) depending on tip-sample distance considering C unity for a weak coupling regime [100]. Both authors neglected the time of electron capture from the substrate assuming it is very fast. As stated in the Supplementary Information of ref. [72] no antibunching was observed in STM-PL of the same ZnPc system pointing towards an exciton lifetime < 50 ps in the nanocavity. The observed exponential decay constant, therefore, likely corresponds to the electron tunneling through the decoupling layer [38] and the exciton lifetime is negligible compared to it.

Optical pump-probe spectroscopy

All the aforementioned methods except for the lifetime estimation from the line broadening are limited by the temporal resolution of the photodetector. The best commercially available single-photon avalanche detectors have a jitter time of around 35 ps [1] thus not suitable for measuring lifetimes or vibrational relaxation on the order of picoseconds. In contrast, pulsed lasers can have a pulse width on the order of femtoseconds and hence provide very high temporal resolution. When considering their utilization in light-STM, the optical system has to be specifically designed in order to avoid distortion of the pulse. To our knowledge, THz pump-probe STM spectroscopy was used for studying single molecular vibration [102] and charge-induced molecular switching [103], but optical pumping and single-molecule exciton study has not been published as yet.

---

[1]3 ps uncertainty in photon arrival was demonstrated using superconducting nanowire single-photon detector [101]

2. Experimental details

All experiments were performed in a laboratory of Department 13 of the Institute of Physics of the Czech Academy of Sciences (`https://splm.fzu.cz/`) using an ultrahigh vacuum low-temperature STM/AFM microscope. The general aspects of the experiments are described in this chapter. More specific information on each experiment can be found in the Methods sections in each chapter.

2.1 The Microscope

The commercial Createc microscope consists of two separate ultra-high vacuum (UHV) chambers. The scanning head of the microscope is located in the main chamber (Type SL009 with XY+Z– Pan type slider [104]) enabling simultaneous STM/AFM measurement using qPlus sensors. Cooling of the head is realized with the LN and LHe bath cryostats with 72 hours hold time. There are several pinholes and viewports in the outer and inner shields attached to the cryostats enabling both optical and mechanical access to the sample and tip. Two shutters on the nitrogen shields movable with a wobble stick are designed to close the ports. The base temperature of the SPM head is around 5 K with closed shutters and 7.5 K with the opened sapphire viewport needed for photon detection. The chamber is pumped both by the ion sublimation pump and by the cryostats working as cryopumps. The base pressure in the chamber is 1×10^{-9} mbar and the pressure within the LHe shield enclosure is expected to be at least in the 10^{-10} mbar range. The chamber is equipped with several flanges with windows, a wobble stick for inserting the samples, a leak valve for CO-dosing, a carousel with a sample and qPlus sensors/tips storage designed by Aleš Cahlík [105] and a gate valve enabling mounting a molecular evaporator for direct deposition on the cold sample inside the head.

A preparation chamber is separated from the main chamber by a desk valve and is equipped with an ion gun, an automated leak valve, 2 evaporators separated by desk valves, a manipulator with a resistive heater, low energy electron diffraction, quadrupole mass spectrometer and is pumped with ion and titanium sublimation pumps. It can also be pumped with a turbomolecular pump prepumped with a foreline pump during e.g. sample preparation. A pneumatic desk valve connected to the interlock is used to open the turbo pump to the preparation chamber. The base pressure in this chamber is better than 10^{-10} mbar. A small load lock chamber is attached to the preparation chamber and serves for inserting the samples/sensors and prepumping the gas lines and evaporators.

2.2 Upgrade of optical setup

The quality of the optical setup is crucial for detecting signals from single molecules. The basic criteria are 1) large numerical aperture of the lens, 2) high transmission and efficiency over a broad spectral range of the optical components enabling maximum signal-to-noise ratio and 3) good spectral resolution all compatible with a low temperature and low mechanical noise scanning tunnel-
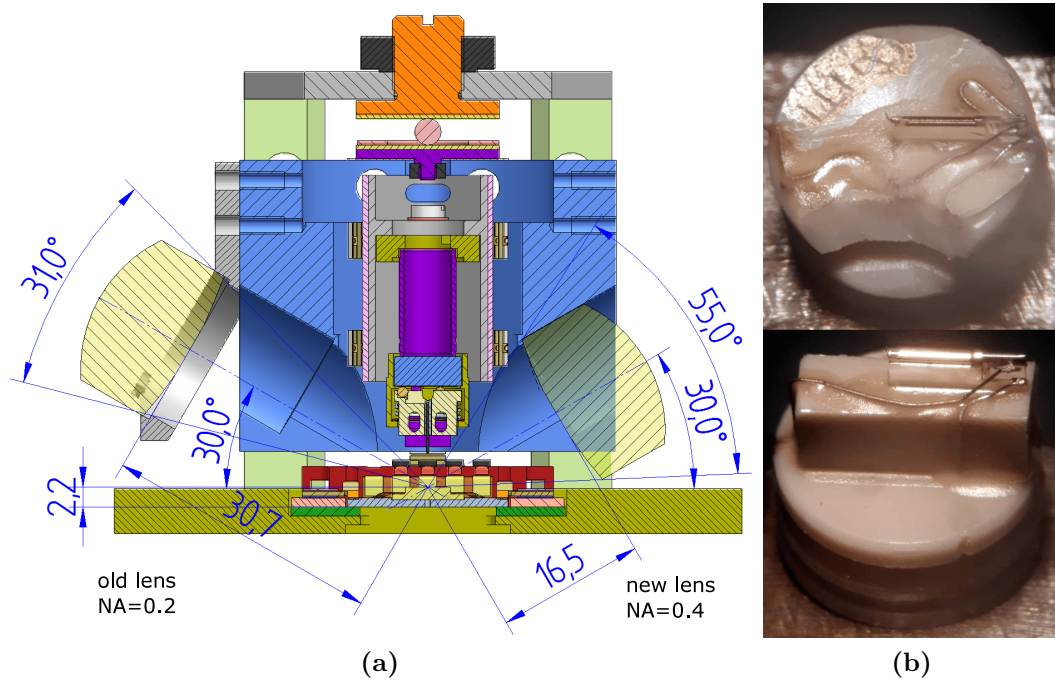
Figure 2.1: a) A cross-section illustrating the collection efficiency of the new and old lenses placed in the Createc STM head. Adapted from communication with Createc Gmbh. b) qPlus PEEK holders with optimized photon collection efficiency from the tunneling junction. Top: Custom design with trimmed PEEK edge of the original Created holder. Bottom: Elevated design provided by Createc.

ing microscope. There are several ways how to collect (and focus) the light from (in) the tunneling junction. A lens [106], a parabolic mirror [107, 108] or even an optical fiber close to the junction can be installed [109], usually covering only a fraction of the full solid angle compared to confocal microscopes. In our case, we have a lens attached to the scanner head, where the tunneling junction is located close to its focal point as can be seen from Fig. 2.1. The lens collects the light generated in the tunneling junction and collimates the beam to pass through two viewports on LHe/LN shields and a fused silica viewport on the DN63CF flange out of the vacuum. The distance between the junction and the flange measured by the time of flight of a laser pulse is approximately 210 mm. The building kit system based on 4 rigid steel rods around the optical axis supporting the quick-exchangeable optical components (Thorlabs 30 mm cage system) is mounted on the air side, where the light can be split into multiple paths or filtered. It is refocused into a fiber and guided to a spectrograph. The optical setup has been constantly developing during my PhD and its latest version is sketched in Fig. 2.2.

Setup inside the STM

Originally, the manufacturer equipped the microscope with a quartz achromatic lens specified for 400–700 nm wavelengths ($f = 30$ mm, NA = 0.2) covering 2% of the half sphere and infrared-blocking (700 nm short pass coating) viewports on LHe and LN shields (results in chapter 3). This was not satisfactory since a

lot of the molecules have optical transitions in the near-infrared spectral range. The viewports were replaced by sapphire ones (chapter 4) and the lens by a new plastic lens from ZEONEX E48R material (Edmund optics #65-988 hybrid aspheric lens with 12 mm diameter and $f = 15$ mm, NA = 0.4) covering more than 7% of the half sphere. The angle between the axis of the lens and the sample normal (see Fig. 2.1a) is 60° where the maximum of the emission is expected [80]. All the experiments from chapter 5 onwards were measured with the new lens. The design of the PEEK holder for the qPlus sensor had to be modified since it can shade a large part of the cone entering the lens, especially for short tips which are desirable for AFM operation. Either an elevated design was provided by Createc, or the shading part of the PEEK was removed by a scalpel (see Fig. 2.1). The advantage of this setup is that the lens-junction distance is fixed (for the same sensor and same height of the sample) during the scanning and coarse motion ($5 \times 5\,\mathrm{nm}^2$ range) and in principle should not require any adjustments of the optics on the air side. However, the head standing on a tripod is rotating in the horizontal plane (ϕ) during the coarse motion by several degrees and also vertically (θ) as the center of mass changes and the head hanging on the springs tilts. This can be compensated by the external optical setup.

External optical setup

A compact external detection setup shown in Fig. 2.3, which fits in tight space around the microscope, is based on Thorlabs 30 mm cage system mounted on the DN63CF flange of the SPM chamber. It houses optical components up to 25 mm in diameter permitting the collection of even a slightly diverging propagating from the inner lens if the junction is located in front of its focal plane. The rotation around ϕ and θ of the STM head with the inner lens was compensated by placing the cage system on a bearing micromanipulator (Thorlabs LX10/M) with a 25 mm travel range. Two reducers between the cage system and the micromanipulator allow changing the ϕ and θ of the setup. Alignment of the collimated beam with the optical axis of the setup was confirmed by observation of the reflection of the fiber and cage on the sample overlapping with the STM junction from the opposite side of the microscope with a CCD camera (Figure 2.5a). The beam was refocused to the circular bunch of optical fibers (30 cores $\times 100\,\mu$m diameter) with an achromatic doublet lens (Thorlabs AC254-030-AB, 25 mm diameter and $f = 30$ mm). Photons are guided by the multimode fibers to the spectrograph, where they are formed into a vertical slit-like termination. Alternatively, for measuring the time resolution in chapter 5, the beam is split by a cube beam splitter 90:10 and the 90% branch is filtered by a bandpass filter and focused to a 200 μm optical fiber, achromatically coupled to the active area of single-photon avalanche diode (SPAD; PerkinElmer, SPCM-AQR-15, jitter time ~ 250 ps).

Spectrograph and CCD camera

The spectrograph together with the sensitive CCD camera are crucial instruments to detect and analyse the light from the tunneling junction. The light focused on the vertically oriented entrance slit is dispersed with the spectrograph grating
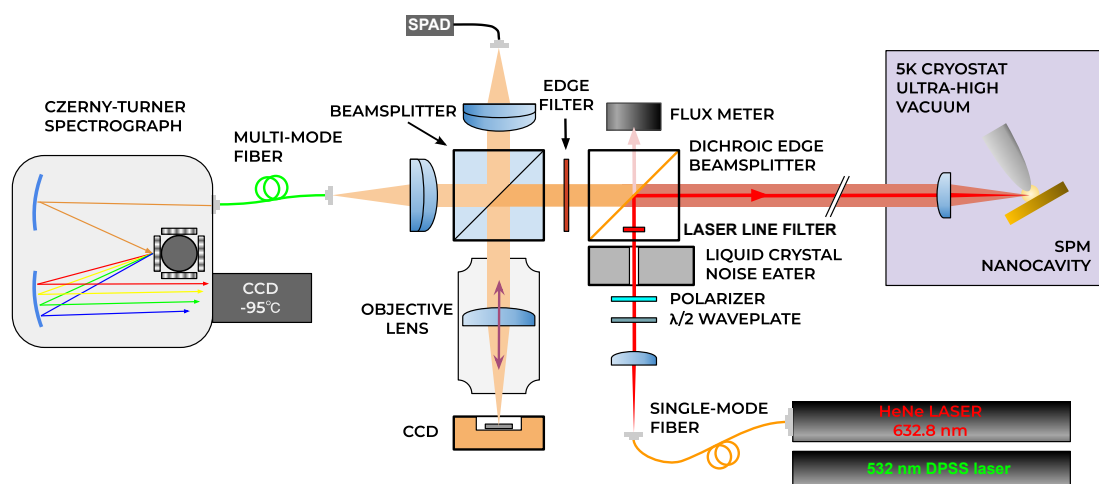
Figure 2.2: a) Schematics of the optical setup which can be used for STM-EL, TERS and STM-PL measurements. Beamsplitters with diverse split ratios depending on the type of experiment are mounted in exchangeable inserts (Thorlabs DFM1T4) magnetically attached to the cage system. Narrow line gas and diode-pumped solid-state (DPSS) continuous wave (CW) lasers can be for photoexcitation and TERS and a pulsed supercontinuum white light laser with tunable filters can be used for photoexcitation and time-resolved measurements.
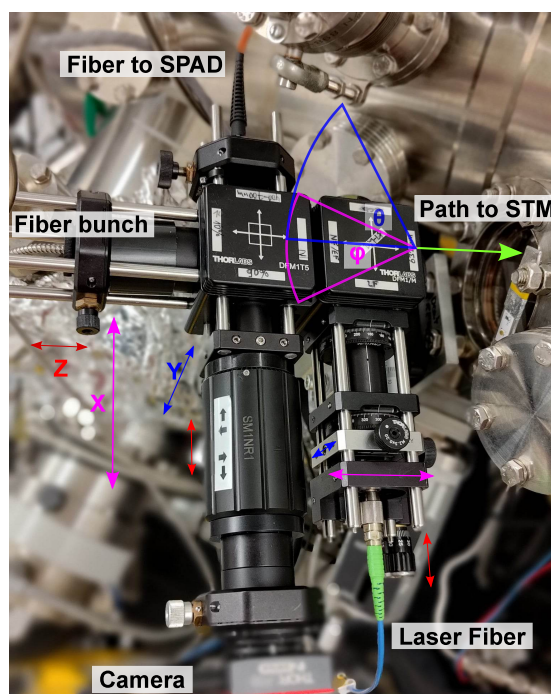
Figure 2.3: a) Photo of the external optical setup sketched in Fig. 2.2. Degrees of freedom of movement which compensate for the SPM head tilting are marked. For photon acquisition, the whole setup is darkened with blackout fabric. Noise eater from Fig. 2.2 is not present in this photo.

and illuminates a 2D chip of the CCD consisting of n horizontal and m vertical pixels. Since every column of vertical pixels is illuminated with photons of the same wavelength the camera can be operated in a full vertical binning mode which integrates the intensity in each column. Compared to the image mode, this reduces to overall noise in the acquired spectra. The signal-to-noise ratio S/N of the camera can be calculated as

$$\frac{S}{N} = \frac{D_{QE}P}{\sqrt{\delta_{\text{signal}}^2 + \delta_{\text{dark}}^2 + \delta_{\text{read}}^2}}, \tag{2.1}$$

where D_{QE} is the detector quantum efficiency, P the number of photons hitting the column of pixels, $\delta_{\text{signal}} = \sqrt{D_{QE}P}$ the shot noise of the Poisson process, δ_{read} the read noise and $\delta_{\text{dark}} = \sqrt{N_e N_{\text{pix}} t}$ the total dark current noise. We can see from the comparison of different cameras in Fig. 2.4 that the read noise is the limiting factor of S/N for short acquisition times and low photon intensity < 1 cps. The dark noise originates from thermally induced electrons in silicon and exponentially decreases with decreasing temperature. Therefore, the chips are cooled down to temperatures around $-100\,°\text{C}$.

In addition, there is another very specific type of noise caused by cosmic rays. At sea level, they consist mostly of GeV-energy muons originating from the decay of mesons from large hadronic cascades of protons and neutrons in the atmosphere [110]. Charged muons generate a lot of electron-hole pairs when travelling through individual pixels. They usually hit only a few pixels on the CCD, but the photon signal from the corresponding columns is lost in the background. The elimination of muon flux is not possible e.g. by any conventional lead shielding and therefore different approaches are used. The CCD is oriented vertically to minimise the cross-section with cosmic rays. The maximum used integration time is around 3 minutes as the number of pixels (columns) hit by the rays can be significant. If the total required acquisition time is more than 1 minute more acquisitions are used and the data are averaged. A median-based (despike) filter can be used for single acquisition spectra, ensuring that it will not crop real peaks. In the case of more acquisitions, a 2D median-based filter is used. Photon maps can be filtered also laterally.

In the beginning, we borrowed an Andor iStar 720 CCD camera (results in chapter 3) from our colleague Lukáš Ondič. Because such camera is not suitable for the detection of very low signals (its quantum efficiency is below 10%), we replaced it with an Andor iDus 401 BV CCD camera. This back-illuminated CCD camera is optimized to detect visible light and has a maximum quantum efficiency 90% at 400 nm. This setup was used in chapter 4. We used an Andor Shamrock 163i spectrograph in chapters 3–4. It houses one grating with 300 grooves per millimeter (gr./mm) providing a broad spectral range of 400 nm but a resolution of only 3.5 nm FWHM (full width at half maximum). The absolute calibration of the manually set spectral range was done using Ar/Hg lamp and 3$^{\text{rd}}$ order polynomial fit of the calibration spectrum.

Finally, in 2020 we commissioned a new CCD camera Andor Newton DU920P-BEX2-DD and an Andor Kymera 328i spectrograph. The back-illuminated camera is optimized for the detection of visible and near-infrared light and provides quantum efficiency $\sim 90\%$ in a broad range from 400 to 850 nm with an absolute

cutoff at 1100 nm determined by the band gap of silicon. Very low dark current ($0.003\,\mathrm{e^-/pix/s}$) and read noise ($4-8\,\mathrm{e^-}$) enable high signal-to-noise ratio usually limited by the shot noise. In comparison with its competitor (Princeton Instruments Pylon Excelon CCD) used by other groups [81, 12, 11] it has one order of magnitude higher dark current but offers continuous operation for weeks thanks to the Peltier-cooled CCD ($-100\,\mathrm{°C}$) instead of an LN cooling ($-120\,\mathrm{°C}$.)

The new spectrograph is equipped with a motorized turret with 4 gratings. **1)** 150 gr./mm blazed for maximum efficiency at 500 nm providing 500 nm spectral range and 1.2 nm resolution, **2), 3)** 600 gr./mm with 500 and 1000 nm blaze respectively providing 125 nm range and 0.5 nm resolution. **4)** 1200 gr./mm with 500 nm blaze providing 60 nm spectral range and 0.2 nm resolution. The resolution can be even slightly improved by limiting the width of the entrance slit at the cost of a lower signal. The nonlinearity of the grating is precalibrated by the manufacturer and our calibration procedure is simplified to image the zero-order diffraction to the center of the CCD chip.
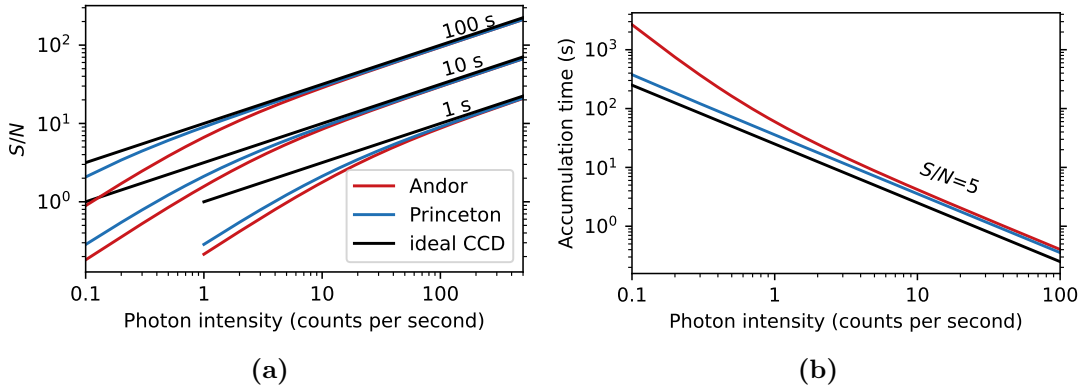
Figure 2.4: a) Signal-to-noise ratio as a function of the photon intensity per column and different acquisition times for our camera (Andor Newton DU920P BEX2-DD), Princeton PyLoN:100BR_eXcelon and an ideal CCD camera (100% Q.E., zero read noise and dark current). b) Acquisition time necessary to accumulate spectra with S/N = 5. Parameters of the CCDs: Andor Newton DU920P BEX2-DD, 90% Q.E., $4\,\mathrm{e^-}$ read noise, 0.003 $\mathrm{e^-/pix/s}$ dark current, 256 vertical pixels $26 \times 26\,\mu\mathrm{m^2}$. Princeton Instruments PyLoN:100BR_eXcelon, 90% Q.E., $3\,\mathrm{e^-}$ read noise, 0.00083 $\mathrm{e^-/pix/s}$ dark current, 100 vertical pixels $20 \times 20\,\mu\mathrm{m^2}$.

2.3 Sensor and tip preparation for electroluminescence

The measurements presented in chapters 3–8 were performed with a qPlus sensor [42] (type S1.0) glued on a PEEK holder. Three metal ball electrodes glued to the bottom of the PEEK base realise a kinematic attachment to the contacts on the piezoelectric scanner for tunneling current and AFM detection. Two cylindrical magnets are encompassed in the PEEK body providing magnetic coupling to the tip holder on the scanner head. The sensor can be exchanged *in situ*. It is commercially available from Createc with a glued 25 μm thick Pt/Ir wire to the

end of the prong. The tips are side-cut by a focused ion beam (TESCAN FERA3 scanning electron microscope with Xe FIB) by Jaromír Kopeček in our institute (see Fig. 2.5). The length of the tip is usually around 300 μm. The added tip mass results in a lowering of the resonant frequency from the original 32.768 kHz to circa 31 kHz. Q factors measured in air at room temperature are $3000 - 4500$ and in the scanning head in vacuum at 6 K can be between $30000 - 80000$.
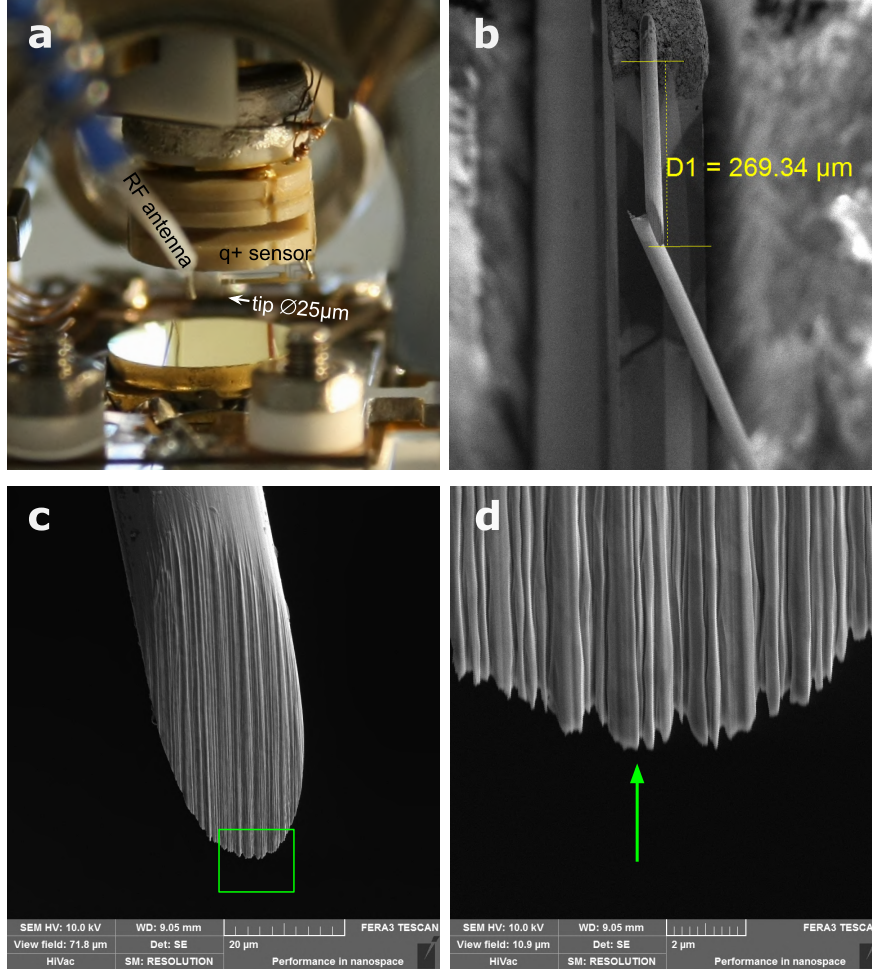
Figure 2.5: a) Image of the STM head with inserted Ag(111) sample and a qPlus sensor with the glued tip. A radiofrequency antenna was used to add GHz modulation AC bias to the applied DC bias in the tunnel junction in chapter 6. b) SEM image of the cut tip on the qPlus tuning fork from a). c) Magnified tip shaft in SEM. d) Zoomed SEM image on the last ripple forming the tip apex.

For the measurements in chapter 3 and 4, tips made of Au and Ag wire respectively were used instead of the Pt/Ir wire. However, we realized that Pt/Ir tips coated with a small amount of Ag/Au from the micro-indentations in the sample [111, 112] can yield similar photon intensity from NCP. Due to their hardness, the Pt/Ir tips cannot be so easily destroyed by a large-scale indentation in the sample as the thin wire rather bends before the mesoscopic shape of the apex is deformed. In addition, the plasmon resonance frequency can be tuned in a very broad range from 550 nm to 900 nm. Therefore the Pt/Ir tips were used in chapters 5–8.

When introduced in the head, the Pt/Ir tip was repeatedly indented in the

clean part of the Ag/Au sample (on an nm to μm range) followed by positive or negative $7-10$ V voltage pulses of tens of milliseconds duration. Very often, the good plasmonic tip (typical measure is spectral electroluminescence intensity at 2.5 V and 1 nA) is formed after a voltage pulse which melts the tip apex and creates a very sharp termination of the atomic cluster on the tip with weak van der Waals force between the tip and the sample. This can be detected in the AFM and usually, good plasmonic tips have $\Delta f \approx -1$ Hz at 100 mV sample bias and 10 pA setpoint on Ag(111). Also, the plasmon can be often centered at a single wavelength. The tip quality is checked in 2 steps. The metallic character of the tip is revealed by the presence of a sharp featureless surface state on Ag(111) or Au(111) in a differential conductance spectrum (see Fig. A.8 b). The sharpness of the tip apex is probed either directly by resolving frontier orbitals of evaporated molecules on NaCl or by a controlled approach of the tip 700 pm towards the sample at zero bias from the setpoint of 100 mV and 10 pA. If a single atom or symmetric cluster is dropped, the tip is considered to be good. If not, further slight indentation at zero bias up to 5 nm can improve the tip. This procedure cannot be repeated too often, since it usually leads to the loss of the picocavity and plasmon intensity [72].

Eventually, for AFM measurements, the tip is functionalized with a carbon monoxide CO-molecule. First, the CO is deposited on the surface by increasing the partial pressure of CO to 5×10^{-8} mbar in the cryostat chamber using a leak valve and opening an evaporation port for 1 min. The tip is positioned above the CO molecule adsorbed on 2–3 ML NaCl. At 2 pA and 300 mV in feedback, the CO appears as a round depression of less than 1 nm in diameter in STM CH image. The feedback is then switched off and the tip approached at 10 mV bias by a few Å until a sudden jump in tunneling current and Δf is detected [113]. The quality of the tip (mainly its spherical symmetry) is checked on molecules on NaCl. The oscillation amplitude setpoint to record the frequency shift images was set to 50 pm.

2.4 Photoluminescence- and Raman-active tips

During the last part of my PhD, we focused on photoexcitation of the gap plasmon. Implementation of photoexcitation in the microscope enriches its capabilities to perform new methodologies such as STM-PL and TERS. The photoexcitation is experimentally challenging as described in the following section and there are only a few groups worldwide that have mastered submolecular resolved single-molecule STM-PL [90, 72] and TERS [8, 114, 115], none of them in combination with AFM yet.

We started our experiments with a setup sketched in Fig. 2.2 and shown in Fig. 2.3. The tip image can be seen magnified with a CCD camera with an objective lens. We realised that the focused image of the junction (focusing was done on a micrometer size impurity located on the sample in the tunneling junction) is at a focal distance of 4 cm while the $f_{\text{lens}} = 10$ cm. This indicates that the tunneling junction is slightly behind the focal plane of the lens on the scanner head and the beam coming from the junction is converging. Focusing on the junction is possible with a slightly diverging laser beam provided that it can pass through the $\varnothing 12$ mm lens on the scanner head. The laser spot diameter in the junction is

therefore quite large (around 20 μm) due to the spherical aberration of the lens.

We realized that the junction was around 1 mm behind the focal point (depending on the exact sensor geometry) for a He-Ne 633 nm laser. Later, the lens repositioned closer to the junction and the laser spot shrunk below 10 μm. The laser is focused by positioning the laser lens in x, y and z-axes (see Fig. 2.3). Movement of the cage system along x, y, z directions and θ and ϕ angles enable the laser beam to enter the microscope lens in its lower half which eliminates shading by the tip/sensor holder. Once the laser is focused on the junction with the tip in contact (the same point where the tip shines in electroluminescence), the excitation of the nanocavity plasmon can be verified in two ways. The first way is to approach the tip in close contact with the sample at low bias voltage (typically 1 mV and > 1 nA) setpoint on Ag(111) and observe the red-shifted photoinduced plasmon on the CCD camera, filtering the laser line with a long-pass filter. The second option relies on measuring the field emission resonances (FERs) [108] and does not require any optical detection. A certain percentage of tunneling electrons gains energy from the laser-induced gap plasmon in their FER spectrum downshift by the laser energy (see Fig. 2.6). The number of excited tunneling electrons N is proportional to the density of the electromagnetic states at the laser energy $\rho_{\mathrm{NCP}}(E_{\mathrm{laser}})$ the laser power P and the coupling efficiency η

$$N \propto \eta \rho_{\mathrm{NCP}}(E_{\mathrm{laser}}) P_{\mathrm{laser}}.$$

The most convenient way to focus the laser on the junction is to set the bias voltage at the maximum of 1$^{\mathrm{st}}$ FER (4.1 V on Ag(111)), set a reasonable bias modulation amplitude $V_{\mathrm{mod}} = 30$ mV and minimize the demodulated current from the lock-in detector proportional to dI/dV in a constant current mode.

When we focused the laser on a Pt/Ir tip shown in Fig. 2.5 with a strong plasmonic STML response at the laser energy no drop in the dI/dV signal was observed. The image of the laser-illuminated tip taken with an edge-filtered CCD camera revealed that the FIB-cut tip shaft (see Fig. 2.5c) was shining very brightly. However, there was no indication of inducing a gap plasmon in contact, i.e. no decrease of the plasmon intensity upon a few-nm tip retraction. We attribute this to the combination of the mesoscopic shape of the Pt/Ir tip shaft which is very rough and the tip material with a much deeper penetration depth and larger ohmic losses than silver. The coupling η of the laser to the nanocavity is therefore very low. In the literature, a lot of effort has been devoted to preparing a good tip for STML and TERS. Most commonly Ag [116] and Au [117] tip-etching procedures producing sharp and smooth tips were used, but FIB milling was also used [118]. After inserting in UHV, short ion sputtering is usually needed to remove characteristic adventitious carbon which shows up in the Raman spectrum with its D and G bands [114].

We decided to prepare the tip made of Ag wire by FIB front sputtering. The wire was first glued with conductive epoxy (EPO-TEK H21D) on a ferromagnetic tip holder compatible with our microscope. The FIB (around 1 μm in diameter) was scanned on a mask covering the area between two concentric circles ($d_1 = 5\,\mu$m, $d_2 = 25\,\mu$m) drawn on the cross-section of the wire, parallel with the axis of the wire (see Fig. 2.7). A sharp and smooth tip apex was formed. In the end, the whole tip was scanned with the FIB and any whiskers around the main apex were removed. The tip was then transferred to our UHV apparatus and further front
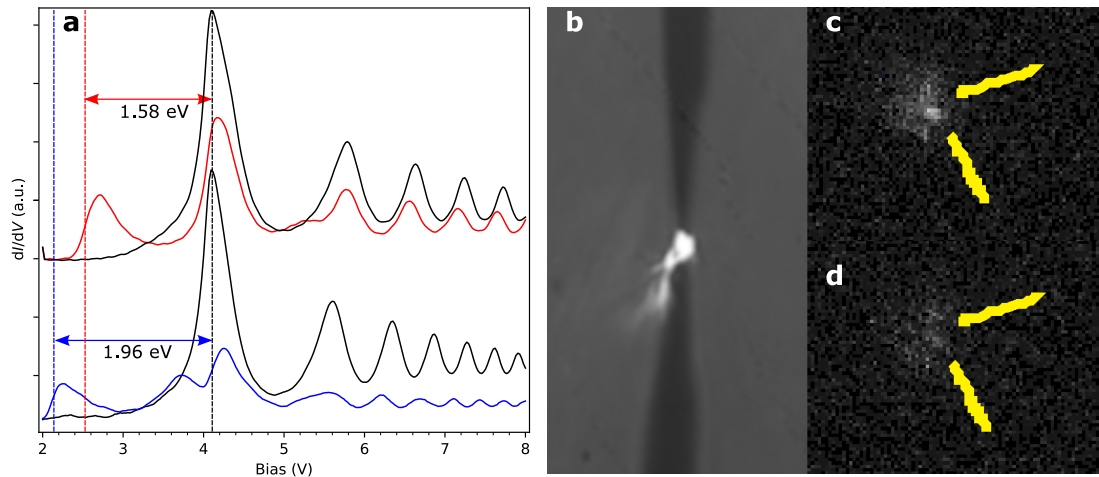
Figure 2.6: a) Field emissions resonances were measured at constant current 300 pA on Ag(111) without laser illumination (black) and with laser illumination (blue curve: He-Ne 633 nm laser; red curve: DPSS 780 nm laser) of 1.2 mW power. Note that not all electrons are photoexcited and the spectrum under illumination is a sum of original and laser offset FERs. The different periods of FER stem from the barrier modification and Stark shift. b) Image of the tip from Fig. 2.5 under laser illumination on the junction. c) Photoinduced redshifted gap plasmon on Ag(111) for tip in tunneling contact (1 nA, 1 mV, 1.2 mW). d) The same image for tip out of contact (5 nm retracted). Yellow freehand lines mark the same position. b)-d) taken with CCD camera via the objective lens.
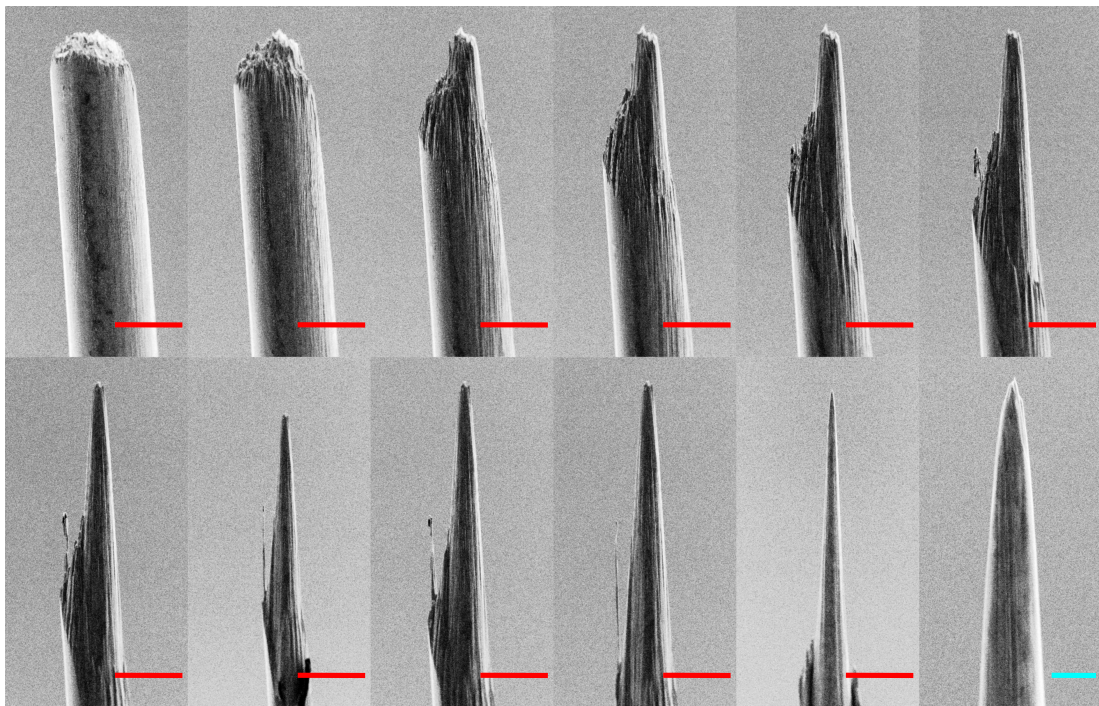
Figure 2.7: Top left to bottom right: SEM images of the 25 μm Ag wire during the front FIB sputtering. Red scale bar 20 μm, aqua scale bar 2 μm. The procedure lasted 25 minutes.

sputtered with Ar^+ 1500 eV energy ions at 8×10^{-6} mbar to remove the carbon contaminants. The tip was gently indented and pulsed (described in section 2.3) until a sharp tip apex with a strong electroluminescence intensity at the laser energy was obtained. These tips possess a strong coupling of the He-Ne laser to the nanocavity plasmons. Even after bending the tip in a pigtail shape, the plasmonic response can be recovered. There can be plasmonic "hot spots" close to the junction contributing to the background signal for a tip out of tunneling contact. The plasmonic response of the tip surface also varies for the excitation energy of the laser. We observed a large background signal coming from the scanner head for excitation wavelength 532 nm (2.33 eV) but a much weaker one for 633 nm (1.96 eV). The deficiency of Ag tips was already mentioned. They are soft and the creation of atomically sharp apex can be tedious. To this end, we were able to prepare several Ag tips made of $25\,\mu$m and $50\,\mu$m thick Ag wires, although the exact shape of the tip is not reproducible. We also succeeded in preparing a photoexcitation active Pt/Ir tip by front FIB sputtering, but it required grabbing a substantially large amount of Ag material which led to destroying the sharp tip apex.

Another challenge, yet not explored, is to use TERS active tips on qPlus tuning forks. In the past [105], the qPlus contacts were shorted with FIB when the whole tuning fork was scanned with ions. Also, the sputtering of the qPlus is not recommended by the manufacturer. We therefore transferred the tips prepared with FIB shown in Fig. 2.7 on the tuning fork. We tested that the qPlus sensor can survive several hours of Ar^+ sputtering which is sufficient for removing the carbon. The tip on the sensor is more sensitive to the thermal drift induced by the laser illumination. Inserting a liquid crystal noise eater (Thorlabs NEL01A/M) in the laser line can stabilize the laser power and reduce the thermal drift fluctuations. Operation of the microscope and measuring STM, AFM and PL or TERS together is possible with low laser intensity below $100\,\mu$W.

2.5   Sample preparation

Single Ag(111) and Au(111) polished crystals with cylinder shape (diameter 10 mm, height 2 mm) purchased from MaTeck or SPL were used. First, the crystals were attached to the molybdenum/tantalum Omicron-type sample holder with thin stripes from the same material (see Fig. 2.8) spot-welded on the sample plate. After introducing to the UHV, the cleaning procedure consists of repeating cycles of Ar^+ ion sputtering at 8×10^{-6} mbar argon pressure with 1500 eV acceleration energy and annealing to 500–550 °C. During my PhD, I fully automated the cleaning procedure by writing a custom LabVIEW software communicating with VAT UHV All-Metal Variable Leak Valve, Specs Coscon ion gun controller, Delta Elektronika voltage source and ion pump controller. It is important to note that the fresh crystals were always first sputtered to remove carbon contaminants before the degassing as the carbon conglomerates into 3D structures after annealing and their removal is impossible due to the low carbon sputter yield. After the last annealing cycle, the sample was partially covered with a shutter and NaCl was evaporated on half of the sample at sample temperature 80–130 °C from a tantalum crucible heated to 607 °C for 3–5 minutes. This leads to the formation of defect-free 2–4 ML height NaCl(100) islands. Higher sample temperature pro-

vides extra kinetic energy to overcome the surface's diffusion barrier, leading to larger islands' growth. On Au(111), the proportion between 2- and 3-ML height NaCl islands can be eventually tuned by increased annealing temperature up to 190 °C [119]. The sample is precooled on the LN cryostat before introducing into
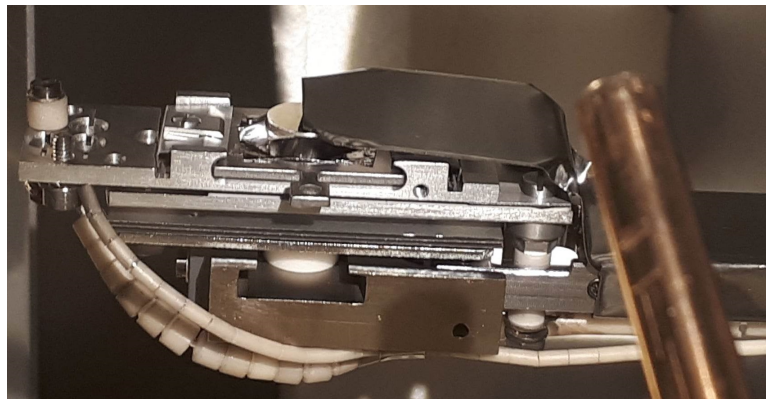
Figure 2.8: a) Image of the Ag sample inserted the manipulator and half-covered with a shutter, which can be slid with a wobble stick (on right).

the STM head. Cooling down to 7.5 K takes around 1 h during which the head is clamped. Single molecules are evaporated from a Ta crucible on a cold sample (< 10 K) to prevent molecular diffusion. The evaporation temperatures are: 331 °C (H_2Pc), 380 °C (MgPc), 415 °C (ZnPc), 420 °C (CuPc), 360 °C (PTCDA) and 210 °C (NTCDA). The phthalocyanine molecules ($> 90\%$ purity) were purchased from Sigma Aldrich and the perylenes were provided by Ruslan Temirov from FZ Juelich. In chapter 7, we heated up the sample slightly (100–150 K) to form molecular clusters from PTCDA molecules on purpose. An overview of such system is shown in Fig. 2.9. The thickness of NaCl layer can be estimated from Δf image. Closer tip-sample distance on NaCl islands at the same tunneling current setpoint results in a more attractive van der Waals interaction and a more negative Δf (scale towards red). Alternatively, the NaCl thickness can be determined from the apparent height of a NaCl step [99].
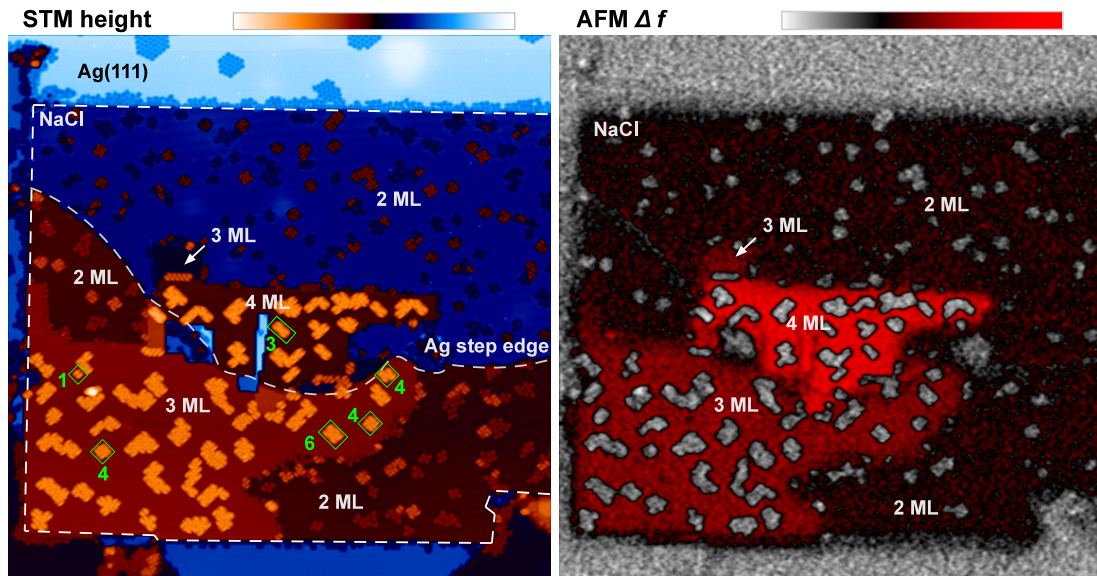
Figure 2.9: STM and AFM image of a prototypical system PTCDA/NaCl/Ag(111) used in this thesis acquired in a constant current mode. The sample was annealed to 150 K for 1 minute resulting in the formation of PTCDA aggregates (the number of PTCDAs in an aggregate is written with green text). The image size is $110 \times 110\,\text{nm}^2$, mapping bias 1.2 V corresponds to the LUMO energy of PTCDA on NaCl and a low 2 pA tunneling current setpoint prevents the tip from picking up adsorbates from NaCl. The image was taken with a metal tip.

2.6 Measurement software

The Createc SPM is controlled by Nanonis Control System including both hardware (a stack of electronics) and software (Nanonis V5) running on a Windows computer. It offers a programming interface based on the LabVIEW functions (VIs) for simultaneous operation with the Nanonis software. Since LabVIEW graphical programming is not time efficient, my supervisor Martin Švec wrote a LabVIEW program based on a case structure sequentially interpreting custom commands. Each command can have up to 3 parameters. It was natural to continue in this scheme and I implemented control of the Andor instruments as well as other instruments (RF generators, SPADs, Time Tagger electronics, Laser etc.) in the LabVIEW scripting framework. Unlike Nanonis, Andor Solis software does not support the simultaneous operation of the software and external commands. In the beginning, when only the CCD camera was remotely controlled, we used Andor Solis software running on another computer and its programming interface based on its Basic language. We were able to change basic parameters, acquire spectra and save them. The communication was based on sending short commands via the RS232 interface. Post-processing was needed to pair the data from CCD with its acquisition parameters in Nanonis. Later, Martin Švec programmed a socket-based interface for Andor CCD and spectrograph operation using the Andor software development kit (SDK) and running on a Ubuntu mini computer. This enabled faster acquisition and real-time browsing through the data which were transferred using Transmission Control Protocol (TCP). Single optical spectra are now saved in Nanonis spectroscopy *.dat* format with a header containing acquisition parameters from both Andor and Nanonis SPM and the

channels "Wavelength" and "Counts". Photon maps are spectra taken on a 2D grid of points. This 3D volume of data is saved when the map is finished in the Nanonis binary *.sxm* file used for the SPM images. The "Current", "Z", "Frequency Shift" and other SPM channels are appended by another 1024 channels corresponding to the number of columns of CCD named by their wavelength value. Individual spectra are perpetually appended to a binary *.3ds* format file as a backup in case of a sudden user interruption. The data are post-processed with a despike filter, the background is subtracted and eventually, the plasmon normalization of the excitonic signal is performed. Software or scripting language based on the user's preferences is used. The majority of the spectroscopic data presented in this thesis are analyzed and plotted using my own Python scripts and Matplotlib visualisation library.

3. Electroluminescence with CO-functionalized tips

The following chapter is based on the publication [32] and reprinted with permission. Copyright 2019 American Chemical Society. Having a strong background in STM and AFM, we focused on the performance of CO-functionalized tips in photon mapping in our first STM-EL study. At that time, only the group on Leo Gross in IBM Zurich showcased the combination of STM, AFM and electroluminescence by inducing a chemical reaction on VOPc [120] and measuring the STM-EL of the product. However, STM-EL was not performed with a CO-tip. Previously, CO-tips were only used in TERS spectroscopy [114]. Since our optical setup was not optimized for photon collection (cryostat windows with the short pass cutoff at 700 nm, CCD camera with quantum efficiency of only 10%) we have chosen ZnPc emitter, well-known for its high quantum efficiency [12, 33, 81]. The original interpretation of the excitation mechanism in our publication [32] was updated to the current understanding and elaborated in detail in subsection 1.4.2 and chapter 5.

3.1 Introduction

Optical properties of molecules are intimately connected to their atomic and electronic structure. In recent years we have seen spectacular advancement in the study of single molecular emitters at the nanoscale [80, 121]. Quantum emission [98, 86] energy-transfer processes [11, 84], or Raman spectroscopy can now be probed with sub-Å resolution [8, 122]. The underlying mechanisms involved in the optoelectronic response at the scale of individual molecules have not been fully elucidated yet and are a subject of intense scientific debate [8, 37, 81, 33]. Scanning tunneling microscopy-induced luminescence (STML) provides a unique platform to examine charge-to-photon conversion on individual molecules with atomic scale precision. Several excitation mechanisms have been proposed to explain the observed molecular emission under varying tunneling conditions, namely direct charge injection, where pairs of opposite charges meet in the molecular emitter to form singlet [123, 124] or triplet [94] states, energy transfer between the plasmon and molecular excitons [84, 85] or between different excitonic states [11], or triplet mediated up-conversion [125]. However, the extent and interplay of these mechanisms are still actively debated.

Independently, advances in noncontact atomic force microscopy (AFM) methodology opened a unique way to directly image the atomic structure of molecules, which has been already applied to an immense variety of systems [126]. Combining information from force maps and photon maps is a long-sought goal since it could help to explore new photophysical phenomena on individual molecular emitters with an unprecedented level of detail and insight [120]. A combination of STML and AFM will be a conceptual scientific advance that will take all the benefits of high-resolution imaging and AFM-related spectroscopies. For example, Kelvin probe and image distortion techniques can be used for investigating the charge of emitters [127, 49], force-distance curves to probe their

adsorption heights, and imaging in combination with probe-particle model can help identify adsorption sites and chemical changes [120].

However, for submolecular imaging with AFM, the tip needs to be functionalized by a probe particle (most frequently a CO). The impact of the probe particle on a tip apex in local optical spectroscopy is an open question that has not been addressed for the case of STML yet [114, 128, 129]. The spatial resolution and contrast of the optical signal may be affected since the exciton formation rate within molecules strongly depends on the charge transport channels, which are defined by the spatial and energetic electronic orbital structure of the tip apex and the molecular interface [80]. As the probe functionalization usually results in a lower junction conductivity, it may prove to be a factor in obtaining sufficiently strong signals on multiple layers of insulating material. Moreover, STML relies on relatively large biases necessary to induce the excitonic state. In contrast, a high-resolution AFM imaging typically uses very low biases in order to avoid spurious effects of the electrostatic force, high tunneling currents resulting in a crosstalk between the tunneling and force channels or a loss of the probe particle. Despite recent advances [120], it is still not clear whether the STML methodology is compatible with the noncontact AFM framework.

In the present letter, we use a combination of STML and AFM to investigate a prototypical example of single molecule emitters: ZnPc/NaCl on two different metal substrates: Ag(111) and Au(111) (see schematics in Fig. 3.1a). We correlate the photon and force maps of individual emitters and determine the feasibility and role of CO tips as the STML probes. We show that CO functionalization is compatible with electroluminescence measurements in STM and leads to enhanced lateral resolution of photon maps due to the involvement of the p-orbitals of the CO-tip in the tunneling process [130]. Since the ZnPc molecules on NaCl have a natural tendency to alternate between two adsorption geometries when exposed to higher tunneling currents [131], we characterize the effect of the motion on the force and photon maps by comparison to a stabilized ZnPc molecule. Finally, by correlating photon maps with the spatial distribution of the molecular orbitals, we address the leading excitation mechanism on each inspected substrate.

3.2   Results and Discussion

In Fig. 3.1b we present a STM constant-current (CC) overview image of the system, prepared on the Ag(111) substrate. The adsorbed ZnPc molecules deposited onto a cold sample (4 K) appear scattered on top of a trilayer NaCl area as well as on the bare metal. Overview shows two ZnPc molecules that exhibit a symmetrical 16-lobe appearance in the CC images scanned at -2.2 V. This appearance is characteristic of their fast angular switching between two equivalent adsorption configurations triggered by the flow of the tunneling current (in the order of 1 pA) [131]. If $|V_{\text{bias}}|$ is decreased sufficiently (< 1 V, 6 pA), the switching rate drops well below frequency cutoff of the tunneling current preamplifier of the STM (1 kHz). This can be manifested by a telegraph noise in the tunneling current channel (Fig. 3.1c) with a tip positioned above the molecule lobe at constant height (CH) with the feedback loop open. The overview in Fig. 3.1b also shows one molecule with 8 lobes, likely stabilized by a defect of the NaCl

structure underneath. We observed a very similar behavior for ZnPc/NaCl on the Au(111) substrate, confirming previous work [81]. Thus, at the biases needed for inducing electroluminescence ($|V_{\text{bias}}| > 1.8$ V), the most commonly found state of the molecules is dynamic.
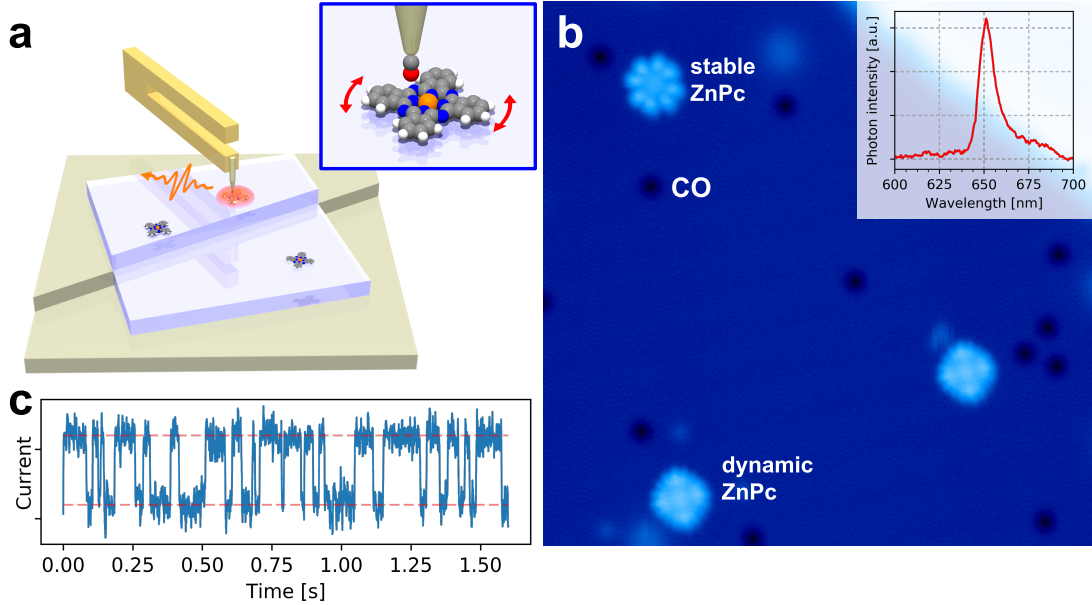
Figure 3.1: (a) Schematics of the experimental setup, in which the STM and AFM signals are collected together with electroluminescence signal on single ZnPc molecules, electronically decoupled from a metal substrate by an insulating NaCl layer. For this purpose, a CO-functionalized tip is used (shown in the inset). Applied current/bias leads to a configuration switching of the adsorption position of the molecule (inset). (b) STM image of dynamic and stable ZnPc molecules on the surface of trilayer NaCl on Ag(111) surface, with an example luminescence spectrum in the inset. The $23 \times 23 \, \text{nm}^2$ image was taken at -2.2 V, 5 pA. (c) Telegraphic noise recorded on a dynamic ZnPc at 1.0 V, 6 pA.

By controlled nanoindentation of the tip into a clean patch of the substrate metal, we have been able to obtain tips that had a strong optical response (measured by plasmon intensity at a fixed current, see Fig. A.1) and had been successfully functionalized by CO picked up from the NaCl layers. With these tips, we recorded luminescence and high-resolution AFM/STM signals using a tuning-fork sensor. The important consequences of the CO attachment are a chemical passivation of the probe apex, change to a prevailing p-type electronic character [130] and enabling the submolecular resolution in AFM, detected as a change of the sensor resonant frequency. This channel provides a contrast closely related to the atomic structure of the emitter [21, 20].

To evaluate the impact of the ZnPc rotation on each measured channel, including the photon emission, we measured two sets of maps on: (i) a dynamic and (ii) a stabilized molecule with a CO-functionalized Au tip. The spatially resolved maps of the tunnel current, frequency shift, and photon channels for both molecules were taken within the same measurement session, with the same tip, found on the same NaCl terrace (see Fig. A.2). The data shown in the upper row of Fig. 3.2 originate from a ZnPc that has been found stabilized in one adsorption position, by the proximity of a step edge of the NaCl trilayer. At a bias of +2.2 V,

the CC STM of this molecule essentially reproduces the shape of the ZnPc LUMO with its characteristic 8 lobes and a pronounced central part [131]. However, in the CH mode, a square-like pattern emerges in the molecular center, which is a telltale sign of imaging by a mixed s- and p-wave tip, confirming the presence of the CO at the apex [130]. The frequency shift map, taken at a considerably lower voltage (25 mV) and with the tip closer to the surface by 250 pm, resolves the pyrrole backbone of the ZnPc molecule and its peripheral benzene rings with high spatial precision. The dynamic molecule shown in the bottom row of Fig. 3.2 exhibits the previously described STM contrast of a dynamic molecule [33]. The AFM taken at 25 mV confirms that there are two distinguishable angular positions without any lateral movement, since the angular switching slows down enough to hold each position at time scale of minutes (shown in Figs. A.3 and A.4). The detail of the frequency shift maps allows to determine the angular orientations of the two metastable configurations for the dynamic molecule as $+11°$ and $-11°$ with respect to the NaCl(001) layer main crystallographic directions and reveals that the stabilized molecule corresponds to one of these metastable configurations. Using the angles, it is possible to reproduce the STM images of the dynamic molecule at 2.2 V in Fig. 3.2, by averaging two mutually rotated and symmetrized STM images of the stable molecule (shown in Fig. A.5). Additional manipulation experiments show that both stable and dynamic type molecules are centered above Cl^- ions (Fig. A.6) [132].
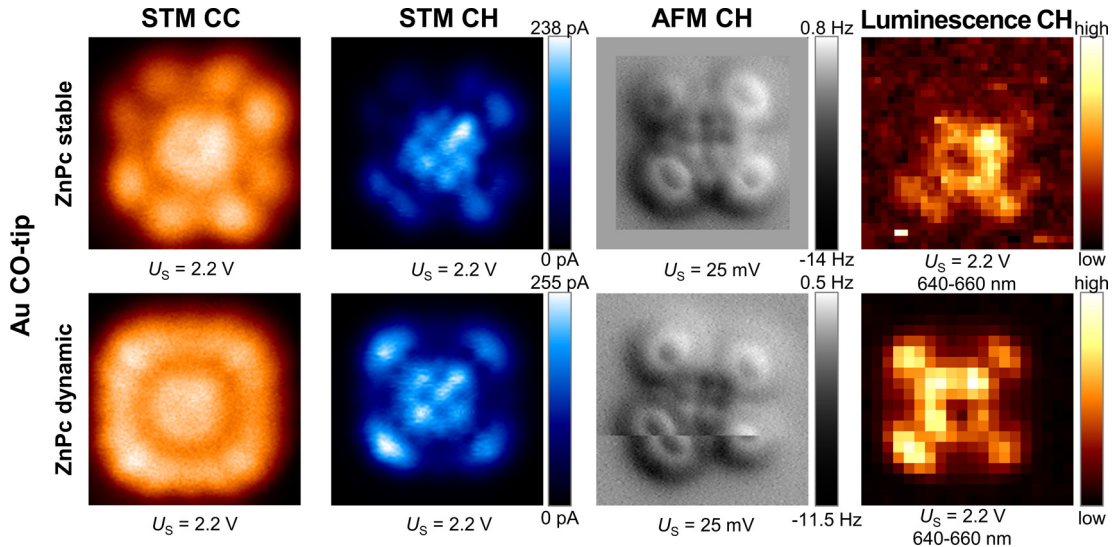
Figure 3.2: Comparison of spatially resolved constant current (CC) STM, constant height (CH) STM, AFM CH, and luminescence CH, obtained by Au-CO-tips on a stable (top row) and a dynamic ZnPc molecule (bottom row), adsorbed on trilayer NaCl on Au(111). All image sizes (including padding at the bottom AFM image) were $2.2 \times 2.2\,nm^2$. The constant current STM images were taken with 1 pA set point. AFM CH maps have been taken at 250 pm closer tip-sample distance with respect to their corresponding STM CH images.

We have recorded the electroluminescence spectra and constant height photon maps at $V_{bias} = +2.2$ V on ZnPc in both states. The spectral fingerprints of the dynamic and the stable molecule do not exhibit significant differences within our resolution; the intense main fluorescence line is located at 653 nm (1.9 eV), accompanied by red-shifted vibronic sideband (Fig. 3.1b inset and Fig. A.2d).

The spatially resolved photon maps of the integrated main emission line (640-660 nm) of the dynamic and stable ZnPc molecules, taken in constant height mode, are shown in the right part of Fig. 3.2. For both dynamic and stabilized molecule, these photon maps resemble at first glance their corresponding CH current images. This observation points to a direct charge carrier injection from the tip as the main mechanism for excitation that precedes the luminescence at this voltage [94, 125, 133, 134]. A deeper inspection of the maps reveals a dip in the photon intensity at the center of the molecule, although the density of states and the CC image reach high values at the same spot. The existence of a minimum in metallo-phthalocyanine photon maps has been observed previously with metallic tips and has been attributed to the spatial variation of the exciton coupling to the nanocavity plasmon modes [135, 71].

To better understand the impact of the tip state on CH luminescence maps, we have performed a detailed characterization of the ZnPc molecules also with bare metal tips. In the case of Au tips, both the CC and CH STM modes show a very similar type of contrast (first row of Fig. 3.3), contrary to the data obtained by Au CO-tips (second row of Fig. 3.3). This rather blunt contrast at the periphery and in the center of the molecule is a consequence of two factors: the overall s-wave character of the bare Au tip and smearing of the features by the rapid angular switching. The CH photon map, again, closely resembles the CH tunneling current maps, except for the dip near to the center. We have observed this dip at various off-center positions (see Fig. A.7), whose lateral shift seems to be related to the mesoscopic tip shape. This is not surprising, as the real tips are likely to deviate from the spherical shape, and therefore they are expected to screen asymmetrically the transient dipole moments involved in the emission process [71].

Detailed luminescence spectra, taken at various positions above the molecule (spectra in the right column of Fig. 3.3) with both CO and metallic tips confirm the strong intensity modulation of the CH photon maps by the tunneling current and suppression of the signal near the molecular center. This observation reveals the direct effect of the tip frontier orbitals in combination with the shape of the ZnPc LUMO on the electroluminescence maps and indicates that injection of electrons from the tip to the molecule triggers the excitation, which can eventually lead to luminescence detection. We now raise the question whether an analogous mechanism is also valid for biases where hole injection is the primary mode of charge transport. Using negative biases on the ZnPc/NaCl/Au(111) system is not suitable since it leads to ZnPc transiently switching to a cationic state. This would result in the preferential activation of a different excitonic state, manifested by a lower energy photon emission below the detection threshold of our optical setup [81]. However, it has been reported that using Ag(111) as a metallic substrate leads to the same 1.9 eV exciton radiative decay detectable at negative biases [33].

Therefore, we performed experiments on the ZnPc/NaCl/Ag(111) system and obtained photon maps with both metal (Ag-coated Au tip) and CO-functionalized tips (third and fourth rows of Fig. 3.3). Here, the photon maps are also closely related to the respective tunneling current. The current flows predominantly through the HOMO of the dynamic molecules decoupled from the substrate by trilayer of NaCl. The effect of the CO on the STM images, apart from a sharp-
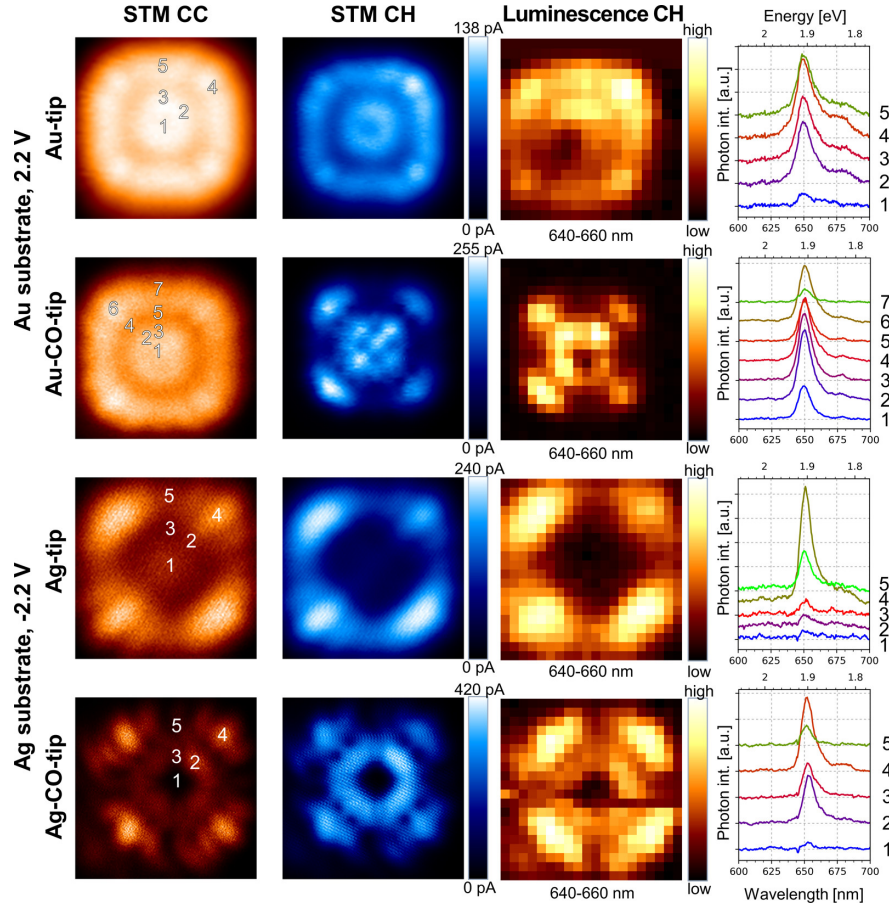
Figure 3.3: Effect of the functionalization (CO-tips vs bare-metal tips) and substrate on the photon maps and point spectra of the dynamic ZnPc molecules. The two upper rows show data taken above ZnPc on the 3 ML-NaCl/Au(111). The two bottom rows are results obtained above ZnPc on 3 ML-NaCl/Ag(111). STM images at CC, CH, STM-induced luminescence maps at constant height measured with metal and CO tips are presented for comparison. The numbered CH spectra shown in the right-hand side column have been taken at the positions marked in the CC STM images. All image sizes are $2.2 \times 2.2\,\text{nm}^2$, and tunneling current set points for CC images were 10 pA and 1 pA on Au and Ag substrate, respectively.

52

ening of the contrast of the peripheral benzenes, is the appearance of the central pyrrolic ring. This pyrrolic ring is very pronounced in the CO-tip maps, but absent from the metal-tip images. This feature is a good indicator for the difference between the current and photon maps in the central part of the molecule. For the metal tip, the photon map faithfully copies the current except for a small central area, where a dip occurs similarly as in the positive biases on Au substrate. For the CO-tip, although the general contrasts of the photon and STM CH maps are similar, the photon signature of the pyrrolic ring is weaker with respect to the periphery of the molecule, contrary to the corresponding CH STM.

Comparing the photon maps obtained on the Au(111) at positive biases and Ag(111) at negative biases with metal and CO-tips, we see striking differences corresponding mainly to the distinct spatial modulation of the charge carrier transport. On both substrates, the spectra show an identical line shape, which implies that we observe the radiative decay of the same final S_1 excited state. This general correspondence between the tunneling current and the luminescence channels indicates that the fluorescence is triggered by a resonant tunneling charge injection into the molecular orbital, in analogy with the explanations suggested for H2Pc and ZnPc/NaCl/Ag(111) in previous studies [37, 125]. This brings us to the discussion of how different excitation mechanisms occurring under given circumstances (bias polarity, workfunction of the substrate) lead to the same excited state of ZnPc and its subsequent radiative decay.

The alignment of the molecular levels relative to EF of the substrate is remarkably different between Au and Ag, as it can be inferred from the differential conductance curves of each system (see Fig. A.8n), caused by the higher work function of Au(111) compared to Ag(111) [81, 33]. On trilayer NaCl/Au(111) substrate, the ZnPc LUMO is detected at +2.2 eV and HOMO at -1.1 eV [81]. On the Ag(111) substrate, the situation is LUMO at +1.0 eV and HOMO at -2.3 eV [33]. Presence of a state near the EF can be detected on the molecule in the differential conductance spectrum (see Fig. A.8). This state matches by energy to the interface state studied at bare NaCl/Ag(111) [119]. A similar state is also known to exist on NaCl/Au(111) [136] and can be involved in the charge transport between the substrate and the molecule by reducing the length of the tunnel path through NaCl [38, 35].

We have detected the predominant 1.9 eV radiative exciton generation occurs in opposite bias polarities on Au and Ag substrates, scaling with the total electric current transported through the ZnPc LUMO and HOMO levels, respectively. We cannot entirely rule out an energy-transfer mechanism between ballistically transported inelastic electrons, decaying in the substrate, and the exciton, however important details as the bipolar character of the electroluminescence is not captured in such a scheme [84, 125, 134]. We believe the mechanism of the excitation needs to be described by the so-called many-body scheme [37] (see subsection 1.4.2 and Fig. 5.5). If the energy of the cation or anion ground state (D_0^+ and D_0^- respectively) is higher than the energy of neutral excited state S_1 the exciton can be created by electron tunneling to/from the positive or negative ion resonances (corresponding to HOMO and LUMO, respectively) and a subsequent hole/electron capture from the metallic substrate.

3.3   Conclusion

To conclude, we have performed a real-space multichannel study of the prototypical molecular emitter, ZnPc, by combining tunneling current, force, and photon maps of the quantum emitter on Au(111) and Ag(111). We demonstrated compatibility of the CO-functionalized tips with electroluminescence measurements. STML maps were compared for two states of the ZnPc: the dynamical angularly switching state, induced by bias and current, and a state stabilized in a single position. The CO functionalization leads to the enhancement of the spatial resolution of photon maps as compared to bare metal tips. By studying the spectra and photon maps obtained by injecting electrons and holes into the molecule by metal and CO-tips, we have found that photon intensity maps are intimately linked to the spatial modulation of the tunneling current, corresponding to charge transport from the tip to the molecule. Electron injection from the tip into the molecule LUMO is triggering the exciton formation events in the ZnPc on NaCl/Au(111), while hole injection into its HOMO initiates the process at NaCl/Ag(111) substrate. Our findings identify the role of the tip status in the STML photon map contrast and open new avenues to spatially resolved optical measurements of single-molecule emitters in combination with submolecular-resolution AFM.

3.4   Methods

All spectra and maps were collected in a photon-counting regime. Photon maps were measured in a constant height mode, by taking a spectrum at every point, with accumulation period per pixel typically 7 s. In the presented maps, each pixel represents part of a corresponding spectrum, integrated in the given range of wavelengths. Photon maps are recorded in constant-height mode. The constant-height mapping mode is a rational choice for taking the photon-maps, since the constant-current mapping may introduce ambiguity due to the variable Z-height, e.g. by modulating the nanocavity optical density, that is likely to produce unphysical features in the photon maps.

4. Environment-controlled molecular emission

The following chapter is based on the publication [137] and reprinted with permission. Copyright 2020 American Chemical Society. We have chosen copper phthalocyanine as the next system to study. The possibility to reversibly switch the molecule between two stable configurations makes it an ideal candidate for studying the effects of the NaCl polar environment on its electronic properties. Moreover, its unexpected doublet fluorescence [138] is of fundamental interest [139] of the research of stabilized radicals which can have up to 100% internal quantum efficiency for electroluminescence.

4.1 Introduction

When a single-molecule emitter (SME) is placed in a solid or onto a surface, it is subjected to hybridization or screening of its electronic orbital structure with the local environment due to Coulomb interaction. One of the typical consequences is a change in the energies of the molecular electronic excitations, sometimes called spectral diffusion [140]. Photoluminescence and related time-resolved techniques have been widely used to measure exciton environmental effects in SMEs [91], but achieving high spatial resolution that can resolve individual emitters has remained a challenge. Efforts to study the local environment of excitons in 3D molecular crystals [141], 2D materials [142, 143, 144], or 1D carbon nanotubes [145, 146] have been made; however, an atomic spatial resolution is still lacking. Recently, STML has emerged as a powerful tool to probe optoelectronic properties on the atomic scale [80], such as exciton charge annihilation [98], coupled modes on molecular dimers [12], superradiance in artificially constructed chains [86], or the charge state [81]. Spectral switching has been investigated by using resonant energy transfer between different excitons in Pc heterodimers [11] and by tautomerization of H_2Pc [147]. Nevertheless, the Coulombic effects of the local environment on the excitonic states of SMEs have not been extensively addressed [124, 123].

For closed-shell single-molecule emitters excited in a tunnel junction, injection is not spin-selective and the formation probability is 75% for dark triplet and only 25% for bright singlet excitons [80]. To obtain higher efficiencies for light-emitting purposes, triplet-to-singlet intersystem crossing [148] and bright triplet states [149] have been proposed to effectively increase the quantum yields. Recently, the discovery of electroluminescence from a doublet, rather than from a singlet or a triplet, has allowed reaching emission quantum yields up to 100% [150]. However, doublet emission has, so far, been only demonstrated for ensembles of radical species easily undergoing chemical degradation, and doublet SMEs have not been reported.

Here, we show using combined STML/AFM measurements and ab initio calculations that the doublet excitonic state of SMEs can be controlled in a deterministic way by atomically precise manipulations. The use of scanning probe technique at cryogenic temperature allows the manipulation of the adsorption

configuration of individual copper phthalocyanine (CuPc) molecules on ultrathin NaCl films on Ag(111) with sub-Å precision and consequently control their excitonic state. CuPc is an open-shell complex with spin $S = 1/2$ due to an unpaired electron residing in the $d_{x^2-y^2}$ (b_{1g}) metal orbital [151, 152, 153]. By injection of charge carriers we create electron-hole pairs in the resulting SMEs and detect the photon emission enhanced by the plasmonic picocavity formed by the tunnel junction. We observe a change in the wavelength of the excitonic emission between two configurations. Combination of atomically resolved STM images with AFM frequency shift maps, local tunneling spectroscopy, and ab initio calculations allows determining the modification of the electronic structure of the molecules and linking it to the observed shift of its excitonic line.

4.2 Results and Discussion

Fig. 4.1 shows a sequence of STM images, an AFM image, and electroluminescence spectra obtained during a manipulation experiment of SMEs. In Fig. 4.1a-c the same two CuPc molecules are resolved in the two possible adsorption positions, namely, dynamic and steady states (see below), on top of a two-monolayer (ML) of NaCl on Ag(111) (for details of sample preparation see the Methods section). In Fig. 4.1a both CuPc molecules manifest a 16-lobe pattern characteristic of molecules in a dynamic configuration arising from a bistable adsorption geometry. The distinctive STM appearance can be rationalized by the overlapping electronic structures of two chirally rotated adsorption configurations oscillating at a frequency well beyond the STM bandwidth [32]. STML spectrum 1 in Fig. 4.1e, typical for dynamic CuPc, taken at -2.5 V above a lobe consists of a sharp line at 1.9 eV on a plasmonic background (Spectrum 6). Spectrum 2 taken on the dynamic molecule on the right-hand side of the panel in Fig. 4.1a however reveals a different spectral fingerprint. It shows the sharp line at 1.9 eV accompanied by an intense shoulder at lower energies, which is an indication of a sudden modification of the molecular exciton state. Indeed, a subsequent image (Fig. 4.1b) confirms the molecule changed its appearance to an eight-lobe shape typical for a steady stabilized molecule. STML spectrum 3 remeasured on the now steady molecule shows a broad peak at the shoulder position at 1.86 eV and disappearance of the 1.9 eV feature. Spectra 4 and 5 reproduce the same behavior on the second molecule upon switching from dynamic to the steady configuration, visualized by the STM in Fig. 4.1b,c. Therefore, spectrum 2 can be rationalized as a linear combination of the spectra from the dynamic and steady states.

In our investigation of the dynamic to steady state conversion of molecules on 2 and 3 MLs of NaCl on Ag(111) we found that molecular switching from the dynamic to the steady state occurs reproducibly after applying 100 pA and -2.3 V or at biases over 2.0 V, similarly as described by Zhang et al. for manipulation of ZnPc molecules [12]. The conversion from a steady to a dynamic state process can be achieved at biases of -2.5 V and below, by applying lateral forces with the CO-passivated tip to prevent picking up the molecule, however with a significantly lower efficiency, strongly indicating that the steady state is energetically favored over the dynamic state (for details see the Supplementary Information in Appendix B). Switching CuPc to a steady state produces a systematic red-shift and broadening of the STML lines of the spectrum. We have measured red-shifts
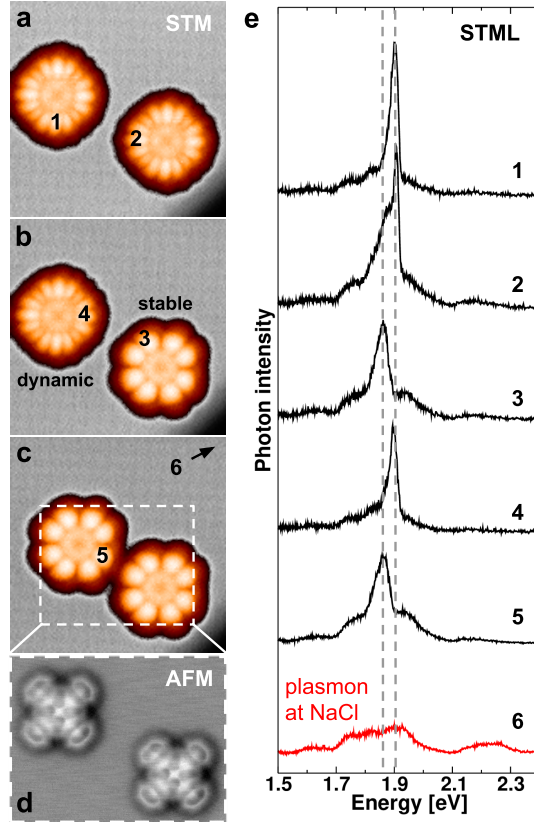
Figure 4.1: Experiment probing the manipulation of the adsorption geometry and its influence on the STML spectra. (a-c) Sequence of STM constant-current images of two CuPc molecules at 2 ML-NaCl/Ag(111), subsequently switched from dynamic to steady state, using a CO-tip. Image parameters: $6 \times 6 \, \mathrm{nm}^2$, -2.5 V, 1 pA. (d) Submolecular-resolution AFM image of the area in (c), taken in constant-height mode with the CO tip, showing the CuPc backbone. Image parameters: $4.2 \times 3.2 \, \mathrm{nm}^2$, 10 mV. (e) STML spectra of the molecules in (a)-(c), numbered correspondingly 1-5, and reference spectrum taken on a bare NaCl (6). Acquisition parameters for the spectra were -2.5 V, 50 pA, 60 s.

of 20.6 ± 3.4 meV for molecules at 3 ML and 34.0 ± 3.5 meV at 2 ML, plus broadenings of $(63 \pm 13)\%$ and $(103 \pm 29)\%$ (Fig. 4.2b, Fig. B.2, and Table B.1), respectively. Both effects are more pronounced on 2 ML of NaCl than on 3 ML. The environmentally induced exciton modification presented here has not been observed in photoluminescence nor in electroluminescence of CuPc single crystals [138] or thin films [154, 155]. The exciton switching of the CuPc must therefore originate from the interaction of the electronic structure of the molecule with its nearest local environment.
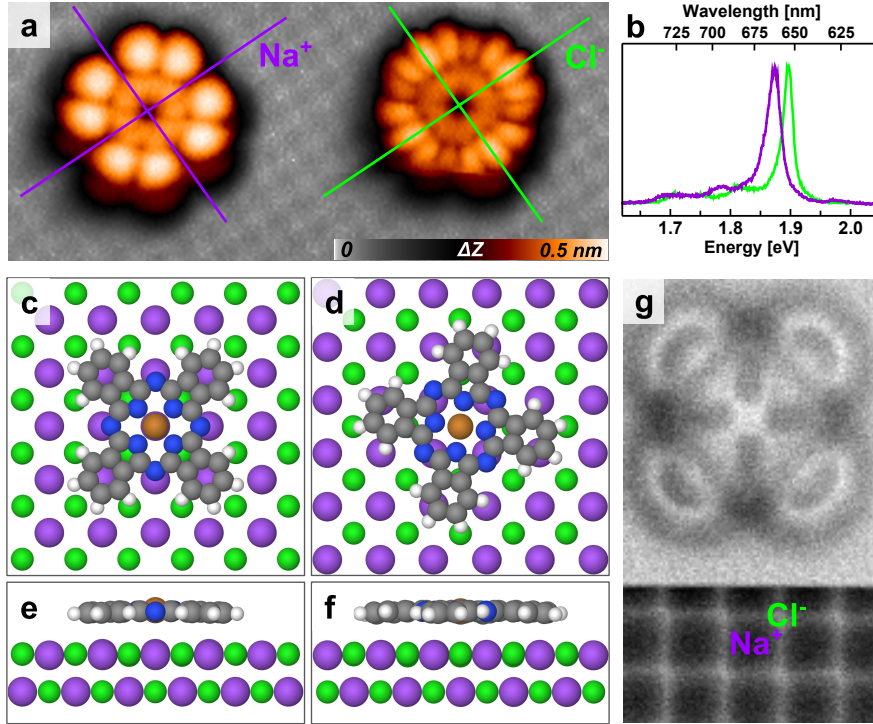
Figure 4.2: Analysis of the adsorption geometry in relation to the STML fingerprint. (a) STM constant-current image of CuPc molecules in the steady and dynamic configurations and their registration with the NaCl lattice obtained with a CO-functionalized tip. Parameters: 7.5×3.2 nm^2, -2.3 V, 1 pA. (b) Representative STML fingerprints of the dynamic (green) and steady (violet) configuration on 3 ML NaCl. (c-f) Computationally optimized theoretical models of the steady (c, e) and dynamic geometries (d, f). (g) AFM constant-height frequency shift map with two different tip heights enabling submolecular resolution on the CuPc and atomic resolution on the NaCl substrate for registration. Parameters: 1.7×2.8 1.7×2.8 nm^2, 25 mV. The spheres in the models in panels (c)-(f) representing the atoms have sizes corresponding to their atomic radii.

An atomic-scale characterization of the steady and dynamic adsorption configurations of CuPc on NaCl provides the link between their adsorption configuration and the spectral switching. A high-resolution STM image obtained with a CO-functionalized tip in Fig. 4.2a shows two molecules, each in one of the configurations, together with the underlying NaCl lattice. It has been shown that STM topographs of NaCl typically image Cl$^-$ ions as protrusions [156, 157]. Accordingly it can be determined that the dynamic molecule is adsorbed with its metal core located on top of a Cl$^-$ site (darker color, higher Z-value), while the steady state latches on top of a Na$^+$ site (brighter color, lower Z-value). This is further confirmed by the frequency shift channel, measured on the steady

configuration in Fig. 4.2g. The image is composed of two sections measured in constant tip-sample height at different offsets facilitating atomic resolution on both the molecule and the substrate. It permits straightforward identification of the molecular backbone (in the upper section of the panel) and enables a very precise registration with the substrate (lower section). As the image is taken in a regime where repulsive forces dominate, the lower frequency shift regions can be unambiguously attributed to Na^+ atoms [158]. By extrapolation of the substrate lattice it is then easily demonstrated that the steady CuPc is centered above a Na^+ site (see AFM simulations in Fig. B.1).

These findings agree with first-principles simulations, in which a model CuPc molecule was positioned with different angles of in-plane rotation with respect to the 2 ML-NaCl lattice, over Na^+ or Cl^- ions. After a self-consistent minimization of the total energy of the system, the most stable configuration is found to be a 45°-rotated molecule above the Na^+ site, and the second most stable at an $\pm 9°$ angle sitting on the Cl^- site (see Fig. 4.2c,e and Fig. 4.2d,f, respectively). These two configurations perfectly match the experimentally observed steady and dynamic configurations, respectively. The calculated total energy difference between them is 90 meV in favor of the steady geometry. The simulated relaxations of the molecular backbone and the separation from the NaCl surface in both configurations are comparable and only marginally different, as in both cases the peripheral parts are slightly bent toward the substrate [159].

The modification of the exciton energy described above can be reproduced by excited-state DFT calculations performed for isolated CuPc and the dynamic and steady configurations on the NaCl substrate, placed on either the Na^+ or Cl^- sites. NaCl is modeled by point charges, and the equilibrium geometries are derived from the previous DFT simulations. The excitation is represented by a transfer of a spin-up or spin-down electron from the highest occupied molecular orbital (HOMO) of CuPc in its ground state D_0 into the lowest unoccupied molecular orbital (LUMO), producing an excited state D_1. In the ground state of the isolated molecule, the singly occupied orbital (SOMO) is energetically below the doubly occupied HOMO and HOMO-1 orbitals (Fig. 4.3a). The corresponding unoccupied orbital (SUMO) is above the degenerate LUMO orbitals. Upon the HOMO to LUMO electron transfer, the HOMO orbital is destabilized and the degeneracy in LUMO orbitals is removed. The orbital ordering below the HOMO is also a subject of rearrangement, mainly reversing the relative energy ordering of the HOMO-1 and SOMO levels. Despite being able to obtain the emission energy solely for the isolated molecule, the scenarios simulating the adsorbed molecules produce consistent values for the absorption in both spin branches and manifest the same orbital energy reordering upon excitation (see Table B.3). Only subtle energy changes ensue as a result of the electrostatic field action, particular for each adsorption configuration on NaCl and due to spin asymmetry. Therefore, we estimate by extrapolation that the optical gap of the steady state is 22 meV lower than of the dynamic state, in good agreement with the experiment. Knowing that the distinct spectral fingerprints are linked to their respective adsorption geometries, we now focus on a detailed electronic structure characterization of CuPc on 3 ML NaCl using differential conductance tunnelling spectroscopy (dI/dV). Fig. 4.4a shows the dI/dV spectra in a bias range encompassing the peaks originating from LUMO and HOMO of the steady and dynamic molecules, measured before
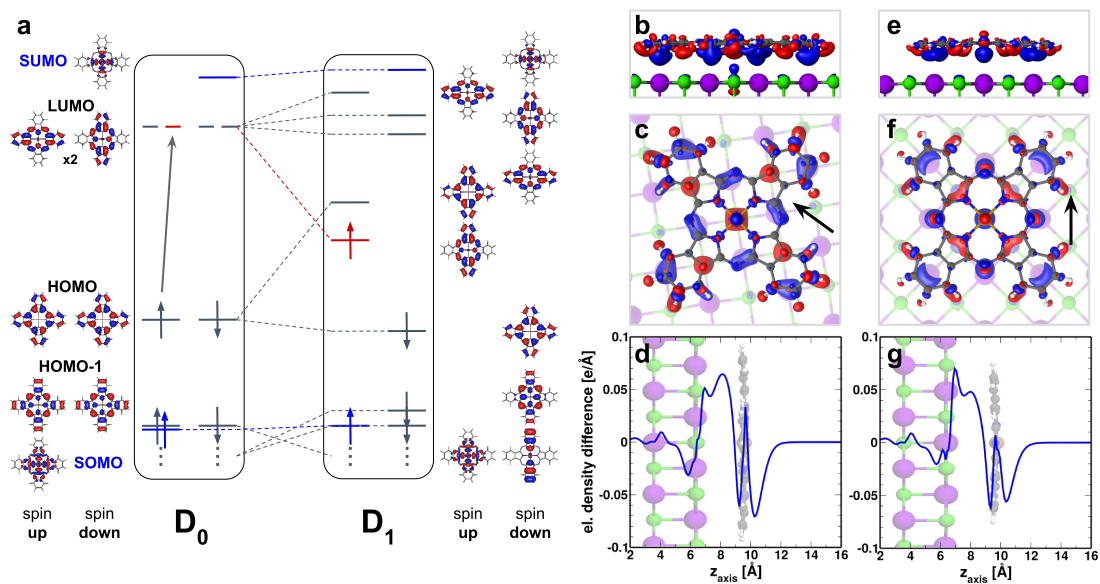
Figure 4.3: Theoretical analyses of the excited and ground states and the impact of the adsorption geometry. (a) Scheme of the simulated orbital energy level reordering upon transfer of an electron (marked by red color) from HOMO to LUMO within an isolated CuPc molecule, showing the occupied and virtual levels of the frontier orbitals. The ground doublet state is denoted as D_0; the excited doublet state as D_1. Corresponding orbital geometries are depicted in the same order, parallel to the scheme for clarity. (b-g) Calculated charge redistribution isosurface plots and profiles, showing the accumulation (blue) and depletion (red) (at $\pm 0.003\,e^-/\text{Å}^3$, respectively) of electrons in the CuPc/2 ML-NaCl systems in the dynamic (b, c) and steady (e, f) configuration. (d, g) Corresponding profiles of the electron density, obtained by integration in the directions parallel to the NaCl surface. Plots are superimposed onto the atomistic model for orientation. The spheres in the models in panels (b)-(g) representing the atoms have sizes corresponding to their atomic radii.

and after a controlled stabilization of the CuPc at their lobes, for various Z set points. Using normalization we determine that the gap of the steady CuPc is about 100 mV narrower than of the dynamic CuPc (Fig. 4.4b,c). The apparent LUMO and HOMO positions of the stabilized molecule are shifted toward the Fermi level by 70 and 30 meV, respectively. Additional local contact potential differences measured with various tips over both configurations using Kelvin probe parabolas show a small shift up to 45 meV (see Fig. B.5), consistent with a decrease of the overall electrostatic potential on the steady molecules with respect to the dynamic ones [127].
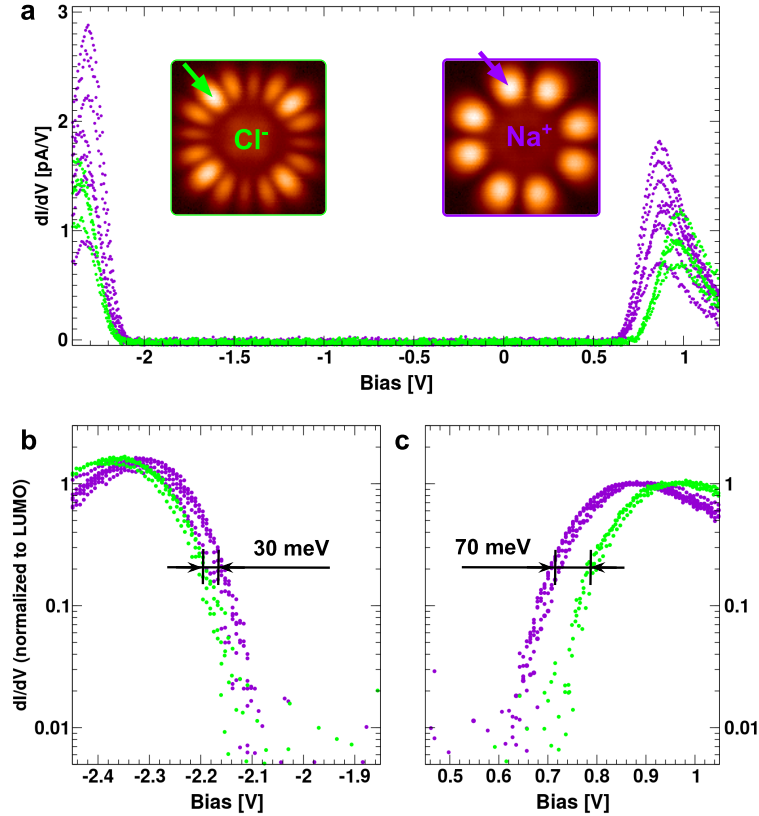
Figure 4.4: Determination of the transport gaps by differential conductance spectroscopy. (a) dI/dV spectra of one CuPc/3 ML-NaCl molecule in a dynamic state (green) and after stabilization (violet), taken at the positions above the molecule lobes, marked by arrows in the STM constant-current images in the insets. The spectra have been taken on the molecular lobes at various current set points (20–90 pA at -2.5 V). Normalized dI/dV plotted in logarithmic scale, corresponding to the HOMO (b) and LUMO (c).

One can anticipate that a lower HOMO-LUMO gap will be reflected in a lower exciton energy upon $D_0 \to D_1$ transition, following an orbital level renormalization. However, the 100 meV value measured by the dI/dV exceeds by far the difference of the corresponding exciton energies obtained from the optical spectroscopy (21 meV). The apparent HOMO-LUMO energy difference measured from dI/dV represents the transport gap of the system, which may generally differ from the real HOMO-LUMO gap due to transient renormalization of the frontier orbital energies upon electron/hole injection [160]. The electronic gap of solid CuPc thin films on Au(111) has been reported to be 3.1 eV by direct and

inverse photoemission [161]. These results compare well with the 3.0 and 2.9 eV gaps measured here by dI/dV for dynamic and steady molecules, respectively, and imply that neither the high electric fields of the tunnel junction nor the presence of the tip and insulating substrate alters the measured electronic bandgap of the molecules significantly.

The difference between the HOMO-LUMO gap derived from dI/dV and the optical gap measured from STML is a strong indication of a modification of the exciton binding energy (E_{BE}) [162]. The difference (ΔE_{BE}) between its values on the Na$^+$ and Cl$^-$ sites ($E_{\text{BE}}^{\text{Cl}}$, $E_{\text{BE}}^{\text{Na}}$) can be estimated using all the measured transport and optical gaps [143, 144]. In particular, taking the measured transport ($E_{\text{GAP}}^{\text{Cl}}$, $E_{\text{GAP}}^{\text{Na}}$) and optical gaps ($E_{\text{OPT}}^{\text{Cl}}$, $E_{\text{OPT}}^{\text{Na}}$) for the dynamic and steady CuPc molecules, ΔE_{BE} follows:

$$\begin{aligned}
\Delta E_{\text{BE}} &= (E_{\text{GAP}}^{\text{Cl}} - E_{\text{OPT}}^{\text{Cl}}) - (E_{\text{GAP}}^{\text{Na}} - E_{\text{OPT}}^{\text{Na}}) \\
&= (E_{\text{GAP}}^{\text{Cl}} - E_{\text{GAP}}^{\text{Na}}) - (E_{\text{OPT}}^{\text{Cl}} - E_{\text{OPT}}^{\text{Na}}) \\
&= (100\,\text{meV}) - (21\,\text{meV}) = 79\,\text{meV}
\end{aligned} \tag{4.1}$$

meaning that the exciton of the steady molecule is less stable than that of the dynamic molecule. We note that this derivation provides the relative differences among the configurations rather than absolute values of the exciton binding energies in CuPc (reported to be 0.6 eV [161]). Since our measurements of the dI/dV gap and STML have been performed for the two very similar systems and with identical tip, most uncertainties are removed, which allows us to conclude that the 79 meV can only be related to the change of the CuPc doublet exciton binding energy.

A detailed analysis of the ab initio calculations of the ground states in Fig. 4.3b-g allows us to evaluate the total electron density redistribution on the two adsorption configurations and points out the origin of the exciton energy difference between the two states. Data show the density difference ($\Delta\rho$) of the fully perturbed CuPc and NaCl substrate relative to their unperturbed states. Isosurface plots (at $\Delta\rho = \pm 0.003\,e^-/\text{Å}^2$) in Fig. 4.3b,c,e,f corresponding to the electron density increase (blue) and depletion (red) reveal the characteristic interaction of individual atoms within the molecule with the Na$^+$ and Cl$^-$ sites in their vicinity. A systematic electron increase is visible under the atoms atop the Na$^+$ in the interface region; conversely for atoms residing above the Cl$^-$ ions an electron density depletion occurs. The most striking difference is on the metal core, where the charge redistribution is of opposite sign for the two configurations centered above Na$^+$ and Cl$^-$. It also leads to the distinct spatial redistributions at the ligand. This can be understood in terms of the simple electrostatic action of the substrate on the electron envelope of the molecule (see the Hartree potential in Fig. B.6).

The net effect of the surface potential on the molecule is an electron accumulation in the interface region and depletion at the molecule, visible in the plots of $\Delta\rho$ integrated across the axes parallel to the surface, plotted as a function of Z (Fig. 4.3d,g). The electron density difference in the interface region is slightly larger in the case of the dynamic configuration, hinting at a higher overall positive field acting on the molecule. Indeed, the total numbers of Na$^+$ and Cl$^-$ ions directly acting on the molecule vary between 9 Na$^+$, 12 Cl$^-$ on the steady and 12 Na$^+$, 13 Cl$^-$ at the dynamic configurations, respectively.

The altered charge redistribution demonstrates the extent to which the exact NaCl lattice orientation and registry with the molecular backbone affect charges within the system. The differences in the Coulomb interaction will impose an inevitable correction on the electron-hole bound state (exciton) and the transport gap. Apparently, as seen from the experiment, the stabilization of the molecule leads to lowering of the electronic gap, exciton and binding energies, and widening of the main spectral line. While the exciton and gap energetics can be explained using the interaction with the substrate potential and screening by the substrate, the spectral line width, which is notoriously difficult to split into individual contributions due to a number of both radiative and nonradiative recombination processes [86, 125] remains an open question. We can merely state, based on the experiments, that the excitons on the steady CuPc appear to have a higher probability of nonradiative decay into the bulk (by, for example, coupling to the phonon bath), causing the spectral line broadening.

4.3   Conclusions

In conclusion, we have demonstrated mechano-optical switching of a single CuPc molecule on NaCl on Ag(111). A change in energetics of its doublet excitonic state could be triggered through atomic-scale manipulations that allow precisely defining the adsorption configuration, with the CuPc molecule centered above either a Na^+ or Cl^- ion. From the measured values of the optical transitions and changes in the system transport gaps, we estimate a difference of the exciton binding energies: the exciton on the dynamic molecule is 79 meV more stable than on the steady one. Theoretical calculations confirm the experimentally determined geometries as the most favored, reproduce the changes in the exciton energy, and provide details on the Coulomb-mediated charge redistribution within these systems. This allows linking the local effect of the NaCl lattice potential on the CuPc orbital levels with modifications in the exciton energy and electronic gaps. Our results represent a step toward a detailed understanding of the effect of the local environment in the many-body excitations in single-molecule emitters.

4.4   Methods

4.4.1   Density Functional Theory Calculations of the Geometries and Charge Redistribution

The calculations were carried out using the FHI-aims code [163] to describe the electronic structure of the CuPc molecule on the bilayer NaCl(100) surface. The calculations were performed using the GGA-PBE approximation of the exchange-correlation potential including the Tkatchenko-Scheffler approach of the van der Waals interactions [164]. The relativistic effects were taken into account by applying the scaled zeroth-order regular approximation [165]. The NaCl(100) surface was modeled by a 7×7 supercell made of two layers on which a single CuPc molecule was placed in on-top position at the Na^+ or Cl^- ion, respectively. The molecule was rotated by 15°, 30°, and 45° with respect to the high-symmetry axes. Structural relaxations of the slab were performed for all the atoms, except

the bottom NaCl layer. The calculations were considered converged when the remaining atomic forces and the total energy were found below 10^{-2} eV/Å and 10^{-5} eV, respectively. A single gamma point was used for the integration in the Brillouin zone. The total energy calculations were conducted to find the best adsorption site. Furthermore, the total density and the Hartree potential were used to determine the electronic interactions between the surface and the molecule.

4.4.2 Excited-State DFT Calculations

Self-consistent solutions of the electron wave functions and geometrical optimization were obtained using the ωB97XD [166] and LC-ωPBE [167, 168, 169] functionals in the spin-unrestricted mode, employing the SVP basis set [170, 171]. Visible absorption and emission spectra were derived using the comparison of the total energies of the $D_0 \rightarrow D_1$ transiently excited systems with their corresponding ground states, independently for both spin branches. The electrostatic field of the NaCl substrate was simulated by a fixed bilayer of charges placed beneath the CuPc, calculated using the B3LYP [172, 173, 174] functional, geometrically equivalent to the Na^+ and Cl^- ion coordinates in the steady and dynamic configurations of the system (for more details see the Supplementary Information in Appendix B). The Gaussian program package (Gaussian 16, revision C.01 [175]) was used for the calculations.

5. Exciton-trion dynamics in a single molecule

The following chapter is based on the publication [176] and reprinted with permission. Copyright 2021 American Chemical Society. Inspired by the recent experimental results of Doppagne et al. [81], where the authors observe the emission from neutral and cation ZnPc on NaCl/Au(111) depending on the applied bias voltage, we have chosen to study the same system but on Ag(111). A lot of questions concerning the electrofluochromism were open. Can we observe various charge states and their characteristic fluorescence emission on thin NaCl layers? It was known, that on thick insulating NaCl layers allowing electron tunneling only between the tip and sample, molecules can be switched between many (up to 4) charge states with the applied bias voltage [177].

Another question, which was not answered in the original publication [81], is the spatial response of exciton and trion intensity and also their dynamics. For studying the dynamics, we used a radio frequency phase-shift (RF-PS) fluorometry. This method was supposed to efficiently determine the lifetimes of the excitons and trions, contrary to the time-consuming Hanbury Brown-Twiss interferometry. We used the same assumption as Merino et al. [98] and Zhang et al. [99] (see section 1.5) that the electron capture by the $ZnPc^+$ via the NaCl layer is fast. In light of the novel findings in the literature and our unpublished photoluminescence data, we learned that this assumption was probably not correct. The lifetime of the excitonic state of a molecule in the nanocavity is believed to be several orders of magnitude shorter, than for a molecule in far-field [178] which is caused by the Purcell effect. Our original interpretation is therefore corrected in the Commentary section 5.4. Yet, the effective time measurements by the RF-PS technique can be useful for the understanding of charge dynamics in double-barrier tunneling junctions.

5.1 Introduction

The dynamics of optical excitations provides insights into the photophysics of many-body quantum states of single molecules [179]. It is also a key to develop efficient single photon quantum cryptography and quantum computing protocols [180, 181, 182]. Although most experiments rely on ensemble or bulk measurements, excitation and control of electron-hole bound states in single molecules and defects in molecular solids are possible for diluted emitters [80, 183]. Recent developments in tip-enhanced spectroscopies, prominently in STML, made it possible to explore at atomic-scale the mechanisms generating singlet [135, 12], triplet [94, 125], and doublet [32] molecular Frenkel excitons and the role of their nanoscopic environment. Emission from positively and negatively charged excitons (trions) was recently discovered for single zinc and platinum phthalocyanine (ZnPc, PtPc) emitters [81, 184]. Despite important advances in measuring fast dynamics of optical excitations on the nanoscale by application of Hanbury Brown Twiss (HBT) interferometry [98, 185, 99, 186, 187, 147] and time-resolved STML [183, 107, 188], capturing the combined dynamics of the molecular excitons and

trions in single molecules remained a challenge. Here we achieve time-resolved measurements of the excitons and trions of a single ZnPc molecule, which we excite by direct charge injection to induce photon emission.

In order to access the trion and exciton dynamics in a single-molecule, we devised phase fluorometry scheme, combining radio frequency (RF) electrical modulation and picosecond single-photon counting detection within a scanning probe microscopy setup equipped with optical path (scheme in Fig. 5.1a). Our radio frequency phase-shift technique is based on evaluation of the phase difference between a harmonic electrical modulation of a given frequency applied at the system and the delayed optical response at particular wavelength, arising due to a finite decay rate of the molecular excitons. The reference and delayed responses are measured as histograms of photon arrival times of a plasmonic signal from the substrate and from the molecule, respectively. The characteristic radiative lifetime (τ) of an exciton in the tunnel junction is determined from the phase difference ($\Delta\phi$) for a given driving frequency f using the relation $\tau = \tan(\Delta\phi)/2\pi f$ (Supplementary Information in Appendix C).
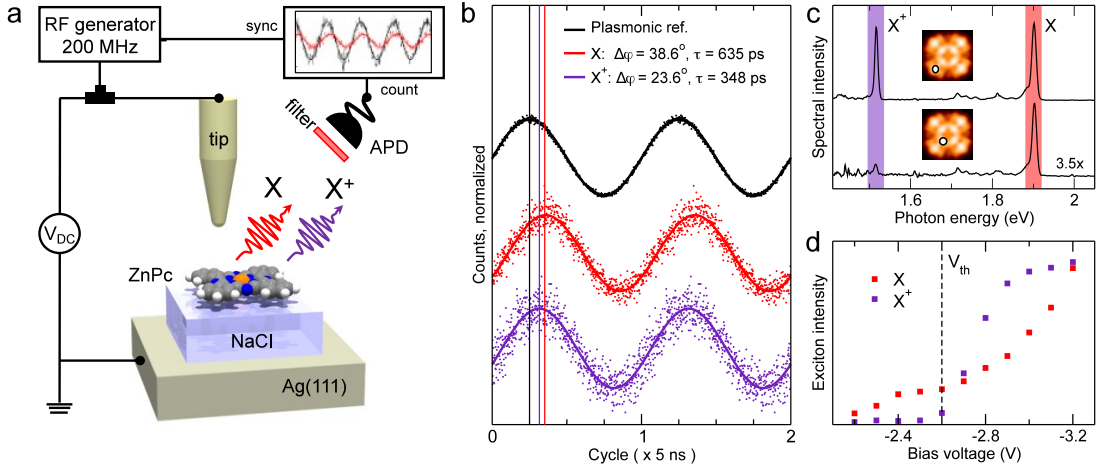
Figure 5.1: Radio-frequency phase shift method in STML applied to a single molecule. (a) Schematic representation of the experimental setup. A single ZnPc molecule on 3 layers of NaCl is inspected by STML. The tunnelling bias voltage (V_{DC}) is modulated with a harmonic signal at 200 MHz (V_{AC}). The photon arrival times are recorded using a single photon detector and counter synchronized with the radiofrequency generator. (b) Radio-frequency phase-shifted waves obtained for a plasmonic reference (black) $V_{DC} = 2.0$ V, $I_t = 70$ pA, $V_{AC} = 100$ mV, integration time 180 s; neutral exciton X (red) $V_{DC} = -2.2$ V, $I_t = 70$ pA, $V_{AC} = 100$ mV, integration time 600 s; and trion X^+ (purple) $V_{DC} = -3.2$ V, $I_t = 120$ pA, $V_{AC} = 100$ mV, integration time 600 s. X and X^+ waves were taken above the ZnPc lobe. The lines mark the phase shift between excited states and the reference. (c) STML spectra obtained on a lobe and a point near the center of ZnPc. $V_{DC} = -3.0$ V, $I_t = 100$ pA, integration time 180 s. The locations of charge injection are marked in the insets. (d) Exciton (red) and trion (purple) intensity dependence on the applied V_{DC} at $I_t = 40$ pA.

5.2 Results and Discussion

By means of the RF-PS method, we measure the dynamics of excitons and trions on the ZnPc on three layers of NaCl on Ag(111). Injecting holes and electrons into a single ZnPc induces optical excitations that can decay radiatively. The emission is enhanced by the increased optical density in the picocavity [189]. The visible/near-infrared electroluminescence spectra of ZnPc (Fig. 5.1c) show peaks corresponding to the emission of neutral ($S_1 \rightarrow S_0$ denoted as X) at 1.89 eV and positively charged excitons ($D_1^+ \rightarrow D_0^+$ denoted X^+) at 1.52 eV, which agree very well with the energies calculated for a free-standing molecule (Table C.2) and the previous measurements made on Au(111) [81]. For each line, we measured the phase shift with respect to the reference and determined the exciton effective lifetimes as 635(51) ps for S_1 and 348(55) ps for D_1^+, at bias voltage (V_{DC}) of -2.2 V and -3.2 V, respectively (see Fig. 5.1b). The lifetime measured for S_1 is in excellent agreement with previous HBT measurements [99, 86]; no determination of the lifetime of D_1^+ is found in the literature as yet.

Electroluminescence intensities of X and X^+ strongly depend on precise location of the charge injection in the molecule (Fig. 5.1c) and on the V_{DC} (Fig. 5.1d). On three layers of NaCl on Ag(111), S_1 and D_1^+ generation is activated at negative V_{DC} with thresholds of -1.9 V and -2.6 V, respectively. The exact value of the thresholds may vary as much as 0.2 eV depending on exact tip condition. Within the picocavity, the X^+ threshold voltage (V_{th}) represents a sizable electric field which triggers transient positive charging in the neutral excited molecule. We find that a hole injection into the peripheral aromatic rings boosts the emission X^+ from the D_1^+ (Fig. 5.1c).

Bias-dependent hyperspectral mapping with p- and s-wave probes using CO-functionalized and metallic apexes (Fig. 5.2a) reveals a spatial anticorrelation between the charge injection locations inducing X and X^+ emission. X intensity appears concentrated at the porphyrazine macrocycle, extending toward the peripheral benzene rings at higher magnitudes of V_{DC}. This is a contrast that is also expected from the shape of the transition density calculated for the transition corresponding to the decay of S_1 (Figs. C.6 and C.7). On the other hand, all X^+ maps observed at $V_{DC} < V_{th}$ show a 12-lobe corral-like pattern with the highest intensity distributed around the periphery of the molecule, whereas a picture more akin to X would be expected from the calculated X^+ transition density (Fig. C.7). X^+ map taken for comparison using a metal apex also displays the intensity clearly concentrated at the peripheral benzenes, confirming that the charge injection into them strongly promotes the transient state leading to the formation of trions. The characteristic differences between the photon map contrasts generated by p- and s-wave tips can be understood in terms of their specific spatial modulation of the tunneling current [32]. At constant height, X and X^+ emission lines red-shift a few nm, which is apparent on a spectral map from a diagonal ZnPc cross-section and maps for each exciton at particular wavelengths (see Fig. 5.2b-e and Fig. C.4). This may be explained in terms of photonic Lamb shift by strong coupling between the optical excitations of ZnPc and the highly confined plasmons and has been observed by tip-enhanced plasmon absorption and photoluminescence [71, 83, 72].

The strong bias dependence of the X and X^+ emission motivated us to study
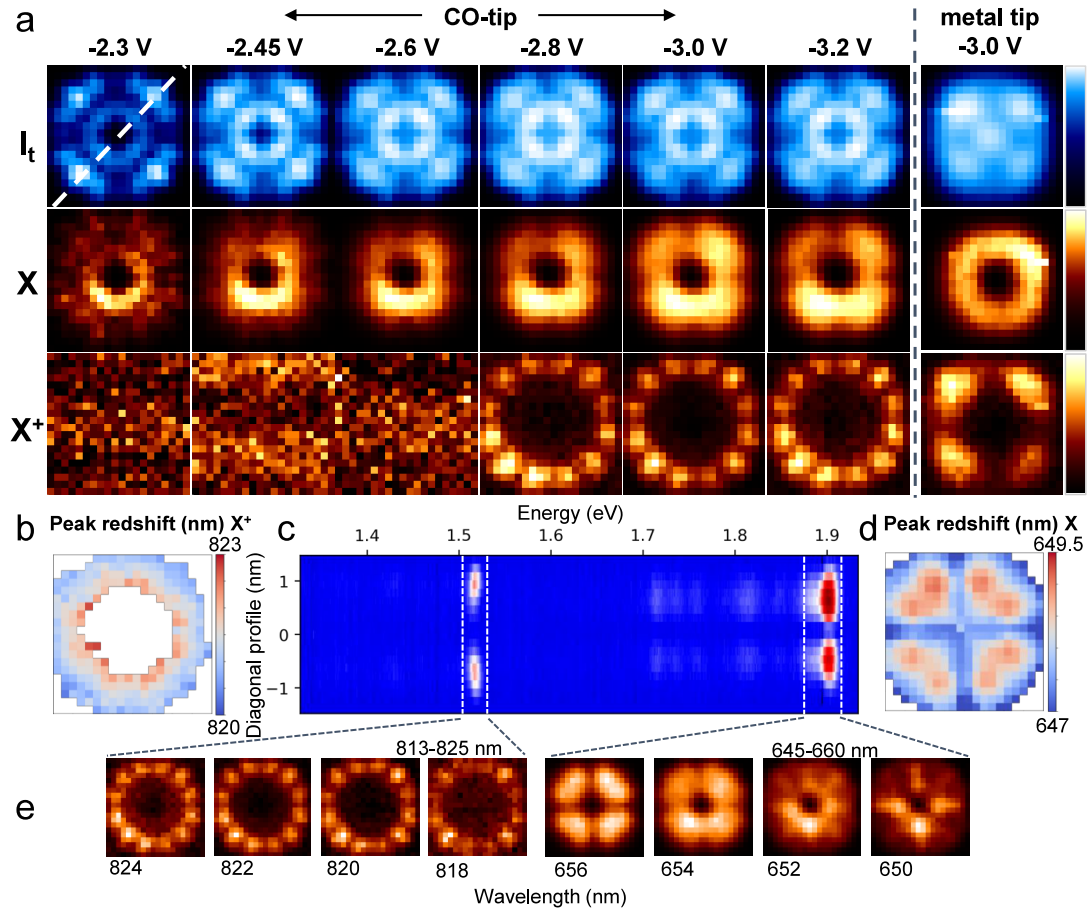
Figure 5.2: Mapping of the exciton and trion. (a) Constant-height tunneling images (I_t) and simultaneously measured electroluminescence photon maps of the neutral exciton emission (X) and trion emission (X^+) of a single ZnPc molecule, using a CO-functionalized- and a metallic tip. The X and X^+ maps represent the total photon intensities in the 645–660 nm and 813–828 nm, respectively. (b) Red-shift map of the X^+ line. (c) spectral cross-section map measured across a diagonal denoted in (A) (white dashed line). (d) Redshift map of the X line. (e) Photon maps at selected wavelengths showing variation of intensity as a function of charge injection positions. (b), (d), (e) were taken with a CO-functionalized tip at V_{DC} = -3.0 V. All images are 1.8×1.8 nm^2.

the dependence of the dynamics on the tunnelling conditions. Series of RF-PS measurements reveal the tunability of the S_1 and D_1^+ effective radiative lifetimes depending on the V_{DC} and on the tunneling gap size given by the relative tip-molecule distance (Z_{rel}), and hence on the tunnelling current (I_t). S_1 and D_1^+ lifetimes (shown in Fig. 5.3a) rise monotonically with increasing Z_{rel} (and with decreasing I_t), showing that closing of the picocavity significantly promotes radiative quenching of the excitations. The trends agree with previous measurements on similar systems [98, 99]. Varying V_{DC} and maintaining the current in the 50-130 pA range, we observe a S_1 lifetime drop from values well above 700 ps to as low as 200 ps upon crossing the V_{th} (see Fig. 5.3b). This drop in the lifetime is also reflected in the X emission intensity. In the intensity vs. V_{DC} measurement for X in Fig. 5.1d we note a superlinear rise of the photon rate for voltages beyond V_{th}, implying that around this value the average interval between photons reduces. At -3.2 V, S_1 lifetime recovers to around 450 ps. The trion (D_1^+) lifetime follows a tendency similar to the neutral exciton (S_1), growing from below the experimental resolution limit at V_{th} to near 600 ps at $V_{DC} < -3.0$ V (Fig. 5.3b). Such similar trends for S_1 and D_1^+ dynamics as a function of voltage indicate that the generation mechanisms and dynamics of both excitations are closely related. The dependence on V_{DC} and Z_{rel} of the lifetimes highlights the crucial role of the picocavity in reducing the observed radiative lifetimes of the chromophore. By increasing the number of NaCl layers and using Au(111) as a substrate, we substantially increase the effective lifetimes to match those obtained for neutral exciton of ZnPc in solution [190] (Fig. C.3).
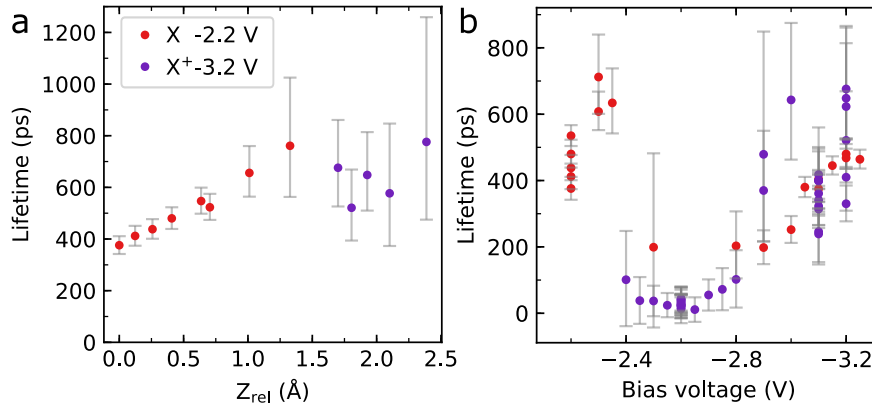
Figure 5.3: Dependence of lifetimes on picocavity size and bias voltage measured via X and X^+ processes. (a) Lifetime of neutral exciton (red) and trion (purple) as a function of tip-molecule relative distance (Z_{rel}). (b) Lifetime of neutral exciton (red) and trion (purple) as a function of applied V_{DC}. A 200 MHz harmonic signal with 100 mV amplitude is used for measuring the phase shift and determination of the lifetimes. The range of I_t was 50–130 pA.

Photon maps in Fig. 5.2 demonstrate the degree to which the X and X^+ emissions are spatially anticorrelated, however, their temporal (anti)correlation remains to be addressed. We take the advantage of the strong nonlinearity of X^+ emission intensity with bias, and apply modulation around V_{th} in order to generate an anharmonic wave on the output, looking for hallmarks of interdependence between the S_1 and D_1^+ formation. By using a V_{DC} value of -2.4 V and a RF amplitude of 250 mV, the D_1^+ is excited only in the first half of the

sinusoidal driving, whereas S_1 can be excited during the entire cycle (Fig. 5.4a). The purpose is to reach conditions at which the time-resolved probability of S_1 formation is dented by the sharply growing probability of charging the molecule and forming D_1^+. In Fig. 5.4b it is evident that the resulting X wave is indeed distorted in the upper portion when X^+ intensity rises. This behavior indicates, given that both excitons are localized within the same molecule and they cannot coexist at the same moment, that the trion is generated by hole capture of the molecule in the neutral excited state.
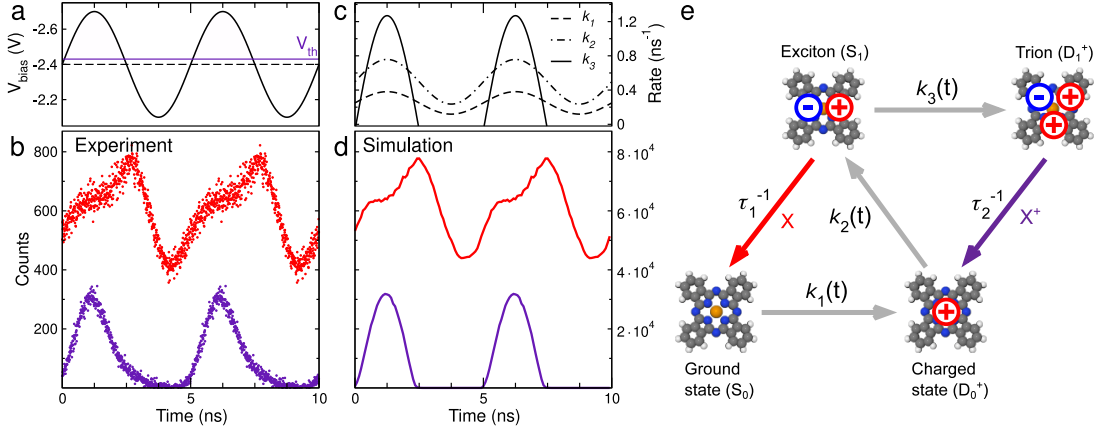
Figure 5.4: Temporal anticorrelation of the exciton and trion decay and simulation. (a) Bias voltage is harmonically modulated across the trion threshold at 200 MHz, $V_{DC} = -2.4$ V and $V_{AC} = 250$ mV, $I_t = 70$ pA. (b) RF-PS waves recorded for the neutral exciton (red) and trion (purple). Dark counts have been subtracted from the experimental waves. (c) Rates of the time-dependent transitions used in the simulation. (d) Simulated RF-PS waves for the neutral exciton (red) and trion (purple). (e) Scheme of the 4-state model with transitions used for simulation of the exciton-trion dynamics in the ZnPc molecule in (d).

In order to describe the evolution of the two interdependent excitonic states under harmonic driving, we perform a simulation of the internal excitation dynamics with a causally deterministic state model, working with a minimized number of states and transitions, schematically represented in Fig. 5.4e. We define four states: the ground state (ZnPc^0 or S_0), positively charged molecule (ZnPc$^+$ or D_0^+), and the corresponding excited states S_1 and D_1^+. The types of transitions allowed in the framework of this model are (i) hole injections, (ii) electron captures and (iii) decays of the excited states. Transitions are simulated either as homogeneous (time-independent) or inhomogeneous (time-dependent) Poissonian processes according to their basic properties. The decay rates of the S_0 and D_1^+ (τ_1^{-1} and τ_2^{-1} in Fig. 5.4c) are constants, fixed to the values of the lifetimes experimentally obtained near V_{th} (1/750 ps^{-1} and 1/50 ps^{-1}, respectively). The time-variable probability rates of the hole injection from ZnPc^0 to ZnPc$^+$ and the electron capture by the ZnPc$^+$ leading to exciton formation, are harmonically (sine) modulated (k_1 and k_2 functions in Fig. 5.4c, respectively), based on the consideration that they are proportional to the electrical field at the junction. Finally, the conversion of the exciton to trion (S_1 to D_1^+) is modeled with a rate modulated with a half-sine (k_3), reflecting the experimentally observed trion emission threshold and the increase of the emission intensity with bias (from Fig. 5.1d). The scaling parameters of the rates k_{1-3} are determined by an iterative

70

least-squares optimization to match the experimental data (compare Fig. 5.4b,d). The model with optimized rates reaches a very good agreement with the measured histograms, in particular comparing the relative count intensities of the X and X^+ emission, and the relative phases and shapes of their time-dependent waves. The details of the model implementation and the rates can be found in Table C.1 and the corresponding section of the Supplementary Information in Appendix C.

5.3 Conclusions

To conclude, our electroluminescence-based RF phase fluorometry method implemented in a scanning probe microscope proved suitable for the determination of exciton dynamics at the nanoscale in molecular adsorbates on surfaces and low dimensional systems and provided advantages over standard methods, in particular, the temporal resolution and useful signal yield. The model is able to validate the proposed exciton-trion dynamics and the possibility of an exciton-to-trion conversion mechanism upon hole trapping, analogous to the one observed for optical excitations in strained 2D materials [191]. However, the observed contrast of the trion emission maps (Fig. 5.2a), unexpectedly very different from the exciton map with a virtually identical transition density (Fig. C.7), raises the question of what is the cause for the increased hole trapping probability when the tip is above the ZnPc molecular lobes. We suggest that the alignment of the tip field with the molecular lobes triggers more easily the renormalization of the electronic structure needed to form a trion bound state. It remains yet to be clarified whether the apparent link between the lifetimes of the two excitons, especially around the V_{th}, has an underlying mechanism or is a mere correlation. In addition, the fast trion lifetimes measured here demonstrate the feasibility of using single molecules as single photon electrooptical transducers in the GHz range.

5.4 Commentary

As discussed in the introductory part of this chapter, the effective lifetime measured with our method comprises both intrinsic exciton lifetime and the electron capture by the ZnPc$^+$ via the NaCl layer with the time constant $1/k_2$ in Fig. 5.4. Assuming now that intrinsic lifetime is on the order of picoseconds (see ref. [72] and Fig. 5.5a showing TCSPC measurements of a single ZnPc exciton decay), the exciton-trion $(S_1 \rightarrow D_1^+)$ conversion path characterized by k_3 in Fig. 5.4e should not be very efficient. The more plausible mechanism for the creation of the trion is via a dication as was suggested by Kaiser et al. [38] and Jiang et al.[36] or via the triplet state which should be longer-lived [38, 192] in a molecule without strong spin-orbit coupling. An elegant single-electron mechanism of trion formation directly from the ground state was suggested by Hung et al. [193], but it is energetically unfavorable if the many-body energy scheme plotted in Fig.5.5b is valid. The electron energy 3.7 eV required for this process (see arrow **b** in Fig. 5.5) is well above the bias voltage used in our measurements.

Let us now analyze what is the origin of long effective lifetimes of S_1 measured from the phase shift of X emission in RF-PS electrofluorometry. It was recently
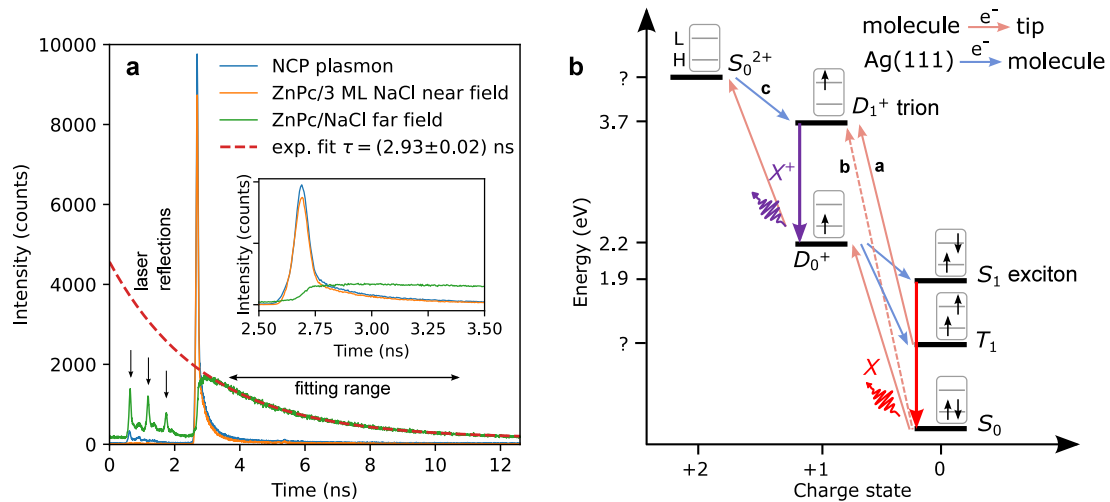
Figure 5.5: a) TCSPC fluorescence lifetime measurement of ZnPc exciton lifetime in micro-PL and STM-PL. The system consisting mostly of 2 and 3 ML NaCl with absorbed isolated ZnPc molecules has an average lifetime of neutral exciton $\approx 3\,\text{ns}$ in the far field (blue) without the presence of the tip. The single molecule on 3 ML/NaCl in the nanocavity (orange) has a much shorter lifetime below the resolution of our method ($20\,\text{ps}$) in agreement with the ref. [72]. The IRF of the system measured on photoinduced nanocavity plasmon (blue) in the same spectral range is indistinguishable from the exciton in nanocavity. See the Methods section for experimental details. b) Many-body scheme of the electronic states and transitions that might take place for ZnPc/3 NaCl/Ag(111) in STML. The energies of the charged states are expected to be smaller than the in-vacuo states obtained from ab-initio calculations due to the reorganisation energy [34]. The scheme was inspired by previous works in refs. [36, 38] and the positive ion resonance energy is determined from dI/dV measurement in Fig. A.8.

shown [38], that the charge state lifetime of molecules is not negligible due to the limited electron tunneling from the substrate to the molecule on NaCl. Therefore the effective measured lifetime of the neutral exciton can be approximated as $\tau_X \approx 1/k_2 + \tau_1$, where k_2 is the rate of the $D_0^+ \to S_1$ process. Since $\tau_1 << 1/k_2$ the effective measured lifetime corresponds the the rate $\tau_X \approx 1/k_2$.

The shorter effective lifetime of D_1^+ measured from the phase shift of X^+ in Fig. 5.3 can be explained with both **a** and **c** pathways shown in Fig. 5.5b leading to the D_1^+ state. The direct excitation of the molecule in this state ($T_1 \to D_1^+$) with bias-modulated hole tunneling from the tip (arrow **a** in Fig. 5.5b) enables to measure the trion intrinsic lifetime τ_2 which is likely below the resolution of the RF-PS method. This would correspond to the effective lifetimes measured at voltages $V_{DC} > -2.8$ V shown in Fig. 5.3. This excitation pathway is supported by the observed threshold voltage of -2.6 V for trion generation considering the triplet state with energy 1.1 eV as observed in phosphorescence in ref. [138]. The 300 ps effective lifetime measured at voltages $V_{DC} < -3$ V can be explained by considering the **c** pathway via dication. The doubly charged state S_0^{2+} might be less stable than the singly charged state D_0^+ and thus the rate $k_c > k_2$ and $\tau_{X+} \approx 1/k_c + \tau_2$ is on the order of hundreds of picoseconds. Given the threshold voltage of about -3 V for longer effective lifetime observation, the energy of the S_0^{2+} state in the many-body diagram in Fig. 5.5b is likely above 5 eV.

The explanation of the decrease in the measured effective lifetime with the decreasing tip-sample distance requires considering a change of the tunneling barrier and an increase of the relative voltage drop across NaCl layer. The nearly linear dependence of the effective lifetime on 3 ML NaCl/Ag(111) (Fig. 5.3) and on 4 ML NaCl/Ag(111) (Fig. C.3) supports this interpretation but is not consistent with the observation in ref. [38]. To explain the observed temporal anticorrelation of exciton and trion in Fig.5.4 with the assumption of a short intrinsic exciton lifetime, reconsideration of the stochastic model is necessary. To conclude, despite its lack of resolution for measuring intrinsic exciton lifetimes of molecules in nanocavity, the RF-PS fluorometry can reveal the excitation mechanism and provide the rates of electron tunneling via thin insulating layers.

5.5 Methods

All optical spectra were collected in constant-current mode with the feedback loop switched on; the photon maps were collected in the constant height mode with the feedback loop switched off. Radio frequency produced by an arbitrary wave generator (Keysight, 81160A) was added to the DC tunneling bias voltage generated from the SPM control electronics (Nanonis GmbH) using a bias-tee (Pasternack, PE1608) and connected to the bias wiring of the microscope on the air side feedthrough. The transmission of the wiring was calibrated at 200 MHz using the broadening of a plasmon high-energy cutoff at 1.8 V on a clean substrate described in chapter 6. The amplitudes reaching the picocavity were varying between 50 and 400 mV peak-to-peak. Synchronization signal from the arbitrary wave generator at 20 MHz (10 cycles) is used as the start trigger for photon arrival time tagging and the APD signal corresponding to the first incoming photon is employed as the stop trigger. Therefore, the range of the time frame was 50 ns. The time tagging and histogramming of the photon arrival times is performed

by dedicated counting electronics and software (Picoquant, PicoHarp 300). The typical bin size was 64 ps. For filtering of the X and X^+ exciton emission we used hard-coated 25 nm bandpass filters (Edmund optics) with center wavelengths 650 nm (for measurements of S_1 lifetime) and 825 nm (for D_1^+). Histograms are accumulated for approximately 3–18 min, depending on the strength of the modulation and the resulting signal-to-noise ratio in the waves.

For measuring the fluorescence lifetime in Fig. 5.5a a pulsed supercontinuum white light laser (SuperK FIANIUM) with tunable filters (SuperK VARIA) was used. The laser center wavelength was 633 nm, the bandwidth 10 nm and the repetition rate was set to 78 MHz. The laser was further spectrally filtered with a 633 nm laser line filter. The laser spot at the sample has a diameter of 10 μm. The sample coverage is around 20 molecules on NaCl per 100×100 μm^2. The NaCl forms dominantly 2 and 3 ML islands. MPD PDM Series 100 μm SPAD and Schwabian Instruments Time Tagger electronics were used for histogramming of the photon arrival times. The bin size was 4 ps. The light coming out of the STM junction was filtered with a dichroic edge beam splitter followed by another edge filter designed for 633 nm lasers (Shamrock). Hard-coated 20 nm bandpass filter (Edmund optics) with center wavelength 661 nm was used for filtering the X line. The fluorescence histograms presented in Fig. 5.5a are accumulated for 90, 360 and 900 s for ZnPc near field (orange curve) , NCP plasmon (blue curve) and ZnPc far field (green curve) respectively. The laser power was $< 100\,\mu$W for near-field measurements and 200 μW for far-field measurements.

All the quantum chemical calculations were carried out with the Gaussian16 package [175]. The molecular structures of ZnPc (neutral) and ZnPc$^+$ (cation) in their ground state were optimized with the density functional theory (DFT) method, with long-range corrected ωB97X-D functional [166] and 6-31G* basis set. All optimizations were run in vacuo. The emission properties were assessed by optimizing the molecular geometry in the lowest excited state, with time-dependent (TD) DFT for ZnPc at the TD-ωB97X-D/6-31G* level of theory. For the ZnPc$^+$ the Tamm-Dancoff approximation (TDA) has been employed (TDA-ωB97X-D/6-31G*). The transition densities were generated with Multiwfn software (isosurface value = 0.0001 e/Bohr^3) [194].

6. Constant amplitude driving of a radio frequency excited plasmonic tunnel junction

The following chapter is based on the publication [195] and reproduced with the permission of AIP Publishing. The RF phase-shift fluorometry method presented in chapter 5 requires a well-calibrated amplitude of the modulation bias. The amplitude is not unity in the MHz-range frequency used in chapter 5 due to imperfect wiring leading to the sample. The use of the well-known energy cutoff of the plasmonic electroluminescence given by the applied DC bias voltage and the shift of the cutoff with the applied AC bias was a natural choice for the amplitude calibration in the RF-PS method, where only a few frequencies are used. However, we realised that this method can be used for measuring the transmission of both the standard and RF-optimized STM wirings in a broad frequency range with reasonable speed and accuracy with our optical setup and therefore is a viable alternative to the standard calibration method using $\mathrm{d}I/\mathrm{d}V$ nonlinearities.

6.1 Introduction

Radio frequency (RF) modulated bias in scanning tunneling microscopy (STM) opens the way for new kinds of spectroscopies with atomic resolution [196, 6, 7, 197, 198, 199, 200, 201, 183, 176]. Operation in the frequency- and time-domain improves the temporal resolution of conventional STM which is usually limited by the small bandwidth of transimpedance amplifiers [6]. In addition, nuclear and electron spin resonance (ESR) spectroscopy [7, 202] can achieve energy resolution on the order of neV compared to conventional tunneling spectroscopies limited by thermal broadening of electronic states to several μeV at mK temperatures. Apart from spin resonance phenomena, the RF modulation of electric field in the tunnel junction permits access to many other physical phenomena relevant at the atomic scale, such as resonant Andreev reflections [198, 200], exciton dynamics [176, 133], or surface acoustic waves [203, 204]. For the detection of these transient phenomena with ultrafast temporal resolution, a detailed knowledge of the transfer function between a RF generator and the tunnel junction is needed [176, 98, 99].

The transfer function of an uncompensated RF line coupled to a tunnel junction in a cryogenic system typically has a complex dependence on the frequency, with a significantly variable attenuation in the GHz range. In order to obtain a harmonic driving with constant amplitude or a well-defined voltage pulse at the tunnel junction [133, 205], the output power of the RF generator has to be compensated for transfer function magnitude $T(f)$. Vector network analyzer can be used to measure it on a wiring [197, 206]; however, in a working STM setup the characterization needs to be performed in situ at the tunnel junction prior to each individual experiment. $T(f)$ has been previously obtained by measuring rectification of the RF voltage on current-voltage nonlinearities [205, 206] and also

by obtaining the instrumental impulse-response function using time-dependent intensity of plasmonic light generated by inelastically tunneling electrons [188]. The former method requires the presence of sharp $I(V)$ nonlinearities such as spin excitation signals in magnetic adatoms, superconducting energy gap onsets or surface states in metal surfaces. The latter method is perfectly suited for tailoring short bias pulses in the ns range, but it is not very practical for the generation of a constant amplitude driving. In addition, both of the in situ characterization methods need absolute amplitude calibration which can be time-demanding.

Here, we present an optical RF calibration method of the $T(f)$ with a wide dynamic range that exploits the physical principle of the plasmonic electroluminescence occurring at the tunnel junction. In the STM, the nanocavity plasmon modes are excited by inelastically tunneling electrons which impose the limit on the highest energy of the detected photons. By measuring the energy distribution of the plasmonic response by optical spectroscopy and determining the high-energy cutoff of the plasmonic spectrum as a function of frequency, we can evaluate the instrumental $T(f)$ at the junction. Using an iterative procedure, we achieve an effective compensation of the transmitted intensity and constant amplitude harmonic driving.

6.2   Methods

The experiments were carried at 8 K. The majority of spectra were taken with 600 gr./mm grating enabling 1.2 nm spectral resolution and 130 nm range in our setup. This corresponds to 3.8 meV resolution at 2.0 eV (620 nm center wavelength) and $1.95 - 2.45$ eV range.

RF harmonic driving was produced by an arbitrary waveform generator Keysight 81160A for frequency below 500 MHz and by a continuous wave generator Keysight E8257D for frequencies up to 18 GHz. For the sub-GHz frequencies, the generator was coupled to a standard 50 Ω shielded bias wiring to the sample stage in STM using a bias-tee (Pasternack, PE1608) on the air side feedthrough. For GHz range, the continuous waveform was fed through a dedicated 50 Ω RF line consisting of two different cables. Inside the cryostat, a semi-rigid cable (COAX Co., Ltd., SC-086/50-SCN-CN, 2 m) is connecting the feedthrough with an in-vacuum SMA (SubMiniature version A) connector above the STM head. In the vacuum, the cable is attached to the outer envelope of the liquid nitrogen vessel for efficient thermalization. From the in-vacuum SMA connector, a short ($\approx$ 10 cm) flexible cable (Teledyne Storm Flex 047) is used to deliver the RF power to the tip. This is achieved by an unshielded termination of the flexible cable (6 mm), which acts as the antenna emitting an RF signal absorbed by the tip, as shown in Fig. 6.1(a). STM tip and antenna are strongly capacitively coupled allowing a high transmission efficiency compared to the standard STM wiring [198, 207, 208, 209]. In a standard STM wiring, the $T(f)$ is far from constant and typically very low ($< 10^{-3}$) in the frequency range above 1 GHz. The antenna-coupled RF line partially overcomes these drawbacks but is limited by the geometry of the antenna and the cavity that cannot be optimized for lossless transmission in the broad frequency range $1 - 25$ GHz. For our iterative compensation procedure, we use a custom software to simultaneously control the RF generator parameters, the Nanonis STM control electronics, and to acquire

the data from the CCD detector at the spectrograph.

6.3 Results

For the purpose of the calibration procedure, a sharp tip and a sample are needed, both from metals with strong plasmonic response in the visible and near-infrared (VNIR) region such as silver, gold, and copper [210]. In our measurements, we used a clean Ag(111) sample and Ag-coated Pt-Ir tip. They are brought close to contact until a tunneling current starts to flow as a result of the applied bias voltage (V) [see Fig. 6.1(a)]. A fraction of the inelastically tunneling electrons excite gap plasmon modes which rapidly decay as photons in the far field [58]. A spectral intensity profile of these photons is defined by the wavelength dependence of the dielectric function of the electrode materials [9], by the tip geometry and tip-sample distances, which are shaping the geometry of the nanocavity [211]. However, the most significant dependence of the plasmon spectrum stems from the applied bias voltage, which defines the range of the available inelastic tunneling channels and determines the quantum cutoff, the maximum energy that can a single tunneling electron transfer to the gap plasmon (i.e., $h\nu_{max} \leq eV$) [58] [see Fig. 6.1(b)]. This $h\nu_{max}$ is indicative of the maximum bias on the tunnel junction including the modulation, and its energy can be precisely determined by measuring an optical spectrum cutoff with a sufficiently high resolution. The total resolution of the method will be limited mostly by stochastic noise in the spectra and the energy-time uncertainty. The upper range of the modulation frequencies detectable in this way is theoretically limited by the typical lifetimes of the gap plasmons, which are in the femtosecond range [212]. This permits to characterize the $T(f)$ far in the region of several tens of GHz [176, 188]. We note that the present method does not use the so-called overbias emission that produces spectral features well above the single electron energy (i.e., caused by multielectron inelastic electron processes) [213]. For the cutoff detection, we assume that the harmonic signal of frequency f produced by the generator at amplitude A is transmitted to the tunnel junction without any distortion, but with attenuated amplitude A' and phase shift ϕ'. The energy cutoff $h\nu_{max}$ corresponds to the maximum value of the time-dependent bias voltage

$$h\nu_{max}(f) = \max[V_0 + A'(f)\sin(2\pi ft + \phi')].\qquad(6.1)$$

The illustration in Fig. 6.1(b) shows the idealized plasmonic spectrum (blue, denoted as RF_{OFF}) for a static bias V_0, without modulation. Switching on the modulation results in a modified plasmon spectrum, corresponding to the RF_{ON} curve (red). This curve can be understood as a weighted average of plasmon at static biases in the interval ($V_0 - A'$, $V_0 + A'$). The weight function (probability density function of the arcsine distribution centered around V_0) is represented in Fig. 6.1(b) by the horizontal, black-shaded area. This function corresponds to the probability distribution of the bias over one sine modulation period, and it peaks at its definition area limits ($V_0 \pm A'$), which gives rise to the new cutoff of the RF_{ON} plasmon at $V_0 + A'$. Direct readout of $A'(f)$ from the plasmon spectra allows to calculate the $T(f)$ as $A'(f)/A$ or as $T_{RF} = 10\log[A'(f)/A]$ in dB [207]. We determine the cutoff by finding a maximum in the second derivative
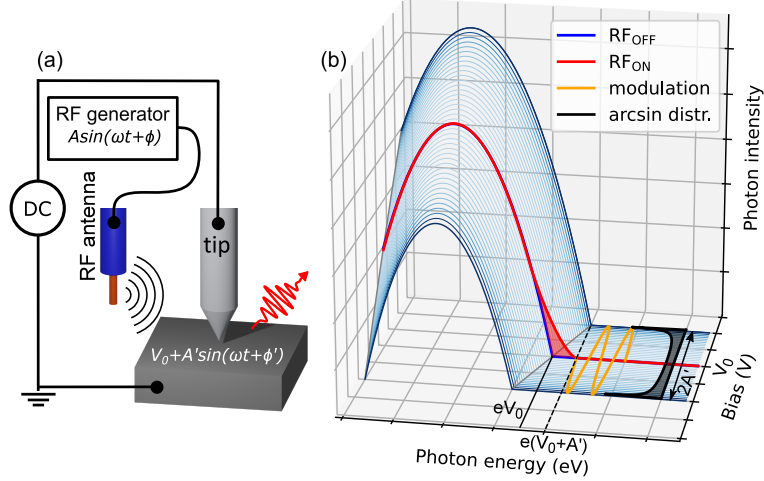
Figure 6.1: (a) Scheme of the optical RF-STM setup with an antenna transmitting harmonic oscillations of the electrical field to the tip, which modulates the spectrum of the plasmon modes generated in the tunnel junction nanocavity. (b) Model of the dependence of the plasmon spectra intensity and high-energy cutoff on the static bias V_0 without modulation (RF_{OFF}, blue curves) and with modulation (RF_{ON}, red spectrum, yellow curve) at the tunnel junction. The red-shaded area highlights the characteristic change in the high-energy cutoff, caused by the modulation averaging effect, weighted by an arcsine distribution (shown as black-shaded area).

of the spectra. In the real conditions, the V_0 is not time-invariant and therefore not simply equal to the preset bias voltage V_{DC}, but includes a component $U(t)$, caused by noise originating from various sources, in particular from electrical noise, thermal broadening and other as detailed below. We can include this correction by rewriting (6.1) as

$$h\nu_{max}(f) = \max[V_0 + U(t) + A'(f)\sin(2\pi ft + \Phi')] = V_0 + U_0 + A'(f). \quad (6.2)$$

In the determination of the frequency-dependent A', we eliminate the offset by subtracting a reference value of $V_{DC} + U_0$, obtained at $A = 0$, assuming that it remains constant in the range of evaluated frequencies. Evolution of the actual shape of a typical plasmonic spectrum, obtained by a Ag-coated tip on Ag(111) sample, is demonstrated in Fig. 6.2(a) with 981 Hz modulation. The transmission through standard wiring at this frequency is expected to be almost ideal (near unity). The detected cutoff value is plotted as a function of the modulation amplitude in Fig. 6.2(b) and manifests good linearity over the entire range. Calculated $T(f)$ in Fig. 6.2(c) indeed converges to unity for higher values of modulation A, due to the decrease in the relative error in $T(f)$, caused mostly by the precision of the edge detection. Targeting an A'_T of 50 mV at the tunnel junction for the calibration of $T(f)$ will therefore achieve a reasonable compensation accuracy ($< 10\%$). Thus, for our specific generator maximum output 4950 mV, we would be able to reliably measure and compensate $T(f) > 0.01$.

In order to compensate the $T(f)$ in the GHz range with sufficient precision for ESR measurements and alike, we apply two iterations as detailed in Figs. 6.3(a)-6.3(c). In the first step, we use a relatively large (≈ 1.4 V) constant driving amplitude. Optical grating and bias voltage are chosen such that they provide a wide dynamic detection range (5–440 mV) for the RF-induced increase in the
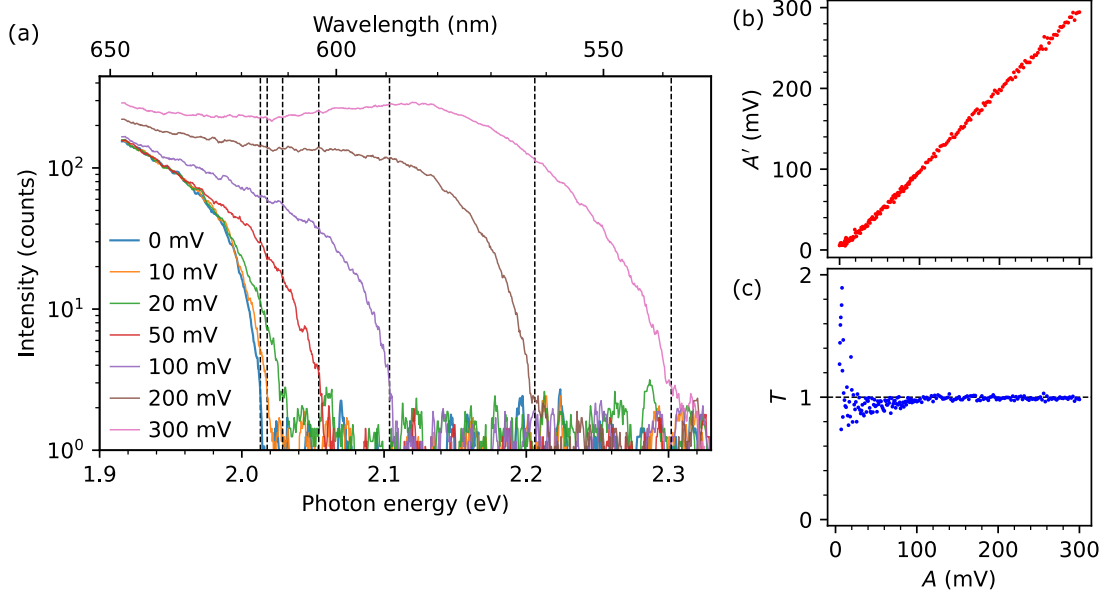
Figure 6.2: (a) Reference plasmon cutoffs measured with $V_{DC} = 2$ V (blue curve) and $f = 981$ Hz modulation with amplitudes in the $10 - 300$ mV range. Black dashed vertical lines mark the cutoff energies. Spectral resolution was 1.2 nm (or 4 meV at 620 nm), using a 600 gr./mm grating. A 11-point zero-order Savitzky-Golay filter was used for filtering of the spectra. (b) Test of the linearity between the amplitudes A' derived from the plasmon spectra cutoffs and the applied modulation A. The values of A' are compensated for the offset (at $A = 0$). (c) Transfer function magnitude (T) calculated from 10 to 300 mV lock-in modulation data from (a).

cutoff. After the first frequency sweep, the $A'(f)$ is evaluated [see Fig. 6.3(a)], the $T(f)$ is calculated as $A'(f)/A$. In a second frequency sweep, we seek a constant target amplitude (A_T') in the tunnel junction of 50 mV, and use therefore driving $A(f) = 50$ mV$/T(f)$. With these parameters, a new $A'(f)$ is measured. It can be seen in Fig. 3(b) that the amplitude is still not perfectly compensated; therefore, we recalculate again the $T(f)$ as $A'(f)/A(f)$. For a third frequency sweep, solely for the purpose of confirmation, we use this refined $T(f)$ and create a new driving $A(f)$ profile with a target amplitude of $A_T' = 20$ mV. The $A'(f)$ measured in this final sweep [see Fig. 6.3(c)] is apparently well-compensated in the entire frequency range, with the exception of a few isolated deviations. The largest deviations from the target $A'(f)$ (e.g., the dips at 2 and 5.5 GHz) occur at frequencies with sharp minima in the $T(f)$ [below the horizontal orange dashed line in Fig. 6.3(d)]. These "dark" bands cannot be effectively compensated due to the limited maximum driving power of the generator and the spurious thermal effects caused by excessive RF power dissipation within the microscope head and should be therefore avoided in the measurements. However, further improvement may be achievable by careful optimization of the entire RF setup.

Fig. 6.4 shows a full-range measurement demonstrating that a reasonable characterization of $T(f)$ for our RF line is possible for large continuous frequency intervals between 500 MHz up to 16 GHz. In comparison, the transmission via standard wiring is very effective in the MHz range, but sharply deteriorates just below 1 GHz. However, strong compensation has not proven practical in the regions of $T(f)$ below 2×10^{-3} (-27 dB), where the power dissipation leads to
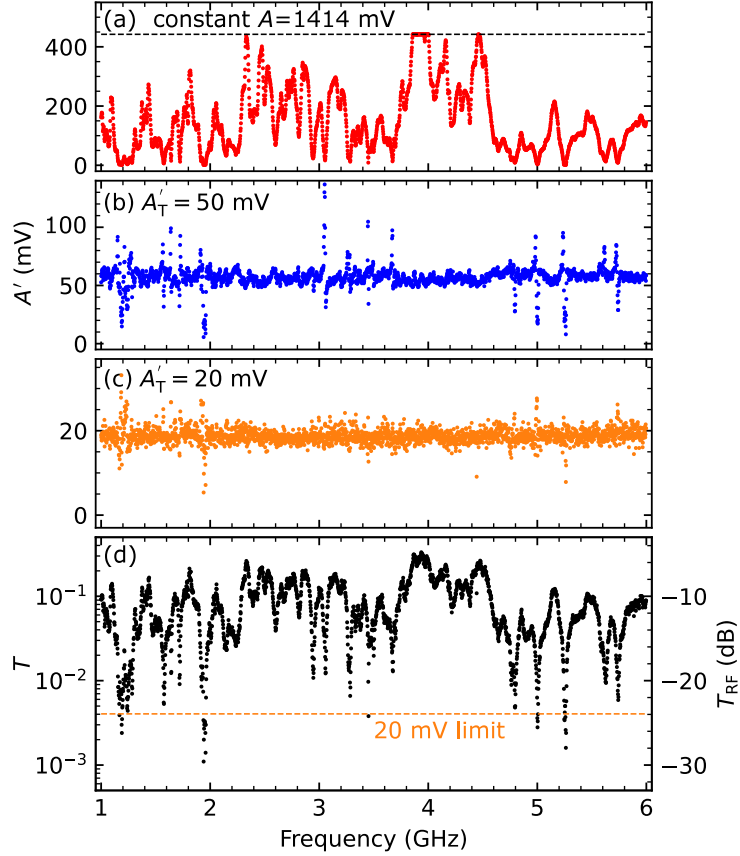
Figure 6.3: (a) Effective amplitude $A'(f)$ of the voltage at the tunnel junction measured as a function of frequency at constant driving amplitude 1414 mV. Black dashed line denotes the upper limit of the photon energy that can be measured with the spectrograph settings of 600 gr./nm grating and center wavelength 570 nm. Each point has been taken at constant tunneling current 3 nA, 2.0 V bias and averaging 2 s for each spectrum. (b) Effective amplitude $A'(f)$ at the junction after first compensation of the RF driving with target amplitude 50 mV using values from (a). Each point was obtained with 5 nA, 2.0 V, 1.5 s, and 600 gr./mm. (c) Effective amplitude $A'(f)$ measured after second compensation using values from (b), with target amplitude 20 mV. Parameters were 5 nA, 3 s, 1200 gr./mm grating for each spectrum. (d) The transfer function magnitude (T) of the system calculated from the values in (c). The orange dashed line marks the lower limit of the T that can be compensated in the setup.

thermally induced movement of the tip with respect to the sample. The positions and depths of the $T(f)$ minima are very sensitive to the actual position of the antenna with respect to the sample and the scanner within the scanning probe assembly. In our repeated measurements, we have observed shifts of the $T(f)$ minima by 100–300 MHz and also their complete disappearance upon macroscopical scanner movements. This can be attributed to the changes in the overall microscope head geometry which forms a very complex RF-cavity. Therefore, the calibration of the $T(f)$ has to be performed prior to every particular experiment with RF driving. Optimization of the RF coupling to the tip-sample junction may decrease the number of minima in $T(f)$. The geometry-dependent transmission in the microscope head also allows seeking an optimal $T(f)$ shape at a particular frequency range by coarse scanner movements.

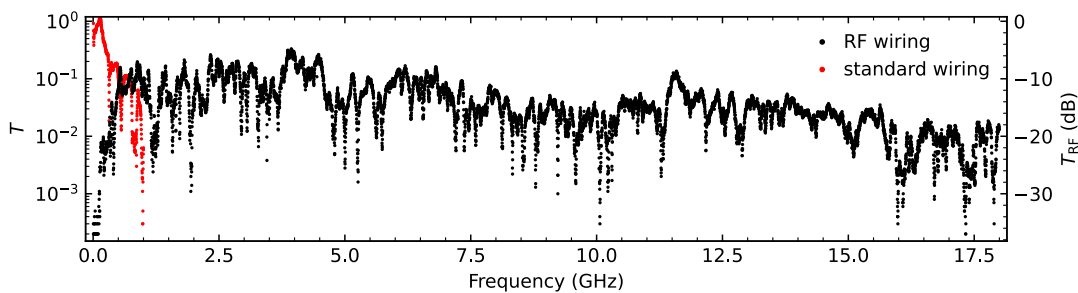**Figure 6.4:** Transfer function magnitude (T) of the system in a broad range of frequencies measured using standard wiring of the STM (red points) and RF wiring with antenna near to the STM tip (black points). Every point has been obtained from plasmonic spectra taken during 3 s at 5 nA, 2 V, with 1200 gr./mm grating.

With our procedure, we were able to get a constant driving with a relative standard deviation of $\approx 8\%$. The major factors causing the broadening of the cutoff in a real plasmonic spectrum are temperature (8 K corresponds to FWHM of 2.2 meV), spectral resolution of the spectrograph (1 nm corresponds to 3.2 meV error at 620 nm), and energy-time uncertainty (200 fs plasmon lifetime [212] corresponds to FWHM of 3.3 meV). The exact value of broadening caused by finite plasmon lifetime is unknown, but we did not observe any significant broadening in the range of tens of meV, in contrast to previous works [214]. Propagation of all errors mentioned above is suppressed when the reference value $V_{\mathrm{DC}} + U_0$ measured with a greater precision is subtracted from the $h\nu_{\mathrm{max}}$. Stochastic noise is therefore the main source of error in the cutoff evaluation.

Our data were obtained using a tip that yielded a typical intensity of $2-6\times10^5$ photons per second at 2.5 V and 1 nA, which enabled fast collection of calibration spectra at each frequency value on the order of seconds when using the 1-10 nA tunneling current range. Therefore, calibration in 10 GHz wide range with 2 MHz step and each spectrum averaging time 2 s takes about 3 h. Faster acquisition is possible by increasing the tunneling current, that yields higher photon intensity, by factor of at least 40, where the cutoff evaluation is not hampered by the overbias emission (see Fig. D.3 in Supplementary Information in Appendix D). For the best signal-to-noise ratio and shortest acquisition time, a very steep cutoff at the photon energy corresponding to the bias $V_0 + A'$ and high derivative of the plasmon intensity between V_0 and $V_0 + A'$ are desirable. For completeness,

we have performed an additional measurement to compare our optical method to the conventionally used method that evaluates the $T(f)$, based on a sharp feature in the tunneling spectroscopy [205, 206], in our case the surface state of Ag(111). The two methods show an excellent agreement in the measured range of frequencies (for details see Supplementary Information in Appendix D). Finally, we have tested the optical calibration for current setpoints in the range 5–200 nA (resulting in $\Delta z = 150$ pm) and found no measurable differences in the $T(f)$, inferring that typical variations in the tunneling distance will not alter the system RF characteristics.

6.4   Conclusions

In summary, we present a direct optical method for measuring the frequency-dependent transfer function of an RF-STM line. This method can be readily adapted to a wide range of instruments provided that they have optical access. The principle of the method does not require the presence of a sharp $I(V)$ non-linearity in the measured system. It is very robust against drift and intensity fluctuations and provides a wide dynamic range well above 1 eV due to the broad character of a typical gap plasmon spectrum. We demonstrated amplitude compensation in our RF-STM with antenna-tip capacitive coupling and constant amplitude driving in the 1-18 GHz range. This method is particularly relevant for RF-phase fluorometry [176] and for future application in optically detected electron paramagnetic resonance in STM. In addition, we envisage possible applications of this method in fields detached from scanning probe microscopy by using integrated light sources —— e.g., on-chip metal-insulator-metal tunnel junctions —— for calibration of RF driving amplitude on directly inaccessible devices. See the Supplementary Information in Appendix D for the comparison between transmission determined from plasmon cutoff detection and from dI/dV at the Ag(111) surface state and for the dependence of the transfer function magnitude on the current and changes in the tip-sample distance.

7. Exciton delocalization in molecular clusters

The following chapter is based on the publication [215] and reprinted with permission. Copyright 2021 American Chemical Society. In their seminal publication [12] Zhang et al. spatially mapped the coherent dipole-dipole exciton coupling in artificially created multimers of ZnPc. In this chapter, we have chosen a PTCDA anion as a building block for larger molecular aggregates to study the delocalization of excitonic states with very high spectral resolution. In the theoretical description, we went beyond the basic dipole-dipolar approximation [12] and used the transition density calculated for each aggregate geometry to generate photon maps comparable with the experiment.

7.1   Introduction

Recently, plenty of effort has been put into the search for nanoscale materials that exhibit strong light-matter interactions with long radiative lifetimes. The manipulation and detection of charged excitons from semiconductors and transition metal dichalcogenide heterostructures holds promise in the development of high-performance ultrathin optoelectronic devices [216, 217, 218, 219, 220, 221]. An alternative to solid-state based excitons are organic-molecule platforms, which manifest generally longer exciton lifetimes. Optically active molecules offer key advantages as quantum emitters due to their very small dimensions, well-defined optical transitions, and photostability [222]. In addition, they can be electrically driven to transduce electric currents into optical signals [80] and can also host charged excitons [176, 81, 223]. Moreover, with the recent development of precise local spectromicroscopy techniques, it is possible to address the photophysics of aggregates at the single-molecule level [224, 86].

Coupling between the excited states of single-molecule emitters leads to the formation of delocalized excitonic states, whose properties finely depend on the exact intermolecular arrangement at the nanoscale [224, 225, 226]. The entanglement between the molecular excited states, specific to molecular aggregates, could be potentially harnessed for use in quantum computing, if it could be controlled. Theoretically, it has been suggested that building quantum bits and quantum-logic gates from dyes is possible by tailoring the chromophore geometries and couplings in an aggregate in order to encode specific quantum transformations [227, 228, 229] that perform the elementary quantum computing operations. Therefore, not only the exact distances and mutual orientations of the molecular units in the aggregates are paramount but also their charge state and local nanoscopic environment, since they determine the eigenstates and shape the characteristic absorption and emission fingerprints.

Traditional far-field spectroscopies have been used to characterize the properties of various molecular aggregates, however, with fundamental limitations which are the inherent lack of spatial resolution and insensitivity to the dark states, whose interaction with the uniform field is forbidden due to the zero total transition dipole moment [226, 230]. Thanks to the recent development, the op-

tical response of individual chromophore clusters in the visible- to near-infrared region can be addressed directly by tip-enhanced scanning probe spectromicroscopies, that allow an actual spatial mapping of the eigenstates and can access the dark or weakly emitting states by coupling them efficiently into the near-field of the nanocavity [86, 135, 12, 11, 231, 33, 232, 233]. Moreover, with such techniques, the geometry of the aggregates can be characterized and controlled with atomic precision [12, 231, 33]. This approach represents a powerful tool for a correct identification of the eigenmodes, of the coupling among the aggregate constituents and the involvement of the excited states of the isolated components.

Excitonic states and energy transfer mechanisms have been mostly studied on neutral chromophores [12, 11, 231] yet no control over the charged exciton states has been achieved at the level of molecular aggregates. Here, using perylenetetracarboxylic dianhydride (PTCDA) anions, we create small clusters that manifest exciton delocalization, and we identify their eigenmodes by a combination of scanning tunneling microscopy-induced luminescence (STML), atomic force microscopy (AFM), time-dependent density functional theory (TD-DFT), and photon map simulations. In addition, we show eigenmode switching by charge state control.

7.2   Results and discussion

Single PTCDA molecules adsorb flat on three monolayer (ML)-NaCl/Ag(111) centered over a Cl^- ion and align with the principal NaCl lattice directions. Under these conditions, when sufficiently decoupled from the metal substrate, PTCDA spontaneously takes up an extra unpaired electron to its lowest unoccupied molecular orbital [234, 235, 236], becoming a molecular anion radical with a total spin $S = 1/2$ (D_0^-). In the nanocavity polarized beyond a threshold bias voltage of -2.1 V, the chromophores emit predominantly in the near-infrared region [94], which is manifested by a sharp peak at 1.332 eV (Fig. 7.1a, taken at -2.5 V), accompanied by red- and blue-shifted sidebands at 1.363 and 1.303 eV. We attribute the main spectral line to the decay from the first excited state (D_1^-) of the PTCDA anion and the sidebands to vibrational features [237]. We base this notion on the following: (i) Measurements by radio frequency phase fluorometry of the dynamics of the excitation that find an effective radiative lifetime below 70 ps, unexpectedly short for a triplet state and shorter than the excited neutral and trion effective lifetimes on ZnPc under comparable conditions [176, 192]. (ii) TD-DFT calculations predicting a strong emission of $D_1^- \rightarrow D_0^-$ at 1.62 eV, close to the experimental value. (iii) Observation of single-exciton state delocalization in assemblies of molecules, driven by Coulombic coupling, compatible only with the interactions among the anions.

Hyperspectral electroluminescence maps measured on a grid of points at constant height of the tip above the chromophore can be correlated with the theoretically calculated excited states [147, 71]. The photon map of the main emission line (Fig. 7.1c) taken with a metallic tip shows high emission intensity at the carbonyl-terminated ends of the PTCDA and can be assigned to a decay from the first excited state to the ground state of the anion ($D_1^- \rightarrow D_0^-$, see Fig. 7.1b). It bears a transition dipole moment along the long axis of PTCDA (hereby denoted as longitudinal mode, see Fig. 7.1d). For generating a theoretical photon
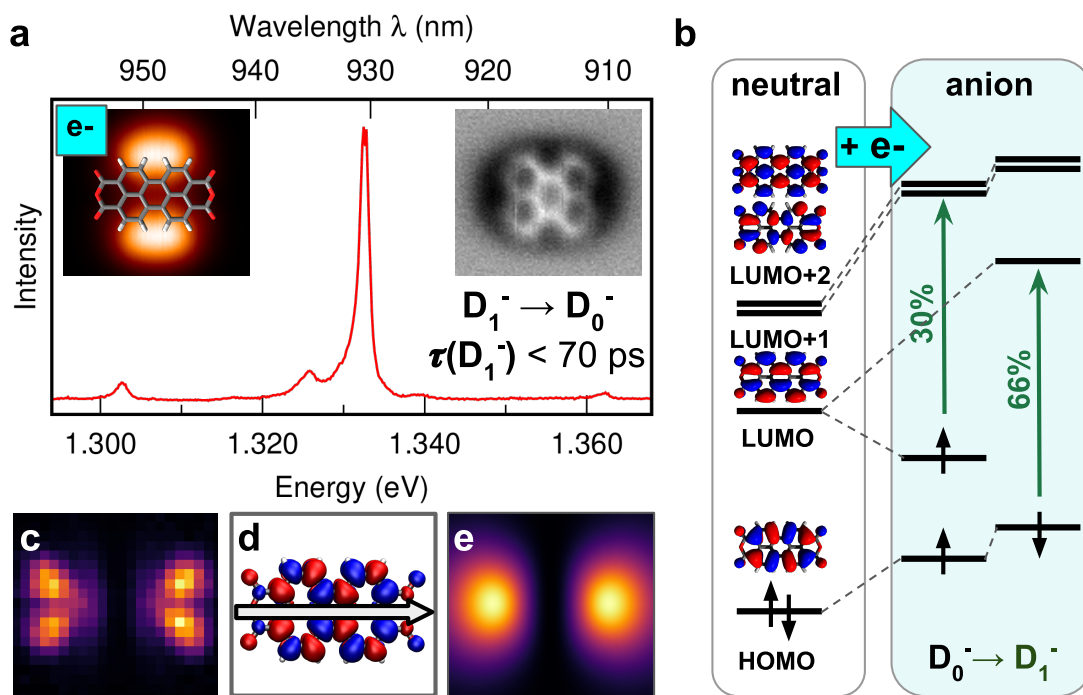
Figure 7.1: (a) $D_1^- \rightarrow D_0^-$ spectral line and the lowest vibrational sidebands of the electroluminescence of PTCDA anion, taken at -2.5 V at the sample, 50 pA. The insets show tunneling current image at constant height, also taken at -2.5 V, with a PTCDA model overlay (left inset) and AFM constant-height image in the repulsive mode (right inset), showing the perylene backbone with atomic resolution. Both images are at the same scale (1.6×1.4 nm^2). (b) Energy level schemes with the corresponding orbitals from calculations on the PTCDA neutral and anion states. Green arrows are marking the main transitions involved in the first excited state D_1^- and their weight in percent. (c) Experimental photon map integrated in the 1332 ± 2 meV range, taken at -2.5 V, at constant height and normalized. (d) Isosurface plots of the transition density of the PTCDA anion first excited state. The arrow denotes the longitudinal transition dipole moment. (e) Simulated photon map based on the transition density in (d).

map, we use the computed corresponding transition density and simulate the coupling of the excitation to the optical field of the laterally scanning nanocavity. Our simulation procedure has the capability to simulate photon maps from any given transition density (see the Supplementary Information in Appendix E). The resulting map for anionic PTCDA (Fig. 7.1e) is in agreement with the experimental observation. The higher detail of features in the experiment compared to the theory can be attributed to laterally inhomogeneous probabilities of charge injection into the frontier orbital and the subsequent formation of the exciton [147, 71, 134].

We have assembled few-unit PTCDA anion clusters by thermally controlled diffusion [234, 235, 238]. The exciton delocalization in the assembly is manifested by a characteristic multiplicity of the exciton peaks (Davydov splitting) due to the emerging eigenmodes resulting from the interaction between the molecular excited states (see Fig. E.7). A nonlinear parallel dimer configuration (Fig. 7.2a–c) represents a geometry in which the longitudinal modes of PTCDA can couple efficiently. The spectra show a dominant contribution at 1.331 eV, with most intensity concentrated at the outer oxygen terminations of the dimer, and a second less intense peak at 1.333 eV, which can be detected in the center of the dimer (Fig. 7.2f). The doubly anionic dimer with one negative charge per molecule is the most stable charge configuration according to calculations (Table E.1) and has a total spin $S = 1$ (T_0^{2-}). The first two excited states of the system, (T_1^{2-} and T_2^{2-}), are dominated by excitations involving the same orbitals as the $D_0^- \to D_1^-$ monomer transition (Fig. 7.2g) and thus can be understood as the in-phase and out-of-phase linear combinations of the longitudinal modes of the individual molecules (Fig. 7.2e). The observation of the out-of-phase mode using the nanocavity, which is otherwise expected to be dark in the far-field measurement (zero total transition dipole moment), is consistent with previous prediction [233]. The exciton states ordering, along with their energy spacing, provided by the calculations is confirmed by the agreement between the simulated and experimental photon maps (Fig. 7.2f).

We have investigated a second dimer motive that adopts a perpendicular arrangement of the molecules (Fig. 7.2h–j). In the framework of the point-dipole approximation, the interaction between the longitudinal modes of the two perpendicular molecules is zero; therefore, negligible coupling between exciton states of the two isolated molecules is expected. Surprisingly, the spectrum of the dimer shows multiple splitting of the main emission line, suggesting an additional exciton coupling mechanism. Three peaks at 1.333 eV (most intense), 1.340 and 1.344 eV are resolved, each generating a distinct contrast in their corresponding photon map. Calculations of the doubly charged dimer, which is also the most stable in this case, show that lowest exciton states T_1^{2-} and T_2^{2-} (Fig. 7.2l) are dominated by a transition that shares the characteristics with the D_1^- monomer state localized on a single-molecule unit (see Fig. 7.2n), but with a non-negligible contribution from a higher energy mode (D_2^-) localized on the adjacent molecule (see Table E.1). Indeed, we experimentally observed an additional line from a higher mode in single PTCDA, a transition at 1.493 eV, when inspecting the molecule on 3 ML-NaCl/Au(111) that can be directly assigned to the calculated $D_2^- \to D_0^-$ emission (see Fig. E.3). According to both experiment and calculations, the D_2^- excitation is energetically close to the D_1^- state and has a transition dipole
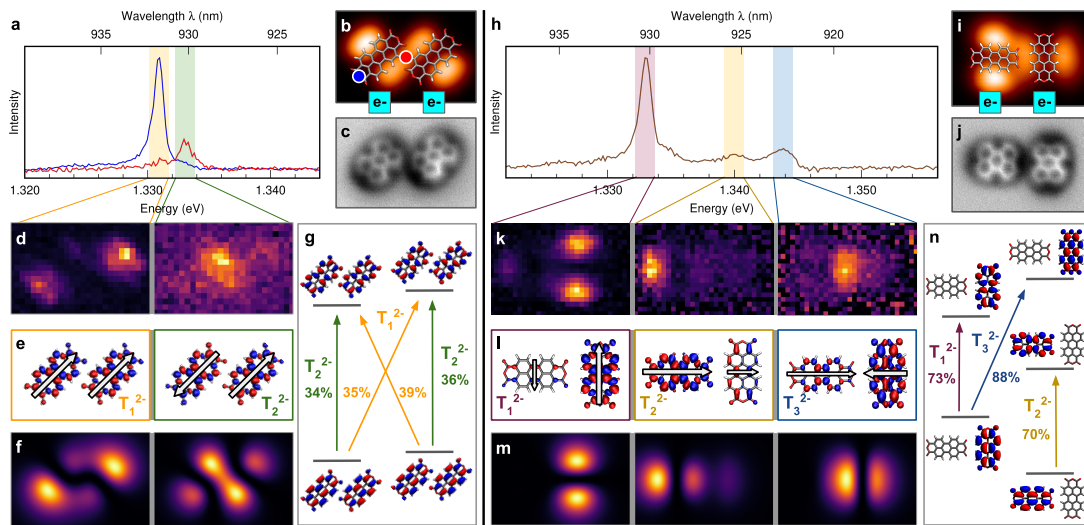
Figure 7.2: (a, h) STML spectra of the parallel and perpendicular dimer emission, respectively. (b, i) Corresponding constant-height current images of the dimers at - 2.5 V with model overlays. The charge state of each molecule is symbolized by a cyan square with e^- within. The representative locations of the spectra in (a) for the parallel dimer are marked by their corresponding colors. (c, j) AFM constant-height images of the backbones taken at 5 mV. (d, k) Experimental photon maps integrated in the ranges marked in the spectra. (e, l) Isosurface plots of the transition densities of the lowest-energy excited states, assigned to the observed peaks in the spectra. White arrows denote schematically the direction of the transition dipole moments of the individual molecules constituting the dimers. (f, m) Simulated photon maps based on the transition densities in (e, l). (g, n) Scheme of the excitations with dominant contributions to the calculated lowest-energy eigenstates (weight in percent).

moment oriented perpendicular to the longitudinal mode (thereby transversal mode). Consequently, the perpendicular arrangement of PTCDA molecules favors the coupling between longitudinal and transversal modes of the neighboring monomers. The transversal mode becomes the dominant contribution in the higher-energy state T_3^{2-}.

We further target the role of the transversal mode by analyzing longer perpendicular arrangements. The PTCDA trimer (Fig. 7.3) represents a simple extension of the perpendicular dimer. Unexpectedly, the tunneling current image taken at negative bias (occupied states, Fig. 7.3b) starkly contrasts with previous measurements on the monomer and dimers. The characteristic two-lobe pattern of the highest occupied level of a single molecule, when tunneling at -2.5 V, is absent from the central molecule. This suggests that the central molecule has a different charge state (neutral) than the peripheral ones (anions). Photon emission measurements show two well-separated emission lines at 1.338 and 1.342 eV indicating that only two longitudinal modes interact (similarly as in the parallel dimer). Photon maps of the lines yield intensity patterns with maxima located at the outer and inner oxygen terminations of the peripheral molecules, respectively. Computed excitation transition densities for a doubly charged trimer with $1e^-$ localized on each peripheral molecule, the lowest energy configuration of the trimer in DFT calculations, yield T_1^{2-} and T_2^{2-} eigenmodes as linear in- and out-of-phase combinations of the longitudinal modes of the charged molecules. The central neutral molecule is effectively excluded from the excitonic interactions in the trimer and acts merely as a spacer. Our calculations indeed confirm that in the neutral molecule there is no available transversal mode to couple with the longitudinal modes of the PTCDA anions.

Reversing the inactive role of the neutral molecule in the trimer can be achieved by controlling the electric field in the nanocavity. By applying positive bias voltages, we drive the system to a total charge of $3e^-$. The current image taken at +2.5 V shows a strong contribution to the tunneling current also at the central molecule. STML spectra at positive polarities display a strong slightly broadened emission band at 1.329 eV (fwhm: 3.3 meV). Comparison of the experimental and theoretical photon maps, computed considering the trimer in a reference quartet spin state Q_0^{3-} (see Table E.2), unambiguously assigns the 1.329 eV line to the lowest excited eigenstate Q_1^{3-}. This excitation originates from the longitudinal mode of the central PTCDA weakly mixing with the transversal modes of its neighbors. The second excited mode Q_2^{3-} is similar in energy and character to the first excitation of the doubly charged trimer T_1^{2-}, but in addition, it incorporates coupling to the transversal mode of the central molecule. The bimodal charge state and the electrofluorochromic character of the PTCDA trimer can be further explained by DFT calculations. The $2e^-$ and $3e^-$ charge states have similar total energies, with the $2e^-$ being the lowest one in the gas phase (see Table E.2). Positive strong bias voltages force the assembly in a triply charged ground state which leads to involvement of the central PTCDA in the exciton interaction. This demonstrates reprogramming of the excitonic system is possible by electric field control.

To further explore the exciton delocalization and the relation to the charge state, we have assembled larger PTCDA aggregates. In the highly symmetrical tetramer introduced in Fig. 7.4, the total number of extra electrons appears to
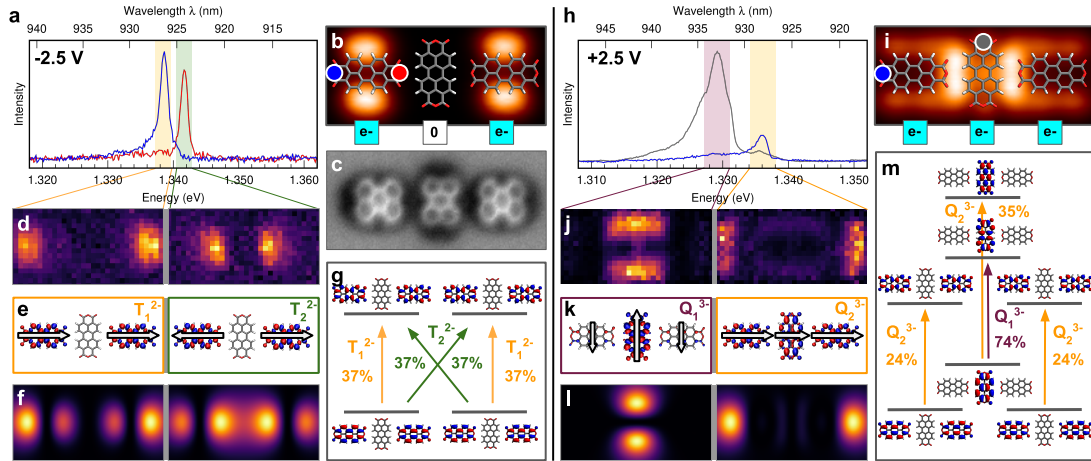
Figure 7.3: STML spectra of the trimer taken at opposite polarities, -2.5 and +2.5 V, respectively, representative of spectra in the locations marked by corresponding colors in (b, i), the constant-height current images of the dimers at -2.5 V with model overlays. The charge state of each molecule is symbolized by a cyan square with a value within. (c) AFM constant-height image of the backbones taken at 5 mV. (d, j) The experimental photon maps integrated in the ranges marked in the spectra. (e, k) Isosurface plots of the transition densities of the lowest-energy excited states, assigned to the observed peaks in the spectra. White arrows denote schematically the directions of the transition dipole moments of the individual molecules constituting the trimers. (f, l) Simulated photon maps based on the transition densities in (e, k). (g, m) Scheme of the excitations with dominant contributions to the calculated lowest-energy eigenstates (with weights in percent).

reach a local equilibrium, where the Coulomb repulsion between charges on adjacent molecules counteract the propensity of PTCDA to take up an electron. In large assemblies, integer charges do not necessarily need to be localized at particular molecules and instead can reside in delocalized orbitals of the whole ensemble. The calculation of the tetramer reveals a near degeneracy between the double ($2e^-$) and triple ($3e^-$) negatively charged configurations (see Table E.2). For the $2e^-$ configuration, the charge is localized on two opposite molecules and for the $3e^-$ case, it evenly distributes among the four molecules ($3/4e^-$ each). In the photon spectra measured at +2.5 V we resolve four modes at energies 1.328, 1.332, 1.335, and 1.339 eV (denoted as 1-4, respectively), which can be theoretically explained by considering the system alternating between the $3e^-$ and $2e^-$ states. The experimental photon maps and the relative energy order of modes 1, 2, and 4 can be rationalized by quartet (Q_n^{3-}, $n = 1, 2, 3$) excited states of the $3e^-$ configuration. In the highest energy mode (4, Q_4^{3-}), the longitudinal modes of the monomers couple with individual dipoles pointing inward, producing a photon map with a characteristic intensity maximum in the center. Conversely, the two lowest energy modes (1 and 2, Q_1^{3-} and Q_4^{3-}) consist of alternative orientations of the longitudinal transition dipole moments which give photon maps with four lobes located in the outer part of the tetramer. Mode 3, showing a spatial distribution with high intensity on both the periphery and the center of the tetramer, is described well by the lowest energy triplet excitation of the doubly charged assembly, T_1^{2-}. For this case as well as for the Q_2^{3-}, the two rotationally equivalent configurations are superimposed in order to simulate

the degeneracy of the $2e^-$ localization. We believe that the tetramer, constantly disturbed from the equilibrium by injection of charges, oscillates between the two states and therefore both contribute to the observed photon maps.
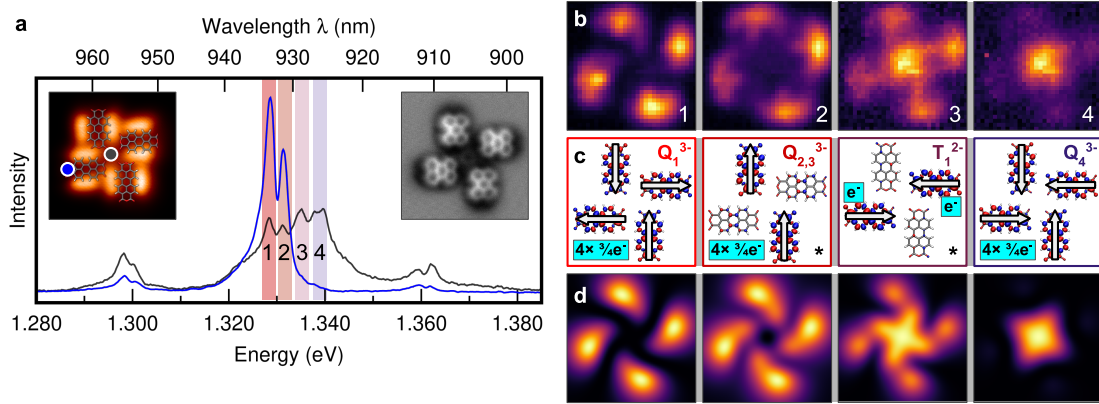

Figure 7.4: (a) STML spectra of the tetramer representative of the peripheral and center locations, marked in the current image taken at constant height (left inset). The bias voltage for the spectra and the current image is +2.5 V. The atomic model is overlaid. AFM high-resolution constant-height image (right inset) is taken at 5 mV. (b) The experimental constant-height photon maps integrated in the ranges marked in the spectra as 1-4. (c) Isosurface plots of the transition densities of the lowest-energy excited states of the $3e^-$ and $2e^-$ configurations, assigned based on the observed photon maps. White arrows denote schematically the direction of the transition dipole moments of the individual molecules. (d) Simulated photon maps based on the transition densities in (c). Maps 2 and 4 are obtained by averaging the corresponding two 90° mutually rotated photon maps.

7.3 Conclusions

In summary, based on the comparison between the experimental hyperspectral maps and the theoretical photon maps, we confirmed that the aggregates made of PTCDA anions host delocalized entangled single-exciton states. We have demonstrated that mapping both the bright and dark states by spectromicroscopy in a nanocavity permits us to understand the coupling between molecules in PTCDA clusters. We used this methodology to identify the dominant exciton coupling as the interaction between the first excited states D_1^- of the single-emitter PTCDA units. Additionally, we have found that a favorable interaction between D_1^- and the second excited D_2^- state, due to their low energy difference, enables exciton coupling between molecular units in a mutually perpendicular geometry, giving rise to delocalized eigenmodes.

8. Exciton-libron coupling in chirally adsorbed single molecules

The following chapter is based on the publication [239] and reprinted with permission. The origin of the linewidth of optical transitions observed in STML spectra is presently a subject of discussion in the scientific community. Since the studied systems are single molecules at low temperatures the linewidth was often directly attributed to the exciton lifetime (see section 1.5) stirring some controversy. We observed that the width can change with varying numbers of NaCl layers and for different adsorption configurations (in chapter 4) and also for different charge states (in chapter 7). In this chapter, we present a detailed study of the trion lineshape performed on various phthalocyanine, which revealed yet unexplored phenomena.

8.1 Introduction

Coupling between excited electronic states and nuclear motion is an essential mechanism for conversion between optical, mechanical and chemical forms of energy in nanosystems. Such excitation-vibration coupling is relevant in biological processes such as photosynthesis [240, 241, 242] light-sensitive proteins in eyes [243, 244] in artificial molecular motors [245, 246] or organic solar cells [247, 248]. Frustrated rotations (librations) represent a particular type of vibration in which the molecule performs a torsional oscillation when subjected to external stimuli and constraints that restrict its orientation. Despite their efficient coupling to electronic transitions, librations have largely eluded spectroscopic detection because of naturally relatively small energy differences between their quantized levels, making it difficult to derive any characteristic parameters from the spectra, especially in large ensembles of molecules. Obtaining well-resolved spectra of librations directly is complicated because they become easily obscured by stochastic thermal motion, the effect of solvents and by a generally limited control over the nanoscopic environment of the chromophores. Therefore, performing experiments in well-controlled environments on the single-molecule level is a key to advancing our fundamental understanding of molecular librations as well as for the development of nanomachines and nanodevices.

Recent progress in tip-enhanced single-molecule spectroscopy permits to overcome the limitations of traditional ensemble-based spectroscopies and study neutral and charged excited states and their coupling to vibrations on single molecules. Scanning tunnelling microscope-induced electroluminescence [80, 10, 11, 12, 81, 98, 32, 88, 223] (STM-EL), photoluminescence [72, 90] (STM-PL) and tip-enhanced Raman scattering [8, 122, 115] (TERS) methodologies operating at cryogenic temperatures can localize and amplify the interaction of electromagnetic radiation with a molecule located in the plasmonic nanocavity, formed between the scanning probe and a metal sample by many orders of magnitude. Using these approaches one can study individual photoactive molecules without the influence of stochastic thermal fluctuations or the presence of solvents and map the electron transitions in the optical near-field with submolecular res-

olution. This resolution is orders of magnitude higher than what can be achieved with in-solution spectroscopy and opens a new window to determine the mechanisms governing the photophysics of molecular systems.

Here we apply STM-EL spectroscopy to investigate coupling between charged excited electronic states (trions) and quantized librations (librons) of zinc, magnesium and free-base phthalocyanine molecules (ZnPc, MgPc and H_2Pc respectively), adsorbed on sodium chloride (NaCl). Phthalocyanines are structurally similar to biological fluorophores (e.g. chlorophyll), therefore their interaction with the crystalline substrate provides a convenient controllable model for more complex interactions in vivo. Also, phthalocyanines on surfaces have been proposed as a model for molecular rotors and switches [249, 103, 250] for their ability to jump between various adsorption geometries on the surface upon electronic or mechanical excitation. We exploit the fact that adsorbed fluorophores exposed to electric fields in the nanocavity show propensity to charge and emit from excited trion states that generally manifest substantially narrower lineshapes, compared to the emission peaks of the neutral excited states [94, 215]. Up to our knowledge, this enables for the first time a high spectroscopic resolution suitable for studying the fine structure arising from the trion-libron coupling in a molecule with high moment of inertia, which we rationalize using the Franck-Condon principle and a harmonic oscillator model based on analysis of DFT and TD-DFT results. Using this approach we can precisely extract parameters of the potential energy landscape of the systems in their respective ground and excited states, the libration eigenenergies and estimate the probability distribution of the librons in the excited states. We can establish a general correlation between adsorption configuration (chiral vs. non-chiral) and the spectral profile, determined from the intensity of Franck-Condon factors of the transitions.

8.2 Results

8.2.1 High-resolution STM-EL spectra of single phthalocyanine adsorbates

Zinc-phthalocyanine (ZnPc) and Magnesium-phthalocyanine (MgPc) adsorb centred on the Cl- site of 2-5 monolayers (ML) of NaCl on Ag(111) and manifest a characteristic 16-lobe appearance in the occupied-state STM images measured at -2.8 V (insets in Fig. 8.1b-c). This appearance is the result of averaging over two geometrically equivalent metastable chiral adsorption configurations, between which the molecule rapidly switches upon injection of electrons [11, 12, 32, 131, 33]. The motion between these two configurations (called switching [32, 131] or shuttling [11, 88]) is represented by the larger grey arrow in Fig. 8.2a. In contrast, free-base phthalocyanine (H_2Pc) adsorbs centred above the Na^+ site and exhibits an 8-lobe pattern in the STM image (inset in Fig. 8.1d). Here, the apparent symmetry is due to averaging over the H_2Pc tautomers with different configurations of the central two H atoms [147]. STM-EL spectra (see Fig. 8.1b-c) acquired at bias voltages at -2.8 V on the molecular lobes of ZnPc and MgPc show distinct emission peaks, corresponding to neutral exciton (Q) and of the cation trion (Q^+). For H_2Pc in the neutral state, the excited states with electric transition dipoles oriented along the x and y axes of the molecule
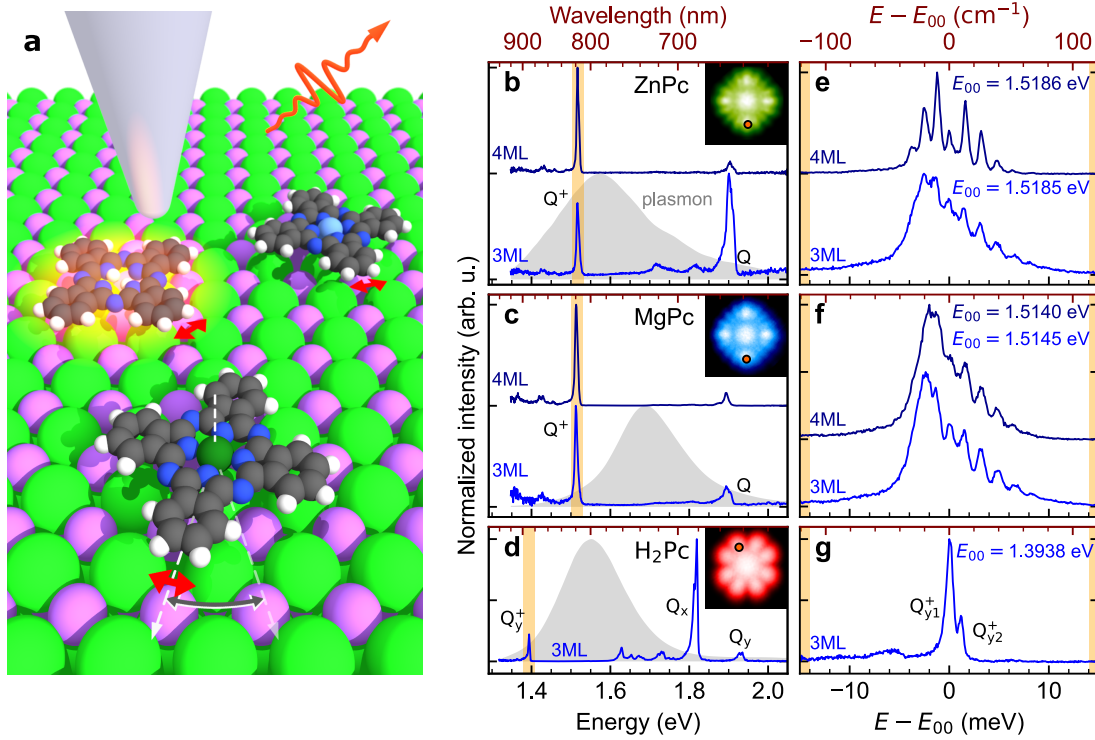
Figure 8.1: STM-EL characterization of phthalocyanines and high-resolution spectra of their cations. a Scheme of the STM-EL measurement of the MgPc, H$_2$Pc, ZnPc molecules (from top to bottom, respectively), performing in-plane librations on the surface of NaCl/Ag. The red arrow denotes small-energy librations while the grey arrow represents switching between two degenerate chiral equilibrium adsorption positions. **b-d** Overview STM-EL spectra of the ZnPc, MgPc and H$_2$Pc at -2.8 V, 100 pA, showing the neutral (Q, Q_x, Q_y) and cation (Q^+, Q_y^+) emission fingerprints plotted with blue solid lines. Grey-filled spectra on the background of each panel are the responses of the nanocavities measured on a clean Ag(111) surface at 2.5 V, 1 nA. **e-g** Spectra measured at the same bias and tunnelling current with 400 μeV resolution on the ZnPc, MgPc and H$_2$Pc cations, respectively, evidencing the fine structure present in the first two cases. The scale is given relative to the peaks within the spectral manifold, which manifest lower intensity with respect to their neighbours. The reference energies E_{00} are set to the assumed zero phonon lines in each spectrum. All molecular spectra in **b-g** are normalized by dividing by their corresponding plasmonic background. Raw spectra are presented in Fig. F.2.

(Q_x and Q_y) are not equivalent, which results in degeneracy lifting and two observable excitonic lines: Q_x and Q_y, the former having lower energy and higher intensity [251]. Interestingly, for H_2Pc in the cationic state only a single trion peak is detected. Based on quantum-chemical calculations (Fig. F.1 and Table F.1), we assign it to the Q_y^+ exciton, as the Q_x^+ is predicted to be of about 200 meV higher in energy (in the Ref. [223], the analogous transition is labeled as X_x^+).

The full width at half maximum (FWHM) of the ZnPc and MgPc neutral Q peaks is typically 8–20 meV (Fig. F.3, Ref. [86]) depending on the exact NaCl thickness, tip-sample separation and nanocavity plasmon-exciton matching [99, 77]. Conversely, the Q_x, Q_y linewidths of neutral H_2Pc are narrower – as low as 4 meV [90, 77], but still several orders of magnitude larger than a homogeneous broadening on a comparable system at 6 K [252, 253]. The width of the $ZnPc^+$ and $MgPc^+$ trion envelopes are in the range of 5–7 meV, however, high-resolution spectra reveal a rich fine structure. When measured at 400 μeV resolution, the spectra manifest a manifold of narrow, nearly regularly spaced peaks (Figs. 8.1e,f), where typically one peak in the central part of the manifold shows less intensity than its neighbours. Surprisingly, such fine structure is absent in the high-resolution spectrum of the H_2Pc^+ trion (in Fig. 8.1g) which shows only a main line, accompanied by a second minor component, likely originating from the second tautomer. Importantly, the spectral manifolds are appearing independently of the rotational switching motion of the molecules, as evidenced by the spectrum in Fig. F.4, obtained on MgPc on 4ML NaCl/Au(111), which is stabilized in a chiral adsorption geometry on a step edge.

8.2.2 Theoretical model of the librations and fitting of the spectra

The spectral fingerprints of the $ZnPc^+$ and $MgPc^+$ trions comprising multiple peaks indicate an efficient coupling between the molecular libration transitions and electronic transitions, i.e. the energy difference generated by change of the quantized energy of libration modifies the energy of the exciton decay. To estimate the potential energy landscape that hosts the librations, we first perform calculations of the total energy E dependence on azimuthal angle ϕ for the planar molecule cations in their doublet ground and first excited states (denoted as D_0, D_1). The results of the $E(\phi)$ calculations are summarized in Fig. 8.2. We find that $ZnPc^+$ and $MgPc^+$ in the ground and trion states have double-well energy landscapes (Figs. 8.2a,b), separated by a barrier of $\sim$200 meV (for the switching of the molecular geometry), with equilibrium azimuthal angle value of $\phi_0 \approx \pm 15°$, somewhat higher compared to previously reported results [131, 254]. The H_2Pc^+ energy landscape consists of a single well with the lowest energy configuration at i.e. $\phi_0 = 45°$ (Fig. 8.2c). For the transitions $D_1 \rightarrow D_0$ in $ZnPc^+$ and $MgPc^+$, parabolic fits of $E(\phi)$ around the equilibrium angle (Fig. 8.2d and Table F.2) quantify a shift in the equilibrium angle $\Delta\phi_0$ of about 0.3° and a change in the stiffness of a few percent. The nonzero $\Delta\phi_0$ is a result of the different asymmetry of substrate electrostatic interaction acting between the NaCl substrate and the ground and excited states of the chirally adsorbed molecules. H_2Pc^+ also shows a comparable change in the stiffness of the potential well upon exci-

94

tation, but at the same time it does not rotate its equilibrium configuration (i.e. $\Delta\phi_0 = 0$), due to its symmetrical adsorption geometry with respect to NaCl. Having learned from the calculations that at the lower energy limit (well below
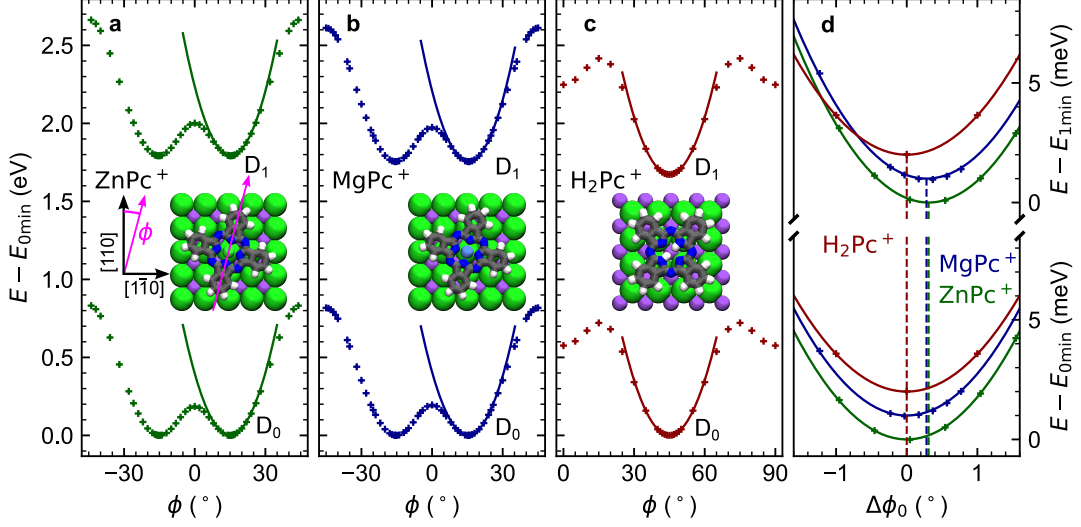

Figure 8.2: TD-DFT evaluation of the potential energy landscape for rotation of phthalocyanines on NaCl. a $ZnPc^+$, **b** $MgPc^+$ and **b** H_2Pc^+ total energy (relative to the energy of the minima E_{0min}) as a function of rotation by angle ϕ for the ground and excited states. The computed energy is plotted with crosses and the corresponding parabolic fits around the local minima with solid lines. The insets show the schematic models of the respective ground state cations in their equilibrium positions. The angle ϕ is defined as between the molecule x-axes (crossing two opposing isoindole groups along N–N atom direction) and the nearest of the [110] and [1$\bar{1}$0] NaCl crystallographic direction, as shown in the inset of **a**. **d** Detailed comparison of the potential well minima of the three cationic chromophores (computed as a difference with the energy of their respective minima E_{0min} or E_{1min}) as a function of the shift in the equilibrium angle positions $\Delta\phi_0$ between the ground and excited states. $MgPc^+$ and H_2Pc^+ ground and excited state are vertically offset by increments of 1 meV for clarity. Note the zero $\Delta\phi_0$ for H_2Pc^+, imposed by the symmetry of the system.

the barriers) librating molecules can be treated as harmonic torsional oscillators, we created a simple model for simulating the spectra. This model, based on the Franck-Condon principle, will allow us to extract relevant quantities of each studied system by fitting. That is, using a harmonic molecule-surface interaction potential $V(\phi)$, defined by the stiffness according to the electronic state (k_0 for ground state and k_1 for excited state) and moment of inertia J, we can determine the corresponding librational eigenenergies (ϵ_i^0, ϵ_i^1, respectively) and wave functions ψ_i^0, ψ_i^1 separately in the ground and excited state as a function of ψ, by solving numerically the stationary 1D Schrödinger equation

$$\left[V(\phi) - \frac{\hbar^2}{2J}\frac{\partial^2}{\partial\phi^2}\right]\psi_i(\phi) = \epsilon_i\psi_i(\phi). \tag{8.1}$$

For the description of exciton-libron coupling we employ the Franck-Condon principle in analogy with the description of vertical vibronic transitions between excited and ground states in molecular systems (see Fig. 8.3a,b). Accordingly, the

intensity I_{mn} of an emission peak associated with the decay from the electronically excited librational state m (ψ_m^1) to the electronic ground librational state n (ψ_n^0) can be approximated as:

$$I_{mn} \propto \mu^2 \omega_m \langle \psi_m^1 | \psi_n^0 \rangle^2, \tag{8.2}$$

where μ is the electronic transition dipole moment between the ground and excited electronic states, and $\langle \psi_m^1 | \psi_n^0 \rangle^2$ is the squared modulus of the overlap integral between the wave functions ψ of librational states, i.e. the Franck-Condon factors. ω_m describes the probability of the system to be in the initial state m of energy ϵ_m^1 at the moment of emission, and we model it by an exponential distribution, using an effective temperature T_{eff} of the system:

$$\omega_m = \frac{1}{Z} \exp(-\epsilon_m^1 / (k_B T_{\text{eff}})), \tag{8.3}$$

where k_B is the Boltzmann constant and $Z = \sum_i \exp(-\epsilon_m^1/(k_B T_{\text{eff}}))$ is the partition function, whose sum runs over all libronic states i.

Next, we simulate the emission spectrum as the sum of all emission lines (up to $m, n = 20$) with energy shifts $\epsilon_m^1 - \epsilon_n^0$ and intensity I_{mn}, convolved with a dressing Gaussian (Lorentzian for H_2Pc^+, see Methods) function to account for the additional spectral broadening, with a parametrically imposed full width at half maximum (γ).

In order to yield an estimation of physically relevant values for each studied case we perform a qualitative comparison between the measured spectra and the spectra simulated with the harmonic model, using different combinations of the potential stiffnesses k_1, k_0 and the angular displacement $\Delta\phi_0$ (shown in Fig. F.5, for more details see Methods). Thus, for $\Delta\phi_0 \approx 0$ the simulation resembles the spectrum of H_2Pc^+, and for nonzero $\Delta\phi_0$ and a k_1/k_0 ratio above 1.10 approximates the spectra observable in the case of $ZnPc^+$ and $MgPc^+$. Although the envelope and energetic distribution of the simulated peaks are in close agreement with the experiments, the relative peak intensities for $ZnPc^+$, $MgPc^+$ cannot be perfectly reproduced for any combination of parameters using the initial state population probability defined in Eq. (8.3). In particular, the overall intensity of the central peaks (including the zero-phonon line with energy E_{00}) generated by the $m = n$ transitions is significantly lower than the one originating from $m - n = \pm 1$. We suggest that this can be caused by an efficient depopulation channel for the lowest energy libron mode of the system in the excited state (i.e. the upper parabola in Fig. 8.3a). To reflect this in the theoretical model we modified the distribution ω'_m in Eq. (8.3) by reducing the probability of the zero-level libron excited state, using a reducing factor $A < 1$ ($\omega'_0 = A \cdot \omega_0$) and fitted the experimental spectra (parameters optimized by fitting are summarized in Table 8.1).

H_2Pc represents a case in which the molecule does not undergo any change of the equilibrium angle upon the excitation due to the symmetrical adsorption geometry (Fig. 8.2d). As a result, the $m \neq n$ transitions are mostly forbidden, except for the ones with non-negligible Franck-Condon factors resulting from the change in the stiffness of the potential ($k_1/k_0 \neq 1$). Conversely, due to non-negligible $\Delta\phi_0$, fitting of the rich spectral features on $ZnPc^+$ and $MgPc^+$ allows a precise determination of the k_0, k_1, $\Delta\phi_0$ parameters (Fig. 8.3 c,d) which
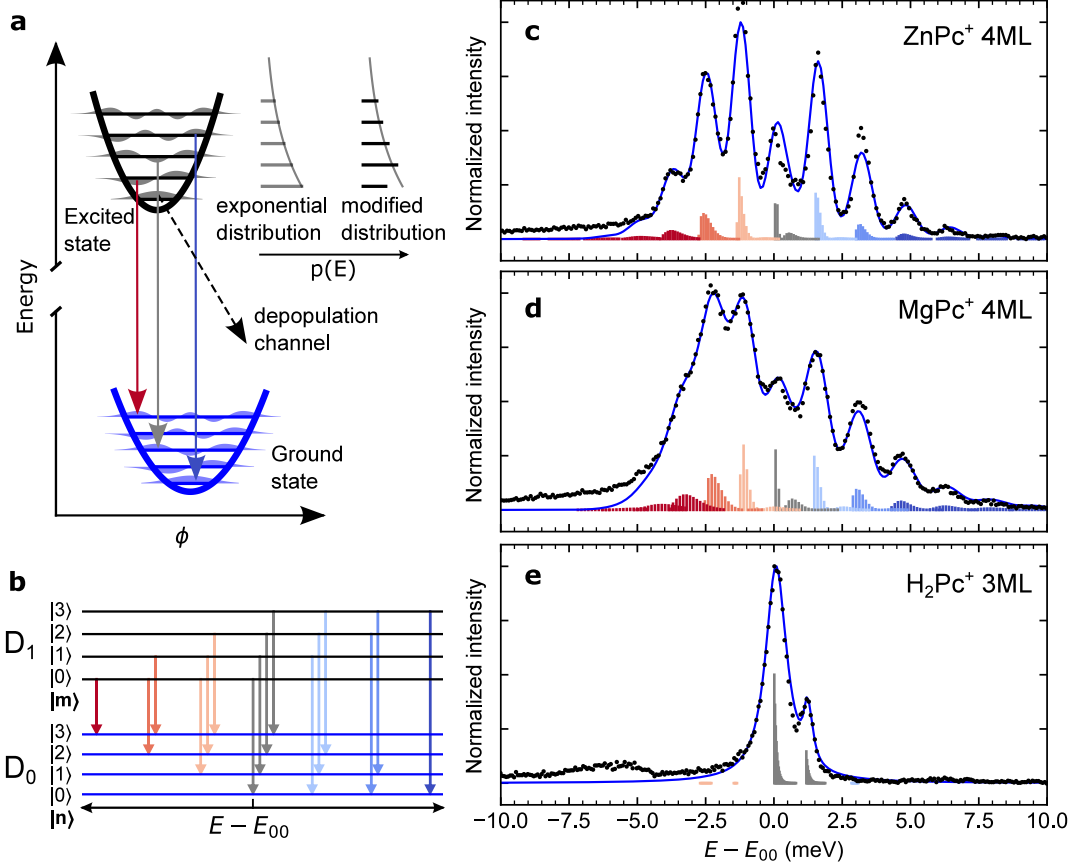
Figure 8.3: Scheme of the electron-libron coupling model and fitting of the spectra. a Scheme of the energy curves of ground and excited states illustrating the libronic vertical downward transitions. Excited-state population probability is considered as exponential distribution or modified exponential distribution with suppressed probability of $m = 0$ state. **b** Scheme of the lowest-energy libronic transitions coupled to the electronic $D_1 \rightarrow D_0$ transition with colours matching the peaks in the panels **c-e**. **c-e** Comparison of experimental (black dots) and simulated (solid blue line) STM-EL fine spectra of Q^+ peak of ZnPc$^+$ and MgPc$^+$ (**c,d**) and Q_{y1}^+ and Q_{y2}^+ of H$_2$Pc$^+$. Measurement parameters were -2.8 V, 50 pA in **c**; -3 V, 60 pA in **d**; -3 V, 100 pA in **e**. The Franck-Condon factors are calculated including the modified exponential distribution and are colour-coded according to the librational quantum number difference between the initial and final state, i.e. $m - n$ (red – negative, blue – positive, grey – null). The energies E_{00} obtained through the fitting are set as the reference in each spectrum. Parameters of the simulated spectra are listed in Table 8.1.

	k_0 (meV/(°)^2)	k_1 (meV/(°)^2)	$\Delta\phi_0$ (°)	T_{eff} (K)	A	γ (meV)	E_{00} (eV)
ZnPc$^+$ 4 ML	1.64	1.84	0.603	62	0.5	0.64	1.5186
MgPc$^+$ 4 ML	1.41	1.69	0.698	75	0.69	0.95	1.5147
H$_2$Pc$^+$ 3 ML (Q_{y1})	1.57*	1.63*	0.001	50*	1*	0.91	1.3938

Table 8.1: Parameters of the simulated spectra in Fig. 8.3c-e. Parameter values for H$_2$Pc$^+$ denoted by an asterisk (*) were fixed; k_0 and k_1 were taken from the TD-DFT simulations and A was set to unity. For fitting of the H$_2$Pc$^+$ spectrum minor component, three additional free parameters (not listed in the table) characterizing the emission peak Q_{y2}^+ of the second tautomer were used: relative intensity $I = 0.29$, FWHM of dressing function $\gamma_2 = 0.31$ meV and mutual energy separation of the tautomers $\Delta E_{00} = 1.17$ meV.

97

are in accord with the values estimated from the calculations (see Table F.2). The effective temperature above 50 K resulting from the fitting indicates that the excess energy of inelastic tunnelling electrons of a few eV can excite high librational states and create a transient initial state population above the zero-level libron state [255].

8.2.3 Nanocavity tuning of the initial zero-level libron state probability

In order to shed light on the mechanisms leading to the modulation of the peak around zero-phonon line in the spectra of the asymmetrically adsorbed molecules, we measure how it is affected by opening/closing the nanocavity. Since it is known [176] that the effective lifetime of the excitation in the phthalocyanines is reduced by the confinement of the optical density of states (Purcell factor), we are expecting a modulation of w_0' due to a variable radiative quenching by the nanocavity. The resulting dependence of the MgPc$^+$/4ML-NaCl spectra on the tip-sample distance is presented in Fig. 8.4a, along with the parameters $A(\Delta z)$, the $E_{00}(\Delta z)$ and the overall line broadening γ in Fig. 8.4b,c that we determined by fitting of each spectrum individually. At the first glance, a significant increase of the central peak intensity with decreasing tip-sample distance Δz is apparent; there is also an overall redshift of the entire spectra (decreasing E_{00}) and peak broadening (increasing γ). The latter two can be attributed to the known Lamb/Stark shift resulting from the coupling of the excited states to the nanocavity [77]. However, the striking variation of the central peak intensity, with factor A changing from 0.40 to 0.93, is indicating a possible suppression of the deexcitation channel due to the faster radiative rate induced by compressing the nanocavity. At the moment, the mechanism responsible for the decreasing intensity of the peak near the zero-phonon line in ZnPc$^+$ and MgPc$^+$ is not fully clear to us. Nonetheless, a competition between the radiative and nonradiative decay rates from the zero-vibration excited states to the vibrational ground state of the trion is a likely explanation for this phenomenon.

At this point, one may wonder if librational peak manifolds could be also observed for the neutral excitons of the molecules. Based on the theoretical calculations on neutral molecules (see Fig. F.6 and Table F.2), revealing very similar values of $\Delta\phi_0$, k_0 and k_1 as the cations (Fig. 8.2), we believe the manifolds are also present in the Q peak of neutral ZnPc and MgPc spectra, although indistinguishable due to a naturally broad energy character of the electroluminescence emission (see Fig. F.3). This might be overcome with a resonant STM-PL that already demonstrated its resolution capability on Q_x of H$_2$Pc/4ML NaCl (0.5 meV linewidth) [90].

To conclude, we found the link between the observation of libronic signatures in the electroluminescence spectra and the chiral adsorption geometry of chromophores on NaCl. The molecules with chirally asymmetric adsorption configurations (Zn-, MgPc$^+$) change the orientation upon excitation, which according to the Franck-Condon principle allows the transitions between different libration states. This gives rise to the observed manifolds of peaks in the spectra of chirally adsorbed chromophores. In contrast, in the reference system (H$_2$Pc$^+$) with a mirror-symmetrical adsorption geometry, the adsorption orientation re-
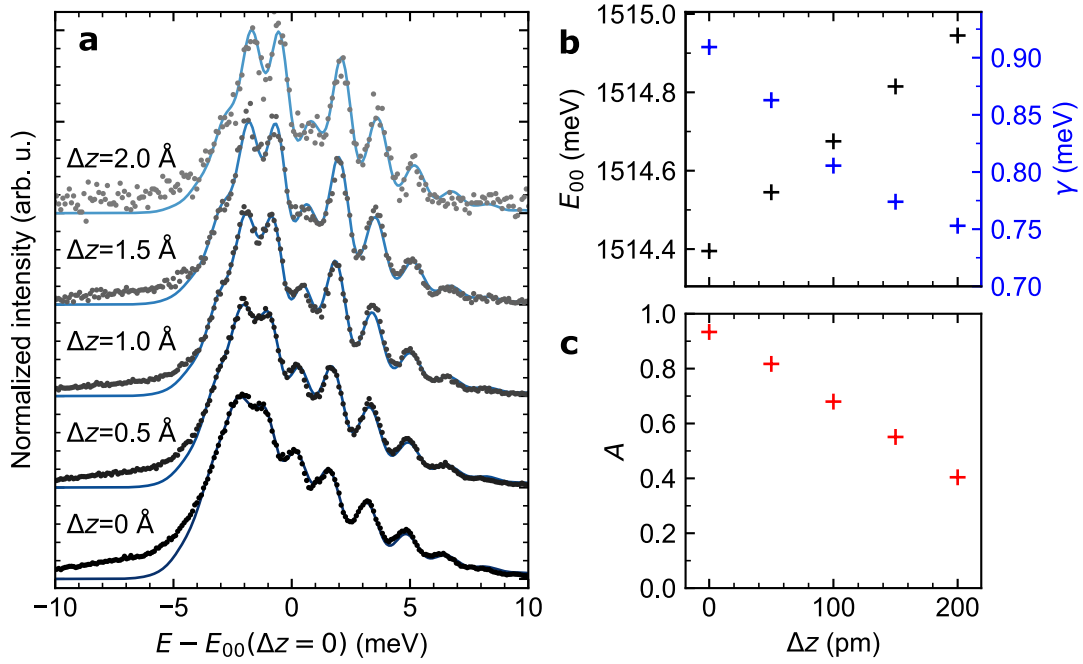
Figure 8.4: Evolution of libronic fingerprints with the gap size. a Experimental (black dots) and simulated (solid blue lines) STM-EL fine spectra of Q^+ peak of MgPc$^+$ as a function of increasing tip-sample separation by Δz. $U = -3$ V, I ranges from 113 pA (bottom spectrum) to 19 pA (top spectrum). Acquisition time was 120 s for $\Delta z= 0$, 0.5, 1 Å and 360 s for $\Delta z = 1.5$ and 2 Å. **b, c** The energy E_{00}, linewidth γ and reducing factor A as a function of Δz obtained from the fitting procedure of data in **a**. Average values of fitting parameters: $k_0 = (1.42 \pm 0.01)$ meV/(°)^2, $k_1 = (1.69 \pm 0.04)$ meV/(°)^2, $\Delta\phi_0 = (0.69 \pm 0.03)$°, $T_{\text{eff}} = (82 \pm 10)$ K.

mains unchanged upon excitation and, therefore, librational sidebands are not arising. From the analysis of the experimental spectra, it follows that the process of excitation gives rise to a non-equilibrium initial libration states population, corroborating one of the previously suggested mechanisms [90] for the spectral broadening in STM-EL. Moreover, changes in the potential well stiffness of the libration, associated with the excitation, leads to an additional peak broadening. All these effects have to be considered for a correct interpretation of the STM-EL spectra of molecules in neutral and charged excited states. Finally, we have found experimental indication of a possible depopulation pathway predominantly affecting the zero-libration state of the trion. It can be effectively suppressed by overall increase of the radiative decay rate by closing the STM-EL nanocavity. We anticipate that the newly emerging methodology of STM-PL [90], enhanced with pump-probe capability could provide insight into the dynamics and physical origin of such deexcitation mechanism.

8.3 Methods

STML measurements

Overview and high-resolution photon spectra were obtained using gratings of 150 and 1200 grooves/mm and 100 μm wide slit, which provide spectral resolutions of 1.2 and 0.2 nm respectively corresponding to the best achievable energy resolution of 300, 400 and 600 μeV for H_2Pc Q_y^+, Q^+ and Q of Mg/ZnPc peaks respectively.

DFT and TD-DFT calculations

The single-molecule calculations were run on H_2Pc, ZnPc and MgPc in both their neutral and cationic state. The ground state molecular structure was optimized in vacuo with density functional method (DFT) and ωB97X-D/6-31G* level of theory [166]. The emission properties are obtained by optimization of the first (and second for H_2Pc) excited states with TD-ωB97X-D/6-31G* for neutral and TDA-ωB97X-D/6-31G* for cations [194]. To calculate the total energy as a function of the molecular adsorption orientation, the electrostatic field of NaCl surface has been modelled as a slab of 3 layers of 6×6 point charges (+1 for Na^+ and -1 for Cl^-) with fixed position, at 3 Å of distance with the molecular plane. The optimized structure in vacuo of the neutral or cation molecule has been employed (B3LYP/6-31G*) and all coordinates are kept fixed except for the azimuthal angle ϕ, varying between 0 and 45° (step of 1°) for ZnPc or MgPc, and between 0 and 90° (step of 5°) for H_2Pc. All calculations were performed with the Gaussian16 package [175].

Spectroscopic fitting procedure

We used an iterative fitting procedure (described below) to minimize the sum of absolute differences between the simulated spectra intensities and experimental data points, by optimization of the free parameters of the model, i.e. the vector $\boldsymbol{v} = (k_0, k_1, E_{00}, \Delta\phi_0, T_{\text{eff}}, A, \gamma)$. First, the Schrödinger equation in (8.1) is solved for the excited and ground state using the parameters k_0, k_1, $\Delta\phi_0$. In the next step, from the wave functions and energies, Franck-Condon factors are calculated

using the parameters Teff and A. The Franck-Condon factors are plotted in Fig. 8.3 as vertical bars at their corresponding energies. The entire spectrum is calculated by summing all Franck-Condon factors, each broadened by convolution with a broadening function of FWHM $= \gamma$. Finally, the spectrum energy range is offset by E_{00} and the simulated spectrum is resampled onto the experimental datapoint energy range. The normalized sum of absolute differences between the simulated and experimental intensity values, corresponding by energy (I_i^{sim} and I_i^{exp} respectively), called R-factor is calculated as

$$R = \frac{\sum_i |I_i^{\text{exp}} - cI_i^{\text{sim}}|}{\sum_i |I_i^{\text{exp}}|} \text{ , where } c = \frac{\sum_i |I_i^{\text{exp}}|}{\sum_i |I_i^{\text{sim}}|}. \tag{8.4}$$

The value of R describes the agreement ($R = 0$ – perfect match).

The iterative optimization procedure first calculates the $R(\boldsymbol{v}_0)$ for an initial guess of the parameters - vector $\boldsymbol{v}_0$. Subsequently, the parameters are repeatedly adjusted by introducing random adjustments ($\Delta\boldsymbol{v}$). For each $\Delta\boldsymbol{v}$ that generates improvement of the R-factor such that $R(\boldsymbol{v}_j) < R(\boldsymbol{v}_{j-1})$ (index j being the number of iteration), the change in the vector is retained, i.e. $\boldsymbol{v}_j = \boldsymbol{v}_{j-1} + \Delta\boldsymbol{v}$, otherwise $\boldsymbol{v}_j = \boldsymbol{v}_{j-1}$ is used. After several thousand iterations (n) we plot the simulated spectrum for $\boldsymbol{v}_n$. The initial parameters ($\boldsymbol{v}_0$) were chosen from the calculations (k_0, k_1, $\Delta\phi_0$) or from initial guesses based on the typology of spectra for different parameters shown in Fig. F.5. To avoid underdetermination of the fit of H_2Pc^+ and to account for its tautomerization-related dual-peak structure, we fixed parameters k_0, k_1, T_{eff} and A as described in the caption of Table 8.1 and fitted simultaneously the Q_{y1}^+ and Q_{y2}^+ peaks, using independent center energies $E_{00}(Q_{y1}^+)$ and $E_{00}(Q_{y2}^+)$, broadening factors γ_1 and γ_2 and with a common $\Delta\phi_0$. The z-axis moment of inertia of the molecules was calculated from the ground state cation optimized structure (B3LYP/6-31G*). The resulting J_z values are 113.7 $m_p$nm^2 for ZnPc$^+$, 114.3 $m_p$nm^2 for MgPc$^+$ and 113.2 $m_p$nm^2 for H_2Pc^+, where m_p is the proton mass. Spectrum of ZnPc$^+$ molecule (Fig. 8.3c) was fitted in the energy range ($E_{00} - 5$ meV, $E_{00} + 10$ meV) and spectra of MgPc$^+$ molecules (Fig. 8.3d, Fig. 8.4a) were fitted in the energy range ($E_{00} - 4$ meV, $E_{00} + 10$ meV). The spectrum of H_2Pc^+ (Fig. 8.3e) was fitted in the range ($E_{00} \pm 4$ meV). (Gaussian for Zn- and MgPc$^+$, Lorentzian for H_2Pc^+). The fitting code with an example file is provided in ref. [256].

Conclusion

During my PhD, I had the opportunity to explore the luminescence of single molecules with a state-of-the-art instrument in nanoscience – the low-temperature UHV SPM microscope. Being at the forefront of a rapidly developing field which has been mastered by less than ten experimental groups worldwide is a dream for a curious physicist. There were a lot of questions at the beginning of fundamental nature. Tackling some of them resulted in a better understanding of the phenomena commonly observed by the community and inevitably generated a plethora of others. My best understanding of STM-induced luminescence, which has been shaped by the literature research, our own experiments, stimulating discussions in the scientific community and peer reviews in journals is summarised in chapter 1. The experimental aspects of this work are summarized in chapter 2. In particular, I focused on giving a clear message to the reader about how the experiments can be performed. Although this "know-how" is often preserved only within the research groups, I find this important for creating good standards in science and making our experimental results more reproducible and credible.

We have proven in chapter 3 that tip functionalization with a CO-molecule, a key ingredient for submolecular resolved AFM, is suitable for utilisation in STM-EL measurements. However, it turned out that the enhanced contrast in photon maps of ZnPc originates mainly from the highly localized tunneling current between the CO and ZnPc orbitals. Photoluminescence excitation might overcome this problem and reveal the role of the CO on the picocavity field enhancement. Moreover, CO-functionalization offers great advantages to the TERS methodology, where the vibrational Stark shift of the CO stretching mode can be detected [114, 122]. This allows for obtaining not only the map of the Raman modes in the molecule but also information about the electric field distribution. In combination with AFM, this can provide a very powerful multichannel spectromicroscopy.

We have further shown the different work functions of the Ag(111) and Au(111) substrates change the alignment of the molecular orbitals with respect to the substrate Fermi level. As a result, various transient charge states and their electroluminescence fingerprints can be observed at different bias polarities. This concept was later used in the thesis in chapter 7 for observation of the second excited state of the PTCDA anion. The substrate work function is therefore a well-defined tuning parameter in the study of fundamental processes such as the excitation mechanism in single molecule emitters in nanocavity.

The study of how the NaCl environment influences the exciton energy is presented in chapter 4. The CuPc molecule can be reproducibly switched between two stable adsorption configurations by tip manipulations permitting precise positioning of the molecule on the NaCl ionic crystal lattice. The molecule centered either on Na^+ or Cl^- ion changes its electronic and optical bandgaps and the exciton binding energy by tens of meV. With the help of TD-DFT theory, we explain this effect by spatially dependent Coulomb interaction occurring at the molecule-insulator interface, which tunes the local dielectric environment of the emitter in analogy to solvatochromic effects known from molecular fluorescence in solutions.

In chapter 5 we have chosen a system of ZnPc/3 ML NaCl/Ag(111) where

both exciton and trion peaks are observed at negative bias voltages. We mapped the exciton and trion emission in real space and explained the photon maps as the probability of exciton and trion formation superimposed on the "expected" photon map image [71]. The proposed RF-PS fluorometry method likely does not have the resolution to measure the intrinsic lifetime of the excited molecular state in the nanocavity with the expected sub-ps to ps range as explained in the comment in chapter 5. Nevertheless, it can bring insights into the excitation mechanism and provide rates of electron tunneling through NaCl layer [38]. The measurement of the real lifetimes of the excited states in nanocavity remains elusive. To some extent, their estimate can be obtained from the emission linewidth measured with the resonant photoluminescence [90, 96], where no excess energy permitting the broadening by $n - n$ vibronic transitions [90] as well as homogeneous broadening by heating the system is present. Pump-probe optical spectroscopy [102] with fs short pulses might be suitable to measure the lifetimes directly if they can be detected, e.g. by the change of the tunneling current when varying the pump-probe delay-time.

The calibration method for measuring the amplitude of RF-bias modulation in tunneling junction is presented in chapter 6. This is a key prerequisite of electron paramagnetic or stochastic resonance in STM [7, 257]. This direct optical method is based on the broadening of the plasmon energy cutoff of the photons observed in electroluminescence. We managed to calculate the transfer function in the GHz range of our RF line terminated with an antenna capacitively coupled to the tip wire. This paves the way for future experiments in coherent control of quantum states in our STM with the possibility of optical writing and readout.

In chapter 7 we have shown the entanglement of single excitonic states in molecular aggregates of PTCDA anion molecules. We took advantage of the self-assembly process during sample annealing up to 150 K. We implemented the model for the photon map simulation proposed in ref. [71] in the probe-particle model [50]. The comparison of simulated photon maps of the aggregates based on the TD-DFT calculations shows a perfect agreement with the hyperspectral mapping and revealed the involvement of the transverse second excited state within perpendicular aggregates. We used the electric field of the tip to control the total charge state of the PTCDA trimer, which showed up in the photon map contrast. Our experiment provides a platform for the future study of e.g. dark and bright excitonic states, topological excitons or exciton-phonon coupling.

Finally, in chapter 8 we have investigated the exciton lineshape of phthalocyanines. The 10 meV linewidth of neutral exciton observed in STML has been previously attributed mainly to the coupling with the NCP [86]. However, the trion linewidth can be one order of magnitude narrower as shown in chapter 7 and ref. [94]. This facilitated the observation of a comblike manifold in trion Q^+ lineshape of molecules which are chirally adsorbed on NaCl. On a mirror-symmetrically adsorbed H_2Pc molecule, the trion peak is narrow and featureless. We attributed the observed spectral features of chirally adsorbed phthalocyanines to the coupling of quantized librational states to the exciton. We create a model of the libronic coupling based on the Franck-Condon principle to simulate the spectral features. Experimentally measured librational spectra match very well the theoretically calculated librational eigenenergies and peak intensities (Franck-Condon factors). However, the observed depopulation of the zeroth librational

excited state which can be tuned by the nanocavity remains an unexplained phenomenon.

I expect new methodologies such as STM-PL and TERS will provide access to various novel model systems such as transition metal dichalcogenides or molecules on thicker insulating NaCl layers where tunneling is suppressed. Photoexcitation has the potential of performing plasmon-induced chemical reactions [258] and the AFM and TERS have great abilities to characterize the products. It can be also used for both nm-resolved near-field and μm resolved far-field spectroscopies on the same system in STML. Another standing question is whether the strong-coupling regime [78] can be realized in the STM junction. For that, the vertical orientation of a molecular dipole would be probably necessary, likely with a better-defined tip geometry obtained e.g. by ion milling [118] or lithography.
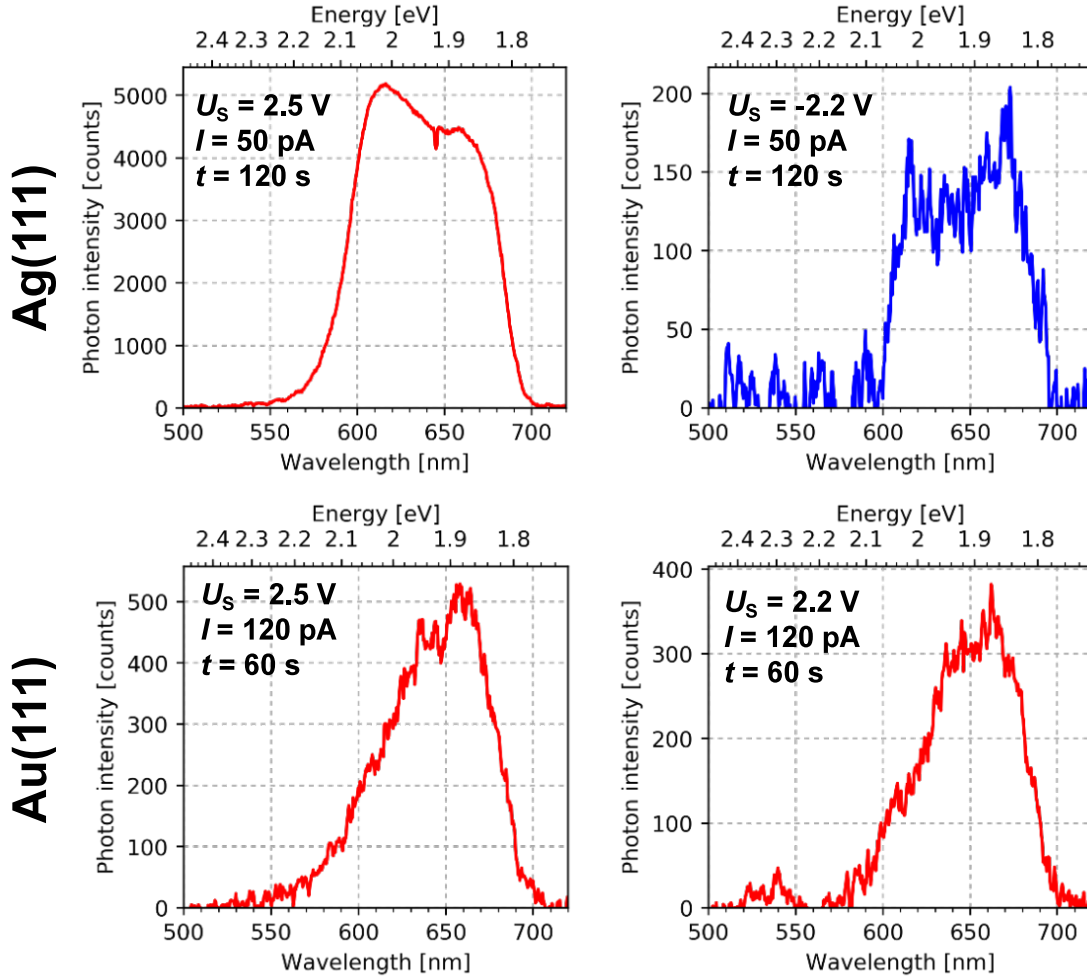
A. Supplementary Information for chapter 3

Figure A.1: Plasmonic spectra of the tips used in the experiments. Typical STML spectra recorded prior to taking the STML photon maps on 3ML-NaCl/substrate on both 3ML-NaCl/Au(111), showing the plasmonic electroluminescence of the tips used in the measurements, presented in the main text. In all cases it was ensured that this plasmonic emission spectrally overlaps with the excitonic line of the ZnPc, for an efficient near-to-far-field coupling, such that they reach maximum around the excitonic line of the neutral ZnPc. The tunneling conditions and integration times are specified in the respective panels. The data are presented as they are, i.e. without any smoothing or filtering.
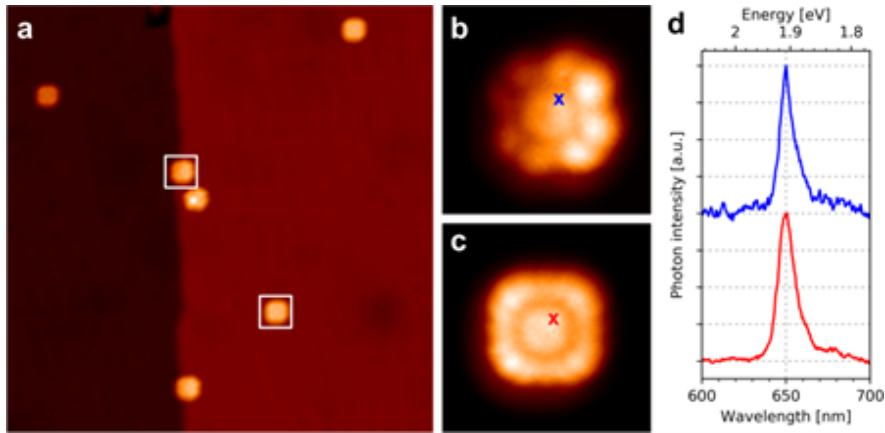
Figure A.2: Overview of the area showing the locations of measured molecules and their STML spectra.a) STM constant-current overview of the area with the stable and dynamic ZnPc/3ML-NaCl/Au(111) molecules used for electroluminescence mapping (marked by white squares). Size $50 \times 50 \, \text{nm}^2$, setpoint 2.2 V, 3 pA. b,c) STM constant-current details of the stable and dynamic molecule, size $3.6 \times 3.6 \, \text{nm}^2$, setpoint 2.2 V, 1 pA. d) Electroluminescence spectra for the stable (blue) and dynamic (red) ZnPc, taken at positions marked in b) and c), at setpoint 2.2 V.
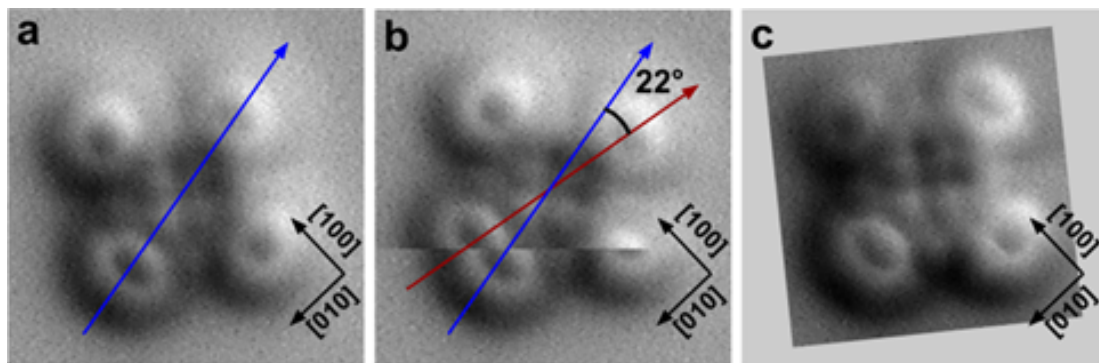

Figure A.3: Analysis of rotational angles of ZnPc molecule from frequency shift maps taken at constant height. a) first and b) second metastable position of the molecule in its rotational state. c) image of a molecule stabilized at a step edge. The blue and red arrows denote orientations of the molecules for comparison. Black arrows mark the directions of principal axes of the NaCl(001) substrate, transferred from STM images. All images are presented at the same scale $2.2 \times 2.2 \, \text{nm}^2$, including the padding in c).
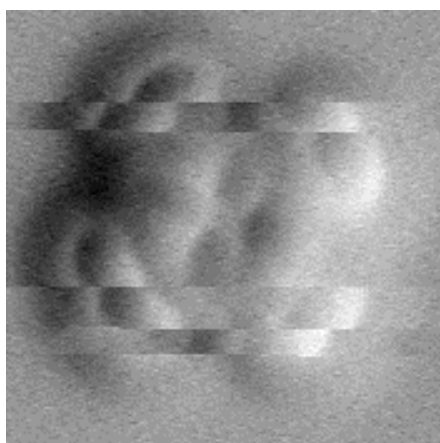
Figure A.4: AFM constant-height image of a dynamically switching molecule. The peripheral benzene rings maintain the same distance from the center of the molecule after rotation, which demonstrates that the molecule does not move laterally while switching. Size of the image is $2.2 \times 2.2 \, \text{nm}^2$, bias 25 mV.
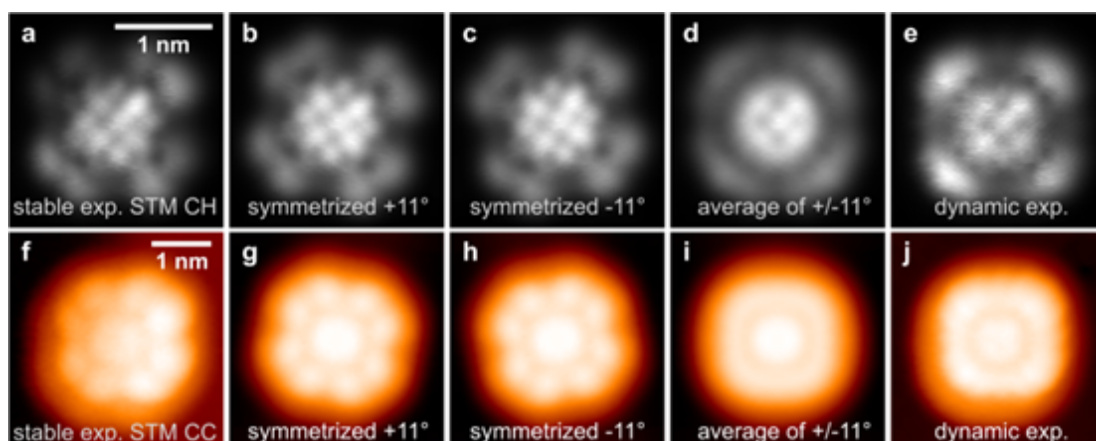

Figure A.5: Test of correspondence between STM contrasts of a dynamic molecule, and a composed image derived from averaging data of a stable molecule rotated computationally. a) The original constant height current map of a stable molecule. b) ideal image of a stable molecule, symmetrized by averaging vertically and horizontally flipped original images in a) and rotated +11°. c) symmetrized image b) rotated -11°. d) an average of b) and c). e) the original constant height current map of a dynamic molecule. Physical size of images a)-e) are $2.2 \times 2.2 \, \text{nm}^2$. f) The original constant current image of a stable molecule. g) ideal image of a stable molecule, symmetrized by averaging vertically and horizontally flipped original images in f) and rotated +11°. h) symmetrized image g) rotated -11°. i) average of g) and h). j) the original constant current image of a dynamic molecule. Physical size of images f)–j) are $3.6 \times 3.6 \, \text{nm}^2$. All the 2D transformations and averaging have been performed in the GNU Data Language program.
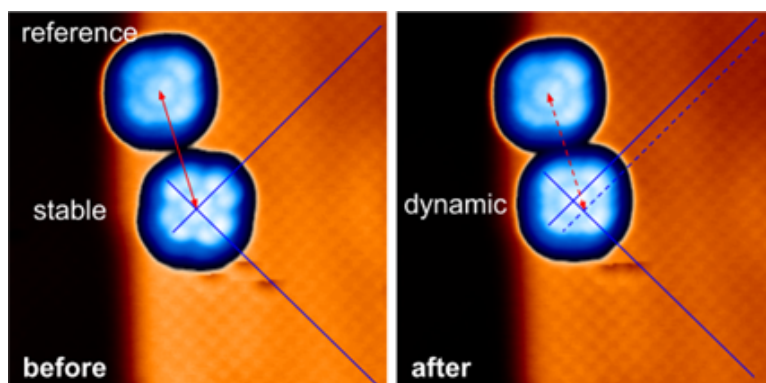
Figure A.6: Example of unpinning of a stable ZnPc/3ML-NaCl/Au(111), starting in one of the rotational orientations. Blue solid lines denote the registry of the molecule center above the Cl-sites and red arrow marks the relative position with respect to a reference dynamic ZnPc. Blue dashed line and dashed arrow show the registry and relative position as it was before the manipulation. The lateral movement of the molecule corresponds to one unit vector of NaCl(001). Dark streaks in the lower part of the image are CO molecules, moved by the tip in the process of scanning. A composite color scale is used to enhance the contrast of the substrate.
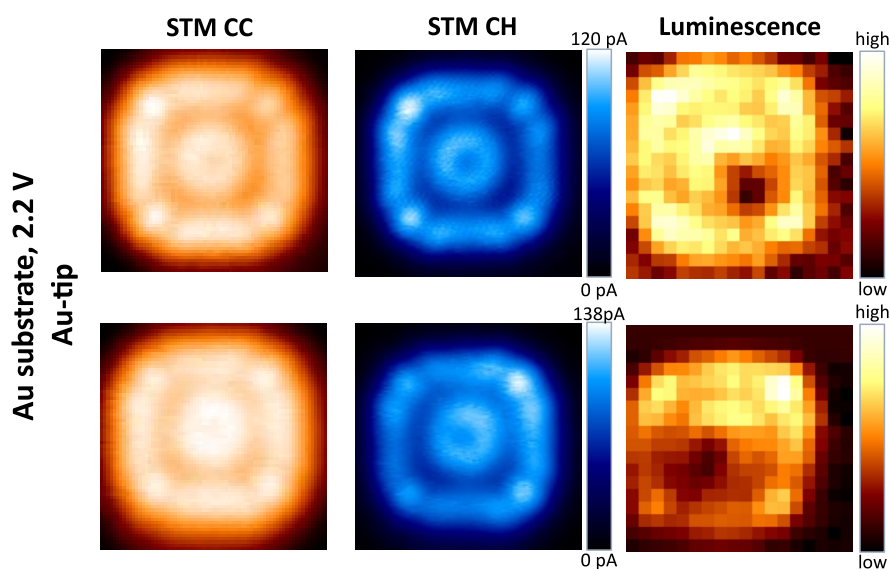
Figure A.7: Tip state and position of the intensity minimum in the photon maps. ZnPc/3ML-NaCl/Au(111) STM CC, STM CC and luminescence CH maps with two different Au tips, measured at 2.2 V. The luminescence maps show pronounced dips in two distinct positions near the center of the molecule. The position of the intensity dip in the photon maps is tip-dependent. The measurements have been taken in two separate sessions, each after a new tip preparation by nanoindentation. A very likely explanation for the variation of the dip position is a strong dependence of the plasmonic coupling of the tip to the molecular emitter on the mesoscopic shape of the tip as implied by other works [135, 71]
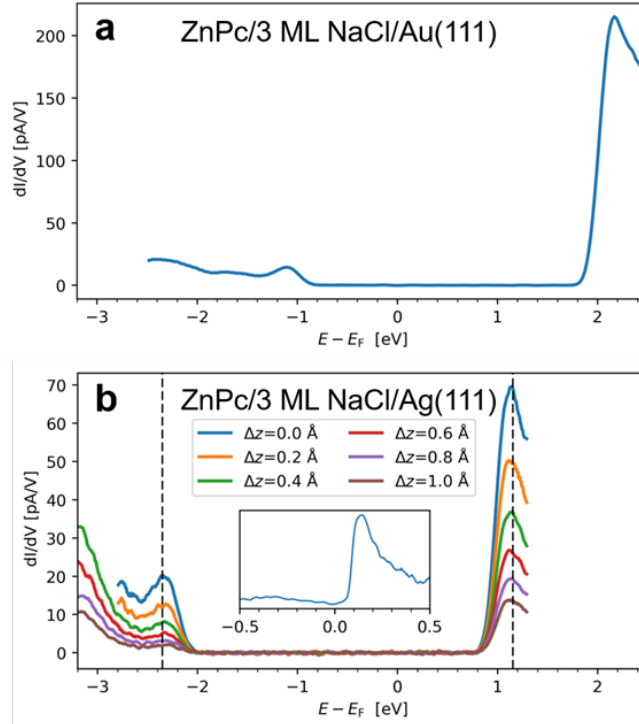
Figure A.8: Differential conductance spectra for ZnPc on the two substrates. a) dI/dV spectrum of ZnPc/3ML-NaCl/Au(111) measured at the molecule lobe. The setpoint was -2.5 V and 200 pA. b) dI/dV spectrum of ZnPc/3ML-NaCl/Ag(111) measured at the molecule lobe as a function of Δz setpoint change, demonstrating a negligible voltage drop effect across the 3ML-NaCl on the HOMO/LUMO energy. The reference $\Delta z = 0$ was set at 1.3 V, 25 pA. The inset shows a detail dI/dV of the interface state near to the Fermi level, detectable at the $\Delta z = -2$ Å (interface state is not changed on the molecule). Dashed lines in mark the positions of HOMO and LUMO.

B. Supplementary Information for chapter 4

B.1 AFM simulations of NaCl and adsorbed CuPc molecule.
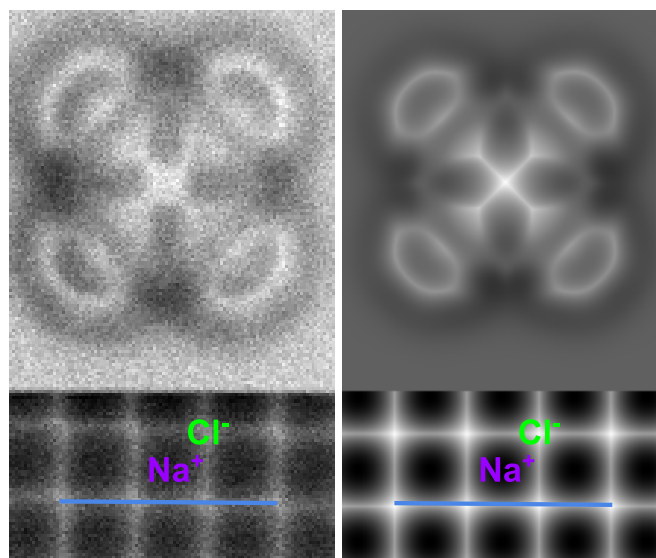
Figure B.1: Comparison of the AFM frequency shift: experimental data (left) and theoretical simulation (right) of CuPc on 2 ML - NaCl in the steady configuration, scanned with a CO-functionalized tip. The images of the NaCl lattice (bottom parts) are obtained with 300 pm smaller tip-sample distance with respect to the CuPc region. The image sizes are 1.70×2.95 nm^2. Bars (light blue) of 3 NaCl unit cell lengths are added for size comparison. Simulated AFM images were obtained using the ProbeParticle code [259, 21], which takes into account the van der Waals (vdW) and the electrostatic interactions between the surface and the CO tip. All the simulations were done with a charge scaling of $-0.5 \; e^-$ a lateral stiffness of 0.25 N/m. The Hartree potential calculated from the DFT calculations was used to obtain the electrostatic forces.

B.2 AFM images of the steady and dynamic configurations.
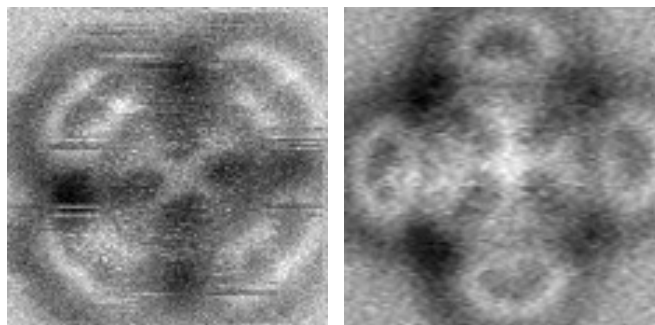
Figure B.2: Comparison of the AFM images of the dynamic (left) and steady (right) states on 2 ML of NaCl on Ag(111), scanned with a CO-functionalized tip. In the dynamic image the fast rotational switching of the CuPc leads to a double appearance of the peripheral benzene rings, as a result of temporal averaging of the AFM signal. The fourfold symmetry of the dynamic configuration indicates that the molecule stays on the same Cl$^-$ ion after its rotation. Image parameters: 1.6×1.6nm^2, $\Delta f_{\min} = -9.5$ Hz, $\Delta f_{\max} = 2.6$ Hz, 5 mV setpoint.

B.3 Statistical analysis of the exciton switching on 2 ML and 3 ML of NaCl.
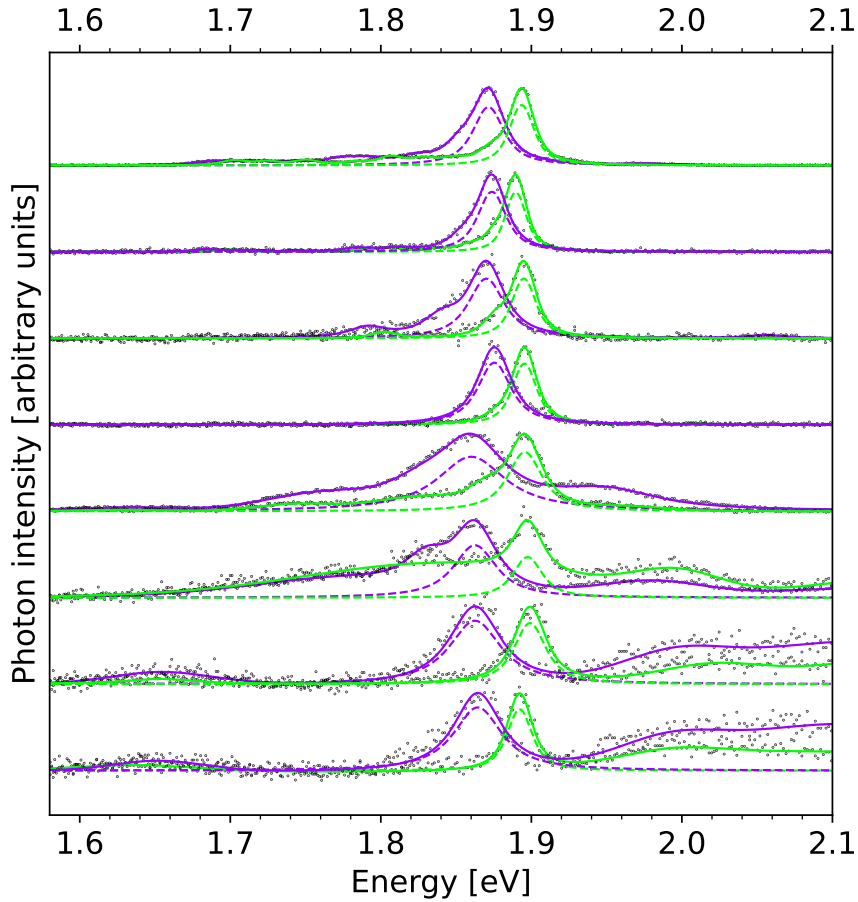
Figure B.3: Overview and fit of STML spectra obtained on CuPc molecules before (green) and after stabilization (violet). Spectra are normalized to their maxima. Main fitted components corresponding to the $D_1 \rightarrow D_0$ transitions (dashed lines) are rescaled to 80% of their original amplitude for clarity. The measurements were performed for 4 molecules on 2 ML - NaCl (lower half of the plot) and for 4 molecules on 3 ML (upper half of the plot). For fitting of all excitonic components, pseudo Voigt profiles were used with a gaussian full width at half maximum fixed to 10 meV, equivalent to 3.5 nm spectral resolution at 650 nm (1.907 eV). Spectra were fitted using the program KolXPD.[260]

		Steady CuPc		Dynamic CuPc		Difference	Avg. broad.	
		$E_{\mathrm{OPT}}^{\mathrm{Na}}$[eV]	$f_{\mathrm{L}}^{\mathrm{Na}}$[meV]	$E_{\mathrm{OPT}}^{\mathrm{Cl}}$[eV]	$f_{\mathrm{L}}^{\mathrm{Cl}}$[meV]	[meV]	$f_{\mathrm{L}}^{\mathrm{Na}}/f_{\mathrm{L}}^{\mathrm{Cl}}$	%
3ML NaCl	average	1.873	20.0	1.893	13.1	20.6	1.63	63
	st. dev.	0.002	2.6	0.002	1.5	3.4	-	-
	max	1.876	24.0	1.895	14.1	25.0	1.74	74
	min	1.870	16.4	1.890	10.4	15.6	1.42	42
2ML NaCl	average	1.862	38.4	1.896	19.4	34.0	2.03	103
	st. dev.	0.002	8.7	0.003	3.3	3.5	-	-
	max	1.864	52.0	1.899	23.6	37.0	2.41	141
	min	1.860	28.0	1.892	14.5	28.0	1.67	67

Table B.1: Fitting and statistical parameters of optical spectra acquired on the steady and dynamic configurations of CuPc on 2 ML and 3 ML - NaCl. The parameters $E_{\mathrm{OPT}}^{\mathrm{Na,Cl}}$ and f_{L} denote the energy position of the line and the full width at half maximum of the Lorentzian component of the Voigt profile used for the fitting, respectively. Difference is defined as $E_{\mathrm{OPT}}^{\mathrm{Cl}} - E_{\mathrm{OPT}}^{\mathrm{Na}}$.

B.4 Switching steady and dynamic state.
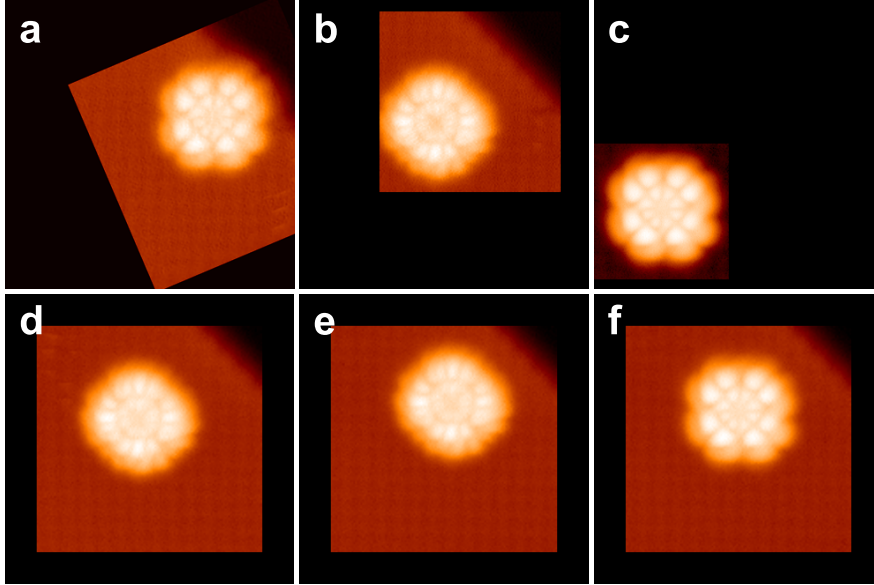
Figure B.4: (a-f) Series of constant current STM images taken with a CO-tip (-2.6 V, 1 pA) showing the same CuPc molecule on a 3 ML - NaCl island being switched back and forth between dynamic and steady states by atomic scale voltage-induced and lateral-force manipulation. Translation, scale and rotation are applied to each image to achieve a correct position in a common reference frame of $77\,\mathrm{nm}^2$, according to their recorded scanning parameters.

B.5 Kelvin probe measurement on steady and dynamic states.
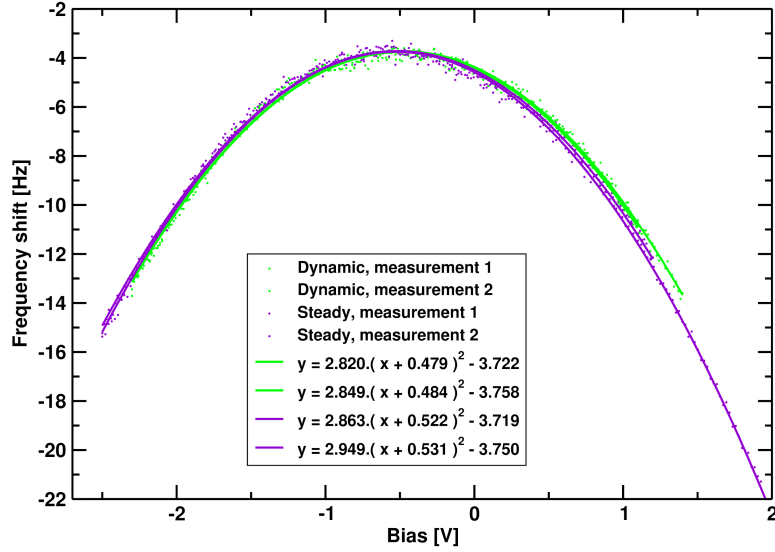
Figure B.5: Kelvin probe measurements on the CuPc / 3 ML - NaCl, switched from dynamic to steady configurations, taken at the molecular lobe position. The data were evaluated using a parabolic fit. The local potential difference on the steady configuration is shifted by -45 meV with respect to the dynamic configuration.

B.6 Theoretical stability of steady and dynamic states.

CuPc orientation to NaCl[100]	on top of Na^+ [eV]	on top of Cl^- [eV]
0°	0.58	0.09
15°	0.49	0.11 (rotates to 9°)
30°	rotates toward 45°	rotates toward 15°
45°	0.000	0.46

Table B.2: Comparison of the total energy offsets, calculated for various adsorption configurations of CuPc on 2 ML - NaCl(100). The steady configuration (on top of the Na ion, 45° with respect to the [100] NaCl axis) with the minimum total energy is taken as a reference.

B.7   2D representation of the Hartree potential for the dynamic and steady states.

Figure B.6: Calculated Hartree potential of CuPc on NaCl for the steady and dynamic configurations (metal core on Na and Cl atoms respectively) obtained from the DFT calculations, projected onto the isosurface of constant total charge density 0.025 $e^-/\text{Å}^3$. Low potential values correspond to blue color and high potential values to red color, respectively. Minimum and maximum values are identical for both panels. The Hartree potentials reveal intramolecular charge transfer between the pyrrole rings and imine nitrogens.
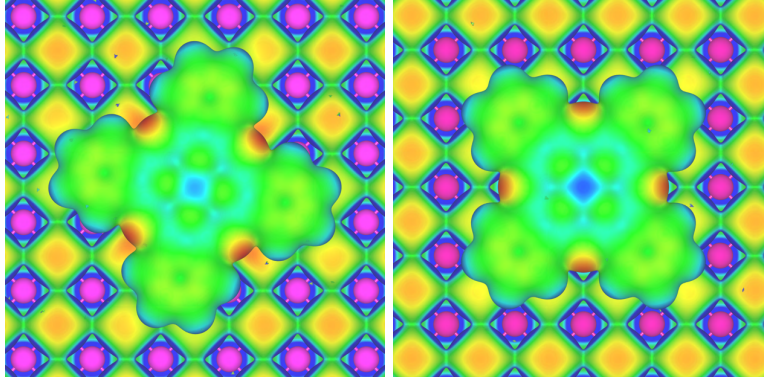
B.8   Exciton energy calculations

method	configuration	unrelaxed transition			geometrically optimized		
		spin up ($\uparrow$)	spin down ($\downarrow$)	$E_{\text{OPT}}\downarrow$-$E_{\text{OPT}}\uparrow$	spin up ($\uparrow$)	spin down ($\downarrow$)	$E_{\text{OPT}}\downarrow$-$E_{\text{OPT}}\uparrow$
LC-ωHPBE	isolated	1.968	2.009	0.041	1.693	1.734	0.041
wB97XD	isolated	1.823	1.86	0.037	1.65	1.686	0.036
LC-ωHPBE	*on Na*	1.961	2.002	0.041	-	-	-
	on Cl	1.983	2.024	0.041	-	-	-
	$E_{\text{OPT}}^{\text{Cl}}$ - $E_{\text{OPT}}^{\text{Na}}$	**0.022**	**0.022**				
wB97XD	*on Na*	1.811	1.848	0.037	-	-	-
	on Cl	*1.855**	1.864	0.009*	-	-	-
	$E_{\text{OPT}}^{\text{Cl}}$ - $E_{\text{OPT}}^{\text{Na}}$	0.044*	**0.022**				

Table B.3: Summary of the unrelaxed and geometrically optimized exciton energies for the isolated CuPc and CuPc subjected to the field of 2 ML - NaCl, represented by point charges, with geometries corresponding to the steady and dynamic configurations. The indices of the exciton energies (E_{OPT}) denote the adsorption site/configuration (Na - steady, Cl - dynamic). The arrows mark the spin subsystem in which the electron has been transferred from HOMO to LUMO. The energies marked by an asterisk (*) were obtained from the last step before the simulated system relaxed to its ground-state (D_0) orbital occupancy, due to instability of the wB97XD simulation method in the case of the dynamic configuration, with excitation within the spin-up subsystem. The differences $E_{\text{OPT}}\downarrow$-$E_{\text{OPT}}\uparrow$ are given to demonstrate independence of the result among the used methods and configurations, which allows a reliable estimate of the difference in the exciton energies $E_{\text{OPT}}^{\text{Cl}}$ - $E_{\text{OPT}}^{\text{Na}}$. All energies are given in eV.

C. Supplementary Information for chapter 5

C.1   Relation of the phase shift and delay

The base concept of the RF-PS method is a harmonically-modulated electrical driving of the system with frequency f and detection of the variation in photon output [261]. The electroluminescent response, i.e. the decay rate of the excitons formed as a result of the electric field, will follow this driving, however, its finite lifetime will cause a phase shift $\Delta\phi$ with respect to the phase of the driving signal. Given that the probability of finding the system in the excited state at time t after excitation decreases *monoexponentially* following the expression $\exp(-t/\tau)$, where τ is the intrinsic lifetime characteristic of the exciton, it can be shown that the relation of $\Delta\phi$ and τ is

$$\tan(\Delta\phi) = 2\pi f\tau. \tag{C.1}$$

This implies that for optimum detection of the lifetime, the corresponding $\Delta\phi$ has to be well below $\pi/2$ (to avoid divergence of the tangent function and excessive attenuation of the output) but at the same time sufficiently high to allow precise-enough detection. This can be ensured by setting an adequate value of f. From the simulated $\Delta\phi$ dependence on f and τ in Fig. C.1, we can see that for example $f = 200$ MHz is suitable for a lifetime range of 70–1200 ps and $f = 50$ for the range of 0.250–5 ns.
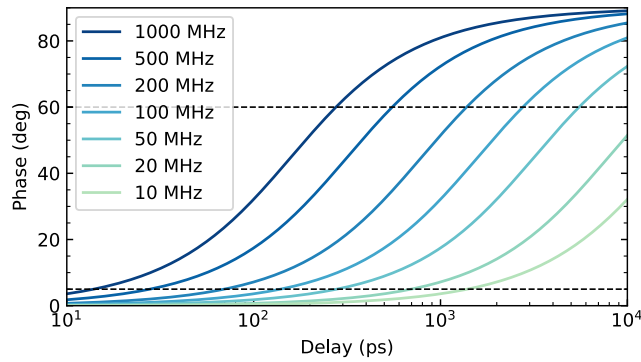
Figure C.1: Simulation of phase shifts dependence on lifetime-related electroluminescent response delay of a system for different voltage modulation frequencies.

C.2   Determination of the phase shift, amplitude and error bars of the RF-PS waves

The periodic photon arrival time histograms (waves) are represented as N couples of discrete bin time tag and photon counts (t_i, c_i). The absolute phase of each wave has been determined as

$$\phi = \arctan\left(\frac{\sum_{i=1}^{N} c_i \sin(2\pi f t_i)}{\sum_{i=1}^{N} c_i \cos(2\pi f t_i)}\right) \tag{C.2}$$

and the amplitude A as

$$A^2 = [\sum_{i=1}^{N} c_i \sin(2\pi f t_i)]^2 + [\sum_{i=1}^{N} c_i \cos(2\pi f t_i)]^2. \qquad \text{(C.3)}$$

For representation in the graphs, the measured waves (ten periods) have been folded in a single period by performing a modulo operation on the t_i values, obtaining $(t_i \bmod 1/f, c_i)$. We should note that the ϕ changes by π upon changing the offset bias polarity at the tunneling junction.

If we assume the noise in the data is white and neglect any quantization noise in the waves, the variance of the phase and amplitude determination scales with by the standard deviation σ and N as $\sigma^2 \frac{2}{N}$. Value of σ is calculated as the difference of the wave and its idealized form

$$\sigma^2 = \frac{1}{N-1} \sum_{i=1}^{N} [c_i - \langle c_i \rangle - A \sin(2\pi f t_i + \phi)]. \qquad \text{(C.4)}$$

Higher and lower error bars of the τ are then obtained in a standard way by combining the Eqs. (C.2) and (C.4) and considering that $\Delta\phi = \phi - \phi_{\text{ref}}$ where ϕ_{ref} is the reference phase measured using plasmonic emission. It is important to note that the effect of detector jitter leads to temporal smearing of the signal and a decrease of A, however, these effects are very mild if jitter is well below the $1/f$, which is the case in our experiments. Therefore σ can be significantly lower than the jitter.

C.3   Measurement of the reference phase

Impedance of the instrumental wiring causes a significant change of the modulation phase and amplitude reaching the junction with respect to the input from the radio frequency generator. The reference phase at the junction can be measured with a high precision using the plasmonic emission from the picocavity formed between tip and substrate. The same setup and tip conditions are used right after for measuring the phase-shift (and lifetime) of the modulated light of excitonic origin. Plasmon lifetimes are typically in the fs range, resulting in a negligible shift in comparison to excitons, making it therefore an ideal calibration measurement of the absolute radio-frequency phase reaching the cavity. Nevertheless, the speed of light propagation through the optical system (mostly through the fibers) is influenced by wavelength-dependent refraction index, which can result in a difference of up to 150 ps between the time-of-flight of photons at 650 and 825 nm using a 2 m fiber leading to the APD. The reference phases for the $f = 200$ MHz used in the experiments were therefore determined for X and X^+ wavelengths independently, taking advantage of the broad nature of the plasmon spectrum and using exclusively the plasmonic photons filtered by the same filters that have been used for measurements of the neutral exciton and trion histograms. The typical error in determining the reference phase, evaluated according to the scheme described above, was below 15 ps.

C.4 Advantages of the phase fluorometry

We are aware of the following main three advantages of the RF-PS technique compared to HBT, which stem from its distinct principle: i) In the case of RF-PS, jitter in general has no effect on the phase and therefore the error only depends on the statistical error, as explained in the previous section. Only at values comparable to the period of modulation, it could lead to a low S/N and long acquisition times. So as long as the jitter of the APD is well below the $1/f$ (which is 5 ns at 200 MHz), the technique provides a significant advantage over the HBT, where the jitter is directly posing a limit on the minimum width of the anticorrelation or correlation feature. ii) The accumulation times and demands on signal strength are significantly more favourable than for HBT, since the S/N of the useful signal scales as $N^{-1/2}$, unlike the HBT which scales only as $N^{-1/4}$. (N = total radiative events). This is especially useful for systems with lower photon yields and allows to study otherwise inaccessible phenomena. iii) As mentioned above, the HBT essentially evaluates the entire cycle of excitation and deexcitation, i.e. the fitted mean time constant cannot be attributed to an individual time interval comprising the chain of events in the cycle between subsequent photons. On the other hand, our technique measures a characteristic time interval between the electrically-modulated process and the emission of a photon, which in the case of a single-molecule emitter should indeed correspond to the exciton effective lifetime.

C.5 Implementation of the state model simulation

The kinetic model is based on discrete states between which the system changes stochastically with defined rates k_a (a being the index of a particular allowed transition). The decay rates from the S_1 and D_1^+ states are kept fixed in time, as they characterize the intrinsic lifetimes of the excitations which are assumed to stay constant in the voltage ranges used in the experiments. However, all other transition rates which represent the charging probability rates (i.e. hole injections and electron captures) are simulated by periodic functions of time, i.e. $k_a(t)$ which account for the varying tunnelling probability at different bias voltages. The numerical simulation is performed as a sequence of homogeneous and inhomogeneous Poissonian processes, with the aim to obtain a series of individual event times t_n , and its subsets T_j^a for each allowed transition. For a large enough total number of transitions j (typically on the order of 10^6), the distributions of the transition events T_j^a (which correspond to the X and X^+ emission events) in a single period can be directly compared to the experimental data.

For an increased efficiency of the simulation, we choose to simulate the time intervals it takes the system to change from one state to another by any of the allowed transitions. For a homogeneous Poissonian process they can be obtained as

$$T_j^a = \frac{-\ln(r_n)}{\sum_x k_x},$$

(C.5)

where r_n is a random number with uniform distribution in the range (0,1) gener-

Name	Transition	Movement of charge	Rate
k_1	$S_0 \to D_0^+$	h^+ injection	$\kappa_1[1 + \alpha \sin(2\pi f t)]$
k_2	$D_0^+ \to S_1$	e^- capture	$\kappa_2[1 + \alpha \sin(2\pi f t)]$
k_3	$S_1 \to D_1^+$	h^+ injection	$\sin(2\pi f t) > L: \ \kappa_3[\sin(2\pi f t) - L]^\omega$ $\sin(2\pi f t) \leq L : 0$
τ_1^{-1}	$S_1 \to S_0$	recombination	$1/\tau_1$
τ_2^{-1}	$D_1^+ \to D_0^+$	recombination	$1/\tau_2$

Table C.1: Transitions allowed in the minimalistic four-state model and their corresponding time-dependent rates.

ated for each transition [262] and the sum runs over all possible states that can follow the current state. The moment of transition T_j^a will be

$$T_j^a = t_n = t_{n-1} + \Delta T_j^a. \tag{C.6}$$

The probability that a transition will undergo a particular allowed transition is

$$P_j^a = \frac{k_a}{\sum_x k_x}, \tag{C.7}$$

which is simulated by a Monte Carlo approach in a straightforward manner using a second uniformly distributed random variable q_n.

In the case of time-dependent rates $k_a(t)$, for the simulation of the T_j^a, a general analytical solution is not feasible, however it can be estimated numerically with a very good precision using again the random variable r_n. The T_j^a can be obtained by integrating the total time-variable rate, from the last event at time t_{n-1}, until the value of the randomized value of r_n is reached [262]:

$$r_n = \int_0^{\Delta T} \sum_x k_x(t_{n-1} + s)ds. \tag{C.8}$$

The $1/f$ periodicity of $k_a(t)$ gives the possibility to speed up the algorithm by precalculating the integral and creating a lookup function to quickly find T_j^a for each pair of r_n and $t_{n-1} \mod 1/f$. Our discrete-step integration is done with a step $ds = 1$ ps, up to $s = 5.104$ ps. For such r_n and $t_{n-1} \mod 1/f$ that reach the upper bound of s, the T_j^a is laid equal to the value at the maximum s.

The probability of transition P_j^a follows Eq. (C.7), however with the time-variable rates at time t_n

$$P_j^a = \frac{k_a(t_n)}{\sum_x k_x(t_n)}. \tag{C.9}$$

In the four-state model, we included the transitions and the time-variable rates listed in Table C.1.

The k_1 rate of hole injection into the molecule is a product of the base rate κ_1 sinusoidally modulated with amplitude α set to 0.5. The rate of electron capture into ZnPc$^+$ k_2 is analogous to k_1, however with its own rate κ_2. The hole injection probability into exciton k_3 is modulated by a sine above a threshold L, raised to the power w and multiplied with its respective base rate κ_3. The w and L have the purpose of accounting for the nonlinear rise of the X^+ above the threshold, and we set them to $w = 1.4$, $L = 0.1$. Lifetimes τ_1 and τ_2 defining the S_1 and D_0^+ decay rates are kept at 750 and 50 ps, respectively, which are the characteristic

values measured around $V = V_\text{th}$. The κ_1, κ_2 and κ_3 are optimized by iterative least-squares approach to the best match of the simulated and experimental X and X^+ decay histograms. The experimental histogram for the X^+ was multiplied by a factor accounting for different relative sensitivities of the entire optical setup to the wavelengths of X and X^+.

C.6 Lifetime measurements on different locations of a molecular trimer

In order to test the role of the injection position on the determination of the excitonic lifetime we have constructed a ZnPc trimer and measured the neutral exciton lifetime across the structure by means of RF-PS. Porphyrin chains have been shown to behave as single photon emitters due to dipole-dipole coupling of the individual monomers, which results in superluminescence of the coupled emitters [12]. The lifetimes of the excitons in the chains as measured by Hanbury Brown-Twiss interferometry, however, remain close to the one observed for single molecules (see Ref. [86] for details). In Fig. C.2 we show that lifetime values measured along the long axis of a trimer remain constant within the error of the measurement. The small modulation observed may be indicative of the different charge injection efficiencies due to the spatial modulation of the molecular orbitals, and highlights the convenience of using RF-PS measurements for studying the photophysics of coupled emitters.
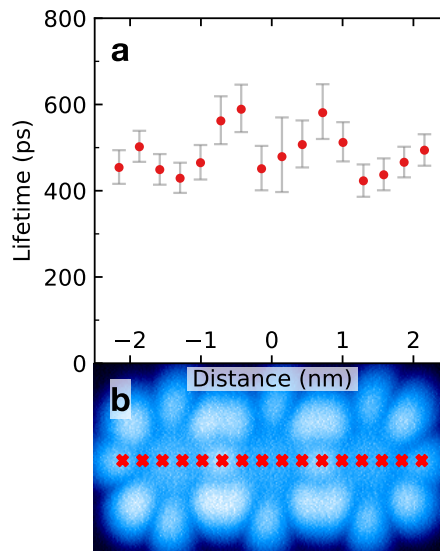

Figure C.2: (a) Lifetime as a function of the tip position above the ZnPc trimer, measured along its long axis. Frequency was 200 MHz, $V_\text{DC} = -2.2$ V and $V_\text{AC} = 100$ mV, $I_\text{t} = 100$ pA. (b) Constant current STM image ($V_\text{DC} = -2.2$ V, $I_\text{t} = 2$ pA). Red crosses denote the locations of the lifetime measurements drawn in (a).

C.7 Lifetime measurements of ZnPc on 4 ML-NaCl/Au(111)

We performed lifetime measurements of ZnPc on 4 ML-NaCl/Au(111), in which neutral exciton appears also at positive bias voltages where the trion is absent (Fig. C.3) [81]. The very sharp bias onset of the measured exciton intensity and high quantum yield allowed us to measure lifetimes up to 4.8 ns at 10 pA current. The tip is closer to the molecule at the same current due to the reduced conductivity of 4 ML of NaCl than on 3 ML. The resulting lifetimes are approximately 5 times longer than for ZnPc on 3 ML-NaCl/Ag(111) and comparable to values reported for ZnPc in solutions [190]. This showcases the usefulness of the method for measurements of longer lifetimes.
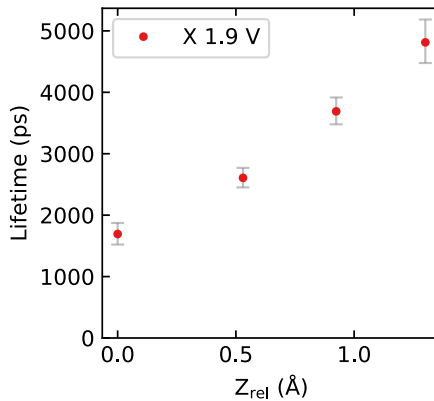

Figure C.3: Dependence of lifetime of neutral exciton in ZnPc/4 ML-NaCl/Au(111) on picocavity size measured at positive bias voltage of 1.9 V. A 50 MHz harmonic signal with 100 mV amplitude is used for measuring the phase shift and determination of the lifetimes. Range of I_t was 10 to 60 pA.

C.8 Redshift maps measured with a metallic tip

To complement the redshift map presented in Fig. 5.2d obtained with a CO-tip we also derive an analogous picture using the data taken with a metallic tip. The map in Fig. C.4 is showing the spectral shift of the X peak as a function of the tip position (and hence primary charge carrier injection location). It closely resembles the data recently reported for photonic Lamb shift in photoluminescence maps of ZnPc [72]. The observed shift can be explained by means of plasmon-exciton interactions at the submolecular level and proves that in the electroluminescent process the picocavity plays a crucial role and can be used for fine tuning of the emission energy. Indeed, comparison of Fig. C.4 with Fig. 5.2d demonstrates how a subtle modification (by picking up a CO molecule with the tip) can alter the spatial character of the photonic Lamb shifts; redshift map with CO-functionalized tip presents eight lobes whereas with metallic tip we observed only four. Future simulations taking into account the presence of the CO probe particles in the picocavities may help to elucidate the photophysical origin of these apparent differences.
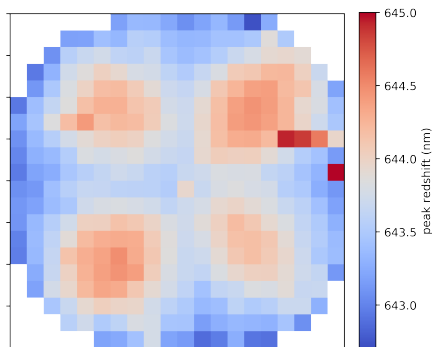
Figure C.4: Peak redshift map of neutral exciton on a single ZnPc measured with a metallic tip at $V_{DC} = -3.1$ V. The redshifts are derived from the dataset presented in Fig. 5.2a.

	Energy (eV)	f	wf. composition
ZnPc	1.92	0.511	94% HOMO $\rightarrow$ LUMO
ZnPc$^+$	1.63	0.205	89% SOMO$_\alpha \rightarrow$ LUMO$_\alpha$

Table C.2: Computed emission energies, oscillator strength (f) and main transitions involved in the first excited states of ZnPc (neutral) and ZnPc$^+$ (cation).

C.9   Dependence of the spectrum on the bias

In Fig. C.5 we plot the raw bias-dependent spectra of the exciton/trion emission measured at constant current tunneling conditions, demonstrating that the position and width of the peaks remain constant in the bias range used in the mapping experiment. This is strong evidence of the optical transition occurring on the molecule and of the absence of an inelastic mechanism mediated by tunnelling from/to initial/final tip states.

C.10   TD-DFT calculations

We performed calculations of the optical properties of the molecule, with the aim of elucidating the difference of the exciton and trion photon maps experimentally measured. The computed excited states of interest are the first singlet excited states of ZnPc and the first doublet excited state of ZnPc$^+$ (Table C.2). The oscillator strengths indicate bright excitons and their emission energy are in very close agreement with the experimentally recorded spectra (see Fig. 5.2c), further corroborating the assignment of the emission peaks. The excited state of ZnPc is doubly degenerate and involves transitions between HOMO to each of the degenerate LUMO orbitals (Fig. C.6). Upon oxidation to generate ZnPc$^+$, an electron is removed from the HOMO orbital with a renormalization of the orbital energies (Fig. C.6). The transition corresponding to trion emission takes place between SOMO (originating from half-occupied HOMO of neutral ZnPc) and each LU-MOs in the same spin branch (LUMO$_\alpha^1$ or LUMO$_\alpha^2$) (Table C.2). Because of the close similarities of the orbitals involved in the transitions from the ground to the first excited state of interest between ZnPc and ZnPc$^+$, the calculated transition densities (Fig. C.7) are very similar and in line with previous calculations.
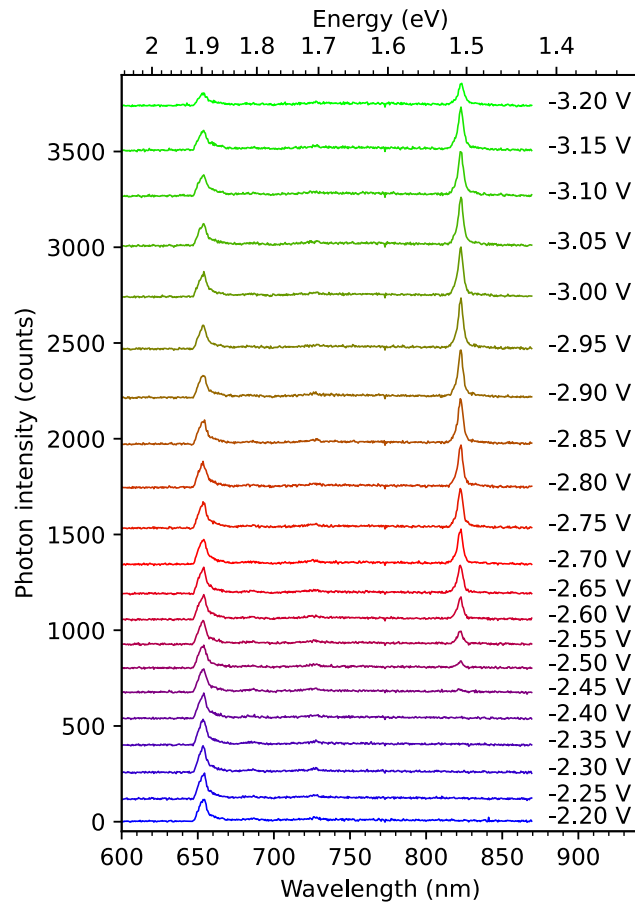
Figure C.5: Spectra of the ZnPc measured as a function of the applied bias voltage. All spectra have been taken above the ZnPc lobe, in a constant-current mode with I_t = 100 pA.
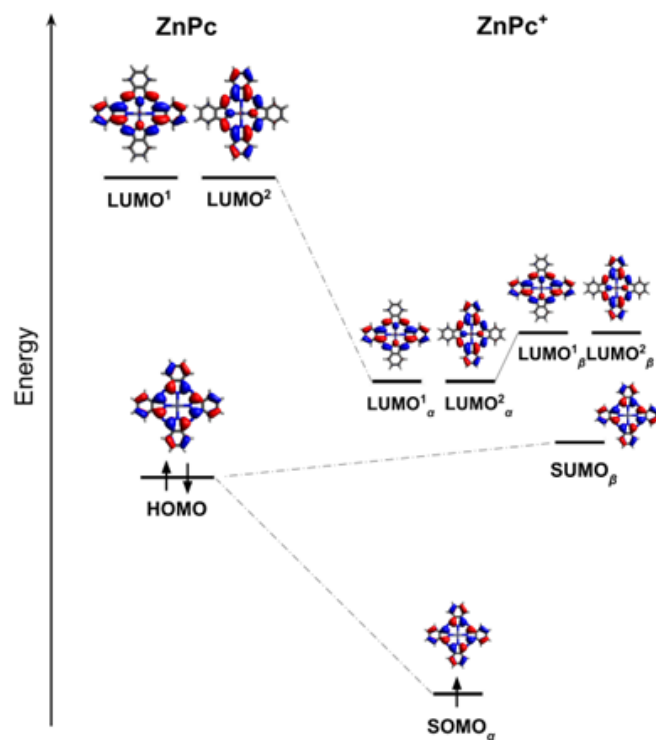
Figure C.6: Ground state frontier molecular orbitals of ZnPc (neutral, left) and ZnPc$^+$ (cation, right).

Figure C.7: Isosurfaces plots of the transition densities, related to transitions from the ground to the first excited state of ZnPc (left) and ZnPc$^+$ (right) (red negative values, blue positive values of the density).

C.11   STS of the ZnPc on 3 ML-NaCl/Ag(111)

Fig. C.8 shows the STS spectrum related to energetic positions of the molecular frontier orbitals. The energies of the maximum of the molecular orbitals resonances as measured by dI/dV on thin insulating layers do not reflect the real energies o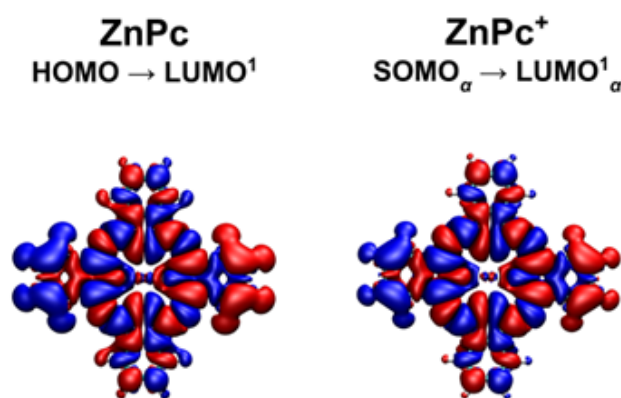f the orbitals, in contrast to molecules adsorbed directly on metals. The peaks rather correspond to resonant electron tunneling channels from/to the HOMO/LUMO, respectively, with energies shifted away from the Fermi level compared to the molecule-on-metal case. Therefore, the spectra are useful mostly for evaluating the energetics of the electrons involved in the tunneling.
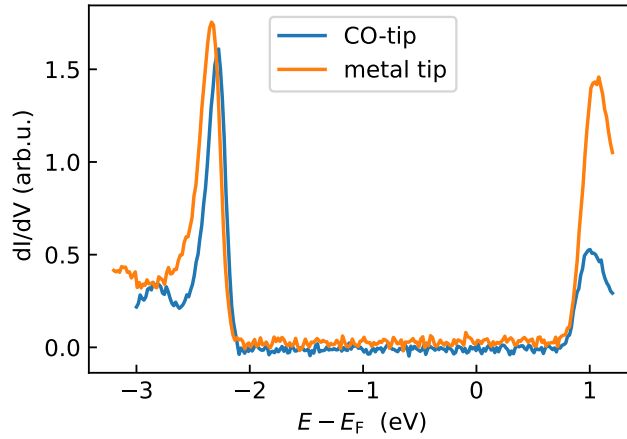
Figure C.8: dI/dV curves, measured on the lobes of ZnPc on 3 ML-NaCl/Ag(111), with the CO-terminated tip and a metal tip.

A first significant increase in the bias dependence of the exciton emission correlates with the voltage at which the peak generated by tunneling to HOMO appears in the STS, i.e. in the -2.3 to -2.4 V range (Fig. 5.1d). In contrast, the relatively sharp onset of the trionic signal observed in the range -2.6 to -2.8 does not have a significant peak in the dI/dV, which supports our interpretation that the trion onset is not triggered by opening any primary tunneling channel. In this sense, STS alone is unable to provide a detailed understanding about the internal exciton formation mechanism or the exciton-trion conversion.

D. Supplementary information for chapter 6

D.1 Comparison between transmission determined from plasmon cutoff detection and from dI/dV at the Ag(111) surface state

For the benchmark of the transfer function magnitude obtained through our optical method (T_{RFplasm}), we performed a comparison to the same function obtained using the conventional procedure ($T_{\mathrm{RFd}I/dV}$) which relies on evaluation of a sharp dI/dV feature broadening. We adopted the procedure from Paul et al. [205] and modified it to perform the two methods simultaneously. We used the lockin technique (modulation of 63 Hz) to obtain broadening of the Ag(111) surface state feature in the dI/dV at the onset energy of the surface state (see spectrum in the inset in Fig. D.1) for the frequency range 0.5–5 GHz. For each frequency point, the tunneling feedback with 3 nA setpoint has been engaged for 20 ms to compensate for any z-drift and after 1 s initial settling time the dI/dV value was measured at bias -70 mV for 2 s. We used a constant driving amplitude of 500 mV.

Because of the generally nonlinear dependence of the dI/dV on the amplitude at the junction (A'), mapping was done (shown in Fig. D.1) for a range of driving amplitudes (A) at 3800 MHz, for which the $T = 0.118$ (obtained with high-precision plasmon cutoff) and therefore $A' = 0.118A$. To have a smooth continuous lookup function of the dI/dV magnitude vs. amplitude, we interpolated the experimental points by a cubic spline.
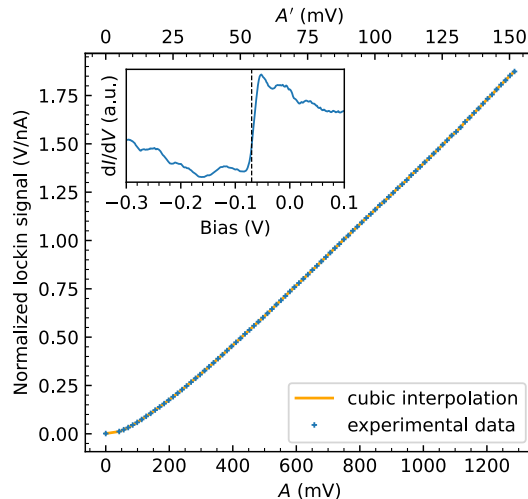
Figure D.1: Dependence of the dI/dV signal measured on the surface state feature of the Ag(111) shown in the inset, on the driving amplitude A at frequency 3800 MHz (blue dots) where $T = 0.118$. The orange line represents the cubic spline interpolation used to obtain a smooth mapping of the dI/dV to the amplitudes at the junction.

The resulting $T_{\mathrm{RFd}I/dV}(f)$ and $T_{\mathrm{RFplasm}}(f)$ are plotted in the Fig. D.2 (with

the red and black dots, respectively) for the entire measured frequency range. The agreement between the methods is excellent except for the regions of high attenuation (around to 1.2, 1.6 and 2.0 GHz, $T < 0.01$), where the error of both methods sharply increases, as it can be appreciated in the second plot which represents the difference $T_{\mathrm{RFd}I/\mathrm{d}V}(f) - T_{\mathrm{RFplasm}}(f)$. All values in this measurement are effectively reduced by 3 dB due to the use of a 6 dB attenuator located at the air side of the RF line.
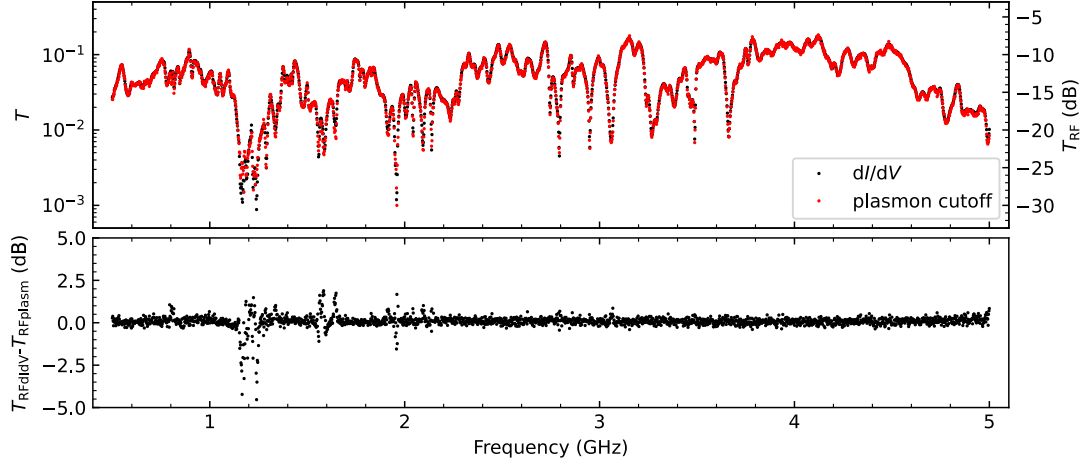

Figure D.2: (top) Transfer function magnitudes (T) simultaneously obtained by the broadening of a sharp $\mathrm{d}I/\mathrm{d}V$ feature corresponding to Ag(111) surface state (black dots) and by the optical plasmon cutoff method (red dots). The integration time for the plasmonic spectra measured at -1.85 V, 5 nA was 2 s, and 2 s (after 1 s initialization) for the averaging of the $\mathrm{d}I/\mathrm{d}V$ signal from the lockin. Modulation frequency of the lockin was set to 63 Hz and time constant to 300 ms. (bottom) The difference of the transfer function magnitudes for the two methods ($T_{\mathrm{RFd}I/\mathrm{d}V} - T_{\mathrm{RFplasm}}$).

D.2 Dependence of the transfer function magnitude on the current and changes in the tip-sample distance

In order to investigate the influence of the current and z-distance on the plasmon cutoff, we have performed a detailed evaluation of the $T(f)$ at various tunneling current setpoints (I_t) in the range 5–200 nA, which correspond to a total change in the tip-sample distance of 150 pm. The Fig.D.3(a) shows the T_{RF} measured for frequency range 3.8–4.2 GHz, specifically chosen to avoid sharp minima in the transmission ($T < 0.01$). The shapes of individual curves are very similar, proving that the influence of the tunneling parameters on the spectral profile of T_{RF} is negligible. However, a detailed look at the spectra is needed to see any systematic shift or smearing affecting the plasmonic cutoff due to high electron flow, associated local heating or nanocavity modification. Fig. D.1(b) shows a set of high-precision plasmonic cutoffs without modulation (averaged each from 5 measurements) for the setpoints used for the T_{RF} in Fig. D.3(a). There is a hint of a trend in the precise cutoff energy, but still within the measurement error

of the spectral cutoff (1.5 meV). For these conditions (1.9 V, 200 nA) there has been no overbias emission which could have an impact on the cutoff evaluation. Consequently, we can conclude that our optical method is providing very robust results in a wide range of tunneling parameters.
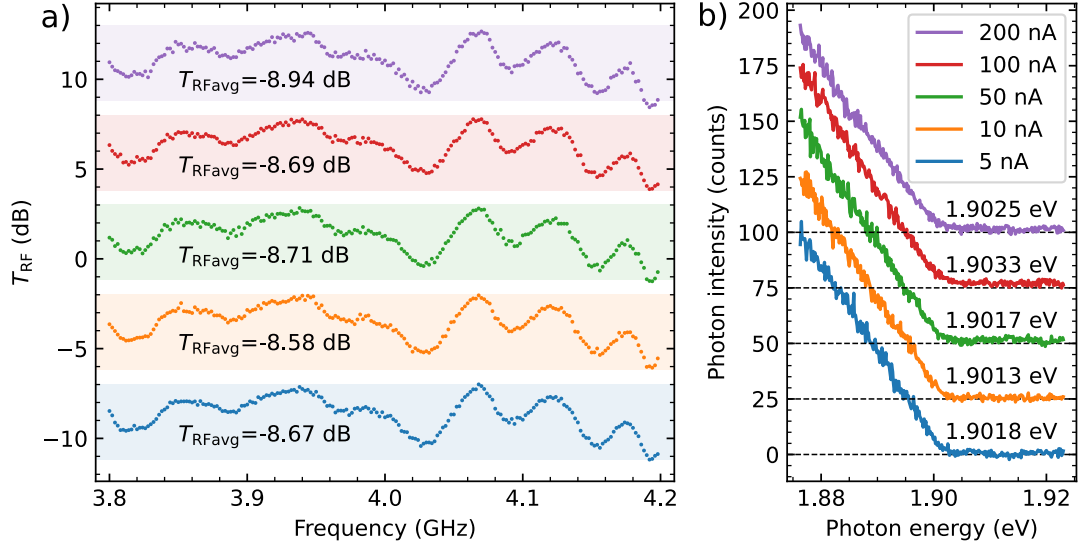
Figure D.3: (a) Dependence of the transfer function magnitude (TRF) on tunneling current setpoint (I_t) in a frequency range 3.8–4.2 GHz, measured from the cutoff of the plasmon spectra. Except for the T_{RF} measured at 5 nA (blue dots), each spectrum is offset by an additional 5 dB. The semi-transparent horizontal bands mark the minimum and maximum values measured with 5 nA I_t setpoint. The integration time per point was set to 8, 4, 0.8, 0.4 and 0.2 s for I_t values of 5, 10, 50, 100 and 200 nA, respectively. The spectral resolution was 0.5 nm at 650 nm (or 1.5 meV at 1.9 V), using a 1200 gr./mm grating. (b) Reference plasmon cutoffs for T_{RF} in (a), measured without any modulation (average of 5 spectra). Except for the cutoff measured at 5 nA, each curve is offset by additional 25 counts for better comparison. A value of V_{DC} is given for every cutoff.

E. Supplementary information for chapter 7

E.1 Simulation of the photon maps

To compare the experimentally measured photon maps with the corresponding theoretical predictions we developed a computationally efficient and universal module within the freely available Probe-Particle package [50], which calculates the interaction between the electric field of a tip-enhanced plasmon, and a molecular or aggregate exciton in the sample. Following the approach developed by Neuman et al. (based on Eq. (1) in ref. [71]), we evaluate the coulomb integral $g(r)$ between the transition density of the excitons ρ_S of the sample (e.g. the molecular cluster) and the electric field V_{TIP} of the metallic tip plasmon:

$$g(r) = \int_{r'} \rho_S(r') V_{\text{TIP}}(r - r') dr', \qquad (E.1)$$

where r represents the relative position of the tip over the sample, corresponding to a pixel in the simulated photon map and r' is a grid coordinate.

We use the calculated function $|g(r)|^2$ directly to generate the photon maps. This represents a simplification of Eq. (1) from ref. [71] by removing its energy dependence, assuming that within the narrow energy range of molecular exciton the spectrum of the plasmon is approximately constant. This approach is sufficient to study the spatial dependence of the coupling (i.e. the dependence on tip position r) and for the purpose of comparison with the normalized experimental photon maps in which the background and spectral dependence is largely suppressed. In our simulation, V_{TIP} is currently approximated by damped multipole expansion:

$$V_{\text{TIP}}(r) = \sum_k C_k \left[\left(\frac{(z - z_0)}{|r|} \right)^{(k-1)} \left(\frac{1}{(|r|^2 - R^2)} \right)^{(k/2)} \right] \qquad (E.2)$$

where k controls the order of multipole ($k = 1$ monopole, $k = 2$ dipole, etc.), z_0 represents the distance of the tip (the centre of the V_{TIP} multipole) from the sample, and R denotes the finite width of the tip (i.e. Lorentzian decay for the dipole). In line with the approach employed in ref. [71], we approximated the tip field plasmon function V_{TIP} as an electric dipole oriented in the z-direction with $z_0 = R = 5$ Å. However, we verified that photon maps are qualitatively similar if simulated using an electric monopole or a dipole oriented along the z-axis. The transition densities ρ_S of the aggregates were obtained directly from the quantum-chemical calculations (see below for details). Both V_{TIP} and ρ_S are sampled on a regular real-space grid with resolution ~ 0.2 Å before the simulation, which allows us to easily update our model in future to include e.g. more a realistic shape of the tip. To calculate the convolution in Eq.(E.1) efficiently, we employ a fast Fourier transform (FFT). This makes our simulation program very efficient and general. For arbitrary spatial distribution of V_{TIP} stored on a real space grid it can simulate photon maps in a few seconds on a standard PC.

E.2   RF-PS measurements

For the RF-PS spectroscopy on a PTCDA anion we used the methodology described in chapter 5. The transmission of the wiring was calibrated at 200 MHz using broadening of a plasmon high-energy cutoff at 1.8 V on a clean substrate described in chapter 6. The time frame is 50 ns and we used 64 ps bin width. For filtering the emission line we used a hard-coated 25 nm bandpass filter (Edmund optics) with center wavelength 925 nm. Histograms are accumulated for approximately 20 min, depending on the strength of the modulation and the resulting signal-to-noise ratio in the waves (Fig. E.1). At the bias of -2.1 V (onset of the luminescence), the obtained effective lifetime of the excited anionic state is within the measurement error, which is < 70 ps in this case.
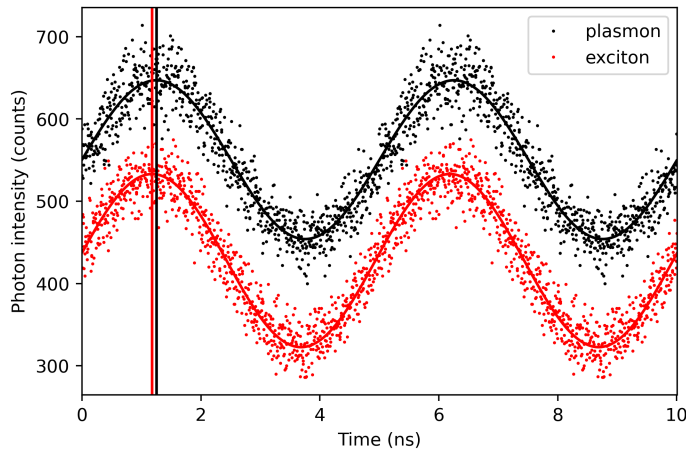

Figure E.1: Radio-frequency phase-shifted waves obtained for a plasmonic reference (black) $V_{DC} = 1.5$ V, $I_t = 1$ nA, $V_{AC} = 200$ mV, integration time 1200 s on Ag(111). First excited anionic state (red) was measured with $V_{DC} = -2.1$ V, $I_t = 50$ pA, $V_{AC} = 200$ mV, integration time 1200 s at oxygen termination position on a single PTCDA on 3ML-NaCl. Sinus function with calculated phase-shift, amplitude, constant term and period as parameters is plotted with a solid line for both plasmonic reference and excited state. The difference between the reference and the excited state is marked by a vertical line.

E.3   Assembly formation on NaCl/Ag(111)

To generate the molecular assemblies of different configurations we have tested several methodologies. While molecular manipulation with the tip of the AFM/STM could be used to form molecular dimers, in order to efficiently form larger assemblies, we have adopted the thermally activated process previously described in the literature [234, 235, 238]. We successfully applied this concept to the PTCDA deposited on NaCl on Ag(111) (evaporation temperature was 380 °C, substrate at 10 K) and subsequently annealed for 1 min by taking the sample with a manipulator (at RT) and putting it in contact with the LN cryostat shield. With the sample cooled back below 10 K, the STM topography shows an abundance of small 2D molecular assemblies (examples at low coverage can be

seen in Fig. E.2). Here the driving interaction of the self-assembly stems from the attraction between the carbonyl oxygens and the hydrogen- termination along the sides of the perylene backbone of the molecules, which pushes the nearest neighbors in the clusters to perpendicular arrangements. The result of the process is sensitive to the concentration of PTCDA on the surface, annealing duration and the number of NaCl layers on which the molecules diffuse. Higher concentrations and higher annealing times tend to produce larger islands (we have prepared clusters of up to 20 units); the largest islands tend to be formed at 3 layers of NaCl compared to 2 and 4-layer NaCl.
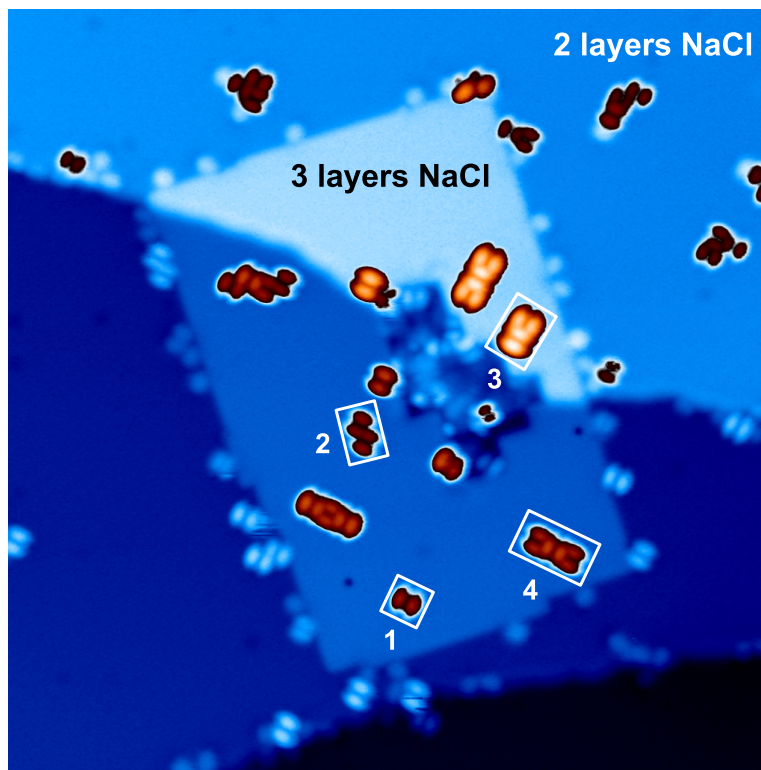
Figure E.2: Example STM topography overview of the PTCDA aggregates on 2 ML- and 3 ML-NaCl/Ag(111) system, formed by allowing diffusion of the molecules. White rectangles mark a monomer (1), two types of dimers (2,3) and a trimer (4) that were the subject of this study. The image parameters were $40 \times 40 \, \text{nm}^2$, 1.2 V.

E.4 Single PTCDA on 3 layers of NaCl/Au(111) at positive bias voltage

For the lack of features and a low signal yield in the photon spectra of PTCDA at energies higher than the anion first excited state, we performed an additional measurement at positive bias voltages. Unfortunately, under these conditions the single molecule experiences instability. Nevertheless, we have discovered that on NaCl/Au(111) it remains relatively stable and therefore we were able to perform the photon spectroscopy and hyperspectral mapping at a single molecule on this surface (Fig. E.3). We found the dominant contribution of the first excited anion state at 1.332 eV and a number of higher-energy peaks with a large

plasmonic background. In particular, the spectra taken over the H-terminated sides present a significantly larger contribution of the signal at 1.493 eV, with respect to the intensity of the first excited state. A photon map at this energy (Fig. E.3c reveals a distribution of the intensity in the real space, indicative of an excited state independent of the $D_1^- \to D_0^-$ transition. We link this feature with the decay of a second excited state (D_2^-), based on the comparison with the theoretical prediction (Fig. E.3d,e), which associates it with a transition dipole moment perpendicular to the longitudinal plane of the molecule, resulting in a characteristic photon map with the intensity localized above the H-terminations of the molecule.
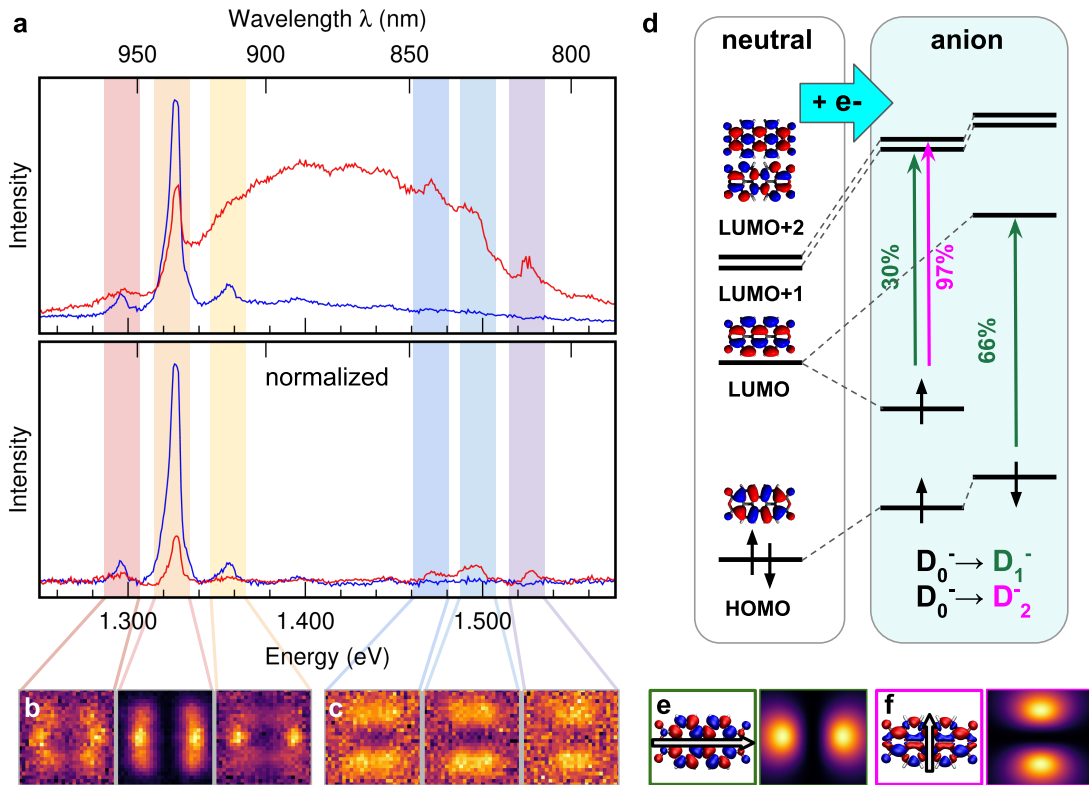
Figure E.3: (a) Averaged electroluminescence spectra of PTCDA anion measured on 3ML-NaCl/Au(111), before and after (top and bottom panels, respectively) normalization by the plasmon. Measurement parameters were set to +2.5 V, 100 pA. (b,c) Photon maps evaluated in the spectral ranges denoted in (a). (d) Energy level schemes and corresponding orbitals obtained from calculations on the PTCDA neutral and anion states (ωB97XD/6-31G*). Green and magenta arrows are marking the main transitions involved in the first two anion excited states D_1^- and D_2^- and their weight in percent. (e,f) Transition densities and their corresponding simulated photon maps of the D_1^- and D_2^- states, respectively.

E.5 Determination of the adsorption geometries with AFM

For a single PTCDA molecule, both types of dimers and the tetramer, we performed a geometrical registration with the substrate (Fig. E.4). We used CO-

functionalized tips to scan the molecule and the surrounding areas of NaCl substrate, each at relative tip-sample distances that yield the atomic resolution. By extrapolating the lattice of the NaCl, we determined the preferred positioning of the PTCDA, which is always on top of a Cl⁻ ion, with the two principal mirror planes aligned with the Cl rows.

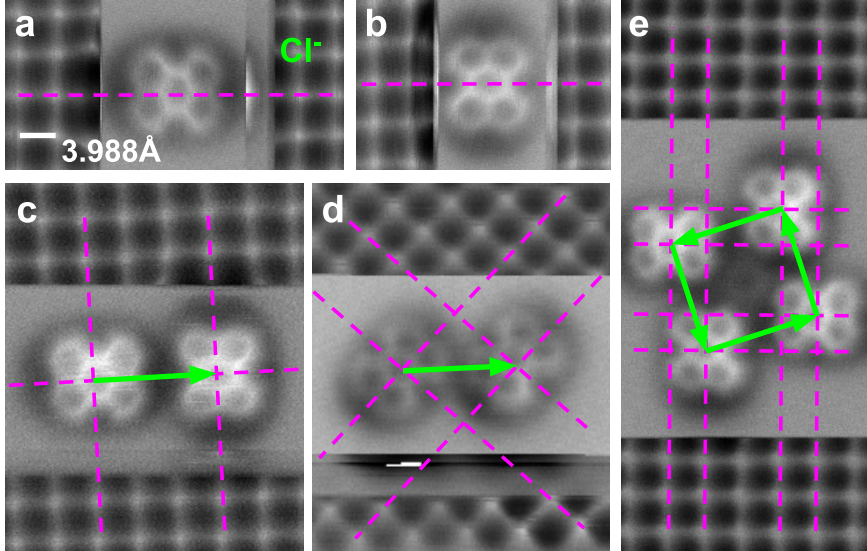**Figure E.4:** AFM analysis of adsorption configurations of the single PTCDA molecules (a), perpendicular dimer (b), parallel dimer (c) and tetramer (d) on NaCl(001) layers on Ag(111). Purple dashed lines mark the Cl rows which cross the centers of the PTCDA, green vectors denote the mutual displacements of the molecules in the aggregates. The bright spots in the lattice correspond to Cl⁻ ion locations. All images have been taken with CO-functionalized tips at bias voltage of 5 mV. The absolute scale of all images can be unambiguously derived from the visible surface lattice of NaCl(001).

E.6 Normalization of the spectra and the photon maps

The individual electroluminescence spectra taken above the molecules are shaped by the spectral character of the nanocavity and the tunneling current, which are inherently dependent on the precise position of the tip relative to the sample with the molecule, in addition to the instrumental function of the optical detection line. This will affect the intensity of emission lines as well as the background in any STML spectrum and consequently the contrast of the photon maps. Experimentally it was observed that the influence on the background intensity is partly mitigated on 3 ML of NaCl in contrast to 2 ML (as shown in our previous work [137]), likely due to weaker direct tunneling of electrons between the tip and the metal below the NaCl. However in the measurements in this study, performed on 3 ML of NaCl the background still plays a non-negligible role, which prevents correct interpretation of weaker excitonic contributions. Therefore we seek a robust normalization procedure that would reliably correct the spurious factors modulating a hyperspectral map.

We assume that the detected photons originate either from plasmons (excited by inelastic electrons directly transported across the tip-molecule-NaCl-metal system) or from the excitons (generated by charge injection into the molecule), as depicted in the scheme in the inset of Fig. E.5. Generation of such plasmonic and excitonic photons would be in a first approximation proportional to the intensity of the flow of charges (current) and the effectiveness of coupling to the nanocavity according to the actual tip-sample geometry. Detected spectra of the excitons and plasmons will finally be modulated by the spectral efficiency of the optical detection setup. We represent the net effect of all these factors by a general modulation function $\Phi(r, E)$, which depends on the tip position r and energy E. The detected intensity of the photons can be then written as

$$I'(r, E) = \alpha I(r, E)\Phi(r, E) + \beta p(E)\Phi(r, E), \qquad \text{(E.3)}$$

where the $I(r, E)$ is the excitonic emission spectrum, $p(E)$ the plasmonic response of the nanocavity material and α and β the respective exciton and plasmon yields. For simplicity, we approximate $p(E)$ as a constant and substitute the term $\beta\Phi(r, E)$ for $\Phi'(r, E)$, which represents the effective measured plasmonic background. With this we obtain

$$I(r, E) \propto \frac{I'(r, E) - \Phi'(r, E)}{\Phi'(r, E)}. \qquad \text{(E.4)}$$

By estimating the $\Phi'(r, E)$ for each position r in the hyperspectral map, we can recover the excitonic spectra and normalize the photon maps for such r and E that yield a nonzero Φ'. For estimation of the plasmonic background, we exploit the continuous character of the plasmonic contribution as opposed to the excitonic signal, which consists of individual lines and can thus be relatively simply distinguished. An example of the photon map normalization is provided in Fig. E.6, which shows the perpendicular dimer before and after the process, including the intermediate step of the background subtraction. The comparison of the raw and processed photon maps to the theoretical prediction demonstrates the necessity of this step in suppressing the background signal of non-excitonic origin in order to yield photon maps suitable for comparison with the theoretical simulations. Nevertheless, a limitation of this approach arises from the assumption that we can determine the $\Phi'(r, E)$ in each location, which fails at very low tunneling currents, leading to a very low photon signal.
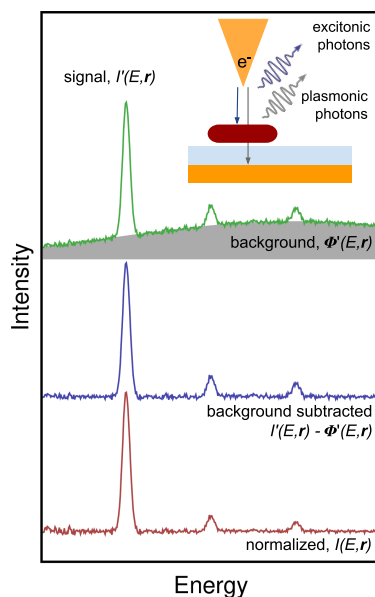
Figure E.5: A visual explanation of the normalization procedure used for individual spectra comprising the hyperspectral maps. The detected signal $I'(r, E)$ is plotted by green color, the effective plasmonic background $\Phi'(r, E)$ by grey filled area. The excitonic part of the signal, plotted in blue, is divided by this general background to obtain the final normalized excitonic spectrum $I(r, E)$ (in red). The inset schematically depicts the basic concept of the electrons tunnelled directly between the tip and the metal substrate, inducing plasmons, or being captured by the molecule, and leading to exciton formation and radiative decay.
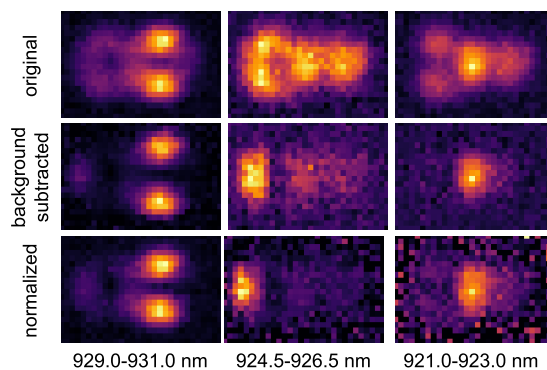
Figure E.6: An example of the background subtraction and normalization of the hyperspectral maps taken at the perpendicular dimer.

E.7   DFT and TD-DFT calculations

All the quantum mechanical calculations were performed with the Gaussian16 package [175]. The ground state calculations were done with density functional method (DFT) employing ωB97XD functional [166] and 6-31G* basis set. The presence of a more stable open shell solution was checked via the stable option and for open-shell systems UDFT has been used. The singlet excited state of neutral systems was computed with time-dependent (TD) DFT at the TD-ωB97XD/6-31G* level of theory. For the triplet neutral and all the charged states, the

Tamm-Dancoff approximation (TDA) has been used (TDA-ωB97X-D/6-31G*). The triplet to singlet excited states transitions were computed with the 50-50 option. PTCDA single molecule was optimized in vacuo in its neutral and anion ground states. The vertical excited states were assessed at the ground state equilibrium geometry and the emission properties were obtained by optimization of the corresponding excited state geometry (Table E.1, Fig. E.7). All aggregate model structures were built on the basis of the information provided by the analysis of the AFM images (Fig. E.6), using the optimized PTCDA neutral geometry as basic units and neglecting the role of the substrate. For each aggregate, several anionic states have been considered, by varying the number of total negative charges, and the most stable have been selected for further calculations (Table E.2). In general, for each given total charge state, all relevant spin multiplicities have been computed with UDFT and provided near degenerate energies, due to a negligible spin interaction between the unpaired electrons. The total amount of charge localized on each molecular unit has been estimated based on Mulliken population analysis, by summing the partial charges on each atom within the molecule [263]. The aggregate exciton states (Tables S3-S8 in [215]) were computed as vertical excitations, at a fixed geometry, on a selected spin state for each charge arrangement listed in Table E.2 along with their oscillator strengths f, which characterize the linear absorption response of the system in the far field. The transition densities of selected states are used to simulate the corresponding photon maps. The transition densities were generated employing Multiwfn software (grid spacing 0.2 Bohr; plot with isosurface value set to 0.0001 e/Bohr^3) [194].

E.8 Calculations on single molecule and aggregates

For the neutral molecule, the first excited state is represented by the HOMO$\rightarrow$LUMO transition, with an energy value 2.50 eV at the full TD-DFT level in excellent agreement with previously reported experimental data at 2.45 eV [94]. The anion displays two low-lying excited states close in energy, with emissions at 1.62 and 1.80 eV, respectively. These values are slightly overestimated compared to the experimental emission (at 1.332 eV and 1.493 eV), consistently with that of the neutral excited state predicted at 2.79 eV when employing the TDA approximation. The corresponding transition dipole moments are oriented along the long and short molecular axes, respectively (see Figs. 7.1 and E.3). The calculation locates the triplet to singlet emission to lower energies, around 1.18 eV, also in agreement with the previous work [94]. The aggregate exciton states computed with TD-DFT are linear combinations of single excitations involving orbitals delocalized on the whole system. In these PTCDA systems, the aggregate orbitals result from linear combinations of the molecular anionic orbitals localized on each molecular unit. Thus, for each aggregate orbital, by a simple visual inspection, the dominant contributions to the combinations of molecular anionic orbitals can be identified. On the basis of this simple analysis it is possible to relate the calculated aggregate excitonic states (along with their corresponding transition densities) to the excitations localized on each molecu-

lar unit (longitudinal and transversal modes), whose interaction generates the excitonic states. The lookup tables and corresponding orbital energy schemes are summarized in Tables S3–S8 and Figs. S8–S13 in ref. [215]. We denote the molecular units in the aggregates with letters (a–d, see Table E.2). The notation of the aggregate orbitals is chosen to reflect the base monomer orbital (H, L, H+1, L+1, etc.), the sign of the orbital linear combination (sign present in the upper index), and localization/delocalization on particular molecular units (a–d in upper indices). The spin branches are marked as α and β.

Charge state	transition	absorption E/eV (f)	absorption wave function [c]	emission E/eV (f)
neutral	$S_0 \leftrightarrow S_1$[a]	2.91 (0.737)	0.98 (H→L)	2.50 (0.716)
	$S_0 \leftrightarrow T_1$[b]	1.77 (0)	0.90 (H→L)	1.18 (0)
anion[b]	$D_0^- \leftrightarrow D_1^-$	1.84 (0.020)	0.66 (H→L) + 0.30 (L→L+1)	1.62 (0.162)
	$D_0^- \leftrightarrow D_2^-$	2.08 (0.072)	0.92 (L→L+2)	1.80 (0.076)

[a] Calculation with TD-ωB97XD/6-31G*. [b] Calculation with TDA-ωB97XD/6-31G*.
[c] Molecular orbital naming refers to the order in the neutral molecule (see Fig. 7.1).

Table E.1: Computed emission energies (E), oscillator strengths (f) and wave functions composition (wf), including the most relevant coefficients and orbitals involved in the dominant excitations) for the isolated PTCDA molecule.
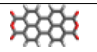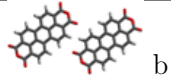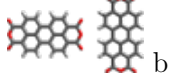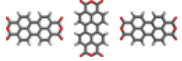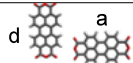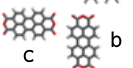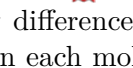
	charge (S) e-	Relative E (eV)	charge localization mol.a	mol.b	mol.c	mol.d	Scheme
monomer	-1 (1/2)	-2.65	-	-	-	-	
dimer parallel	-2 (1 or 0)	-3.63	-1.00	-1.00	-	-	a ... b
dimer perp.	-2 (1 or 0)	-3.64	-0.97	-1.03	-	-	a ... b
trimer	-2 (1 or 0)	-4.67	-0.97	-0.06	-0.97	-	
	-3 (3/2 or 1/2)	-4.09	-0.97	-1.06	-0.97	-	a b c
tetramer	-3 (3/2)	-3.95	-0.75	-0.75	-0.75	-0.75	
	-3 (1/2)	-3.98	-0.50	-1.00	-0.50	-1.00	
	-2 (1 or 0)	-4.01	-0.01	-0.99	-0.01	-0.99	

Table E.2: Total charge and spin of each system, absolute energy difference with respect to the neutral ground state, and amount of charge localized on each molecule of the aggregate (labeled according to the scheme in the last column), computed at the ωB97XD/6-31G* level of theory.
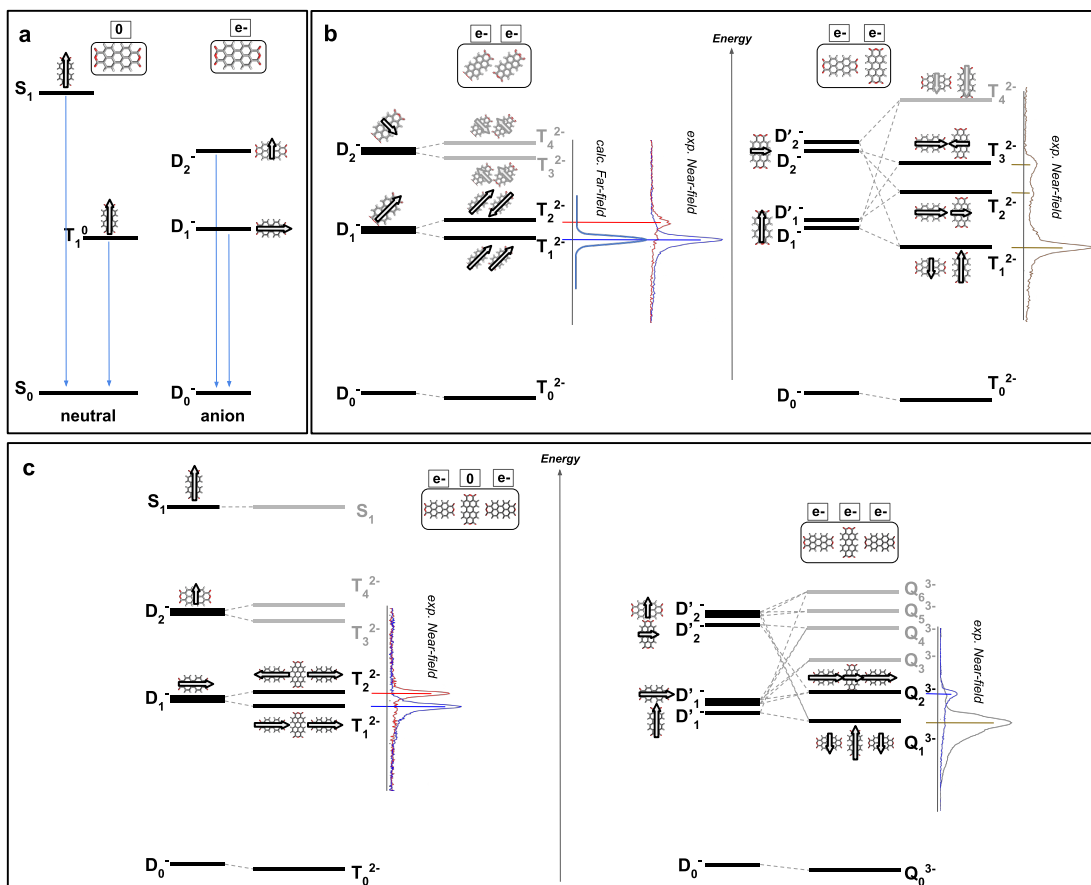
Figure E.7: (a) Energy level scheme of the PTCDA neutral and anion monomer excited states (see Table E.1). (b) Energy level scheme of PTCDA dimer excitonic states (parallel dimer on the left and perpendicular dimer on the right, see also Tables S3 and S4 in [215]): their relation with respect to the monomer states in terms of energies and wave functions (represented by the transition dipole moment arrow) and relation to the experimental spectra (Figs. 7.1, 7.2, 7.3). For the parallel dimer (left), the comparison with the computed far-field spectrum is highlighted. (c) Energy level scheme of PTCDA trimer excitonic states, for total charge -2 (left) and -3 (right) (see Tables S3 and S4 in [215]) and their relation with the composing monomer states and with the experimental spectra (Figs. 7.1, 7.2, 7.3).

F. Supplementary information for chapter 8
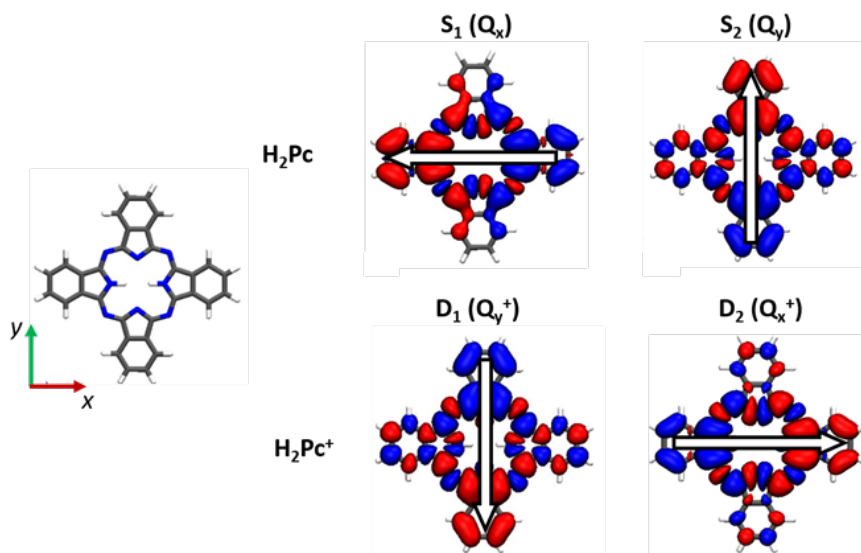
Figure F.1: Transition densities and transition dipole moments (white arrow) of the first two excited states of H_2Pc neutral (S_1 and S_2 states) and cation (D_1 and D_2 states), see Table F.1. Calculations TD(TDA)-ωB97XD/6-31G*. Isosurface 0.002 au.

	n.state(sym)	Exc/eV (osc.)	band a	exp.
H_2Pc neutral	S_1 (B1u)	1.89 (0.472)	Q_x	1.80
	S_2 (B2u)	2.04 (0.542)	Q_y	1.93
H_2Pc^+ cation	D_1 (B2u)	1.50 (0.241)	Q_y^+	1.39
	D_2 (B1u)	1.71 (0.172)	Q_x^+	-
ZnPc neutral	S_1	1.92 (0.510)	Q	1.89
$ZnPc^+$ cation	D_1	1.63 (0.205)	Q^+	1.52
MgPc neutral	S_1	1.88 (0.502)	Q	1.89
$MgPc^+$ cation	D_1	1.59 (0.205)	Q^+	1.51

a For H_2Pc, x-axis oriented along N-H .... H-N direction, see Fig. F.1

Table F.1: Calculations TD- (TDA-)ωB97XD/6-31G* of H_2Pc, ZnPc, MgPc neutral (cation): state number (with symmetry label), emission energy, oscillator strengths and band assignment. Comparison with experimental excitation energies taken from the spectra of Fig. F.2.
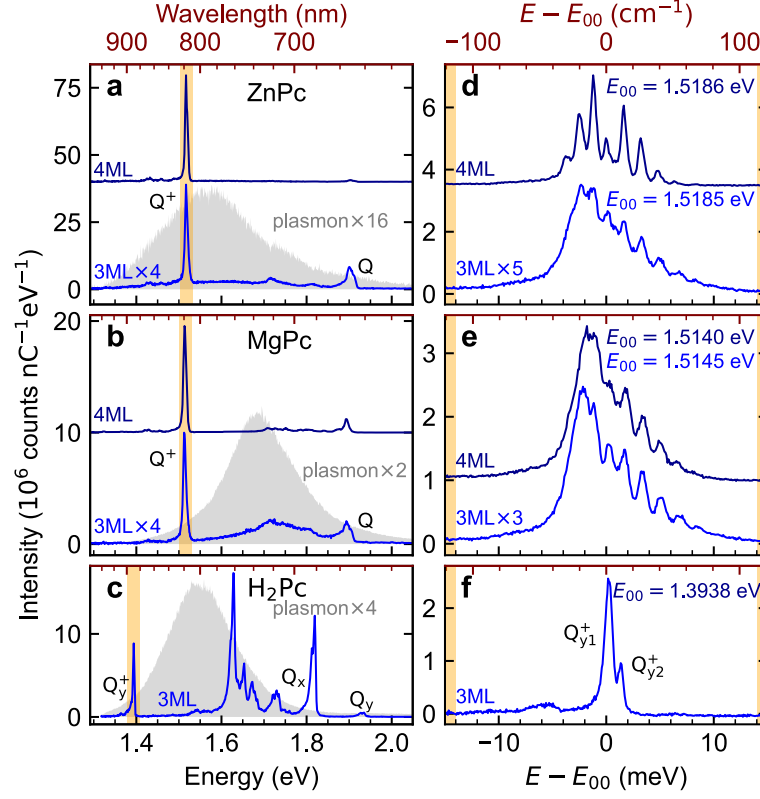
Figure F.2: a-c Raw overview STM-EL spectra of the ZnPc, MgPc and H$_2$Pc at -2.8 V, 100 pA, showing the neutral (Q, Q_x, Q_y) and cation (Q^+, Q_y^+) emission fingerprints plotted with blue solid lines. Grey-filled spectra on the background of each panel are the responses of the nanocavities measured on a clean Ag(111) surface at 2.5 V, 1 nA. **d-f** Raw spectra measured at the same bias and tunnelling current with 400 μeV resolution on the ZnPc, MgPc and H$_2$Pc cations, respectively, evidencing the fine structure present in the first two cases. The scale is given relative to the peaks within the spectral manifold, which manifest lower intensity with respect to their neighbours. The reference energies E_{00} are set to the assumed zero phonon lines in each spectrum.
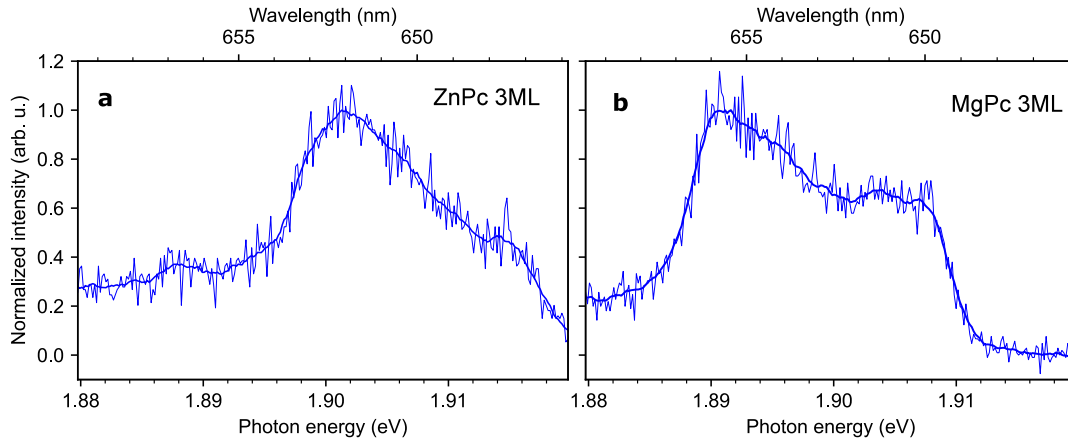
Figure F.3: High-resolution STM-EL spectra measured at the lobe position corresponding to the neutral Q peak of ZnPc in **a** and MgPc molecule in **b** on 3 ML NaCl. Acquisition parameters: energy resolution 600 μeV, a) $U_S = -2.8$ V , $t = 60$ s , $I = 133$ pA, b) $U_S = -2.8$ V, $t = 60$ s, $I = 100$ pA. The estimated FWHM is 13 meV in **a** and 20 meV in **b**.
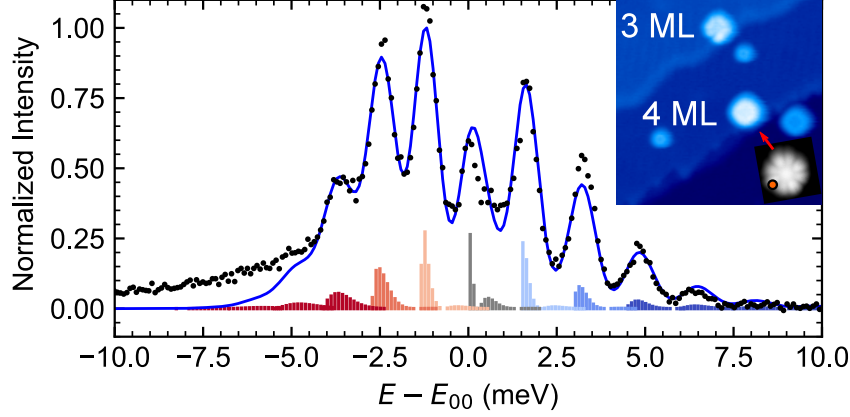
Figure F.4: Experimental (black dotted, $U_S = -2.9$ V, $t = 180$ s , $I = 20$ pA) and simulated (solid blue line) STM-EL fine spectrum of Q^+ peak of chirally adsorbed step-edge stabilized $MgPc^+$ on 4 ML NaCl/Au(111) (see inset image). The Franck-Condon factors are calculated including the modified exponential distribution and are colour-coded according to the vibration quantum number difference between the initial and final state, i.e. $m - n$ (red – negative, blue – positive, grey – null). The energies E_{00} obtained through the fitting are set as the reference in each spectrum. Parameters of the simulated spectrum: $k_0 = 1.60$ meV/$(°)^2$, $k_1 = 1.86$ meV/$(°)^2$,$\Delta\phi_0 = 0.685°$, $T_{eff} = 63$ K, $A = 0.68$, $\gamma = 0.65$ meV, $E_{00} = 1.5144$ eV.

	cation			neutral		
	k_0 (meV/$(°)^2$)	k_1 (meV/$(°)^2$)	$\Delta\phi_0$ (°)	k_0 (meV/$(°)^2$)	k_1 (meV/$(°)^2$)	$\Delta\phi_0$ (°)
ZnPc	1.769	1.904	0.31	1.459	1.527	0.42
MgPc	1.747	1.880	0.28	1.461	1.535	0.41
H$_2$Pc	1.569	1.634	0.00	1.633	1.675	0.00

Table F.2: Parameters of parabolic fitting of total energies computed by TDDFT (see also Fig. 8.2 and Fig. F.6).
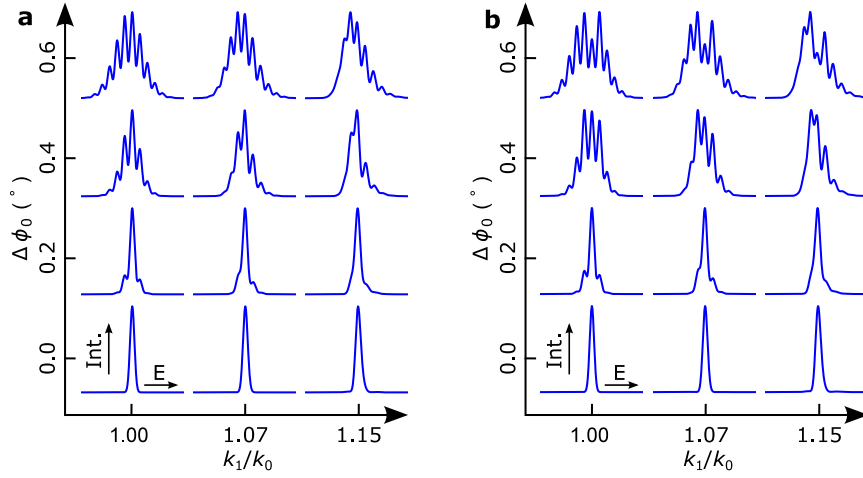
Figure F.5: Typology of simulated STM-EL spectra for varying values of excited/ground state equilibrium angle $\Delta\phi_0$, potential stiffness ratio k_1/k_0 and reduction factor $A = 1$ in a) and $A = 0.5$ in b) (using $T = 70$ K, $\gamma = 0.83$ meV, $k_1 = 1.83$ meV/$(°)^2$ and $J = 113 m_p \text{nm}^2$). In the limiting case of $\phi_0 = 0$ and $k_1/k_0 = 1$, the spectrum consists of a single peak resulting from the sum of all $m = n$ transitions. Increasing $\Delta\phi_0 > 0$ leads to significant overlap among different initial and final librational states $(m - n \neq 0)$ and consequent appearance of the red- and blue-shifted peak progressions. The ratio $k_1/k_0 \neq 1$ affects the asymmetry of the spectral envelope around E_{00} and the energy spacings among the peaks. For $k_1/k_0 > 1$, the interpeak energy difference in the red-shifted branch becomes smaller compared to the blue-shifted branch of the spectrum.
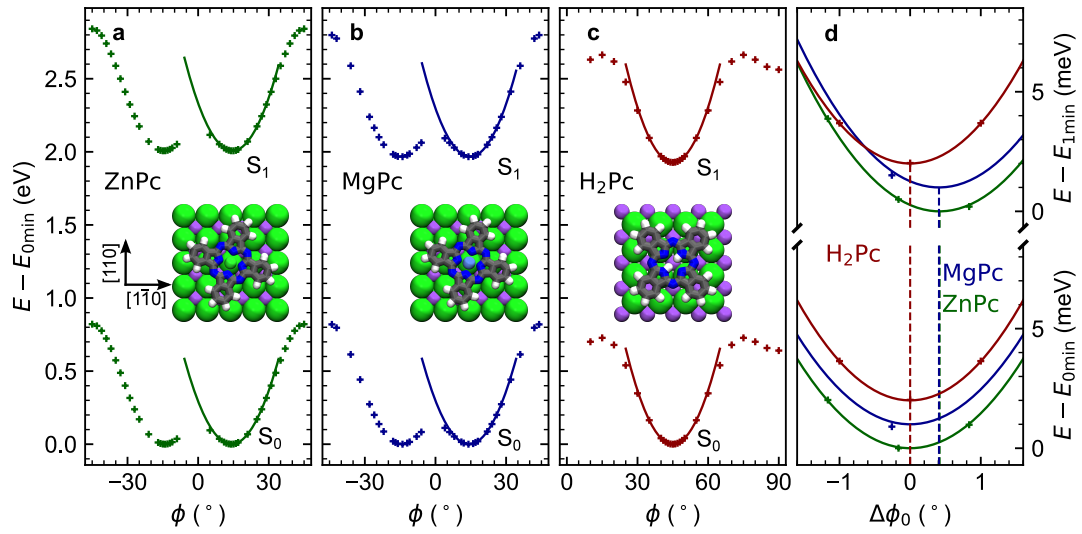
Figure F.6: ZnPc, **b** MgPc and **b** H_2Pc total energy (relative to the energy of the minima E_{0min}) as a function of rotation by angle ϕ for the ground and excited states. The computed energy is plotted with crosses and the corresponding parabolic fits around the local minima with solid lines. The insets show the schematic models of the respective ground state cations in their equilibrium positions. **d** Detailed comparison of the potential well minima of the three cationic chromophores (computed as a difference with the energy of their respective minima E_{0min} or E_{1min}) as a function of the shift in the equilibrium angle positions $\Delta\phi_0$ between the ground and excited states. $MgPc^+$ and H_2Pc^+ ground and excited state are vertically offset by increments of 1 meV for clarity. Note the zero $\Delta\phi_0$ for H_2Pc^+, imposed by the symmetry of the system. Fitting parameters are summarized in Table F.2.

Bibliography

[1] Arieh Aviram and Mark A Ratner. Molecular rectifiers. *Chemical physics letters*, 29(2):277–283, 1974.

[2] Albert V Crewe, J Wall, and J Langmore. Visibility of single atoms. *science*, 168(3937):1338–1340, 1970.

[3] Gerd Binnig, Heinrich Rohrer, Ch Gerber, and Eddie Weibel. Tunneling through a controllable vacuum gap. *Applied Physics Letters*, 40(2):178–180, 1982.

[4] Michael F Crommie, Christopher P Lutz, and Donald M Eigler. Confinement of electrons to quantum corrals on a metal surface. *Science*, 262(5131):218–220, 1993.

[5] Leo Gross, Fabian Mohn, Nikolaj Moll, Peter Liljeroth, and Gerhard Meyer. The chemical structure of a molecule resolved by atomic force microscopy. *Science*, 325(5944):1110–1114, 2009.

[6] Sebastian Loth, Markus Etzkorn, Christopher P Lutz, Donald M Eigler, and Andreas J Heinrich. Measurement of fast electron spin relaxation times with atomic resolution. *Science*, 329(5999):1628–1630, 2010.

[7] Susanne Baumann, William Paul, Taeyoung Choi, Christopher P Lutz, Arzhang Ardavan, and Andreas J Heinrich. Electron paramagnetic resonance of individual atoms on a surface. *Science*, 350(6259):417–420, 2015.

[8] Renhe Zhang, Yao Zhang, ZC Dong, S Jiang, C Zhang, LG Chen, L Zhang, Y Liao, J Aizpurua, Y ea Luo, et al. Chemical mapping of a single molecule by plasmon-enhanced raman scattering. *Nature*, 498(7452):82–86, 2013.

[9] Richard Berndt, James K Gimzewski, and Peter Johansson. Inelastic tunneling excitation of tip-induced plasmon modes on noble-metal surfaces. *Physical review letters*, 67(27):3796, 1991.

[10] XH Qiu, GV Nazin, and W Ho. Vibrationally resolved fluorescence excited with submolecular precision. *Science*, 299(5606):542–546, 2003.

[11] Hiroshi Imada, Kuniyuki Miwa, Miyabi Imai-Imada, Shota Kawahara, Kensuke Kimura, and Yousoo Kim. Real-space investigation of energy transfer in heterogeneous molecular dimers. *Nature*, 538(7625):364–367, 2016.

[12] Yang Zhang, Yang Luo, Yao Zhang, Yun-Jie Yu, Yan-Min Kuang, Li Zhang, Qiu-Shi Meng, Yi Luo, Jin-Long Yang, Zhen-Chao Dong, et al. Visualizing coherent intermolecular dipole–dipole coupling in real space. *Nature*, 531(7596):623–627, 2016.

[13] Russell Young, John Ward, and Fredric Scire. The topografiner: an instrument for measuring surface microtopography. *Review of Scientific Instruments*, 43(7):999–1011, 1972.

[14] Gerd Binnig, Heinrich Rohrer, Ch Gerber, and Edmund Weibel. Surface studies by scanning tunneling microscopy. *Physical review letters*, 49(1):57, 1982.

[15] Gerd Binnig, Heinrich Rohrer, Ch Gerber, and Eduard Weibel. 7× 7 reconstruction on si (111) resolved in real space. *Physical review letters*, 50(2):120, 1983.

[16] Gerd Binnig, Calvin F Quate, and Ch Gerber. Atomic force microscope. *Physical review letters*, 56(9):930, 1986.

[17] Franz J Giessibl. Atomic resolution of the silicon (111)-(7x7) surface by atomic force microscopy. *Science*, 267(5194):68–71, 1995.

[18] Toshu An, Toyoaki Eguchi, Kotone Akiyama, and Yukio Hasegawa. Atomically-resolved imaging by frequency-modulation atomic force microscopy using a quartz length-extension resonator. *Applied Physics Letters*, 87(13):133114, 2005.

[19] Franz J Giessibl. Advances in atomic force microscopy. *Reviews of modern physics*, 75(3):949, 2003.

[20] Nikolaj Moll, Leo Gross, Fabian Mohn, Alessandro Curioni, and Gerhard Meyer. The mechanisms underlying the enhanced resolution of atomic force microscopy with functionalized tips. *New Journal of Physics*, 12(12):125020, 2010.

[21] Prokop Hapala, Georgy Kichin, Christian Wagner, F Stefan Tautz, Ruslan Temirov, and Pavel Jelínek. Mechanism of high-resolution stm/afm imaging with functionalized tips. *Physical Review B*, 90(8):085421, 2014.

[22] Jiří Doležal. Modification of silicon surfaces for selective adsorption, 2018. http://hdl.handle.net/20.500.11956/104394.

[23] AB Balantekin and N Takigawa. Quantum tunneling in nuclear fusion. *Reviews of Modern Physics*, 70(1):77, 1998.

[24] William SC Williams. *Nuclear and particle physics.* Clarendon Press, 1991.

[25] Robert J McMahon. Chemical reactions involving quantum tunneling. *Science*, 299(5608):833–834, 2003.

[26] James D Watson and Francis HC Crick. The structure of dna. In *Cold Spring Harbor symposia on quantitative biology*, volume 18, pages 123–131. Cold Spring Harbor Laboratory Press, 1953.

[27] Per-Olov Löwdin. Proton tunneling in dna and its biological implications. *Reviews of Modern Physics*, 35(3):724, 1963.

[28] Chunli Bai. *Scanning tunneling microscopy and its application*, volume 32. Springer Science & Business Media, 2000.

[29] John Bardeen. Tunnelling from a many-particle point of view. *Physical review letters*, 6(2):57, 1961.

[30] Bert Voigtländer. *Scanning Probe Microscopy*. Springer, 2016.

[31] Jascha Repp, Gerhard Meyer, Sladjana M Stojković, André Gourdon, and Christian Joachim. Molecules on insulating films: scanning-tunneling microscopy imaging of individual molecular orbitals. *Physical Review Letters*, 94(2):026803, 2005.

[32] Jiří Doležal, Pablo Merino, Jesus Redondo, Lukas Ondic, Ales Cahlik, and Martin Švec. Charge carrier injection electroluminescence with co-functionalized tips on single molecular emitters. *Nano letters*, 19(12):8605–8611, 2019.

[33] Benjamin Doppagne, Michael C Chong, Etienne Lorchat, Stéphane Berciaud, Michelangelo Romeo, Hervé Bulou, Alex Boeglin, Fabrice Scheurer, and Guillaume Schull. Vibronic spectroscopy with submolecular resolution from stm-induced electroluminescence. *Physical review letters*, 118(12):127401, 2017.

[34] Shadi Fatayer, Bruno Schuler, Wolfram Steurer, Ivan Scivetti, Jascha Repp, Leo Gross, Mats Persson, and Gerhard Meyer. Reorganization energy upon charging a single molecule on an insulator measured by atomic force microscopy. *Nature nanotechnology*, 13(5):376–380, 2018.

[35] Jascha Repp, Gerhard Meyer, and Karl-Heinz Rieder. Snell's law for surface electrons: refraction of an electron gas imaged in real space. *Physical review letters*, 92(3):036803, 2004.

[36] Song Jiang, Tomáš Neuman, Remi Bretel, Alex Boeglin, Fabrice Scheurer, Eric Le Moal, and Guillaume Schull. Many-body description of stm-induced fluorescence of charged molecules. *arXiv preprint arXiv:2210.00126*, 2022.

[37] Kuniyuki Miwa, Hiroshi Imada, Miyabi Imai-Imada, Kensuke Kimura, Michael Galperin, and Yousoo Kim. Many-body state description of single-molecule electroluminescence driven by a scanning tunneling microscope. *Nano letters*, 19(5):2803–2811, 2019.

[38] Katharina Kaiser, Leonard-Alexander Lieske, Jascha Repp, and Leo Gross. Charge-state lifetimes of single molecules on ultrathin insulating films. *arXiv preprint arXiv:2211.01051*, 2022.

[39] Abhishek Grewal. *Single molecule fluorescence and phosphorescence studies using a scanning tunneling microscope*. PhD thesis, EPFL, Lausanne, 2022.

[40] Seizo Morita, Roland Wiesendanger, and Ernst Meyer. *Noncontact Atomic Force Microscopy*, volume 1434. Springer, 2002.

[41] TR Albrecht, Pr Grütter, D Horne, and Do Rugar. Frequency modulation detection using high-q cantilevers for enhanced force microscope sensitivity. *Journal of applied physics*, 69(2):668–673, 1991.

[42] Franz J Giessibl. The qplus sensor, a powerful core for the atomic force microscope. *Review of Scientific Instruments*, 90(1):011101, 2019.

[43] Franz J Giessibl. Forces and frequency shifts in atomic-resolution dynamic-force microscopy. *Physical Review B*, 56(24):16010, 1997.

[44] Joachim Welker, Esther Illek, and Franz J Giessibl. Analysis of force-deconvolution methods in frequency-modulation atomic force microscopy. *Beilstein journal of nanotechnology*, 3(1):238–248, 2012.

[45] Taras Chutora. *Study of molecular structures on solid state surfaces.* PhD thesis, Palacký University Olomouc, Olomouc, 2019.

[46] Leo Gross, Fabian Mohn, Peter Liljeroth, Jascha Repp, Franz J Giessibl, and Gerhard Meyer. Measuring the charge state of an adatom with non-contact atomic force microscopy. *Science*, 324(5933):1428–1431, 2009.

[47] Thomas Leoni, Olivier Guillermet, Hermann Walch, Véronique Langlais, Andrew Scheuermann, Jacques Bonvoisin, and Sébastien Gauthier. Controlling the charge state of a single redox molecular switch. *Physical Review Letters*, 106(21):216103, 2011.

[48] B Mallada, A Gallardo, M Lamanec, B De La Torre, V Špirko, Pavel Hobza, and P Jelinek. Real-space imaging of anisotropic charge of σ-hole by means of kelvin probe force microscopy. *Science*, 374(6569):863–867, 2021.

[49] Prokop Hapala, Martin Švec, Oleksandr Stetsovych, Nadine J Van Der Heijden, Martin Ondráček, Joost Van Der Lit, Pingo Mutombo, Ingmar Swart, and Pavel Jelínek. Mapping the electrostatic force field of single molecules from high-resolution scanning probe images. *Nature communications*, 7(1):1–8, 2016.

[50] Prokop Hapala. Probeparticle model. `https://github.com/Probe-Particle/ppafm`, 2014.

[51] Sampsa K Hämäläinen, Nadine van der Heijden, Joost van der Lit, Stephan den Hartog, Peter Liljeroth, and Ingmar Swart. Intermolecular contrast in atomic force microscopy images without intermolecular bonds. *Physical review letters*, 113(18):186102, 2014.

[52] E. Abbe. Beitraäge zur theorie des mikroskops und der mikroskopischen-wahrnehmungn. *Archiv für mikroskopische Anatomie*, 7:413–420, 1873.

[53] Ernst Ruska. The development of the electron microscope and of electron microscopy. *Reviews of modern physics*, 59(3):627, 1987.

[54] L Kipp, M Skibowski, RL Johnson, R Berndt, R Adelung, S Harm, and R Seemann. Sharper images by focusing soft x-rays with photon sieves. *Nature*, 414(6860):184–188, 2001.

[55] AMAA Lewis, Michael Isaacson, Alec Harootunian, and A Muray. Development of a 500 å spatial resolution light microscope: I. light is efficiently transmitted through $\lambda/16$ diameter apertures. *Ultramicroscopy*, 13(3):227–231, 1984.

[56] Dieter W Pohl, Winfried Denk, and Mark Lanz. Optical stethoscopy: Image recording with resolution $\lambda/20$. *Applied physics letters*, 44(7):651–653, 1984.

[57] John Lambe and SL McCarthy. Light emission from inelastic electron tunneling. *Physical Review Letters*, 37(14):923, 1976.

[58] James K Gimzewski, J K Sass, R R Schlitter, and J Schott. Enhanced photon emission in scanning tunnelling microscopy. *Europhysics Letters*, 8(5):435–440, 1989.

[59] Lukas Novotny and Bert Hecht. Surface plasmons. In *Principles of Nano-Optics*, page 369–413. Cambridge University Press, 2 edition, 2012.

[60] Uwe Kreibig and Michael Vollmer. *Optical properties of metal clusters*, volume 25. Springer Science & Business Media, 2013.

[61] Stefan A Maier et al. *Plasmonics: fundamentals and applications*, volume 1. Springer, 2007.

[62] Dimitrios Tzarouchis and Ari Sihvola. Light scattering by a dielectric sphere: Perspectives on the mie resonances. *Applied Sciences*, 8(2):184, 2018.

[63] K Kolwas, S Demianiuk, and M Kolwas. Optical excitation of radius-dependent plasmon resonances in large metal clusters. *Journal of Physics B: Atomic, Molecular and Optical Physics*, 29(20):4761, 1996.

[64] Seungwoo Lee. Nanoparticle-on-mirror cavity: a historical view across nanophotonics and nanochemistry. *Journal of the Korean Physical Society*, pages 1–8, 2022.

[65] Wenqi Zhu, Ruben Esteban, Andrei G Borisov, Jeremy J Baumberg, Peter Nordlander, Henri J Lezec, Javier Aizpurua, and Kenneth B Crozier. Quantum mechanical effects in plasmonic structures with subnanometre gaps. *Nature communications*, 7(1):1–14, 2016.

[66] Emil Prodan, Corey Radloff, Naomi J Halas, and Peter Nordlander. A hybridization model for the plasmon response of complex nanostructures. *science*, 302(5644):419–422, 2003.

[67] A Downes, ME Taylor, and ME Welland. Two-sphere model of photon emission from the scanning tunneling microscope. *Physical Review B*, 57(11):6706, 1998.

[68] Xiao-Jun Tian, Fan-Fang Kong, Yun-Jie Yu, Shi-Hao Jing, Xian-Biao Zhang, Yuan Liao, Yao Zhang, Yang Zhang, and Zhen-Chao Dong. Plasmon-enhanced s2 electroluminescence from the high-lying excited state of a single porphyrin molecule. *Applied Physics Letters*, 117(24):243301, 2020.

[69] Peter B Johnson and R-WJPrB Christy. Optical constants of the noble metals. *Physical review B*, 6(12):4370, 1972.

[70] J H Weaver, H P R Frederikse, and David R Lide. Optical properties of selected elements. In *CRC handbook of chemistry and physics*, volume 85, chapter 12, pages 133–156. CRC press, 2004.

[71] Tomáš Neuman, Ruben Esteban, David Casanova, Francisco J García-Vidal, and Javier Aizpurua. Coupling of molecular emitters and plasmonic cavities beyond the point-dipole approximation. *Nano letters*, 18(4):2358–2364, 2018.

[72] Ben Yang, Gong Chen, Atif Ghafoor, Yufan Zhang, Yao Zhang, Yang Zhang, Yi Luo, Jinlong Yang, Vahid Sandoghdar, Javier Aizpurua, et al. Sub-nanometre resolution in single-molecule photoluminescence imaging. *Nature Photonics*, 14(11):693–699, 2020.

[73] Jascha Repp and Gerhard Meyer. Chapter 2 - stm manipulation of single atoms and molecules on insulating films. In Andrew J. Mayne and Gérald Dujardin, editors, *Atomic and Molecular Manipulation*, volume 2 of *Frontiers of Nanoscience*, pages 17–49. Elsevier, 2011.

[74] Fernando Aguilar-Galindo, Mario Zapata-Herrera, Sergio Díaz-Tendero, Javier Aizpurua, and Andrei G Borisov. Effect of a dielectric spacer on electronic and electromagnetic interactions at play in molecular exciton decay at surfaces and in plasmonic gaps. *ACS Photonics*, 8(12):3495–3505, 2021.

[75] E. M. Purcell, H. C. Torrey, and R. V. Pound. Resonance absorption by nuclear magnetic moments in a solid. *Phys. Rev.*, 69:37–38, Jan 1946.

[76] Willis E Lamb Jr and Robert C Retherford. Fine structure of the hydrogen atom by a microwave method. *Physical Review*, 72(3):241, 1947.

[77] Anna Rosławska, Tomáš Neuman, Benjamin Doppagne, Andrei G Borisov, Michelangelo Romeo, Fabrice Scheurer, Javier Aizpurua, and Guillaume Schull. Mapping lamb, stark, and purcell effects at a chromophore-picocavity junction with hyper-resolved fluorescence microscopy. *Physical Review X*, 12(1):011012, 2022.

[78] Rohit Chikkaraddy, Bart De Nijs, Felix Benz, Steven J Barrow, Oren A Scherman, Edina Rosta, Angela Demetriadou, Peter Fox, Ortwin Hess, and Jeremy J Baumberg. Single-molecule strong coupling at room temperature in plasmonic nanocavities. *Nature*, 535(7610):127–130, 2016.

[79] Oluwafemi S Ojambati, Rohit Chikkaraddy, William D Deacon, Matthew Horton, Dean Kos, Vladimir A Turek, Ulrich F Keyser, and Jeremy J Baumberg. Quantum electrodynamics at room temperature coupling a single vibrating molecule with a plasmonic nanocavity. *Nature communications*, 10(1):1–7, 2019.

[80] Klaus Kuhnke, Christoph Grosse, Pablo Merino, and Klaus Kern. Atomic-scale imaging and spectroscopy of electroluminescence at molecular interfaces. *Chemical reviews*, 117(7):5174–5222, 2017.

[81] Benjamin Doppagne, Michael C Chong, Hervé Bulou, Alex Boeglin, Fabrice Scheurer, and Guillaume Schull. Electrofluorochromism at the single-molecule level. *Science*, 361(6399):251–255, 2018.

[82] Z-C Dong, X-L Guo, AS Trifonov, PS Dorozhkin, K Miki, K Kimura, Shiyoshi Yokoyama, and S Mashiko. Vibrationally resolved fluorescence from organic molecules near metal surfaces in a scanning tunneling microscope. *Physical review letters*, 92(8):086801, 2004.

[83] Yao Zhang, Qiu-Shi Meng, Li Zhang, Yang Luo, Yun-Jie Yu, Ben Yang, Yang Zhang, Ruben Esteban, Javier Aizpurua, Yi Luo, et al. Subnanometre control of the coherent interaction between a single molecule and a plasmonic nanocavity. *Nature Communications*, 8(1):1–7, 2017.

[84] Hiroshi Imada, Kuniyuki Miwa, Miyabi Imai-Imada, Shota Kawahara, Kensuke Kimura, and Yousoo Kim. Single-molecule investigation of energy dynamics in a coupled plasmon-exciton system. *Physical review letters*, 119(1):013901, 2017.

[85] Jörg Kröger, Benjamin Doppagne, Fabrice Scheurer, and Guillaume Schull. Fano description of single-hydrocarbon fluorescence excited by a scanning tunneling microscope. *Nano Letters*, 18(6):3407–3413, 2018.

[86] Yang Luo, Gong Chen, Yang Zhang, Li Zhang, Yunjie Yu, Fanfang Kong, Xiaojun Tian, Yao Zhang, Chongxin Shan, Yi Luo, et al. Electrically driven single-photon superradiance from molecular chains in a plasmonic nanocavity. *Physical Review Letters*, 122(23):233901, 2019.

[87] Yang Luo, Fan-Fang Kong, Xiao-Jun Tian, Yun-Jie Yu, Li Zhang, Gong Chen, Yao Zhang, Yang Zhang, and Zhen-Chao Dong. What can single-molecule fano resonance tell? *The Journal of Chemical Physics*, 154(4):044309, 2021.

[88] Tzu-Chao Hung, Brian Kiraly, Julian H Strik, Alexander A Khajetoorians, and Daniel Wegner. Plasmon-driven motion of an individual molecule. *Nano letters*, 21(12):5006–5012, 2021.

[89] Kirill Vasilev, Benjamin Doppagne, Tomáš Neuman, Anna Rosławska, Hervé Bulou, Alex Boeglin, Fabrice Scheurer, and Guillaume Schull. Internal stark effect of single-molecule fluorescence. *Nature communications*, 13(1):1–8, 2022.

[90] Hiroshi Imada, Miyabi Imai-Imada, Kuniyuki Miwa, Hidemasa Yamane, Takeshi Iwasa, Yusuke Tanaka, Naoyuki Toriumi, Kensuke Kimura, Nobuhiko Yokoshi, Atsuya Muranaka, et al. Single-molecule laser nanospectroscopy with micro–electron volt energy resolution. *Science*, 373(6550):95–98, 2021.

[91] William E Moerner. Nobel lecture: Single-molecule spectroscopy, imaging, and photocontrol: Foundations for super-resolution microscopy. *Reviews of Modern Physics*, 87(4), 2015.

[92] S Kummer and Th Basche. Measurement of optical dephasing of a single terrylene molecule with nanosecond time resolution. *The Journal of Physical Chemistry*, 99(47):17078–17081, 1995.

[93] SW Wu, GV Nazin, and W Ho. Intramolecular photon emission from a single molecule in a scanning tunneling microscope. *Physical Review B*, 77(20):205430, 2008.

[94] Kensuke Kimura, Kuniyuki Miwa, Hiroshi Imada, Miyabi Imai-Imada, Shota Kawahara, Jun Takeya, Maki Kawai, Michael Galperin, and Yousoo Kim. Selective triplet exciton formation in a single molecule. *Nature*, 570(7760):210–213, 2019.

[95] Fan-Fang Kong, Xiao-Jun Tian, Yang Zhang, Yao Zhang, Gong Chen, Yun-Jie Yu, Shi-Hao Jing, Hong-Ying Gao, Yi Luo, Jin-Long Yang, et al. Wave-like electronic energy transfer in donor–acceptor molecular systems through quantum coherence. *Nature Nanotechnology*, pages 1–8, 2022.

[96] Hiroshi Imada, Miyabi Imai-Imada, Xingmei Ouyang, Atsuya Muranaka, and Yousoo Kim. Anti-kasha emissions of single molecules in a plasmonic nanocavity. *The Journal of Chemical Physics*, 157(10):104302, 2022.

[97] Th Basché, WE Moerner, M Orrit, and H Talon. Photon antibunching in the fluorescence of a single dye molecule trapped in a solid. *Physical review letters*, 69(10):1516, 1992.

[98] P Merino, C Große, A Rosławska, K Kuhnke, and K Kern. Exciton dynamics of c60-based single-photon emitters explored by hanbury brown–twiss scanning tunnelling microscopy. *Nature communications*, 6(1):1–6, 2015.

[99] Li Zhang, Yun-Jie Yu, Liu-Guo Chen, Yang Luo, Ben Yang, Fan-Fang Kong, Gong Chen, Yang Zhang, Qiang Zhang, Yi Luo, et al. Electrically driven single-photon emission from an isolated single molecule. *Nature communications*, 8(1):1–7, 2017.

[100] P Michler, A Imamoğlu, MD Mason, PJ Carson, GF Strouse, and SK Buratto. Quantum correlation among photons from a single quantum dot at room temperature. *Nature*, 406(6799):968–970, 2000.

[101] Boris Korzh, Qing-Yuan Zhao, Jason P Allmaras, Simone Frasca, Travis M Autry, Eric A Bersin, Andrew D Beyer, Ryan M Briggs, Bruce Bumble, Marco Colangelo, et al. Demonstration of sub-3 ps temporal resolution with a superconducting nanowire single-photon detector. *Nature Photonics*, 14(4):250–255, 2020.

[102] Tyler L Cocker, Dominik Peller, Ping Yu, Jascha Repp, and Rupert Huber. Tracking the ultrafast motion of a single molecule by femtosecond orbital imaging. *Nature*, 539(7628):263–267, 2016.

[103] Dominik Peller, Lukas Z Kastner, Thomas Buchner, Carmen Roelcke, Florian Albrecht, Nikolaj Moll, Rupert Huber, and Jascha Repp. Sub-cycle atomic-scale forces coherently control a single-molecule switch. *Nature*, 585(7823):58–62, 2020.

[104] SH Pan, Eric W Hudson, and JC Davis. 3 he refrigerator based very low temperature scanning tunneling microscope. *Review of scientific instruments*, 70(2):1459–1463, 1999.

[105] Aleš Cahlík. *Study of molecular structures on solid surfaces with scanning probe microscopy*. PhD thesis, Czech Technical University in Prague, 2021.

[106] K Kuhnke, A Kabakchiev, W Stiepany, F Zinser, R Vogelgesang, and K Kern. Versatile optical access to the tunnel gap in a low-temperature scanning tunneling microscope. *Review of Scientific Instruments*, 81(11):113102, 2010.

[107] Joonhee Lee, Shawn M Perdue, Alejandro Rodriguez Perez, and Vartkess Ara Apkarian. Vibronic motion with joint angstrom–femtosecond resolution observed through fano progressions recorded within one molecule. *ACS nano*, 8(1):54–63, 2014.

[108] Shuyi Liu, Martin Wolf, and Takashi Kumagai. Plasmon-assisted resonant electron tunneling in a scanning tunneling microscope junction. *Physical Review Letters*, 121(22):226802, 2018.

[109] Kevin Edelmann, Lukas Gerhard, Moritz Winkler, Lars Wilmes, Vibhuti Rai, Martin Schumann, Christian Kern, Michael Meyer, Martin Wegener, and Wulf Wulfhekel. Light collection from a low-temperature scanning tunneling microscope using integrated mirror tips fabricated by direct laser writing. *Review of Scientific Instruments*, 89(12):123107, 2018.

[110] Don Groom. Cosmic rays and other nonsense in astronomical ccd imagers. *Experimental Astronomy*, 14(1):45–55, 2002.

[111] Benjamin Doppagne. *Hyper-Resolved Fluorescence Microscopy with STM*. PhD thesis, Université de Strasbourg, 2020.

[112] Bruno Schuler, Katherine A Cochrane, Christoph Kastl, Edward S Barnard, Edward Wong, Nicholas J Borys, Adam M Schwartzberg, D Frank Ogletree, F Javier García de Abajo, and Alexander Weber-Bargioni. Electrically driven photon emission from individual atomic defects in monolayer ws2. *Science advances*, 6(38):eabb5988, 2020.

[113] Bruno Schuler. *Characterizing and identifying single molecules by scanning probe microscopy using functionalized tips*. PhD thesis, Universität Regensburg, October 2015.

[114] Nicholas Tallarida, Joonhee Lee, and Vartkess Ara Apkarian. Tip-enhanced raman spectromicroscopy on the angstrom scale: Bare and co-terminated ag tips. *ACS nano*, 11(11):11393–11401, 2017.

[115] Rafael B Jaculbia, Hiroshi Imada, Kuniyuki Miwa, Takeshi Iwasa, Masato Takenaka, Bo Yang, Emiko Kazuma, Norihiko Hayazawa, Tetsuya Taketsugu, and Yousoo Kim. Single-molecule resonance raman effect in a plasmonic nanocavity. *Nature nanotechnology*, 15(2):105–110, 2020.

[116] C Zhang, B Gao, LG Chen, QS Meng, H Yang, R Zhang, X Tao, HY Gao, Y Liao, and ZC Dong. Fabrication of silver tips for scanning tunneling microscope induced luminescence. *Review of Scientific Instruments*, 82(8):083101, 2011.

[117] Bo Yang, Emiko Kazuma, Yasuyuki Yokota, and Yousoo Kim. Fabrication of sharp gold tips by three-electrode electrochemical etching with high controllability and reproducibility. *The Journal of Physical Chemistry C*, 122(29):16950–16955, 2018.

[118] Hannes Böckmann, Shuyi Liu, Melanie Müller, Adnan Hammud, Martin Wolf, and Takashi Kumagai. Near-field manipulation in a scanning tunneling microscope junction with plasmonic fabry-pérot tips. *Nano letters*, 19(6):3597–3602, 2019.

[119] Koen Lauwaet, Koen Schouteden, Ewald Janssens, Chris Van Haesendonck, and Peter Lievens. Dependence of the nacl/au (111) interface state on the thickness of the nacl layer. *Journal of Physics: Condensed Matter*, 24(47):475507, 2012.

[120] Katharina Kaiser, Leo Gross, and Fabian Schulz. A single-molecule chemical reaction studied by high-resolution atomic force microscopy and scanning tunneling microscopy induced light emission. *ACS nano*, 13(6):6947–6954, 2019.

[121] Frédéric Rossel, Marina Pivetta, and Wolf-Dieter Schneider. Luminescence experiments on supported molecules with the scanning tunneling microscope. *Surface Science Reports*, 65(5):129–144, 2010.

[122] Joonhee Lee, Kevin T Crampton, Nicholas Tallarida, and V Apkarian. Visualizing vibrational normal modes of a single molecule with atomically confined light. *Nature*, 568(7750):78–82, 2019.

[123] Christoph Große, Olle Gunnarsson, Pablo Merino, Klaus Kuhnke, and Klaus Kern. Nanoscale imaging of charge carrier and exciton trapping at structural defects in organic semiconductors. *Nano Letters*, 16(3):2084–2089, 2016.

[124] Christoph Große, Pablo Merino, Anna Rosławska, Olle Gunnarsson, Klaus Kuhnke, and Klaus Kern. Submolecular electroluminescence mapping of organic semiconductors. *ACS nano*, 11(2):1230–1237, 2017.

[125] Gong Chen, Yang Luo, Hongying Gao, Jun Jiang, Yunjie Yu, Li Zhang, Yang Zhang, Xiaoguang Li, Zhenyu Zhang, and Zhenchao Dong. Spin-triplet-mediated up-conversion and crossover behavior in single-molecule electroluminescence. *Physical Review Letters*, 122(17):177401, 2019.

[126] Leo Gross, Bruno Schuler, Niko Pavliček, Shadi Fatayer, Zsolt Majzik, Nikolaj Moll, Diego Peña, and Gerhard Meyer. Atomic force microscopy for molecular structure elucidation. *Angewandte Chemie International Edition*, 57(15):3888–3908, 2018.

[127] Fabian Mohn, Leo Gross, Nikolaj Moll, and Gerhard Meyer. Imaging the charge distribution within a single molecule. *Nature nanotechnology*, 7(4):227–231, 2012.

[128] Rebecca LM Gieseking, Joonhee Lee, Nicholas Tallarida, Vartkess Ara Apkarian, and George C Schatz. Bias-dependent chemical enhancement and nonclassical stark effect in tip-enhanced raman spectromicroscopy of co-terminated ag tips. *The journal of physical chemistry letters*, 9(11):3074–3080, 2018.

[129] Joonhee Lee, Nicholas Tallarida, Xing Chen, Lasse Jensen, and V Ara Apkarian. Microscopy with a single-molecule scanning electrometer. *Science advances*, 4(6):eaat5472, 2018.

[130] Leo Gross, Nikolaj Moll, Fabian Mohn, Alessandro Curioni, Gerhard Meyer, Felix Hanke, and Mats Persson. High-resolution molecular orbital imaging using a p-wave stm tip. *Physical Review Letters*, 107(8):086101, 2011.

[131] Kuniyuki Miwa, Hiroshi Imada, Shota Kawahara, and Yousoo Kim. Effects of molecule-insulator interaction on geometric property of a single phthalocyanine molecule adsorbed on an ultrathin nacl film. *Physical Review B*, 93(16):165419, 2016.

[132] Sarah-Charlotta Heidorn, Cord Bertram, Pepa Cabrera-Sanfelix, and Karina Morgenstern. Consecutive mechanism in the diffusion of D_2O on a nacl (100) bilayer. *ACS nano*, 9(4):3572–3578, 2015.

[133] Anna Rosławska, Pablo Merino, Christoph Große, Christopher C Leon, Olle Gunnarsson, Markus Etzkorn, Klaus Kuhnke, and Klaus Kern. Single charge and exciton dynamics probed by molecular-scale-induced electroluminescence. *Nano Letters*, 18(6):4001–4007, 2018.

[134] Pablo Merino, Anna Rosławska, Christoph Große, Christopher C Leon, Klaus Kuhnke, and Klaus Kern. Bimodal exciton-plasmon light sources controlled by local charge carrier injection. *Science advances*, 4(5):eaap8349, 2018.

[135] Chi Chen, Ping Chu, CA Bobisch, DL Mills, and W Ho. Viewing the interior of a single molecule: vibronically resolved photon imaging at submolecular resolution. *Physical Review Letters*, 105(21):217402, 2010.

[136] Sarah-Charlotta Heidorn, André Sabellek, and Karina Morgenstern. Size dependence of the dispersion relation for the interface state between nacl (100) and ag (111). *Nano letters*, 14(1):13–17, 2014.

[137] Pingo Doležal, Jiříand Mutombo, Dana Nachtigallová, Pavel Jelínek, Pablo Merino, and Martin Švec. Mechano-optical switching of a single molecule with doublet emission. *ACS nano*, 14(7):8931–8938, 2020.

[138] PS Vincett, EM Voigt, and KE Rieckhoff. Phosphorescence and fluorescence of phthalocyanines. *The Journal of Chemical Physics*, 55(8):4131–4140, 1971.

[139] Ryota Matsuoka, Asato Mizuno, Takuto Mibu, and Tetsuro Kusamoto. Luminescence of doublet molecular systems. *Coordination Chemistry Reviews*, 467:214616, 2022.

[140] WE Moerner. Examining nanoenvironments in solids on the scale of a single, isolated impurity molecule. *Science*, 265(5168):46–53, 1994.

[141] X-Y Zhu, Q Yang, and M Muntwiler. Charge-transfer excitons at organic semiconductor surfaces and interfaces. *Accounts of chemical research*, 42(11):1779–1787, 2009.

[142] Archana Raja, Andrey Chaves, Jaeeun Yu, Ghidewon Arefe, Heather M Hill, Albert F Rigosi, Timothy C Berkelbach, Philipp Nagler, Christian Schüller, Tobias Korn, et al. Coulomb engineering of the bandgap and excitons in two-dimensional materials. *Nature communications*, 8(1):1–7, 2017.

[143] Miguel M Ugeda, Aaron J Bradley, Su-Fei Shi, Felipe H Da Jornada, Yi Zhang, Diana Y Qiu, Wei Ruan, Sung-Kwan Mo, Zahid Hussain, Zhi-Xun Shen, et al. Giant bandgap renormalization and excitonic effects in a monolayer transition metal dichalcogenide semiconductor. *Nature materials*, 13(12):1091–1095, 2014.

[144] Zhizhan Qiu, Maxim Trushin, Hanyan Fang, Ivan Verzhbitskiy, Shiyuan Gao, Evan Laksono, Ming Yang, Pin Lyu, Jing Li, Jie Su, et al. Giant gate-tunable bandgap renormalization and excitonic effects in a 2d semiconductor. *Science advances*, 5(7):eaaw2347, 2019.

[145] Andrew G Walsh, A Nickolas Vamivakas, Yan Yin, Stephen B Cronin, M Selim Ünlü, Bennett B Goldberg, and Anna K Swan. Screening of excitons in single, suspended carbon nanotubes. *Nano letters*, 7(6):1485–1488, 2007.

[146] Jack Deslippe, Mario Dipoppa, David Prendergast, Marcus VO Moutinho, Rodrigo B Capaz, and Steven G Louie. Electron- hole interaction in carbon nanotubes: novel screening and exciton excitation spectra. *Nano letters*, 9(4):1330–1334, 2009.

[147] Benjamin Doppagne, Tomáš Neuman, Ruben Soria-Martinez, Luis E Parra López, Hervé Bulou, Michelangelo Romeo, Stéphane Berciaud, Fabrice Scheurer, Javier Aizpurua, and Guillaume Schull. Single-molecule tautomerization tracking through space-and time-resolved fluorescence spectroscopy. *Nature nanotechnology*, 15(3):207–211, 2020.

[148] Kenichi Goushi, Kou Yoshida, Keigo Sato, and Chihaya Adachi. Organic light-emitting diodes employing efficient reverse intersystem crossing for triplet-to-singlet state conversion. *Nature Photonics*, 6(4):253–258, 2012.

[149] Michael A Becker, Roman Vaxenburg, Georgian Nedelcu, Peter C Sercel, Andrew Shabaev, Michael J Mehl, John G Michopoulos, Samuel G Lambrakos, Noam Bernstein, John L Lyons, et al. Bright triplet excitons in caesium lead halide perovskites. *Nature*, 553(7687):189–193, 2018.

[150] Xin Ai, Emrys W Evans, Shengzhi Dong, Alexander J Gillett, Haoqing Guo, Yingxin Chen, Timothy JH Hele, Richard H Friend, and Feng Li. Efficient radical-based light-emitting diodes with doublet emission. *Nature*, 563(7732):536–540, 2018.

[151] Cornelius Krull, Roberto Robles, Aitor Mugarza, and Pietro Gambardella. Site-and orbital-dependent charge donation and spin manipulation in electron-doped metal phthalocyanines. *Nature Materials*, 12(4):337–343, 2013.

[152] A Atxabal, M Ribeiro, S Parui, L Urreta, E Sagasta, X Sun, R Llopis, F Casanova, and LE Hueso. Spin doping using transition metal phthalocyanine molecules. *Nature communications*, 7(1):1–7, 2016.

[153] Marc Warner, Salahud Din, Igor S Tupitsyn, Gavin W Morley, A Marshall Stoneham, Jules A Gardener, Zhenlin Wu, Andrew J Fisher, Sandrine Heutz, Christopher WM Kay, et al. Potential for spin-based information processing in a thin-film molecular semiconductor. *Nature*, 503(7477):504–508, 2013.

[154] Benjamin W Caplins, Tyler K Mullenbach, Russell J Holmes, and David A Blank. Femtosecond to nanosecond excited state dynamics of vapor deposited copper phthalocyanine thin films. *Physical Chemistry Chemical Physics*, 18(16):11454–11459, 2016.

[155] T Uemura, M Furumoto, T Nakano, M Akai-Kasaya, A Saito, M Aono, and Y Kuwahara. Local-plasmon-enhanced up-conversion fluorescence from copper phthalocyanine. *Chemical Physics Letters*, 448(4-6):232–236, 2007.

[156] Fredrik E Olsson, Mats Persson, Jascha Repp, and Gerhard Meyer. Scanning tunneling microscopy and spectroscopy of nacl overlayers on the stepped cu (311) surface: Experimental and theoretical study. *Physical Review B*, 71(7):075419, 2005.

[157] Marina Pivetta, François Patthey, Massimiliano Stengel, Alfonso Baldereschi, and Wolf-Dieter Schneider. Local work function moiré pattern on ultrathin ionic films: Nacl on ag (100). *Physical Review B*, 72(11):115404, 2005.

[158] Michael Ellner, Niko Pavlicek, Pablo Pou, Bruno Schuler, Nikolaj Moll, Gerhard Meyer, Leo Gross, and Rubén Peréz. The electric field of co tips and its relevance for atomic force microscopy. *Nano Letters*, 16(3):1974–1980, 2016.

[159] Philipp Scheuerer, Laerte L Patera, Felix Simbürger, Fabian Queck, Ingmar Swart, Bruno Schuler, Leo Gross, Nikolaj Moll, and Jascha Repp. Charge-induced structural changes in a single molecule investigated by atomic force microscopy. *Physical Review Letters*, 123(6):066001, 2019.

[160] Dietrich RT Zahn, Gianina N Gavrila, and Mihaela Gorgoi. The transport gap of organic semiconductors studied using the combination of direct and inverse photoemission. *Chemical Physics*, 325(1):99–112, 2006.

[161] IG Hill, A Kahn, ZG Soos, and RA Pascal Jr. Charge-separation energy in films of π-conjugated organic molecules. *Chemical Physics Letters*, 327(3-4):181–188, 2000.

[162] Martin Knupfer. Exciton binding energies in organic semiconductors. *Applied Physics A*, 77(5):623–626, 2003.

[163] Volker Blum, Ralf Gehrke, Felix Hanke, Paula Havu, Ville Havu, Xinguo Ren, Karsten Reuter, and Matthias Scheffler. Ab initio molecular simulations with numeric atom-centered orbitals. *Computer Physics Communications*, 180(11):2175–2196, 2009.

[164] Alexandre Tkatchenko and Matthias Scheffler. Accurate molecular van der waals interactions from ground-state electron density and free-atom reference data. *Physical review letters*, 102(7):073005, 2009.

[165] E van Lenthe, Evert-Jan Baerends, and Jaap G Snijders. Relativistic regular two-component hamiltonians. *The Journal of chemical physics*, 99(6):4597–4610, 1993.

[166] Jeng-Da Chai and Martin Head-Gordon. Long-range corrected hybrid density functionals with damped atom–atom dispersion corrections. *Physical Chemistry Chemical Physics*, 10(44):6615–6620, 2008.

[167] Oleg A Vydrov and Gustavo E Scuseria. Assessment of a long-range corrected hybrid functional. *The Journal of chemical physics*, 125(23):234109, 2006.

[168] Oleg A Vydrov, Jochen Heyd, Aliaksandr V Krukau, and Gustavo E Scuseria. Importance of short-range versus long-range hartree-fock exchange for the performance of hybrid density functionals. *The Journal of chemical physics*, 125(7):074106, 2006.

[169] Oleg A Vydrov, Gustavo E Scuseria, and John P Perdew. Tests of functionals for systems with fractional electron number. *The Journal of chemical physics*, 126(15):154109, 2007.

[170] Ansgar Schäfer, Hans Horn, and Reinhart Ahlrichs. Fully optimized contracted gaussian basis sets for atoms li to kr. *The Journal of Chemical Physics*, 97(4):2571–2577, 1992.

[171] Ansgar Schäfer, Christian Huber, and Reinhart Ahlrichs. Fully optimized contracted gaussian basis sets of triple zeta valence quality for atoms li to kr. *The Journal of Chemical Physics*, 100(8):5829–5835, 1994.

[172] A Becke. Density-functional thermochemistry. iii. the role of exact exchange (1993) j. *Chem. Phys*, 98:5648.

[173] Chengteh Lee, Weitao Yang, and Robert G Parr. Development of the colle-salvetti correlation-energy formula into a functional of the electron density. *Physical review B*, 37(2):785, 1988.

162

[174] Philip J Stephens, Frank J Devlin, Cary F Chabalowski, and Michael J Frisch. Ab initio calculation of vibrational absorption and circular dichroism spectra using density functional force fields. *The Journal of physical chemistry*, 98(45):11623–11627, 1994.

[175] MJ Frisch, GW Trucks, HB Schlegel, GE Scuseria, MA Robb, JR Cheeseman, G Scalmani, VPGA Barone, GA Petersson, HJRA Nakatsuji, et al. Gaussian 16 Revision C.01, 2016.

[176] Jiří Doležal, Sofia Canola, Pablo Merino, and Martin Švec. Exciton-trion conversion dynamics in a single molecule. *ACS nano*, 15(4):7694–7699, 2021.

[177] Shadi Fatayer, Florian Albrecht, Yunlong Zhang, Darius Urbonas, Diego Peña, Nikolaj Moll, and Leo Gross. Molecular structure elucidation with charge-state control. *Science*, 365(6449):142–145, 2019.

[178] Anika Kinkhabwala, Zongfu Yu, Shanhui Fan, Yuri Avlasevich, Klaus Müllen, and William E Moerner. Large single-molecule fluorescence enhancements produced by a bowtie nanoantenna. *Nature photonics*, 3(11):654–657, 2009.

[179] VA Apkarian and N Schwentner. Molecular photodynamics in rare gas solids. *Chemical Reviews*, 99(6):1481–1514, 1999.

[180] Brahim Lounis and William E Moerner. Single photons on demand from a single molecule at room temperature. *Nature*, 407(6803):491–493, 2000.

[181] Alexios Beveratos, Rosa Brouri, Thierry Gacoin, André Villing, Jean-Philippe Poizat, and Philippe Grangier. Single photon quantum cryptography. *Physical review letters*, 89(18):187901, 2002.

[182] Jeremy L O'brien. Optical quantum computing. *Science*, 318(5856):1567–1570, 2007.

[183] Anna Rosławska, Christopher C Leon, Abhishek Grewal, Pablo Merino, Klaus Kuhnke, and Klaus Kern. Atomic-scale dynamics probed by photon correlations. *ACS nano*, 14(6):6366–6375, 2020.

[184] Aftab Farrukh, Xiao-jun Tian, Fan-fang Kong, Yun-jie Yu, Shi-hao Jing, Gong Chen, Yao Zhang, Yuan Liao, Yang Zhang, and Zhen-chao Dong. Bias-polarity dependent electroluminescence from a single platinum phthalocyanine molecule. *Chinese Journal of Chemical Physics*, 34(1):87–94, 2021.

[185] Pablo Merino, Anna Rosławska, Christopher C Leon, Abhishek Grewal, Christoph Große, Cesar González, Klaus Kuhnke, and Klaus Kern. A single hydrogen molecule as an intensity chopper in an electrically driven plasmonic nanocavity. *Nano letters*, 19(1):235–241, 2018.

[186] Christopher C Leon, Anna Rosławska, Abhishek Grewal, Olle Gunnarsson, Klaus Kuhnke, and Klaus Kern. Photon superbunching from a generic tunnel junction. *Science advances*, 5(5):eaav4986, 2019.

[187] Christopher C Leon, Olle Gunnarsson, Dimas G de Oteyza, Anna Rosławska, Pablo Merino, Abhishek Grewal, Klaus Kuhnke, and Klaus Kern. Single photon emission from a plasmonic light source driven by a local field-induced coulomb blockade. *ACS nano*, 14(4):4216–4223, 2020.

[188] Christoph Grosse, Markus Etzkorn, Klaus Kuhnke, Sebastian Loth, and Klaus Kern. Quantitative mapping of fast voltage pulses in tunnel junctions by plasmonic luminescence. *Applied Physics Letters*, 103(18):183108, 2013.

[189] Alberto Martín-Jiménez, Antonio I Fernández-Domínguez, Koen Lauwaet, Daniel Granados, Rodolfo Miranda, Francisco J García-Vidal, and Roberto Otero. Unveiling the radiative local density of optical states of a plasmonic nanocavity by stm. *Nature communications*, 11(1):1–8, 2020.

[190] Xian-Fu Zhang and Hui-Jun Xu. Influence of halogenation and aggregation on photosensitizing properties of zinc phthalocyanine (znpc). *Journal of the Chemical Society, Faraday Transactions*, 89(18):3347–3351, 1993.

[191] Moshe G Harats, Jan N Kirchhof, Mengxiong Qiao, Kyrylo Greben, and Kirill I Bolotin. Dynamics and efficient conversion of excitons to trions in non-uniformly strained monolayer ws2. *Nature Photonics*, 14(5):324–329, 2020.

[192] Jinbo Peng, Sophia Sokolov, Daniel Hernangómez-Pérez, Ferdinand Evers, Leo Gross, John M Lupton, and Jascha Repp. Atomically resolved single-molecule triplet quenching. *Science*, 373(6553):452–456, 2021.

[193] Tzu-Chao Hung, Roberto Robles, Brian Kiraly, Julian H Strik, Bram A Rutten, Alexander A Khajetoorians, Nicolas Lorente, and Daniel Wegner. Bipolar single-molecule electroluminescence and electrofluorochromism. *arXiv preprint arXiv:2210.11118*, 2022.

[194] Tian Lu and Feiwu Chen. Multiwfn: a multifunctional wavefunction analyzer. *Journal of computational chemistry*, 33(5):580–592, 2012.

[195] Jiří Doležal, Pablo Merino, and Martin Švec. Constant amplitude driving of a radio frequency excited plasmonic tunnel junction. *Applied physics letters*, 118(19):193301, 2021.

[196] U Kemiktarak, T Ndukum, KC Schwab, and KL Ekinci. Radio-frequency scanning tunnelling microscopy. *Nature*, 450(7166):85–88, 2007.

[197] Stefan Müllegger, Amal K Das, Karlheinz Mayr, and Reinhold Koch. Radio-frequency excitation of single molecules by scanning tunnelling microscopy. *Nanotechnology*, 25(13):135705, 2014.

[198] Olof Peters, Nils Bogdanoff, Sergio Acero Gonzalez, Larissa Melischek, J Rika Simon, Gael Reecht, Clemens B Winkelmann, Felix von Oppen, and Katharina J Franke. Photon-assisted tunneling at the atomic scale: Probing resonant andreev reflections from yu-shiba-rusinov states. *arXiv preprint arXiv:2001.09534*, 2020.

[199] J Friedlein, J Harm, P Lindner, L Bargsten, M Bazarnik, S Krause, and R Wiesendanger. A radio-frequency spin-polarized scanning tunneling microscope. *Review of Scientific Instruments*, 90(12):123705, 2019.

[200] Piotr Kot, Robert Drost, Maximilian Uhl, Joachim Ankerhold, Juan Carlos Cuevas, and Christian R Ast. Microwave-assisted tunneling and interference effects in superconducting junctions under fast driving signals. *Physical Review B*, 101(13):134507, 2020.

[201] Fabian D Natterer, François Patthey, Tobias Bilgeri, Patrick R Forrester, Nicolas Weiss, and Harald Brune. Upgrade of a low-temperature scanning tunneling microscope for electron-spin resonance. *Review of Scientific Instruments*, 90(1):013706, 2019.

[202] Kai Yang, Philip Willke, Yujeong Bae, Alejandro Ferrón, Jose L Lado, Arzhang Ardavan, Joaquín Fernández-Rossier, Andreas J Heinrich, and Christopher P Lutz. Electrically controlled nuclear polarization of individual atoms. *Nature nanotechnology*, 13(12):1120–1125, 2018.

[203] E Chilla, W Rohrbeck, H-J Fröhlich, R Koch, and KH Rieder. Scanning tunneling microscopy of rf oscillating surfaces. *Annalen der Physik*, 506(1):21–27, 1994.

[204] Thorsten Hesjedal. Surface acoustic wave-assisted scanning probe microscopy—a summary. *Reports on progress in Physics*, 73(1):016102, 2009.

[205] William Paul, Susanne Baumann, Christopher P Lutz, and Andreas J Heinrich. Generation of constant-amplitude radio-frequency sweeps at a tunnel junction for spin resonance stm. *Review of Scientific Instruments*, 87(7):074703, 2016.

[206] M Hervé, M Peter, and W Wulfhekel. High frequency transmission to a junction of a scanning tunneling microscope. *Applied Physics Letters*, 107(9):093101, 2015.

[207] Tom S Seifert, S Kovarik, Corneliu Nistor, Luca Persichetti, Sebastian Stepanow, and Pietro Gambardella. Single-atom electron paramagnetic resonance in a scanning tunneling microscope driven by a radio-frequency antenna at 4 k. *Physical Review Research*, 2(1):013032, 2020.

[208] A Roychowdhury, M Dreyer, JR Anderson, CJ Lobb, and FC Wellstood. Microwave photon-assisted incoherent cooper-pair tunneling in a josephson stm. *Physical Review Applied*, 4(3):034011, 2015.

[209] Greg P Kochanski. Nonlinear alternating-current tunneling microscopy. *Physical review letters*, 62(19):2285, 1989.

[210] Matthew Rycenga, Claire M Cobley, Jie Zeng, Weiyang Li, Christine H Moran, Qiang Zhang, Dong Qin, and Younan Xia. Controlling the synthesis and assembly of silver nanostructures for plasmonic applications. *Chemical reviews*, 111(6):3669–3712, 2011.

[211] Javier Aizpurua, S Peter Apell, and Richard Berndt. Role of tip shape in light emission from the scanning tunneling microscope. *Physical Review B*, 62(3):2065, 2000.

[212] Ulrich Dieter Felix Keil, Taekjip Ha, Jacob Riis Jensen, and Jorn M Hvam. Femtosecond tunneling response of surface plasmon polaritons. *Applied physics letters*, 72(23):3074–3076, 1998.

[213] Guillaume Schull, Nicolas Néel, Peter Johansson, and Richard Berndt. Electron-plasmon and electron-electron interactions at a single atom contact. *Physical review letters*, 102(5):057401, 2009.

[214] E Ekici, P Kapitza, CA Bobisch, and R Möller. Electron-induced photon emission above the quantum cutoff due to time-energy uncertainty. *Optics Letters*, 42(22):4585–4588, 2017.

[215] Jiří Doležal, Sofia Canola, Prokop Hapala, Rodrigo Cezar de Campos Ferreira, Pablo Merino, and Martin Švec. Real space visualization of entangled excitonic states in charged molecular assemblies. *ACS nano*, 16(1):1082–1088, 2021.

[216] Sangeeth Kallatt, Sarthak Das, Suman Chatterjee, and Kausik Majumdar. Interlayer charge transport controlled by exciton–trion coherent coupling. *npj 2D Materials and Applications*, 3(1):1–8, 2019.

[217] Weitao Su, Honglei Dou, Dexuan Huo, Ning Dai, and Li Yang. Enhancing photoluminescence of trion in single-layer mos2 using p-type aromatic molecules. *Chemical Physics Letters*, 635:40–44, 2015.

[218] Kin Fai Mak, Keliang He, Jie Shan, and Tony F Heinz. Control of valley polarization in monolayer mos2 by optical helicity. *Nature nanotechnology*, 7(8):494–498, 2012.

[219] Kin Fai Mak, Keliang He, Changgu Lee, Gwan Hyoung Lee, James Hone, Tony F Heinz, and Jie Shan. Tightly bound trions in monolayer mos2. *Nature materials*, 12(3):207–211, 2013.

[220] Fengnian Xia, Han Wang, Di Xiao, Madan Dubey, and Ashwin Ramasubramaniam. Two-dimensional material nanophotonics. *Nature Photonics*, 8(12):899–907, 2014.

[221] Delphine Pommier, Rémi Bretel, Luis E Parra López, Florentin Fabre, Andrew Mayne, Elizabeth Boer-Duchemin, Gérald Dujardin, Guillaume Schull, Stéphane Berciaud, and Eric Le Moal. Scanning tunneling microscope-induced excitonic luminescence of a two-dimensional semiconductor. *Physical Review Letters*, 123(2):027402, 2019.

[222] C Toninelli, I Gerhardt, AS Clark, A Reserbat-Plantey, Stephan Götzinger, Z Ristanović, M Colautti, P Lombardi, KD Major, I Deperasińska, et al. Single organic molecules for photonic quantum technologies. *Nature Materials*, 20(12):1615–1628, 2021.

[223] Vibhuti Rai, Lukas Gerhard, Qing Sun, Christof Holzer, Taavi Repän, Marjan Krstić, Liang Yang, Martin Wegener, Carsten Rockstuhl, and Wulf Wulfhekel. Boosting light emission from single hydrogen phthalocyanine molecules by charging. *Nano letters*, 20(10):7600–7605, 2020.

[224] C Hettich, C Schmitt, J Zitzmann, S Kuhn, Ilja Gerhardt, and Vahid Sandoghdar. Nanometer resolution and coherent optical dipole coupling of two individual molecules. *Science*, 298(5592):385–389, 2002.

[225] Bengt Nordén. Quantum entanglement: facts and fiction–how wrong was einstein after all? *Quarterly Reviews of Biophysics*, 49, 2016.

[226] Nicholas J Hestand and Frank C Spano. Molecular aggregate photophysics beyond the kasha model: novel design principles for organic materials. *Accounts of chemical research*, 50(2):341–350, 2017.

[227] Maria A Castellanos, Amro Dodin, and Adam P Willard. On the design of molecular excitonic circuits for quantum computing: the universal quantum gates. *Physical Chemistry Chemical Physics*, 22(5):3048–3057, 2020.

[228] Minhaeng Cho. Coherent two-dimensional optical spectroscopy. *Chemical reviews*, 108(4):1331–1418, 2008.

[229] Michael A. Nielsen and Isaac L. Chuang. *Quantum Computation and Quantum Information: 10th Anniversary Edition*. Cambridge University Press, 2010.

[230] Volkhard May and Oliver Kühn. *Charge and energy transfer dynamics in molecular systems*. John Wiley & Sons, 2008.

[231] Shuiyan Cao, Anna Rosławska, Benjamin Doppagne, Michelangelo Romeo, Michel Féron, Frédéric Chérioux, Hervé Bulou, Fabrice Scheurer, and Guillaume Schull. Energy funnelling within multichromophore architectures monitored with subnanometre resolution. *Nature Chemistry*, 13(8):766–770, 2021.

[232] Guohui Dong, Zhubin Hu, Xiang Sun, and Hui Dong. Structural reconstruction of optically invisible state in a single molecule via scanning tunneling microscope. *The Journal of Physical Chemistry Letters*, 12(41):10034–10039, 2021.

[233] Xing Gao and Alexander Eisfeld. Near-field spectroscopy of nanoscale molecular aggregates. *The Journal of Physical Chemistry Letters*, 9(20):6003–6010, 2018.

[234] Katherine A Cochrane, Agustin Schiffrin, Tanya S Roussy, Martina Capsoni, and Sarah A Burke. Pronounced polarization-induced energy level shifts at boundaries of organic semiconductor nanostructures. *Nature communications*, 6(1):1–8, 2015.

[235] SA Burke, W Ji, JM Mativetsky, JM Topple, S Fostner, H-J Gao, H Guo, and P Grütter. Strain induced dewetting of a molecular system: bimodal growth of ptcda on nacl. *Physical review letters*, 100(18):186104, 2008.

167

[236] Martin Zonda, Oleksandr Stetsovych, Richard Korytár, Markus Ternes, Ruslan Temirov, Andrea Raccanelli, F Stefan Tautz, Pavel Jelínek, Tomáš Novotny, and Martin Švec. Resolving ambiguity of the kondo temperature determination in mechanically tunable single-molecule kondo systems. *The journal of physical chemistry letters*, 12(27):6320–6325, 2021.

[237] A Paulheim, C Marquardt, M Sokolowski, M Hochheim, T Bredow, H Aldahhak, E Rauls, and WG Schmidt. Surface induced vibrational modes in the fluorescence spectra of ptcda adsorbed on the kcl (100) and nacl (100) surfaces. *Physical Chemistry Chemical Physics*, 18(48):32891–32902, 2016.

[238] Philipp Scheuerer, Laerte L Patera, and Jascha Repp. Manipulating and probing the distribution of excess electrons in an electrically isolated self-assembled molecular structure. *Nano Letters*, 20(3):1839–1845, 2020.

[239] Jiří Doležal, Sofia Canola, Prokop Hapala, Rodrigo Cezar de Campos Ferreira, Pablo Merino, and Martin Švec. Evidence of exciton-libron coupling in chirally adsorbed single molecules. *Nature Communications*, 13(6008), 2022.

[240] Jianshu Cao, Richard J Cogdell, David F Coker, Hong-Guang Duan, Jürgen Hauer, Ulrich Kleinekathöfer, Thomas LC Jansen, Tomáš Mančal, RJ Dwayne Miller, Jennifer P Ogilvie, et al. Quantum biology revisited. *Science Advances*, 6(14):eaaz4888, 2020.

[241] Vivek Tiwari, William K Peters, and David M Jonas. Electronic resonance with anticorrelated pigment vibrations drives photosynthetic energy transfer outside the adiabatic framework. *Proceedings of the National Academy of Sciences*, 110(4):1203–1208, 2013.

[242] Gitt Panitchayangkoon, Dmitri V Voronine, Darius Abramavicius, Justin R Caram, Nicholas HC Lewis, Shaul Mukamel, and Gregory S Engel. Direct evidence of quantum transport in photosynthetic light-harvesting complexes. *Proceedings of the National Academy of Sciences*, 108(52):20908–20912, 2011.

[243] C Schnedermann, X Yang, M Liebel, KM Spillane, J Lugtenburg, I Fernández, A Valentini, I Schapiro, Massimo Olivucci, P Kukura, et al. Evidence for a vibrational phase-dependent isotope effect on the photochemistry of vision. *Nature chemistry*, 10(4):449–455, 2018.

[244] Susanne Hahn and Gerhard Stock. Quantum-mechanical modeling of the femtosecond isomerization in rhodopsin. *The Journal of Physical Chemistry B*, 104(6):1146–1149, 2000.

[245] Gregg S Kottas, Laura I Clarke, Dominik Horinek, and Josef Michl. Artificial molecular rotors. *Chemical Reviews*, 105(4):1281–1376, 2005.

[246] Jamie Conyard, Kiri Addison, Ismael A Heisler, Arjen Cnossen, Wesley R Browne, Ben L Feringa, and Stephen R Meech. Ultrafast dynamics in the power stroke of a molecular rotary motor. *Nature chemistry*, 4(7):547–551, 2012.

[247] Veaceslav Coropceanu, Xian-Kai Chen, Tonghui Wang, Zilong Zheng, and Jean-Luc Brédas. Charge-transfer electronic states in organic solar cells. *Nature Reviews Materials*, 4(11):689–707, 2019.

[248] Alberto Torres, Robson S Oliboni, and Luis GC Rego. Vibronic and coherent effects on interfacial electron transfer dynamics. *The journal of physical chemistry letters*, 6(24):4927–4935, 2015.

[249] Johannes Schaffert, Maren C Cottin, Andreas Sonntag, Hatice Karacuban, Christian A Bobisch, Nicolás Lorente, Jean-Pierre Gauyacq, and Rolf Möller. Imaging the dynamics of individually adsorbed molecules. *Nature materials*, 12(3):223–227, 2013.

[250] Jens Kügel, Lucas Klein, Markus Leisegang, and Matthias Bode. Analyzing and tuning the energetic landscape of h2pc tautomerization. *The Journal of Physical Chemistry C*, 121(50):28204–28210, 2017.

[251] Yannick Baeten, Eduard Fron, Christian Ruzié, Yves Henri Geerts, and Mark Van Der Auweraer. Investigation of the qx–qy equilibrium in a metal-free phthalocyanine. *ChemPhysChem*, 16(18):3992–3996, 2015.

[252] A Paulheim, C Marquardt, H Aldahhak, E Rauls, WG Schmidt, and M Sokolowski. Inhomogeneous and homogeneous line broadening of optical spectra of ptcda molecules adsorbed at step edges of alkali halide surfaces. *The Journal of Physical Chemistry C*, 120(22):11926–11937, 2016.

[253] Christian Marquardt, Alexander Paulheim, Manuel Hochheim, Thomas Bredow, and Moritz Sokolowski. Homogeneous and inhomogeneous line shape of the electronic excitation of a single molecule on a surface. *Physical Review B*, 104(4):045415, 2021.

[254] Laerte L Patera, Fabian Queck, Philipp Scheuerer, Nikolaj Moll, and Jascha Repp. Accessing a charged intermediate state involved in the excitation of single molecules. *Physical Review Letters*, 123(1):016001, 2019.

[255] Alberto Martín-Jiménez, Koen Lauwaet, Óscar Jover, Daniel Granados, Andrés Arnau, Vyacheslav M Silkin, Rodolfo Miranda, and Roberto Otero. Electronic temperature and two-electron processes in overbias plasmonic emission from tunnel junctions. *Nano Letters*, 21(16):7086–7092, 2021.

[256] Jiří Doležal, Martin Švec, and Prokop Hapala. Franck–condon model. https://doi.org/10.5281/zenodo.6726424, 2022.

[257] Max Hänze, Gregory McMurtrie, Susanne Baumann, Luigi Malavolti, Susan N Coppersmith, and Sebastian Loth. Quantum stochastic resonance of individual fe atoms. *Science Advances*, 7(33):eabg2616, 2021.

[258] Emiko Kazuma, Jaehoon Jung, Hiromu Ueba, Michael Trenary, and Yousoo Kim. Real-space and real-time observation of a plasmon-induced chemical reaction of a single molecule. *Science*, 360(6388):521–526, 2018.

[259] Prokop Hapala, Ruslan Temirov, F Stefan Tautz, and Pavel Jelínek. Origin of high-resolution iets-stm images of organic molecules with functionalized tips. *Physical review letters*, 113(22):226101, 2014.

[260] Jiří Libra. Kolxpd. https://kolibrik.net.

[261] Joseph R Lakowicz. Time-domain lifetime measurements. In *Principles of fluorescence spectroscopy*, pages 95–140. Springer, 2006.

[262] Fabrizio Gabbiani and Steven J Cox. *Mathematics for neuroscientists*. Academic Press, 2017.

[263] Robert S Mulliken. Electronic population analysis on lcao–mo molecular wave functions. i. *The Journal of Chemical Physics*, 23(10):1833–1840, 1955.

List of Abbreviations

AC   alternating current

AFM   atomic force microscopy

AM   amplitude modulation

APD   avalanche photodetector

CCD   charge-coupled device

cps   counts per second

CW   continuous wave

DC   direct current

DFT   density functional theory

DNA   Deoxyribonucleic acid

DPSS   diode-pumped solid-state

EF   Fermi level

EM   electromagnetic

ESR   electron spin resonance

FF   far field

FHI-aims   Fritz Haber Institute ab initio materials simulations

FIB   focused ion beam

FM   frequency modulation

FM-AFM   frequency modulation atomic force microscopy

FWMH   full width at half-maximum

GGA-PBE   Generalized Gradient Approximation Pedrew, Burke, Ernzerhof

H2Pc   free-base phthalocyanine

HBT   Hanbury Brown Twiss

HOMO   highest occupied molecular orbital

CH   constant height

IBM   International Business Machines Corporation

IC   internal conversion

IRF   instrumental response function

ISC   intersystem crossing

LCPD local contact potential difference

LDOS local density of states

LHe   liquid helium

LN   liquid nitrogen

LUMO lowest unoccupied molecular orbital

MgPc magnesium phthalocyanine

ML   monolayer

nc-AFM noncontact atomic force microscopy

NCP   nanocavity plasmon

NF   near field

NIR   negative ion resonance

NPoM nanoparticle-on-mirror

PEEK Polyether ether ketone

PIR   positive ion resonance

PLL   Phase-locked loop

PTCDA Perylenetetracarboxylic dianhydride

RC   resistor-capacitor

RET   resonant electron transfer (or resonant energy transfer)

RF-PS radio frequency phase-shift

S/N   signal-to-noise

SEM   scanning electron microscope

SOMO singly occupied molecular orbital

SMA   SubMiniature version A

SPAD single photon avalanche detector

SPCM single photon counting module

SPM   scanning probe microscopy

SPP   surface plasmon polariton

STM   scanning tunneling microscopy

STM-EL   STM-induced electroluminescence

STML   STM-induced luminescence

STM-PL   STM-induced photoluminescence

STS   scanning tunneling spectroscopy

SUMO   singly occupied molecular orbital

SVP   split valence polarization

TCP   Transmission Control Protocol

TCSPC   time-correlated single photon counting

TDA   Tamm-Dancoff approximation

TD-DFT   time-dependent density functional theory

TERS   tip-enhanced Raman scattering

UHV   ultra high vacuum

UV   ultra violet

vdW   van der Waals

VNIR   visible-near infrared

ZnPc   zinc phthalocyanine

List of Publications

1. **Jiří Doležal**, Sofia Canola, Prokop Hapala, Rodrigo Cezar de Campos Ferreira, Pablo Merino and Martin Švec.
   Evidence of exciton-libron coupling in chirally adsorbed single molecules.
   Nature Communications, 13 (6008), 2022.

2. **Jiří Doležal**, Sofia Canola, Prokop Hapala, Rodrigo Cezar de Campos Ferreira, Pablo Merino and Martin Švec.
   Real space visualization of entangled excitonic states in charged molecular assemblies.
   ACS nano, 16 (1), 1082-1088, 2022.

3. **Jiří Doležal**, Sofia Canola, Pablo Merino and Martin Švec.
   Constant amplitude driving of a radio frequency excited plasmonic tunnel junction.
   Applied Physics Letters, 118 (19), 193301, 2021.

4. **Jiří Doležal**, Pablo Merino, Sofia Canola and Martin Švec.
   Exciton-Trion Conversion Dynamics in a Single Molecule.
   ACS Nano, 15 (4), 7694-7699, 2021.

5. **Jiří Doležal**, Pingo Mutombo, Dana Nachtigallová, Pavel Jelínek, Pablo Merino and Martin Švec.
   Mechano-Optical Switching of a Single Molecule with Doublet Emission.
   ACS Nano, 14 (7), 8931-8938, 2020.

6. **Jiří Doležal**, Pablo Merino, Jesus Redondo, Lukáš Ondič, Aleš Cahlík and Martin Švec.
   Charge carrier injection electroluminescence with CO functionalized tips on single molecular emitters.
   Nano letters, 19 (12), 8605-8611, 2019.

Author contributions

The thesis is based on the 6 published papers presented in chapters 3–8 and listed above of which I am the first author. In all cases, I carried out the majority of experiments, analyzed the experimental data and contributed to the preparation of figures and writing of the manuscript. I am a corresponding author of publications No 1 and 3. Nevertheless, this work would not be possible without my collaborators.

Theoreticians Pingo Mutombo and Pavel Jelínek performed the DFT simulations and Dana Nachigallová performed the TD-DFT simulations presented in publication No 5. Sofia Canola performed the TD-DFT calculations and prepared the corresponding figures in publications No 1, 2 and 4. Prokop Hapala implemented the "photon map simulation" tool in his Probe-Particle model in publication No 2 and devised the Franck-Condon model used in publication No 1. Another substantial part of the presented work resulted from the collaboration with experimentalists. Jesus Redondo and Aleš Cahlík helped with carrying out the experiments in publication No 6. Lukáš Ondič helped us with setting out the optical setup, especially for publication No 6. Rodrigo Cezar de Campos Ferreira Contributed to the measurements and data analysis in publications No 1 and 2. Pablo Merino helped to conceive some of the experiments and contributed to the data interpretation and writing of all manuscripts. Other people who contributed to this work are Jaromír Kopeček, who operates the FIB and prepared all the tips, Petr Kahan who etched silver tips for FIB milling and Amandeep Sagwal. Martin Švec as the last author of all papers supervised the experiments, but also analyzed data and created figures mainly for publications No 2 and 5. All authors discussed the data and contributed to the preparation of the manuscripts.